University of Groningen

New insights and predictions on high-redshift galaxies from wide-area infrared surveys

van Mierlo, Sophie Emiley

DOI:
10.33612/diss.922211586

IMPORTANT NOTE: You are advised to consult the publisher's version (publisher's PDF) if you wish to cite from it. Please check the document version below.

Document Version
Publisher's PDF, also known as Version of record

Publication date:
2024

Link to publication in University of Groningen/UMCG research database

Citation for published version (APA):
van Mierlo, S. E. (2024). *New insights and predictions on high-redshift galaxies from wide-area infrared surveys*. [Thesis fully internal (DIV), University of Groningen]. University of Groningen. https://doi.org/10.33612/diss.922211586

Copyright
Other than for strictly personal use, it is not permitted to download or to forward/distribute the text or part of it without the consent of the author(s) and/or copyright holder(s), unless the work is under an open content license (like Creative Commons).

The publication may also be distributed here under the terms of Article 25fa of the Dutch Copyright Act, indicated by the “Taverne” license. More information can be found on the University of Groningen website: https://www.rug.nl/library/open-access/self-archiving-pure/taverne-amendment.

Take-down policy
If you believe that this document breaches copyright please contact us providing details, and we will remove access to the work immediately and investigate your claim.

Downloaded from the University of Groningen/UMCG research database (Pure): http://www.rug.nl/research/portal. For technical reasons the number of authors shown on this cover page is limited to 10 maximum.

Download date: 24-06-2024

New insights and predictions on high-redshift galaxies from wide-area infrared surveys

Sophie Emiley van Mierlo

university of groningen

faculty of science
and engineering

kapteyn astronomical
institute

The work described in this thesis was carried out at the Kapteyn Astronomical Institute at the University of Groningen.

Cover design: Sophie van Mierlo
Cover image: Hand-drawn pictures of real galaxies identified from the *JWST*/NIRCam F277W/F356W/F444W composite image in PRIMER. The galaxies' redshifts increase consecutively in rows from left to right, and subsequently in columns from the bottom up, ranging from $z = 0$ in the lower left corner to $z = 7$ in the upper right corner.

rijksuniversiteit
groningen

New insights and predictions on high-redshift galaxies from wide-area infrared surveys

Proefschrift

ter verkrijging van de graad van doctor aan de
Rijksuniversiteit Groningen
op gezag van de
rector magnificus prof. dr. ir. J.M.A. Scherpen
en volgens besluit van het College voor Promoties.

De openbare verdediging zal plaatsvinden op

dinsdag 19 maart 2024 om 12.45 uur

door

Sophie Emiley van Mierlo

geboren op 16 juli 1996
te Stramproy

Promotores

Prof. dr. K.I. Caputi
Prof. dr. P. van der Werf

Beoordelingscommissie

Prof. dr. R.F. Peletier
Prof. dr. M.J. Jarvis
Prof. dr. C. Maraston

Voor het thuisasiel.

CONTENTS

1

INTRODUCTION

In order to understand the Universe as we see it today, it is crucial that we study its formation and development from early on. We want to observe the change of galaxy properties over time, starting at the earliest point of galaxy formation: the Epoch of Re-ionization. During this time, the first stars began to form and ionize their surroundings, allowing stellar light to pierce the neutral hydrogen state of the Universe. Important questions in galaxy evolution are when exactly the first galaxies formed, what the physical properties of these primordial galaxies are, and how they evolve over time to resemble what we observe in the local Universe.

1.1. ON THE IMPORTANCE OF STUDYING GALAXIES IN THE EARLY UNIVERSE

After the first $\sim 380\,000$ years since the formation of our Universe, when the temperature had dropped sufficiently due the expanding space and the ionized electrons and protons that slowly formed after the Big Bang first recombined into neutral hydrogen, the Universe underwent its first phase transition. Photons that were previously coupled to ionized matter could finally escape, which we detect nowadays as the cosmic microwave background (CMB). With no significant radiation sources to be found, the Universe entered an epoch called the Dark Ages. During this phase, hydrogen remained largely neutral, with the occasional photon being emitted at $\lambda = 21$ cm through the rare electron spin-flip transition. However, during these times, small fluctuations in the dark matter density field started growing via gravitational instability, collapsing into the first haloes. If the halo was massive enough, baryonic material would fall in and condense into the first stars and galaxies.

The formation of the first stars marks the end of the Dark Ages and the start of the Epoch of Re-ionization (EoR). These first stars are thought to be extremely luminous, massive, and hot due to the abundance of pristine gas, its lack of metal enrichment inhibiting the cooling processes. The extreme flux of rest-frame ultraviolet (UV) photons originating from these sources started to ionize the surrounding neutral Universe, creating bubbles of ionized hydrogen gas, and thus prompting a second phase transition on our cosmic timeline. Re-ionization is thought to be a patchy and inhomogeneous process with local variations in the neutral gas fraction (e.g., Pentericci et al. 2014; Becker et al. 2018; Tilvi et al. 2020), until the bubbles finally overlapped into a largely ionized intergalactic medium as we observe today.

Determining the exact start and duration of the EoR is a difficult task, as the very first stars are only pinpricks of light in a vastly neutral Universe that obscures their light from us observers. Currently, it is believed that the process of re-ionization started at $z \sim 30$ and ended at $z \simeq 6$–8 (Dayal & Ferrara, 2018), although evidence for a late scenario where re-ionization only ends at $z \sim 5.5$ is accumulating steadily (e.g, Bosman et al. 2022; Zhu et al. 2022). These constraints on the ending of the EoR are measured from the rest-frame spectra of ultra-luminous quasars at $z > 5$, in which a complete absorption of the flux bluewards of Lyα emission by the neutral hydrogen is observed (the so-called Gunn-Peterson trough; Gunn & Peterson 1965). Small transmission spikes and dark gaps at these wavelengths trace the abundance of ionized patches. Alternatively, the timing of the EoR can be derived from the dampening of small-scale anisotropies in the CMB caused by Thompson scattering of the CMB photons and free electrons, which put the height of re-ionization at $z = 7.7$ (Planck Collaboration et al., 2020). A final but crucial constraint comes from tracing high-redshift star-forming galaxies that emit Lyα photons at $\lambda = 1216\,\text{Å}$. The detection of so-called Lyα emitters (LAEs) at $z > 6$ is strongly inhibited as the Lyα photons are scattered from the line-of-sight by volumes of neutral hydrogen in the IGM. Therefore, the observed declining fraction of LAEs between $z = 6$–8 has been interpreted as direct evidence for re-ionization (e.g., De Barros et al. 2017; Mason et al. 2018).

Various potential drivers of re-ionization have been considered over the years, including black holes and annihilating dark matter, but the consensus is that re-ionization is primarily driven by faint, low-mass, star-forming galaxies, as demonstrated by both observations (e.g., Bouwens et al. 2015; Finkelstein et al. 2015; Robertson et al. 2015) and theoretical models (e.g., Choudhury & Ferrara 2007; Mason et al. 2015; Dayal et al. 2020). However, to what degree exactly is still uncertain, as it depends on poorly constrained parameters such as the initial stellar mass function (IMF) of high-redshift galaxies (e.g., Jermyn et al. 2018; Parsons et al. 2022), the production efficiency of Lyman continuum (LyC) photons and the escape fraction of LyC photons (see Fig. 15 in Dayal & Ferrara 2018; Trebitsch et al. 2017; Saxena et al. 2023).

In conclusion, tracing galaxy evolution all the way back to the EoR is an important but challenging endeavor. The number densities and physical properties of $z > 6$ galaxies provide key information regarding the state of the early Universe, and place crucial constraints on galaxy formation models. However, their study is inhibited by their poor visibility and subsequent lack of statistically relevant samples, such that variation in detection techniques and cosmic variance itself introduce significant uncertainty in their perceived nature. To expand our current sample of securely detected high-redshift galaxies with deep photometric and spectroscopic campaigns and consistent analysis tools is therefore an ongoing effort in the astronomy community, and should provide valuable insights as to how the Universe we live in today came into existence.

1.2. EVOLUTION OF HIGH-Z GALAXIES FROM THE PERSPECTIVE OF IR GALAXY SURVEYS

One of the ultimate goals in galaxy evolution studies is to construct a complete picture of the formation of stars and subsequent assembly of galaxy stellar mass M_* through cosmic time. In this section, I explain how observations at infrared (IR) wavelengths contribute to this aim, by discussing star formation rate (SFR) tracers at high-redshift and the resulting studies of the cosmic star formation rate density. I then highlight the importance of the galaxy stellar mass function and SFR-M_* relation as diagnostic tools.

1.2.1. PHYSICAL PROCESSES TRACED BY REST-FRAME IR LIGHT

For the longest part of human existence, we have perceived the Universe through the optical light emitted by relatively hot and young stars. However, the thermal view of our Universe is just as important, as it emerges from a myriad of physical processes - tracing stars, planets, and their building blocks. The rest-frame near-infrared (NIR) regime, with wavelengths spanning $\lambda \sim 1$–$5\ \mu$m, is dominated by the light from cooler, red stars. Amongst them are red dwarfs, which are invisible to rest-frame optical studies but are the most abundant type of star, and red giants, which are low- to intermediate-mass stars that are nearing the end of their lifespan. As NIR light is transparent to dust, it provides a direct tracer of the older, established population of stars in a galaxy, which can be converted to a stellar mass measurement assuming a certain mass-to-light ratio (M/L).

Moving toward redder wavelengths, the mid-infrared (MIR) light at $\lambda \sim 5$–$40\ \mu$m traces a complex mix of physical processes. The underlying continuum is dominated by warm dust. Silicate and carbonaceous dust grains in the interstellar medium (ISM) will subsequently absorb and re-emit the UV light from stars at longer wavelengths. In addition, active galactic nuclei (AGN) play an important role in this regime, as they are surrounded by a thick torus of dust, which is heated from the highly energetic radiation produced by the AGN. Lastly, the presence of complex molecules called polycyclic aromatic hydrocarbons give rise to distinct spectral features between 3 and 17 μm, which provide insight into the chemistry of the ISM.

Dust reprocessing further extends into the far-infrared (FIR) regime, $\lambda \sim 40$–$1000\ \mu$m, as the blackbody emission from cold dust dominates the smooth continuum at these wavelengths. As this light indirectly traces the young, UV-bright stellar population, it is a vital component for constraining the total SFR of a galaxy. The FIR SED also contains occasional molecular rotational emission lines, arising from giant molecular clouds where new stars are birthed in their dense cores.

It should be noted that the exact distinctions between the near-, mid-, and far-IR are not universally defined, although the IR luminosity is commonly measured between 8 and 1000 μm.

1.2.2. COSMIC STAR FORMATION DENSITY

There are several tools for measuring star formation in galaxies. The rest-frame UV luminosity measured at 1500-2000 Å is directly emergent from young, massive stars, such that it is sensitive to the global SFR but not to fluctuations on a 10^7 yr time span. Space-based facilities operating at UV to NIR wavelengths like the *Hubble Space Telescope* (*HST*) are capable of measuring the UV flux out to the EoR. The conversion from UV luminosity L_ν to $\mathrm{SFR_{UV}}$ is straightforward through the factor K_{UV}, which depends amongst others on the initial mass function (IMF) and galaxy metallicity. The greatest drawback for the $\mathrm{SFR_{UV}}$ is dust obscuration, as extinction is particularly strong in the UV. Corrections for dust extinction can be made, but require a good understanding of the galaxy SED and the color extinction $E(B-V)$. Alternatively, as dust re-emits the absorbed stellar UV light at IR wavelengths, the total IR luminosity at 8-1000 μm can be converted in an IR-based SFR, although in practice, AGN and older stars contribute to dust heating as well. A sub-/millimeter facility such as the Atacama Large Millimeter Array (ALMA) is ideal for tracing the $\mathrm{SFR_{IR}}$ back to the EoR through its broad and continuous sampling of the sub-mm wavelength regime. Ideally, panchromatic observations for the galaxy of interest are available, such that $\mathrm{SFR_{tot}} = \mathrm{SFR_{UV}} + \mathrm{SFR_{IR}}$ can be determined.

As young stars are surrounded by ionized gas in HII regions, nebular emission lines, e.g. hydrogen recombination lines Hα and Lyα, are also useful SFR indicators. In particular, photo-ionization of Hα is dominated by the intense UV radiation from OB stars, and the Hα line strength is known to be stable against variations in ISM density, enrichment, or temperature, such that it is considered a reliable SFR tracer. Especially toward higher redshifts, the Hα rest-frame equivalent width (EW) can easily reach values as large as 1000 Å such that Hα SFRs can even be derived from broad-band photometry rather than precise line spectroscopy (Mármol-Queraltó et al., 2016; Smit et al., 2016; Caputi et al., 2017; Faisst et al., 2019).

The cosmic star formation rate density (SFRD) is one of the most important tools to trace galaxy evolution over time. It describes total number of stars formed per year in a certain cosmological volume at a certain redshift. It has been long established that the SFRD peaks at $z \sim 2$ ('cosmic noon', ~ 3.5 billion years after the Big Bang) and steadily declines toward the present time, such that global star formation has slowly diminished as material gets locked into existing stars (Madau & Dickinson, 2014). However, at $z \gtrsim 6$ ('cosmic dawn', ~ 1 billion years after the Big Bang), the SFRD is difficult to constrain, as sample sizes of EoR galaxies are small. Prior to the *James Webb* Space Telescope (*JWST*), UV luminosity-based cosmic SFRD determinations have been constructed out to $z = 9$ (e.g., Finkelstein et al. 2015; Bouwens et al. 2022).

However, in order to reconstruct the complete picture of high-redshift star formation, it is necessary to extend the studies from the rest-frame UV/optical to FIR wavelengths, to take into account the reprocessing of stellar light by cosmic dust grains. In fact, several studies have shown that the SFRD is dominated by dust-obscured star formation out to at least $z = 4$ (Bouwens et al., 2016; Dunlop et al., 2017; Gruppioni et al., 2020; Zavala et al., 2021). Recently, Algera et al. (2023) used ALMA observations of 45 $z \sim 7$ galaxies from the REBELS program (Bouwens et al., 2022) to show how the dust-obscured cosmic SFRD only moderately decreases from $z = 3$ to $z = 7$, such that the contribution of dust-obscured star formation to the SFRD at $z = 7$ is still 30 %. For illustration, I show the dust-obscured SFRD

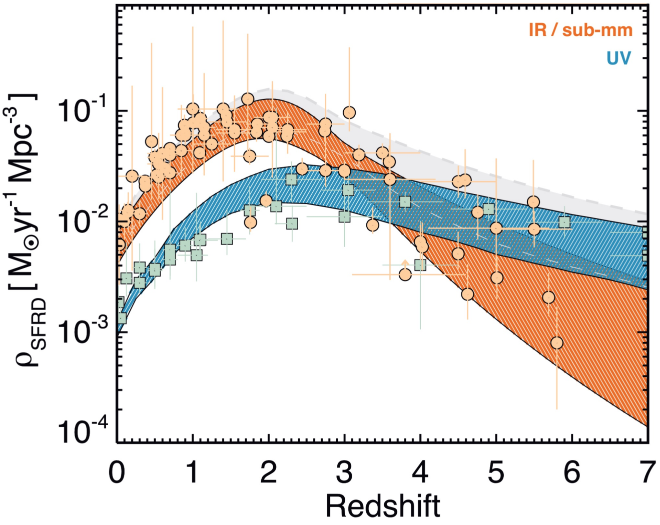

Figure 1.1 | Figure adapted from Zavala et al. (2021), showing the cosmic star formation rate density at $z = 0$–7. The orange and blue shaded regions show the dust-obscured SFRD based on IR/sub-mm surveys and the unobscured SFRD from rest-frame UV optical surveys, respectively (latter taken from Finkelstein et al. 2015.) The total inferred SFRD as derived by Zavala et al. (2021) is shown in grey.

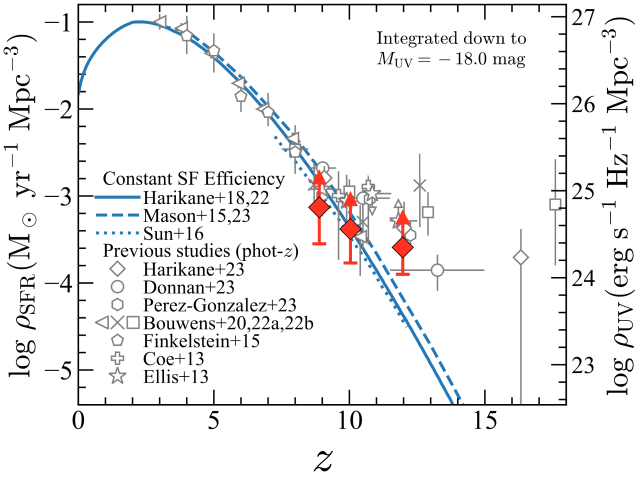

Figure 1.2 | Figure adapted from Harikane et al. (2023a), showing the cosmic star formation rate density at $z = 0$–18. The red diamonds represent the SFRD constraints from a sample of 25 spectroscopically-confirmed $z = 8.6$–12.3 galaxies obtained in Harikane et al. (2023a). Results from recent *JWST*-based photometric studies as well as other UV-based studies from the literature are shown, together with model predictions on the SFRD assuming a constant star formation efficiency.

determinations at $z = 0$–7 from Zavala et al. (2021) in Fig. 1.1 in orange, as determined from the 2 mm MORA survey. Shown in blue is the average unobscured SFRD derived from rest-frame UV optical data, not corrected for dust attenuation (Finkelstein et al., 2015).

The minor but significant contribution of dust-obscured star formation to the cosmic SFRD during the EoR is a puzzling discovery. Since metals are produced by stars, it would be expected that the first galaxies have very low dust content that is only slightly enriched by Population III stellar endings. However, *JWST* detections of abundant dusty star-forming galaxy populations at $z = 2$–6 that were previously undetected in optical/NIR studies (Barrufet et al., 2023; Pérez-González et al., 2023), together with the discovery of highly dust-obscured galaxies at $z > 7$ (Akins et al., 2023) prove that the role of dust during the first few billions years of the Universe is larger than expected, and careful evaluation of dust-producing mechanisms at high-z is necessary.

Lastly, in the past year, *JWST* observations have extended the study of the cosmic SFRD all the way to $z \sim 13$ with statistically meaningful samples. In Fig.1.2, I show the SFRD from Harikane et al. (2023b), which was constructed from 25 galaxies at spectroscopically-confirmed redshifts $z = 8.6$–13.2 from *JWST*/NIRSpec observations. They found that the SFRD is ~ 5 times higher at $z \sim 12$ than what is expected from model predictions assuming a constant star formation efficiency. Indeed, other authors have found supporting evidence for larger specific star formation rates (sSFRs) and increased star formation efficiency at early times (e.g., Bouwens et al. 2023; Endsley et al. 2023; Qin et al. 2023; Whitler et al. 2023). Harikane et al. (2023b) list alternative explanations for the perceived increase at $z \sim 12$, such as AGN contamination of the UV light, a top-heavy IMF, a larger scatter in the halo mass to SFR relation, or simply cosmic variance. As the *JWST*-discovered sample of EoR galaxies steadily grows, time will shed more light on star formation in the very first galaxies.

1.2.3. TRACING THE BUILD UP OF STELLAR MASS THROUGH TIME

One of the biggest questions in galaxy evolution is when the bulk of stellar mass in our Universe was formed. Our current understanding of galaxy evolution is that of a bottom-up scenario: small, dwarf-like galaxies form first, and subsequently merge into larger galaxies whilst at the same time growing through gas accretion. As discussed in the previous section, the cosmic SFRD peaks at $z \sim 2$, such that most of the material available for star formation is already locked into place when the Universe was only ~ 3.5 billion years old. However, detections of extremely massive galaxies ($M_* \sim 10^{11}$) in the first few billions years of the Universe raise important questions on how rapidly galaxy mass assembly takes place from the very first galaxies (Caputi et al., 2006, 2015).

Stellar masses are relatively straightforward to measure from photometry, as the normalization of the SED fit scales directly with the stellar mass. The galaxy luminosity derived from that normalization is converted into a stellar mass through a certain assumed M/L. The M/L correlates with galaxy optical/NIR colors, such that the reddest galaxies have the largest ratios (Bell & de Jong, 2001). The reference band for this normalization should be minimally effected by M/L variations through stellar population properties (age, metallicity, star formation history) and dust attenuation, e.g., the rest-frame K-band

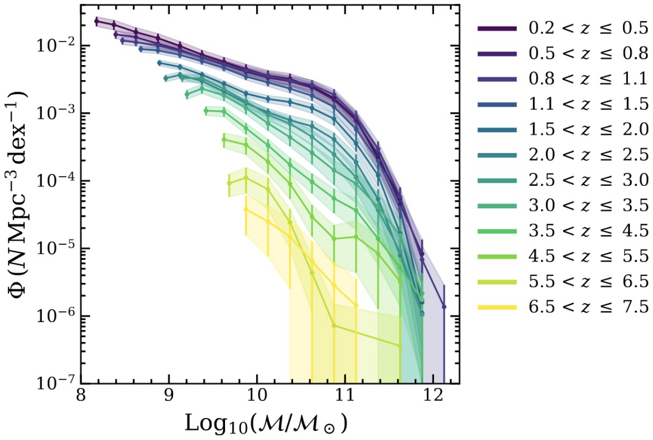

Figure 1.3 | Figure adapted from Weaver et al. (2022a), showing the galaxy stellar mass function over 12 redshift bins spanning $z = 0.2$–7.5 constructed over 1.3 deg^2 of the COSMOS field, demonstrating smooth, monotonic evolution in the GSMF over the vast majority of cosmic time.

at $\sim 2.2\,\mu$m (e.g., Caputi et al. 2006).

The galaxy stellar mass function (GSMF) represents the number density of galaxies binned by stellar mass at a certain redshift. Studying its shape and evolution with time provides valuable understanding of the build up of stellar mass through the history of the Universe, and the physical processes that shape galaxy assembly such as supernova and AGN feedback. In addition, the GSMF provides important constraints for theoretical models and numerical simulations (see Dayal & Ferrara 2018 for a review). Naturally, the GSMF has been studied in numerous works, with ever increasing completeness in probed mass and redshift range (e.g., Peng et al. 2010; Caputi et al. 2011; Muzzin et al. 2013; Grazian et al. 2015; Song et al. 2016; Deshmukh et al. 2018; McLeod et al. 2021; Weaver et al. 2022a; Navarro-Carrera et al. 2023; Santini et al. 2023). As an example, I show the GSMF study from Weaver et al. (2022b) in Fig. 1.3, determined for 12 redshift bins spanning $z = 0.2$–7.5 and constructed over 1.3 deg^2 of the COSMOS field.

As seen in Fig. 1.3, the normalization of the GSMF rapidly evolves from the EoR to $z = 2$. In addition, the faint-end slope of the GSMF flattens over cosmic time, such that low-mass galaxies were relatively more abundant at early times. The general consensus is that the GSMF can be parameterized by a Schechter function (Schechter, 1976), such that the number density at the low-mass end is governed by a power law with slope α, which turns over at the characteristic mass M^* into an exponential drop-off at the high-mass end.

The study of massive galaxies in the first few billion years of the Universe can provide valuable insights into the processes that facilitate rapid mass assembly. Although these sources are relatively rare compared to low-mass galaxies (see Fig. 1.3), many examples have been found out to $z \sim 6$ (e.g., Caputi et al. 2011, 2015; Stefanon et al. 2015; Glazebrook et al. 2017; Deshmukh et al. 2018; Marsan et al. 2022), providing decent constraints on the high-mass end of the GSMF. However, recent advents with the *JWST* are discovering an abundance of massive ($\log(M_*/M_\odot) \simeq$ 10-11) quiescent galaxies at $z = 3$–5 (Carnall et al., 2023a; Nanayakkara et al., 2022; Pérez-González et al., 2023; Rodighiero et al., 2023). These galaxies, that are no longer forming significant amounts of new stars, were previously undetected due to a lack of ultra-deep imaging at $\lambda < 2\,\mu$m. Because of their quiescent nature, such galaxies must have formed the bulk of their stellar mass by $z = 10$, creating tension between observations and models that struggle to reproduce such rapid mass assembly and extreme quenching necessary for $z > 3$ quiescent galaxies.

Stellar mass studies of the high-redshift Universe greatly benefit from the new *JWST* observations in general. Previous studies based on *HST* and *Spitzer* imaging suffered from the limited wavelength coverage from *HST* filters, such that these data by itself are sensitive to stellar masses up to $z \sim 3$, and from the poor IRAC resolution. In addition, the *HST* imaging of $z > 3$ galaxies samples the UV spectrum which is affected by dust, but a lack of consensus exists on the dust attenuation curve of high-redshift galaxies (e.g., Ferrara et al. 2022). Improper constraining of the dust attenuation in high-redshift galaxies can introduce significant uncertainties in the SED fitting and therefore stellar mass. With the extensive IR wavelength coverage of the *JWST*, stellar masses of EoR galaxies can now be probed in a direct and resolved manner instead. In fact, Santini et al. (2023) already demonstrated that NIRCam data for $z > 7$ galaxies improves the stellar mass accuracy by at least a factor 5–10 compared to previous high-quality data sets.

Toward the EoR, the number of massive galaxies is expected to decline dramatically. However, in the first months since the *JWST* has commenced observations, surprisingly many luminous and massive galaxy candidates at high-redshift have been identified (e.g., Carnall et al. 2022; Castellano et al. 2022; Finkelstein et al. 2022; Naidu et al. 2022a; Adams et al. 2023; Atek et al. 2023a,b; Donnan et al. 2023; Labbé et al. 2023), finding galaxies with $\log(M_*/M_\odot) \simeq$ 10-11 at $z =$ 6-10. Some works claim to find EoR galaxies so massive that they are in tension with number density upper limits assuming our current ΛCDM cosmology (Behroozi & Silk, 2018; Boylan-Kolchin, 2022; Naidu et al., 2022b; Labbé et al., 2023; Prada et al., 2023).

Naturally, the legitimacy of these high stellar masses has been thoroughly questioned in the past months. Strong variations in photometric redshifts from different studies of the same *JWST* galaxies have already been observed (Adams et al., 2023), which naturally lead to entirely different mass estimates for the same galaxy. Santini et al. (2023) found a large scatter in the UV M/L of *JWST* $z > 7$ galaxies, which can affect template-derived stellar masses. Steinhardt et al. (2023) showed how adopting an IMF optimized for EoR astrophysics yields significantly lower stellar masses than using a Galactic IMF. de Barros et al. (2014) already showed that the inclusion of nebular emission lines for SED templates leads to lower stellar mass estimates, which is relevant for *JWST* high-redshift science, as various works are finding high EW for O[III]+Hβ, Hα and other emission lines at $z > 6$ (e.g., Adams et al. 2023; Matthee et al. 2023; Rinaldi et al. 2023). Finally, multiple works have shown how non-parametric SFHs systematically overestimate stellar masses of $z > 7$ galaxies, as compared to traditional parametric SFHs (Tacchella et al., 2022; Topping et al., 2022b; Whitler et al., 2022). In conclusion, all of the above mentioned issues can significantly affect stellar mass estimates for early Universe galaxies, and should be critically evaluated before taking $\log(M_*/M_\odot) \approx 11$ results at face value.

1.2.4. A CORRELATION BETWEEN SFR AND STELLAR MASS

Over the past two decades, many different works have established that the bulk of star-forming galaxies lie on a tight relation between the stellar mass and SFR (e.g., Noeske et al. 2007; Rodighiero et al. 2011; Speagle et al. 2014; Whitaker et al. 2014; Schreiber et al. 2015; Caputi et al. 2017; Santini et al. 2017; Khusanova et al. 2021; Rinaldi et al. 2022. This empirically-derived, so-called star-forming main sequence (MS) implies that more massive galaxies are forming stars at higher rates. The tightness of this relation suggests that star formation is typically governed by steady gas accretion. Additionally, the normalization of the MS appears to evolve with redshift, such that the sSFRs of galaxies increase toward early times (Speagle et al., 2014). Indeed, sub-/mm studies have shown how at fixed stellar mass, the molecular gas mass increases with redshift at fixed stellar mass, such that more fuel for star formation is available (e.g, Tacconi et al. 2018; Liu et al. 2019a).

Beyond the typical scatter in the SFR-M_* relation, a minor population of star-forming galaxies appear to have significantly higher sSFRs. These so-called starburst (SB) galaxies are in a presumably temporary phase of enhanced star formation, which may be explained by stochastic process such as major gas-rich mergers, or intrinsic processes such as having overall higher star formation efficiency than typical star-forming galaxies. In the local Universe, SB galaxies are rare, but their incidence steadily increases toward $z \sim 2$, albeit still forming a minority of star-forming galaxies (Rodighiero et al., 2011; Bisigello et al., 2018). Going to higher redshifts, the starburst fraction can range significantly between different works, at least in part because there is no official definition of a starburst galaxy. Miettinen et al. (2017) showed that for a large sample of sub-mm detected galaxies at a median redshift of $z = 2.3$, the fraction of starburst is as high as $\sim 40\%$. In addition, Rinaldi et al. (2022) have recently shown that at $z = 3$–6.5, the starburst fraction is at least $\sim 20\,\%$ amongst star-forming galaxies of $\log(M_*/M_\odot) \gtrsim 9$, and are especially abundant at $z = 4$–5, constituting 40 % of the star-forming population.

I show a selection of SFR-M_* relations taken from the literature in Fig. 1.4, mostly focused on the epoch $z = 4$–5. For each relation, I indicate at what redshift it was measured and what SFR indicator was adopted, distinguishing between UV-based, Hα-based, and sub-mm based studies, as well as a composite study using some or all of the aforementioned SFR indicators. At $z = 4$–5, I show the relations from Caputi et al. (2017) (Hα-based) and Rinaldi et al. (2022) (UV-based), who both separate SB galaxies from MS galaxies. I also highlight the so-called starburst envelope, defined as sSFR $\geq -7.6\ \mathrm{yr}^{-1}$ by Caputi et al. (2021). Additionally, I include $z = 4$–5 relations from the literature that do not separate starburst galaxies, but rather fit the whole population with one relation (Speagle et al., 2014; Santini et al., 2017; Khusanova et al., 2021). Between these relations, the scatter in the MS normalization is as much as 1 dex.

It should be noted that a direct comparison between SFR-M_* relations should be done with care. The MS relation from Rinaldi et al. (2022) appears to lie below all other MS relations in Fig.,1.4, but this is because they explicitly separate the SFR-M_* plane into the SB and MS populations. Between the other works at $z = 4$–5, the scatter is only ~ 0.5 dex. To demonstrate that indeed the normalization of the SFR-M_* relation increases towards higher redshifts, I also show the MS fits from Schreiber et al. (2015) at $z \sim 3$ and Whitaker et al. (2014) at $z = 2$–2.5. Whereas most works fit the MS with a simple linear

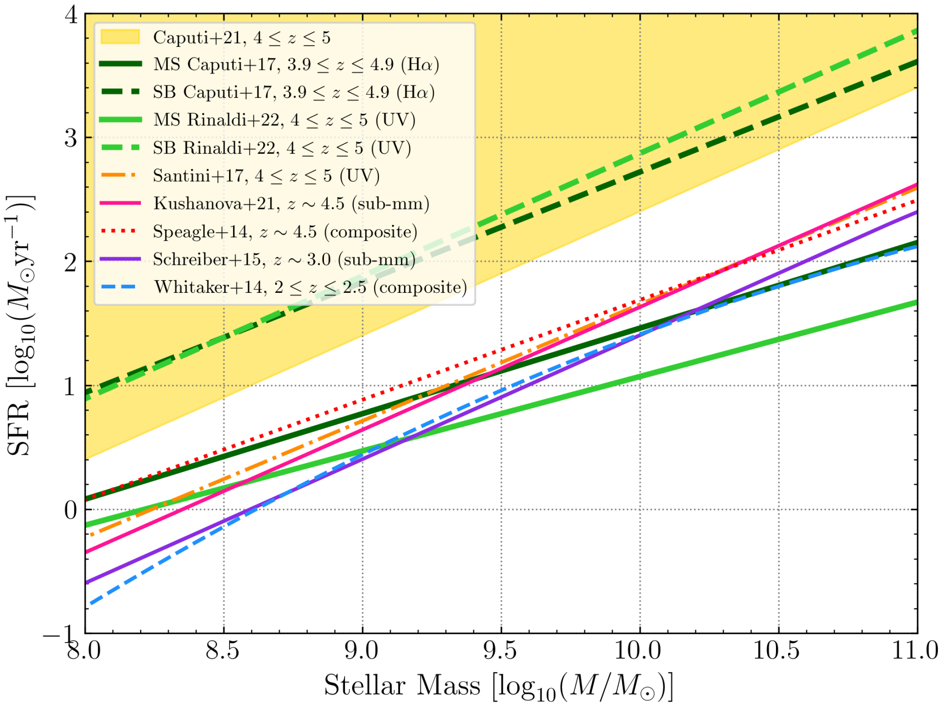

Figure 1.4 | The relation between star formation rate and stellar mass, taken from the literature. The starburst envelope as defined by Caputi et al. (2021) is shown with yellow shading. I show the main sequence relations at $z = 4$–5 (Speagle et al., 2014; Caputi et al., 2017; Santini et al., 2017; Khusanova et al., 2021; Rinaldi et al., 2022), where I indicate for each work if the SFRs were based on the rest-frame UV fluxes, sub-mm detections, Hα emission line measurements, or a composite of the aforementioned techniques. Additionally, I show the $z \sim 3$ relation from Schreiber et al. (2015) and the $z = 2$–2.5 relation from Whitaker et al. (2014).

relation, Whitaker et al. (2014) actually find a correlation between the MS slope and the stellar mass, observing a flattening in SFRs for the most massive galaxies, supported by the results from e.g. Tomczak et al. (2016). Finally, Shapley et al. (2023) have derived the Hα SFRs for $z = 2.7$–6.5 galaxies with *JWST*/NIRSpec, tracing for the first time the main-sequence at these redshifts with spectroscopic measurements.

1.2.5. THE ROLE OF POORLY-CONSTRAINED, OPTICALLY/NIR-FAINT GALAXIES

Even though most IR galaxy surveys are supported by deep ancillary UV/optical photometry, not all IR galaxies are detected at optical wavelengths. These galaxies are relatively bright at 3μm, but faint or even completely undetected at NIR wavelengths ($\lambda = 1$–3 μm), such that they are typically referred to as *H*-band dropout or *HST*-dark galaxies. These rather elusive, extremely red galaxies have long been at interest, and studies found them to mostly at $z = 3$–6 (e.g., Caputi et al. 2012; Wang et al. 2019), as significant contributors to the massive galaxy population (Caputi et al., 2015). Follow-up observations at sub-/mm wavelengths have identified these galaxies as dusty star-forming galaxies (e.g, Ikarashi et al. 2017; Shu et al. 2022), which are significant contributors to the cosmic SFRD at $z > 3$ (Zavala et al., 2021).

Pre-*JWST*, the *Spitzer* Space Telescope has enabled studies of galaxies with red NIR to MIR colors, finding that high equivalent emission lines such as Hα and O[III]+Hβ in high-redshift galaxies can significantly boost the IRAC 3.6 and 4.5 μm flux measurements (e.g., Smit et al. 2016; Roberts-Borsani et al. 2016; Caputi et al. 2017; Faisst et al. 2019). However, good constraints on the NIR SED are necessary to properly identify the IRAC flux excess in such galaxies; no particular connection between line emitters and true dropout galaxies has been found so far.

With the advent of the *JWST*, interest in H-dropout galaxies has surged once again, as *JWST* can provide deep, highly-resolved NIR to MIR data of these sources that finally constrain their physical properties. Several recent works have studied *HST*-dark galaxies with *JWST*/NIRCam data, finding them to be mostly star-forming galaxies at z =2–8 that are massive with $\log(M_*/M_\odot)$ = 9–11 and highly dust-obscured (Barrufet et al., 2023; Nelson et al., 2023; Pérez-González et al., 2023; Rodighiero et al., 2023). Instead, some of these extremely red sources are identified as extremely massive, quiescent galaxies at $z = 3$–5, or young starburst galaxies with high equivalent-width emission lines at $z = 6$–7 (Pérez-González et al., 2023; Rodighiero et al., 2023).

JWST has also been used to follow up on a sub-mm galaxy that was previously undetected in any deep imaging at $\lambda < 850\,\mu$m, finding it to be an extremely dust-obscured galaxy at $z \sim 5$ (McKinney et al., 2023). Taking this further, Smail et al. (2023) have identified a $z = 4.3$ sub-mm galaxy that is wholly undetected at $\lesssim 2\,\mu$m, even with *JWST*, and found it be highly dust obscured and extremely massive with $\log(M_*/M_\odot) = 11.8$.

In conclusion, the recent discoveries on the abundance of massive and dusty galaxies at $z > 2$ demonstrate that our knowledge on the contribution of dusty star-forming galaxies to both the cosmic SFRD and the GSMF is far from complete, such that these galaxies play greater roles in galaxy formation and evolution than previously thought.

1.3. IDENTIFICATION OF GALAXIES WITH LARGE PHOTOMETRIC SURVEYS

Galaxy populations are typically studied in a few select fields on the sky, in which many different telescopes operating at different wavelengths have conducted observations, in an effort to create a complete multiwavelength coverage of these extragalactic fields. Examples of such well-studied fields are the Cosmic Evolution Survey (COSMOS; Scoville et al. 2007), the Hubble Ultra Deep Field (HUDF; Beckwith et al. 2006) and the Great Observatories Origins Deep Survey (GOODS; Giavalisco et al. 2004). These collective efforts provide a wealth of information spanning from X-ray to radio wavelengths, which many research groups have used to characterize the properties of galaxies from present time down to the formation of the very first galaxies (e.g., Skelton et al. 2014; Laigle et al. 2016; Weaver et al. 2022b).

On a galaxy-to-galaxy basis, the most fundamental parameter to constrain is the redshift z. It denotes how much the light coming from the galaxy has been stretched out as it travels through the expanding Universe toward us; to know the redshift is to know the location of the galaxy in space and time. The redshift is most precisely measured from spectroscopy; by comparing observed spectral lines with composite rest-frame stellar models, the wavelength shift between them, which goes as $\sim 1/(1+z)$, enables us to measure the redshift. Large efforts have been dedicated to obtain spectroscopy in the aforementioned extragalactic fields (e.g., Lilly et al. 2007; Le Fèvre et al. 2015; Inami et al. 2017; Hasinger et al. 2018). However, spectroscopy is costly both in observation time and data analysis, such that it remains challenging to study spectroscopically-identified galaxy populations with large statistics.

A more efficient although less precise alternative to spectroscopy is to determine galaxy properties from photometric measurements. With this technique, the galaxy spectrum can be broadly constrained by measuring its light directly from images at different wavelengths. Using photometry, the galaxy redshift can be determined by employing the Lyman Break technique (Steidel et al., 1996): all photons emitted by the galaxy at wavelengths $< 912\,\text{Å}$ are absorbed by neutral hydrogen present in the Universe, resulting in a sharp drop in its observed spectrum, i.e. the Lyman break. By comparing images at succeeding wavelengths, one can identify at which wavelength the galaxy "disappears" in the observer frame, thereby deriving its so-called photometric redshift. The accuracy of this technique relies on the number of photometric measurements available, which should sample a wide wavelength range, ideally covering the rest-frame UV to IR spectrum of the galaxy.

1.3.1. THE BASICS OF SPECTRAL ENERGY DENSITY FITTING

Spectral energy density (SED) fitting is a common practice that utilizes the Lyman break and other characterizing features in the galaxy spectrum to determine its redshift from photometry. In essence, SED fitting codes compare the galaxy photometry with synthetic fluxes generated in the observed filter set drawn from stellar population models, to recover the model that best fits the data. I show the basics of the SED-fitting process by means of a flowchart taken from Pacifici et al. (2023) in Fig. 1.5. The choice of SED-fitting code is highly dependent on the input data, such that there must be a match in wavelength range and redshift regime in which the code operates. Moreover, the choice of priors applied in the SED-fitting is of critical importance; the user needs to define the parameter space in advance, i.e., making appropriate range assumptions for e.g. the IMF, stellar population models, emission line recipes, dust attenuation, metallicity, and star formation history. Most importantly, these choices need to make physical sense, where empirical priors are incredibly useful. For example, it has been shown that the SFR is universally correlated with stellar mass (e.g., Whitaker et al. 2012; Schreiber et al. 2015; Rinaldi et al. 2022), or that the high-redshift galaxies are generally more metal-poor than low-redshift equivalents (e.g., (Tremonti et al., 2004; Maiolino et al., 2008)). Especially when fitting a large, blind sample of galaxies, their properties unknown, it is important to verify that the chosen parameter space is appropriate, for example by comparing the observed photometric colors with those of the models. Priors can additionally be verified by evaluating the output of the SED fitting for a spectroscopic validation sample. All

Figure 1.5 | Figure taken from Pacifici et al. (2023), illustrating the basic flow of the SED-fitting process.

together, these considerations make SED fitting a highly iterative process.

The basic ingredients to model the SED of a simple stellar population (SSP) are stellar evolution theory, an IMF, and stellar spectral libraries. The latter can be theoretical and/or empirical; theoretical models are susceptible to approximations due to our limited knowledge on the inner workings of stars, but allows one to include stellar spectra that are not directly observable (i.e., those of low-metallicity, population III stars; vice versa for empirical libraries). Examples of stellar evolutionary models are the so-called Padova 1994 isochrones (Alongi et al., 1993; Bressan et al., 1993; Fagotto et al., 1994a,b; Girardi et al., 1996) and the MESA Isochrones and Stellar Tracks (MIST; Choi et al. 2016; Dotter 2016), which can be can be combined with stellar spectra from for example the semi-empirical BaSeL 3.1 library (Lejeune et al., 1997, 1998; Westera et al., 2002), the observational STELLIB library (Le Borgne et al., 2003), and the observational MILES library (Falcón-Barroso et al., 2011). Subsequently, by making assumptions on the chemical enrichment history and star formation history (SFH), the SSPs are combined into composite stellar population (CSPs). These contain stars with both a range in age and metallicity, as well as dust. An abundance of stellar population libraries are available in the literature (e.g., Leitherer et al. 1999; Bruzual & Charlot 2003; Maraston 2005; Conroy et al. 2009). I refer the reader to Conroy (2013) for a thorough review on the intricacies of stellar population synthesis.

A traditional treatment of the SFH is an exponentially declining function $\propto e^{-t/\tau}$, although recently, flexible, non-parametric descriptions of the SFH have risen in popularity, which account for star formation triggering events that a galaxy may experience later on its life. The choice of SFH can have significant consequences for estimation of galaxy parameters such as stellar mass and age, introducing variations of 0.1–0.5 dex (Carnall et al., 2019; Tacchella et al., 2022).

The second step in SED fitting is to compare the theoretical galaxy SEDs with the observed data. Synthetic observed fluxes need to be derived from these theoretical SEDS, which involves redshifting and sampling them through the filter response curves of the instruments. As many research groups have developed their own SED fitting frameworks over time, there are various methods to achieve this. Some codes like LEPHARE (Arnouts et al., 1999; Ilbert et al., 2006), MAGPHYS (da Cunha et al., 2008, 2015; Battisti et al., 2020), and CIGALE (Burgarella et al., 2005; Noll et al., 2009; Boquien et al., 2019) construct very large libraries of pre-compiled galaxy SEDs or galaxy colors; other codes like EAZY (Brammer et al., 2008; Kriek et al., 2009) or STARDUST (Kokorev et al., 2021) use more economical solutions by constructing galaxy templates from linear combinations, thereby reducing the parameter space and thus the compilation time. Some SED fitting codes such as BAGPIPES (Carnall et al., 2018) and PROSPECTOR (Johnson et al., 2021) even forgo the template library construction, but rather build the theoretical templates on the fly whilst using a nested sampler to converge on the best-fit physical parameters. The latter two codes incorporate highly customizable models for stellar, nebular and dust emission components of the galaxy.

To decide on said best-fit parameters, again, different codes employ different methods. For example, LEPHARE operates under a frequentist approach: it returns one best-fit solution, based on a model SED χ^2-minimization routine against the observed photometry. However, if uncertainty on the photometry is large because of noisy imaging, this statistic may not necessarily return the most physically accurate solution. For example, when the probability distribution function (PDF) of the redshift is strictly bimodal, and a competing redshift solution is similarly viable, the best-fit redshift can be virtually meaningless. It is therefore highly recommended to critically evaluate the best-fit redshifts whilst taking into account the PDF(z). Alternatively, many SED fitting codes adopt a Bayesian approach, which critically assess the reliability of the model themselves, and evaluates a likelihood function. The redshift and SED of the source may then be derived as the maximization of said likelihood function or from a χ^2 evaluation, but most importantly, the PDF of each parameter can be investigated. This ensures that one can directly evaluate the usefulness of the prior choices, given that when the PDF of the prior is identical to that of the output parameter, this information is not used in the fit and may be reconsidered.

Another distinction between SED fitting codes is in which wavelength regime they operate. The UV to sub-mm wavelength regime is dominated by stellar light, either emitted directly by stars or absorbed and re-emitted by dust grains. However, only a subset of codes in the literature are panchromatic, suitable of including theoretical FIR to sub-mm galaxy SEDs. Examples are CIGALE, PROSPECTOR, STARDUST, and MAGPHYS, the latter which constrains the output of an SED using an energy balance argument between the stellar component and modeled dust SED. However, resolved observations of dusty star-forming galaxies have shown spatial offsets between the dust and stellar emitting regions (e.g., Hodge et al. 2016; Kaasinen et al. 2020), such that other codes do not employ this balancing argument (e.g., STARDUST). Considering the FIR data for a galaxy enables one to derive important parameters such as the IR luminosity, the IR SFR, the dust temperature, and dust mass.

Lastly, machine-learning techniques are also rapidly being developed, as these codes are fast and computationally inexpensive compared to traditional template-fitting methods. This makes them especially useful for large cosmological surveys, although machine-learning techniques under-perform toward higher redshifts (Euclid Collaboration: Desprez et al., 2020), as the availability of large, representative, spectroscopically-confirmed training samples is still lacking.

LIMITATIONS

It is well known that photometric redshift codes are prone to confusing certain low-redshift objects with high-redshift galaxies. Red galaxies are particularly sensitive to degeneracies, as their red observed UV to NIR colors can be explained through multiple physical phenomena. First and foremost, the observer-frame stellar spectrum may appear red because of the galaxy redshift: for example, at $z = 6$ the Lyman break redshifts beyond 6000 Å, such that instruments operating in the UV to near-visible regime would not detect any flux. However, dust absorbs UV light from young stars and re-emits it at FIR/sub-mm wavelengths, such that this obscuration can explain the red UV to NIR spectrum instead. Lastly, as a galaxy ages, it builds up a substantial population of older stars, which through chemical enrichment produce increasingly strong metal absorption lines in their atmospheres. As star formation eventually ceases over time, a deficiency of young, bright stars together with these absorption line cause a strong break in the galaxy spectrum at 4000 Å, the so-called Balmer break or 4000 Å break, which results in red UV to NIR colors. The redshift-age-dust degeneracy is problematic for SED fitting codes, but can be mitigated through physically-motivated priors for the mock SEDs.

To illustrate the typical photometric degeneracies from which SED fitting codes suffer, in Fig. 1.6, I provide an example of a high-redshift $z = 7.5$ galaxy which has a significant secondary solution at $z = 1.8$. The red $[Y - J]$ color combined with the flat spectrum redwards of the J band makes that this color can either be interpreted as the Lyman break of a high-redshift galaxy, or as the 4000 Å break for a dusty, low-redshift galaxy. In this scenario, the bimodal distribution favors the high-redshift solution, which seems reasonable given the low significance of the photometric data points at $< 1\mu$m.

Furthermore, it has been shown that cool, brown L, T, and Y dwarf stars have similar colors to Y-drop selected $z > 7$ galaxies and can therefore severely contaminate this high-redshift population (e.g., Stern et al. 2007; Wilkins et al. 2014). Another source of contamination are extreme emission line galaxies, that have faint continua and strong line emission, so that in flux-limited observations they can mimic the Lyman Break and contaminate sources at $z > 6$ (e.g., Atek et al. 2011; Huang et al. 2015).

Given the variety of SED fitting codes available in the literature, critical assessment between their performances is necessary. Dahlen et al. (2013) found between eleven

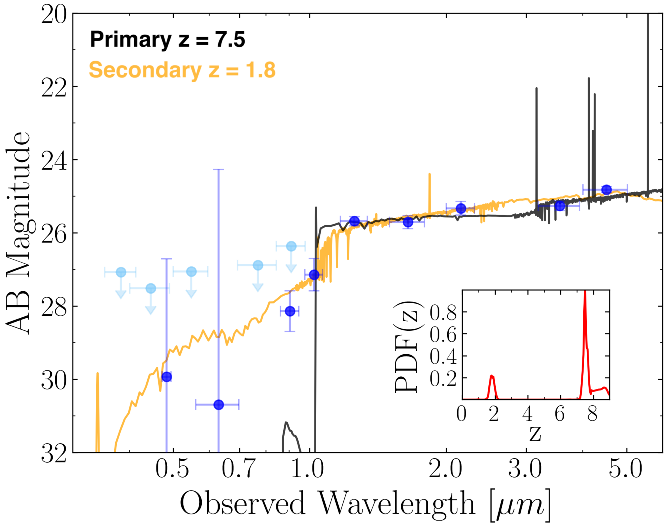

Figure 1.6 | Best-fit SED for a $z_{\rm phot} = 7.5$ galaxy that has a secondary solution at $z = 1.8$ (shown in orange). Photometric data points are shown in blue, upper limits in cyan. The probability distributions function of the redshift is shown in the inset panel.

template-fitting algorithms tested on a spectroscopic control sample spanning $z = 0$–6 that none of the codes produce significantly better photometric redshifts than the others. They do find that training on spectroscopic redshifts to improve the correspondence between the template SEDs and photometry through zeropoint corrections significantly improves the redshift results. Regarding physical parameters, on a photometric sample of $z \sim 3$ galaxies, Pacifici et al. (2023) show between fourteen codes that all return similar stellar mass distributions, with modeling uncertainties between the codes of 0.15-0.3 dex for the stellar mass, SFR, and dust attenuation A_V.

1.3.2. FACILITIES FOR HIGH-REDSHIFT SCIENCE

The works presented in this thesis are based on a wealth of data from different telescopes and instruments, operating at wavelengths spanning the optical to the mm regime. Here, I broadly describe their specifics and highlight important scientific contributions from the key facilities that have made this thesis possible.

THE *Spitzer* SPACE TELESCOPE

First and foremost, the vast majority of galaxies discussed throughout this thesis were either identified, or at least observed with the *Spitzer* Space Telescope (Werner et al., 2004). This 0.85 m telescope carries three instruments on board: an Infrared Array Camera (IRAC; Fazio et al. 2004), a Multiband Imaging Photometer (MIPS; Rieke et al. 2004), and an Infrared Spectrograph (IRS; Houck et al. 2004), that altogether sample the wavelength range 3.6 to 160 μm. As of early 2020, the telescope was decommissioned, but after 16 years of operations its contribution to understanding galaxy evolution has been of immeasurable value. In the high-redshift universe ($z > 6$), this telescope has been vital for constraining photometric redshift and granted us access to rest-frame optical properties such as stellar mass and age. The IRAC broad-band photometry at 3.6 and 4.5 μm was used to measure high $\mathrm{EW}_0 > 2000$ for nebular emission lines such as Hα and [OIII]+Hβ (e.g., Smit et al. 2014; Roberts-Borsani et al. 2016; Stefanon et al. 2019; Strait et al. 2020), painting a picture of more evolved galaxy populations in the early Universe than previously thought. At intermediate redshifts ($z = 2$–6), *Spitzer* has been able to provide robust stellar masses, as well as SFR estimates from MIR observations to contribute to our understanding of the cosmic star formation density (see Madau & Dickinson 2014 for a review). In addition, *Spitzer* was used to study Hα-derived SFRs at $z \approx 4$-5 in detail (Mármol-Queraltó et al., 2016; Smit et al., 2016; Caputi et al., 2017; Faisst et al., 2019). I refer the reader to Bradač (2020) for a great summary of *Spitzer*'s most important scientific contributions to high-redshift IR science.

Many campaigns have been undertaken with *Spitzer* (e.g., Giavalisco et al. 2004; Sanders et al. 2007; Postman et al. 2012; Ashby et al. 2013, 2015). Amongst the largest of these efforts is the *Spitzer* Matching Survey of the UltraVISTA ultra-deep Stripes (SMUVS; PI K. Caputi; Ashby et al. 2018), for which extremely deep (25 AB mag, 4σ) IRAC 3.6 and 4.5 μm imaging was obtained in the deepest parts of the UltraVISTA observations in COSMOS, over a total area of 0.66 deg^2. Because of this large area coverage and homogeneous sensitivity, this data has been and further will be of incredible use for numerous endeavors of high-redshift science (Caputi et al., 2017; Deshmukh et al., 2018; Cowley et al., 2019; Rinaldi et al., 2022).

THE *James Webb* SPACE TELESCOPE

The *James Webb* Space Telescope (*JWST*) is the highly-anticipated successor to *Spitzer* that began operations in July 2022, observing at NIR to MIR wavelengths with four instruments: a Near Infrared Camera (NIRCam), a Near Infrared Spectrograph (NIRSpec), a Near Infrared Imager and Slitless Spectrograph (NIRISS), and a Mid-Infrared Instrument (MIRI), that all together span the wavelength range 0.6 to 28.5 μm. Through its large 6.5 m primary mirror, *JWST* achieves resolution and sensitivity exceeding that of the *HST*, enabling us for the first time to study the observed optical to MIR SED with minimum source blending in the longest wavelength channels.

In the first year of operations, *JWST* has already revolutionized our understanding of the early Universe. Hundreds of $z > 7$ galaxies have been identified through imaging (Bradley et al., 2022; Naidu et al., 2022a; Topping et al., 2022a; Adams et al., 2023; Atek et al., 2023b; Austin et al., 2023; Carnall et al., 2023b; Casey et al., 2023a; Castellano et al., 2023; Endsley et al., 2023; Franco et al., 2023; Harikane et al., 2023b; Labbé et al., 2023; Rinaldi et al., 2023; Santini et al., 2023; Whitler et al., 2023), and even a significant number of galaxies at $z > 15$ have been discovered (Castellano et al., 2022; Naidu et al., 2022b; Atek et al., 2023a; Bouwens et al., 2023; Donnan et al., 2023). Moreover, with NIRSpec and NIRISS, *JWST* has been able to spectroscopically confirm a number of EoR galaxies (Roberts-Borsani et al., 2022; Álvarez-Márquez et al., 2023; Arrabal Haro et al., 2023; Cameron et al., 2023; Hsiao et al., 2023; Roberts-Borsani et al., 2023; Sun et al., 2023), going as far as $z \sim 13$ (Fujimoto et al., 2023; Harikane et al., 2023a; Robertson et al., 2023; Wang et al., 2023). These record-breaking discoveries have taken place over several surveys, including GLASS (Treu et al., 2022), UNCOVER (Bezanson et al., 2022), JADES (Eisenstein et al., 2023), COSMOS-Web (Casey et al., 2023b), CEERS (PI: S. Finkelstein), and PRIMER (PI: J. Dunlop). For the most part, these early Universe campaigns are finding young, low-metallicity galaxies with masses $\lesssim 10^8\,M_\odot$, but some studies have discovered unexpectedly massive galaxies ($\gtrsim 10^9 - 10^{10}\,M_\odot$) at these epochs (e.g., Naidu et al. 2022b; Casey et al. 2023a; Labbé et al. 2023), sparking discussion on galaxy formation theories beyond standard ΛCDM cosmology (e.g., Boylan-Kolchin 2022; Haslbauer et al. 2022; Lovell et al. 2023). Beyond star-forming and quiescent galaxies, *JWST* has spectroscopically confirmed the existence of an AGN at $z \sim 10$ (Goulding et al., 2023) and a B-type supergiant star at $z \sim 5$ (Furtak et al., 2023). Vanzella et al. (2023) have even found a lensed Population III candidate stellar complex at $z = 6.6$ with *JWST*/NIRSpec, tracing the very first generation of stars. In conclusion, it has become clear that *JWST* enables us to probe a wealth of new astronomical phenomena, some of which I will discuss in this thesis.

Euclid

Euclid is a medium-class ESA optical to NIR space mission that was launched in July 2023 (Laureijs et al., 2011). The 1.2 m Korsch telescope is equipped with a visual instrument (VIS) and a NIR instrument (NISP), which contains a three bands photometer (Y, J and H band) and a slitless spectrometer, that all together covers the wavelength range 0.6 to 2 μm.

The primary science goal of the *Euclid* mission is of cosmological nature: it aims to map the dark matter distribution in the nearby universe and show how cosmic acceleration modified the expansion of the Universe. This will be achieved with the *Euclid* Wide Survey, a 15,000 deg^2 survey of the darkest sky measuring the shapes and redshifts of billions of nearby galaxies, including high signal-to-noise spectroscopy for thirty million of these galaxies. In addition, *Euclid* will perform deep imaging and spectroscopy in three Euclid Deep Fields, to investigate the evolution of galaxies in the early Universe. Roughly 10 percent of the mission time will be dedicated to the deep survey with multiple visits over time, reaching 28.2 and 26.4 mag (AB) in the VIS and NISP bands respectively (Laureijs et al., 2011; Euclid Collaboration: Scaramella et al., 2022). The *Euclid* Deep Fields are situated at three different locations on the sky (ESA, 2019). The Deep Field North (EDFN), close to the North Ecliptic Pole, covers 20 deg^2 and has maximum visibility throughout the year, as well as large overlap with existing *Spitzer* surveys. The Deep Field Fornax (EDFF) is located in the Fornax constellation on the southern sky and covers a 10 deg^2 area, in which the Chandra Deep Field South (CDFS) is located. The Deep Field South (EDFS), close to the South Ecliptic Pole, is the largest deep field, covering 23 deg^2 and contains relatively little ancillary data.

Because *Euclid* carries only four photometric bands, in order to determine redshifts and physical properties of sources, the availability of external data is crucial to the *Euclid* mission. The aim of mission is to provide data in a minimum of 7 bands per source, a combination of Euclid bands and additional ground-based data (Consortium, 2016). Currently, several ground- and space-based facilities are being used to observe parts of the Deep Fields (e.g., Masters et al. 2019; Euclid Collaboration: Moneti et al. 2022). In addition, both Southern fields will be supported by optical to NIR photometry from the Vera C. Rubin Observatory in the Large Survey of Space and Time (LSST; Ivezić et al. 2019).

THE ATACAMA LARGE MILLIMETER ARRAY

The Atacama Large Millimeter Array (ALMA; Wootten & Thompson 2009) is a ground-based interferometer consisting of 66 antennas, operating at sub-/mm wavelengths spanning 0.32-3.6 mm in 10 bands. ALMA can achieve angular resolution down to 0.01 arcseconds, which is a significant improvement over single-dish telescopes. The large wavelength range covered by ALMA enables one to probe virtually the full thermal dust spectrum of high-redshift galaxies, including a wealth of molecular, atomic and ionization emission lines.

Sub-mm bright galaxies are typically found to be massive ($\log(M_* / M_\odot) > 10$), with high SFRs of 100-1000 $M_\odot \mathrm{yr}^{-1}$ (e.g., Miettinen et al. 2017; Dudzevičiūtė et al. 2020). Due to its unprecedented sensitivity, ALMA instead has been able to detect faint ($S_{1.2\mathrm{mm}} \lesssim 1$ mJy) galaxies from deep, blind surveys, tracing the dust continuum and FIR emission lines of normal, main-sequence star-forming galaxies at $z > 2$ (e.g., Aravena et al. 2016; Dunlop et al. 2017; Aravena et al. 2020; Franco et al. 2020; Yamaguchi et al. 2020). Because of the small field-of-view (FOV) of only a few tens arcsecond (FWHM of the primary beam, as compared to the *HST* and *Spitzer* FOV of > 1 arcminute^2) blind field surveys are expensive in terms of telescope time, such that ALMA is very effective for targeted follow-up observations of well-studied UV/optical-selected galaxies (e.g., Walter et al. 2016; Bouwens et al. 2016; Liu et al. 2019b; Le Fèvre et al. 2020; Tadaki et al. 2020; Bouwens et al. 2022).

The [CII] 158 μm line is the dominant coolant line of the ISM and so can be a powerful tool for studying the ISM in high-redshift galaxies. In addition, the C[II] emission can be converted to a SFR out to high-z through empirical calibrations (De Looze et al., 2014; Loiacono et al., 2021). ALMA has successfully detected this line numerous times, providing valuable insights star-forming galaxies at $z > 6$ (e.g., Smit et al. 2018; Bouwens et al. 2022; Schouws et al. 2023). Moreover, both dust continuum and C[II] line emission detections have been essential in determining the importance of dust from the EoR down to present time, finding that star formation at $z \sim 2$ primarily takes place in the dustiest galaxies. Their importance decreases toward earlier times, although it remains unclear whether dusty star-forming galaxies in the first ~ billion years of cosmic time are indeed a minority due to gradual chemical enrichment, or because they simply are difficult to detect. I refer the reader to Hodge & da Cunha (2020) for an extensive review on high-redshift science with ALMA.

1.4. THIS THESIS

Globally throughout this thesis, I study the properties of high-redshift galaxies using various IR facilities. At the basis of each chapter lies the exploitation of the SMUVS catalog (Deshmukh et al., 2018), a NIR-selected ($\lambda \sim 1.6$-2.2 μm) collection of ~ 300 000 galaxies at $z_{\mathrm{phot}} = 0$–9 located in the UltraVISTA ultra-deep stripes of the COSMOS field. I have maintained and updated this catalog accordingly through data releases 4 and 5 of the UltraVISTA ultra-deep survey along the duration of my PhD project.

In Chapter 2, I use the SMUVS catalog to make predictions on the recovery of $z = 6$–8 galaxies with the *Euclid* telescope in the *Euclid* Deep Fields. Using the fiducial best-fit SEDs, I simulate *Euclid* and ancillary rest-frame optical and NIR data, from which I rederive photometric redshifts in eight scenarios of data availability. I explore the degree of contamination by intermediate-z interlopers amongst the apparent $z > 6$ population, quantifying how this improves from including ancillary photometry, applying color cuts, and imposing signal-to-noise ratio requirements, in preparation for upcoming high-redshift science with *Euclid*.

In Chapter 3, I focus on one peculiar $z \sim 7$ galaxy located in COSMOS, for which other authors claim an unexpectedly high stellar mass of $\log(M_* / M_\odot) = 11.2$ that is discrepant with my own estimate from the SMUVS catalog. I measure independent 17-band rest-frame optical to NIR photometry for this source, on which I test a number of SED fitting codes in order to reassess its stellar mass, and generally to qualitatively compare the effects of certain modeling choices of said codes.

In Chapter 4, I pre-select a sample of 26 *Spitzer*/IRAC-detected, apparent H- and K_s-band dropout galaxies using the SMUVS catalog restricted to the *JWST* PRIMER field. I follow-up on these sources with newly-acquired, high-resolution *JWST*/NIRCam data in 7 bands and ancillary *HST* imaging, to study their rest-frame optical and NIR physical properties in unprecedented detail. I measure Hα rest-frame EWs from broad-band *JWST* photometry, and study the nature of these galaxies on the SFR-M_* plane.

In the last scientific Chapter 5, in a joint effort with my co-author Tomoko Suzuki, we study the stellar properties of $z > 2$ sub-mm galaxies by cross-matching the SMUVS catalog with an archival ALMA-detected source catalog. We derive UV- and IR-based SFRs for ALMA-detected and non-detected SMUVS sources and place both samples on the SFR-M_* plane, in an effort to quantify the physical differences between NIR-selected galaxies that are either detected or undetected at sub-mm wavelengths.

Finally, in Chapter 6, I summarize the conclusions of the presented works and comment on future endeavors for high-redshift IR science.

REFERENCES

Adams, N. J., Conselice, C. J., Ferreira, L., et al. 2023, MNRAS, 518, 4755, doi: `10.1093/mnras/stac3347`

Akins, H. B., Casey, C. M., Allen, N., et al. 2023, arXiv e-prints, arXiv:2304.12347, doi: `10.48550/arXiv.2304.12347`

Algera, H. S. B., Inami, H., Oesch, P. A., et al. 2023, MNRAS, 518, 6142, doi: `10.1093/mnras/stac3195`

Alongi, M., Bertelli, G., Bressan, A., et al. 1993, A&AS, 97, 851

Álvarez-Márquez, J., Crespo Gómez, A., Colina, L., et al. 2023, A&A, 671, A105, doi: `10.1051/0004-6361/202245400`

Aravena, M., Decarli, R., Walter, F., et al. 2016, ApJ, 833, 71, doi: `10.3847/1538-4357/833/1/71`

Aravena, M., Boogaard, L., Gónzalez-López, J., et al. 2020, ApJ, 901, 79, doi: `10.3847/1538-4357/ab99a2`

Arnouts, S., Cristiani, S., Moscardini, L., et al. 1999, MNRAS, 310, 540, doi: `10.1046/j.1365-8711.1999.02978.x`

Arrabal Haro, P., Dickinson, M., Finkelstein, S. L., et al. 2023, ApJL, 951, L22, doi: `10.3847/2041-8213/acdd54`

Ashby, M. L. N., Willner, S. P., Fazio, G. G., et al. 2013, ApJ, 769, 80, doi: `10.1088/0004-637X/769/1/80`

—. 2015, ApJS, 218, 33, doi: `10.1088/0067-0049/218/2/33`

Ashby, M. L. N., Caputi, K. I., Cowley, W., et al. 2018, ApJS, 237, 39, doi: `10.3847/1538-4365/aad4fb`

Atek, H., Siana, B., Scarlata, C., et al. 2011, ApJ, 743, 121, doi: `10.1088/0004-637X/743/2/121`

Atek, H., Shuntov, M., Furtak, L. J., et al. 2023a, MNRAS, 519, 1201, doi: `10.1093/mnras/stac3144`

Atek, H., Chemerynska, I., Wang, B., et al. 2023b, MNRAS, 524, 5486, doi: `10.1093/mnras/stad1998`

Austin, D., Adams, N., Conselice, C. J., et al. 2023, ApJL, 952, L7, doi: `10.3847/2041-8213/ace18d`

Barrufet, L., Oesch, P. A., Weibel, A., et al. 2023, MNRAS, 522, 449, doi: `10.1093/mnras/stad947`

Battisti, A. J., Cunha, E. d., Shivaei, I., & Calzetti, D. 2020, ApJ, 888, 108, doi: `10.3847/1538-4357/ab5fdd`

Becker, G. D., Davies, F. B., Furlanetto, S. R., et al. 2018, ApJ, 863, 92, doi: `10.3847/1538-4357/aacc73`

Beckwith, S. V. W., Stiavelli, M., Koekemoer, A. M., et al. 2006, AJ, 132, 1729, doi: `10.1086/507302`

Behroozi, P., & Silk, J. 2018, MNRAS, 477, 5382, doi: `10.1093/mnras/sty945`

Bell, E. F., & de Jong, R. S. 2001, ApJ, 550, 212, doi: `10.1086/319728`

Bezanson, R., Labbe, I., Whitaker, K. E., et al. 2022, arXiv e-prints, arXiv:2212.04026, doi: `10.48550/arXiv.2212.04026`

Bisigello, L., Caputi, K. I., Grogin, N., & Koekemoer, A. 2018, A&A, 609, A82, doi: `10.1051/0004-6361/201731399`

Boquien, M., Burgarella, D., Roehlly, Y., et al. 2019, A&A, 622, A103, doi: `10.1051/0004-6361/201834156`

Bosman, S. E. I., Davies, F. B., Becker, G. D., et al. 2022, MNRAS, 514, 55, doi: 10.1093/mnras/stac1046

Bouwens, R., Illingworth, G., Oesch, P., et al. 2023, MNRAS, 523, 1009, doi: 10.1093/mnras/stad1014

Bouwens, R. J., Illingworth, G. D., Oesch, P. A., et al. 2015, ApJ, 803, 34, doi: 10.1088/0004-637X/803/1/34

Bouwens, R. J., Aravena, M., Decarli, R., et al. 2016, ApJ, 833, 72, doi: 10.3847/1538-4357/833/1/72

Bouwens, R. J., Smit, R., Schouws, S., et al. 2022, ApJ, 931, 160, doi: 10.3847/1538-4357/ac5a4a

Boylan-Kolchin, M. 2022, arXiv e-prints, arXiv:2208.01611. https://arxiv.org/abs/2208.01611

Bradač, M. 2020, Nature Astronomy, 4, 478, doi: 10.1038/s41550-020-1104-5

Bradley, L. D., Coe, D., Brammer, G., et al. 2022, arXiv e-prints, arXiv:2210.01777, doi: 10.48550/arXiv.2210.01777

Brammer, G. B., van Dokkum, P. G., & Coppi, P. 2008, ApJ, 686, 1503, doi: 10.1086/591786

Bressan, A., Fagotto, F., Bertelli, G., & Chiosi, C. 1993, A&AS, 100, 647

Bruzual, G., & Charlot, S. 2003, MNRAS, 344, 1000, doi: 10.1046/j.1365-8711.2003.06897.x

Burgarella, D., Buat, V., & Iglesias-Páramo, J. 2005, MNRAS, 360, 1413, doi: 10.1111/j.1365-2966.2005.09131.x

Cameron, A. J., Saxena, A., Bunker, A. J., et al. 2023, arXiv e-prints, arXiv:2302.04298, doi: 10.48550/arXiv.2302.04298

Caputi, K. I., Cirasuolo, M., Dunlop, J. S., et al. 2011, MNRAS, 413, 162, doi: 10.1111/j.1365-2966.2010.18118.x

Caputi, K. I., McLure, R. J., Dunlop, J. S., Cirasuolo, M., & Schael, A. M. 2006, MNRAS, 366, 609, doi: 10.1111/j.1365-2966.2005.09887.x

Caputi, K. I., Dunlop, J. S., McLure, R. J., et al. 2012, ApJL, 750, L20, doi: 10.1088/2041-8205/750/1/L20

Caputi, K. I., Ilbert, O., Laigle, C., et al. 2015, ApJ, 810, 73, doi: 10.1088/0004-637X/810/1/73

Caputi, K. I., Deshmukh, S., Ashby, M. L. N., et al. 2017, ApJ, 849, 45, doi: 10.3847/1538-4357/aa901e

Caputi, K. I., Caminha, G. B., Fujimoto, S., et al. 2021, ApJ, 908, 146, doi: `10.3847/1538-4357/abd4d0`

Carnall, A. C., Leja, J., Johnson, B. D., et al. 2019, ApJ, 873, 44, doi: `10.3847/1538-4357/ab04a2`

Carnall, A. C., McLure, R. J., Dunlop, J. S., & Davé, R. 2018, MNRAS, 480, 4379, doi: `10.1093/mnras/sty2169`

Carnall, A. C., Begley, R., McLeod, D. J., et al. 2022, arXiv e-prints, arXiv:2207.08778. `https://arxiv.org/abs/2207.08778`

Carnall, A. C., McLeod, D. J., McLure, R. J., et al. 2023a, MNRAS, 520, 3974, doi: `10.1093/mnras/stad369`

Carnall, A. C., Begley, R., McLeod, D. J., et al. 2023b, MNRAS, 518, L45, doi: `10.1093/mnrasl/slac136`

Casey, C. M., Akins, H. B., Shuntov, M., et al. 2023a, arXiv e-prints, arXiv:2308.10932, doi: `10.48550/arXiv.2308.10932`

Casey, C. M., Kartaltepe, J. S., Drakos, N. E., et al. 2023b, ApJ, 954, 31, doi: `10.3847/1538-4357/acc2bc`

Castellano, M., Fontana, A., Treu, T., et al. 2022, ApJL, 938, L15, doi: `10.3847/2041-8213/ac94d0`

—. 2023, ApJL, 948, L14, doi: `10.3847/2041-8213/accea5`

Choi, J., Dotter, A., Conroy, C., et al. 2016, ApJ, 823, 102, doi: `10.3847/0004-637X/823/2/102`

Choudhury, T. R., & Ferrara, A. 2007, MNRAS, 380, L6, doi: `10.1111/j.1745-3933.2007.00338.x`

Conroy, C. 2013, ARA&A, 51, 393, doi: `10.1146/annurev-astro-082812-141017`

Conroy, C., Gunn, J. E., & White, M. 2009, ApJ, 699, 486, doi: `10.1088/0004-637X/699/1/486`

Consortium, E. 2016, Euclid Ground Segment, `https://www.euclid-ec.org/?page_id=2625`

Cowley, W. I., Caputi, K. I., Deshmukh, S., et al. 2019, ApJ, 874, 114, doi: `10.3847/1538-4357/ab089b`

da Cunha, E., Charlot, S., & Elbaz, D. 2008, MNRAS, 388, 1595, doi: `10.1111/j.1365-2966.2008.13535.x`

da Cunha, E., Walter, F., Smail, I. R., et al. 2015, ApJ, 806, 110, doi: `10.1088/0004-637X/806/1/110`

Dahlen, T., Mobasher, B., Faber, S. M., et al. 2013, ApJ, 775, 93, doi: `10.1088/0004-637X/775/2/93`

Dayal, P., & Ferrara, A. 2018, PhR, 780, 1, doi: `10.1016/j.physrep.2018.10.002`

Dayal, P., Volonteri, M., Choudhury, T. R., et al. 2020, MNRAS, 495, 3065, doi: `10.1093/mnras/staa1138`

de Barros, S., Schaerer, D., & Stark, D. P. 2014, A&A, 563, A81, doi: `10.1051/0004-6361/201220026`

De Barros, S., Pentericci, L., Vanzella, E., et al. 2017, A&A, 608, A123, doi: `10.1051/0004-6361/201731476`

De Looze, I., Cormier, D., Lebouteiller, V., et al. 2014, A&A, 568, A62, doi: `10.1051/0004-6361/201322489`

Deshmukh, S., Caputi, K. I., Ashby, M. L. N., et al. 2018, ApJ, 864, 166, doi: `10.3847/1538-4357/aad9f5`

Donnan, C. T., McLeod, D. J., Dunlop, J. S., et al. 2023, MNRAS, 518, 6011, doi: `10.1093/mnras/stac3472`

Dotter, A. 2016, ApJS, 222, 8, doi: `10.3847/0067-0049/222/1/8`

Dudzevičiūtė, U., Smail, I., Swinbank, A. M., et al. 2020, MNRAS, 494, 3828, doi: `10.1093/mnras/staa769`

Dunlop, J. S., McLure, R. J., Biggs, A. D., et al. 2017, MNRAS, 466, 861, doi: `10.1093/mnras/stw3088`

Eisenstein, D. J., Willott, C., Alberts, S., et al. 2023, arXiv e-prints, arXiv:2306.02465, doi: `10.48550/arXiv.2306.02465`

Endsley, R., Stark, D. P., Whitler, L., et al. 2023, MNRAS, 524, 2312, doi: `10.1093/mnras/stad1919`

ESA. 2019, Three Dark Fields for Euclid's Deep Survey, `https://sci.esa.int/s/890pJqW`

Euclid Collaboration: Desprez, G., Paltani, S., Coupon, J., et al. 2020, A&A, 644, A31, doi: `10.1051/0004-6361/202039403`

Euclid Collaboration: Moneti, A., McCracken, H. J., Shuntov, M., et al. 2022, A&A, 658, A126, doi: `10.1051/0004-6361/202142361`

Euclid Collaboration: Scaramella, R., Amiaux, J., Mellier, Y., et al. 2022, A&A, 662, A112, doi: `10.1051/0004-6361/202141938`

Fagotto, F., Bressan, A., Bertelli, G., & Chiosi, C. 1994a, A&AS, 104, 365

—. 1994b, A&AS, 105, 29

Faisst, A. L., Capak, P. L., Emami, N., Tacchella, S., & Larson, K. L. 2019, ApJ, 884, 133, doi: `10.3847/1538-4357/ab425b`

Falcón-Barroso, J., Sánchez-Blázquez, P., Vazdekis, A., et al. 2011, A&A, 532, A95, doi: `10.1051/0004-6361/201116842`

Fazio, G. G., Hora, J. L., Allen, L. E., et al. 2004, ApJS, 154, 10, doi: `10.1086/422843`

Ferrara, A., Sommovigo, L., Dayal, P., et al. 2022, MNRAS, 512, 58, doi: `10.1093/mnras/stac460`

Finkelstein, S. L., Ryan, Russell E., J., Papovich, C., et al. 2015, ApJ, 810, 71, doi: `10.1088/0004-637X/810/1/71`

Finkelstein, S. L., Bagley, M. B., Arrabal Haro, P., et al. 2022, ApJL, 940, L55, doi: `10.3847/2041-8213/ac966e`

Franco, M., Elbaz, D., Zhou, L., et al. 2020, A&A, 643, A30, doi: `10.1051/0004-6361/202038312`

Franco, M., Akins, H. B., Casey, C. M., et al. 2023, arXiv e-prints, arXiv:2308.00751, doi: `10.48550/arXiv.2308.00751`

Fujimoto, S., Wang, B., Weaver, J., et al. 2023, arXiv e-prints, arXiv:2308.11609, doi: `10.48550/arXiv.2308.11609`

Furtak, L. J., Meena, A. K., Zackrisson, E., et al. 2023, arXiv e-prints, arXiv:2308.00042, doi: `10.48550/arXiv.2308.00042`

Giavalisco, M., Ferguson, H. C., Koekemoer, A. M., et al. 2004, ApJL, 600, L93, doi: `10.1086/379232`

Girardi, L., Bressan, A., Chiosi, C., Bertelli, G., & Nasi, E. 1996, A&AS, 117, 113

Glazebrook, K., Schreiber, C., Labbé, I., et al. 2017, Nature, 544, 71, doi: `10.1038/nature21680`

Goulding, A. D., Greene, J. E., Setton, D. J., et al. 2023, arXiv e-prints, arXiv:2308.02750, doi: `10.48550/arXiv.2308.02750`

Grazian, A., Fontana, A., Santini, P., et al. 2015, A&A, 575, A96, doi: `10.1051/0004-6361/201424750`

Gruppioni, C., Béthermin, M., Loiacono, F., et al. 2020, A&A, 643, A8, doi: `10.1051/0004-6361/202038487`

Gunn, J. E., & Peterson, B. A. 1965, ApJ, 142, 1633, doi: `10.1086/148444`

Harikane, Y., Nakajima, K., Ouchi, M., et al. 2023a, arXiv e-prints, arXiv:2304.06658, doi: `10.48550/arXiv.2304.06658`

Harikane, Y., Ouchi, M., Oguri, M., et al. 2023b, ApJS, 265, 5, doi: 10.3847/1538-4365/acaaa9

Hasinger, G., Capak, P., Salvato, M., et al. 2018, ApJ, 858, 77, doi: 10.3847/1538-4357/aabacf

Haslbauer, M., Kroupa, P., Zonoozi, A. H., & Haghi, H. 2022, ApJL, 939, L31, doi: 10.3847/2041-8213/ac9a50

Hodge, J. A., & da Cunha, E. 2020, Royal Society Open Science, 7, 200556, doi: 10.1098/rsos.200556

Hodge, J. A., Swinbank, A. M., Simpson, J. M., et al. 2016, ApJ, 833, 103, doi: 10.3847/1538-4357/833/1/103

Houck, J. R., Roellig, T. L., van Cleve, J., et al. 2004, ApJS, 154, 18, doi: 10.1086/423134

Hsiao, T. Y.-Y., Abdurro'uf, Coe, D., et al. 2023, arXiv e-prints, arXiv:2305.03042, doi: 10.48550/arXiv.2305.03042

Huang, X., Zheng, W., Wang, J., et al. 2015, ApJ, 801, 12, doi: 10.1088/0004-637X/801/1/12

Ikarashi, S., Caputi, K. I., Ohta, K., et al. 2017, ApJL, 849, L36, doi: 10.3847/2041-8213/aa9572

Ilbert, O., Arnouts, S., McCracken, H. J., et al. 2006, A&A, 457, 841, doi: 10.1051/0004-6361:20065138

Inami, H., Bacon, R., Brinchmann, J., et al. 2017, A&A, 608, A2, doi: 10.1051/0004-6361/201731195

Ivezić, Ž., Kahn, S. M., Tyson, J. A., et al. 2019, ApJ, 873, 111, doi: 10.3847/1538-4357/ab042c

Jermyn, A. S., Steinhardt, C. L., & Tout, C. A. 2018, MNRAS, 480, 4265, doi: 10.1093/mnras/sty2123

Johnson, B. D., Leja, J., Conroy, C., & Speagle, J. S. 2021, ApJS, 254, 22, doi: 10.3847/1538-4365/abef67

Kaasinen, M., Walter, F., Novak, M., et al. 2020, ApJ, 899, 37, doi: 10.3847/1538-4357/aba438

Khusanova, Y., Bethermin, M., Le Fèvre, O., et al. 2021, A&A, 649, A152, doi: 10.1051/0004-6361/202038944

Kokorev, V. I., Magdis, G. E., Davidzon, I., et al. 2021, ApJ, 921, 40, doi: 10.3847/1538-4357/ac18ce

Kriek, M., van Dokkum, P. G., Labbé, I., et al. 2009, ApJ, 700, 221, doi: 10.1088/0004-637X/700/1/221

Labbé, I., van Dokkum, P., Nelson, E., et al. 2023, Nature, 616, 266, doi: `10.1038/s41586-023-05786-2`

Laigle, C., McCracken, H. J., Ilbert, O., et al. 2016, ApJS, 224, 24, doi: `10.3847/0067-0049/224/2/24`

Laureijs, R., Amiaux, J., Arduini, S., et al. 2011, arXiv e-prints, arXiv:1110.3193. `https://arxiv.org/abs/1110.3193`

Le Borgne, J. F., Bruzual, G., Pelló, R., et al. 2003, A&A, 402, 433, doi: `10.1051/0004-6361:20030243`

Le Fèvre, O., Tasca, L. A. M., Cassata, P., et al. 2015, A&A, 576, A79, doi: `10.1051/0004-6361/201423829`

Le Fèvre, O., Béthermin, M., Faisst, A., et al. 2020, A&A, 643, A1, doi: `10.1051/0004-6361/201936965`

Leitherer, C., Schaerer, D., Goldader, J. D., et al. 1999, ApJS, 123, 3, doi: `10.1086/313233`

Lejeune, T., Cuisinier, F., & Buser, R. 1997, A&AS, 125, 229, doi: `10.1051/aas:1997373`

—. 1998, A&AS, 130, 65, doi: `10.1051/aas:1998405`

Lilly, S. J., Le Fèvre, O., Renzini, A., et al. 2007, ApJS, 172, 70, doi: `10.1086/516589`

Liu, D., Schinnerer, E., Groves, B., et al. 2019a, ApJ, 887, 235, doi: `10.3847/1538-4357/ab578d`

Liu, D., Lang, P., Magnelli, B., et al. 2019b, ApJS, 244, 40, doi: `10.3847/1538-4365/ab42da`

Loiacono, F., Decarli, R., Gruppioni, C., et al. 2021, A&A, 646, A76, doi: `10.1051/0004-6361/202038607`

Lovell, C. C., Harrison, I., Harikane, Y., Tacchella, S., & Wilkins, S. M. 2023, MNRAS, 518, 2511, doi: `10.1093/mnras/stac3224`

Madau, P., & Dickinson, M. 2014, ARA&A, 52, 415, doi: `10.1146/annurev-astro-081811-125615`

Maiolino, R., Nagao, T., Grazian, A., et al. 2008, A&A, 488, 463, doi: `10.1051/0004-6361:200809678`

Maraston, C. 2005, MNRAS, 362, 799, doi: `10.1111/j.1365-2966.2005.09270.x`

Mármol-Queraltó, E., McLure, R. J., Cullen, F., et al. 2016, MNRAS, 460, 3587, doi: `10.1093/mnras/stw1212`

Marsan, Z. C., Muzzin, A., Marchesini, D., et al. 2022, ApJ, 924, 25, doi: `10.3847/1538-4357/ac312a`

Mason, C. A., Trenti, M., & Treu, T. 2015, ApJ, 813, 21, doi: `10.1088/0004-637X/813/1/21`

Mason, C. A., Treu, T., Dijkstra, M., et al. 2018, ApJ, 856, 2, doi: `10.3847/1538-4357/aab0a7`

Masters, D. C., Stern, D. K., Cohen, J. G., et al. 2019, ApJ, 877, 81, doi: `10.3847/1538-4357/ab184d`

Matthee, J., Mackenzie, R., Simcoe, R. A., et al. 2023, ApJ, 950, 67, doi: `10.3847/1538-4357/acc846`

McKinney, J., Manning, S. M., Cooper, O. R., et al. 2023, arXiv e-prints, arXiv:2304.07316, doi: `10.48550/arXiv.2304.07316`

McLeod, D. J., McLure, R. J., Dunlop, J. S., et al. 2021, MNRAS, 503, 4413, doi: `10.1093/mnras/stab731`

Miettinen, O., Delvecchio, I., Smolčić, V., et al. 2017, A&A, 606, A17, doi: `10.1051/0004-6361/201730762`

Muzzin, A., Marchesini, D., Stefanon, M., et al. 2013, ApJ, 777, 18, doi: `10.1088/0004-637X/777/1/18`

Naidu, R. P., Oesch, P. A., Dokkum, P. v., et al. 2022a, ApJL, 940, L14, doi: `10.3847/2041-8213/ac9b22`

Naidu, R. P., Oesch, P. A., Setton, D. J., et al. 2022b, arXiv e-prints, arXiv:2208.02794. `https://arxiv.org/abs/2208.02794`

Nanayakkara, T., Glazebrook, K., Jacobs, C., et al. 2022, arXiv e-prints, arXiv:2212.11638, doi: `10.48550/arXiv.2212.11638`

Navarro-Carrera, R., Rinaldi, P., Caputi, K. I., et al. 2023, arXiv e-prints, arXiv:2305.16141, doi: `10.48550/arXiv.2305.16141`

Nelson, E. J., Suess, K. A., Bezanson, R., et al. 2023, ApJL, 948, L18, doi: `10.3847/2041-8213/acc1e1`

Noeske, K. G., Weiner, B. J., Faber, S. M., et al. 2007, ApJL, 660, L43, doi: `10.1086/517926`

Noll, S., Burgarella, D., Giovannoli, E., et al. 2009, A&A, 507, 1793, doi: `10.1051/0004-6361/200912497`

Pacifici, C., Iyer, K. G., Mobasher, B., et al. 2023, ApJ, 944, 141, doi: `10.3847/1538-4357/acacff`

Parsons, J., Mas-Ribas, L., Sun, G., et al. 2022, ApJ, 933, 141, doi: `10.3847/1538-4357/ac746b`

Peng, Y.-j., Lilly, S. J., Kovač, K., et al. 2010, ApJ, 721, 193, doi: `10.1088/0004-637X/721/1/193`

Pentericci, L., Vanzella, E., Fontana, A., et al. 2014, ApJ, 793, 113, doi: `10.1088/0004-637X/793/2/113`

Pérez-González, P. G., Barro, G., Annunziatella, M., et al. 2023, ApJL, 946, L16, doi: `10.3847/2041-8213/acb3a5`

Planck Collaboration, Aghanim, N., Akrami, Y., et al. 2020, A&A, 641, A6, doi: `10.1051/0004-6361/201833910`

Postman, M., Coe, D., Benítez, N., et al. 2012, ApJS, 199, 25, doi: `10.1088/0067-0049/199/2/25`

Prada, F., Behroozi, P., Ishiyama, T., Klypin, A., & Pérez, E. 2023, arXiv e-prints, arXiv:2304.11911, doi: `10.48550/arXiv.2304.11911`

Qin, Y., Balu, S., & Wyithe, J. S. B. 2023, MNRAS, doi: `10.1093/mnras/stad2448`

Rieke, G. H., Young, E. T., Engelbracht, C. W., et al. 2004, ApJS, 154, 25, doi: `10.1086/422717`

Rinaldi, P., Caputi, K. I., van Mierlo, S. E., et al. 2022, ApJ, 930, 128, doi: `10.3847/1538-4357/ac5d39`

Rinaldi, P., Caputi, K. I., Costantin, L., et al. 2023, ApJ, 952, 143, doi: `10.3847/1538-4357/acdc27`

Roberts-Borsani, G., Morishita, T., Treu, T., et al. 2022, ApJL, 938, L13, doi: `10.3847/2041-8213/ac8e6e`

Roberts-Borsani, G., Treu, T., Chen, W., et al. 2023, Nature, 618, 480, doi: `10.1038/s41586-023-05994-w`

Roberts-Borsani, G. W., Bouwens, R. J., Oesch, P. A., et al. 2016, ApJ, 823, 143, doi: `10.3847/0004-637X/823/2/143`

Robertson, B. E., Ellis, R. S., Furlanetto, S. R., & Dunlop, J. S. 2015, ApJL, 802, L19, doi: `10.1088/2041-8205/802/2/L19`

Robertson, B. E., Tacchella, S., Johnson, B. D., et al. 2023, Nature Astronomy, 7, 611, doi: `10.1038/s41550-023-01921-1`

Rodighiero, G., Bisigello, L., Iani, E., et al. 2023, MNRAS, 518, L19, doi: `10.1093/mnrasl/slac115`

Rodighiero, G., Daddi, E., Baronchelli, I., et al. 2011, ApJL, 739, L40, doi: `10.1088/2041-8205/739/2/L40`

Sanders, D. B., Salvato, M., Aussel, H., et al. 2007, ApJS, 172, 86, doi: `10.1086/517885`

Santini, P., Fontana, A., Castellano, M., et al. 2017, ApJ, 847, 76, doi: `10.3847/1538-4357/aa8874`

—. 2023, ApJL, 942, L27, doi: `10.3847/2041-8213/ac9586`

Saxena, A., Bunker, A. J., Jones, G. C., et al. 2023, arXiv e-prints, arXiv:2306.04536, doi: `10.48550/arXiv.2306.04536`

Schechter, P. 1976, ApJ, 203, 297, doi: `10.1086/154079`

Schouws, S., Bouwens, R., Smit, R., et al. 2023, ApJ, 954, 103, doi: `10.3847/1538-4357/ace10c`

Schreiber, C., Pannella, M., Elbaz, D., et al. 2015, A&A, 575, A74, doi: `10.1051/0004-6361/201425017`

Scoville, N., Aussel, H., Brusa, M., et al. 2007, ApJS, 172, 1, doi: `10.1086/516585`

Shapley, A. E., Sanders, R. L., Reddy, N. A., Topping, M. W., & Brammer, G. B. 2023, arXiv e-prints, arXiv:2301.03241, doi: `10.48550/arXiv.2301.03241`

Shu, X., Yang, L., Liu, D., et al. 2022, ApJ, 926, 155, doi: `10.3847/1538-4357/ac3de5`

Skelton, R. E., Whitaker, K. E., Momcheva, I. G., et al. 2014, ApJS, 214, 24, doi: `10.1088/0067-0049/214/2/24`

Smail, I., Dudzeviciute, U., Gurwell, M., et al. 2023, arXiv e-prints, arXiv:2306.16039, doi: `10.48550/arXiv.2306.16039`

Smit, R., Bouwens, R. J., Labbé, I., et al. 2016, ApJ, 833, 254, doi: `10.3847/1538-4357/833/2/254`

—. 2014, ApJ, 784, 58, doi: `10.1088/0004-637X/784/1/58`

Smit, R., Bouwens, R. J., Carniani, S., et al. 2018, Nature, 553, 178, doi: `10.1038/nature24631`

Song, M., Finkelstein, S. L., Ashby, M. L. N., et al. 2016, ApJ, 825, 5, doi: `10.3847/0004-637X/825/1/5`

Speagle, J. S., Steinhardt, C. L., Capak, P. L., & Silverman, J. D. 2014, ApJS, 214, 15, doi: `10.1088/0067-0049/214/2/15`

Stefanon, M., Marchesini, D., Muzzin, A., et al. 2015, ApJ, 803, 11, doi: `10.1088/0004-637X/803/1/11`

Stefanon, M., Labbé, I., Bouwens, R. J., et al. 2019, ApJ, 883, 99, doi: `10.3847/1538-4357/ab3792`

Steidel, C. C., Giavalisco, M., Pettini, M., Dickinson, M., & Adelberger, K. L. 1996, ApJL, 462, L17, doi: `10.1086/310029`

Steinhardt, C. L., Kokorev, V., Rusakov, V., Garcia, E., & Sneppen, A. 2023, ApJL, 951, L40, doi: `10.3847/2041-8213/acdef6`

Stern, D., Kirkpatrick, J. D., Allen, L. E., et al. 2007, ApJ, 663, 677, doi: `10.1086/516833`

Strait, V., Bradač, M., Coe, D., et al. 2020, ApJ, 888, 124, doi: `10.3847/1538-4357/ab5daf`

Sun, F., Egami, E., Pirzkal, N., et al. 2023, ApJ, 953, 53, doi: `10.3847/1538-4357/acd53c`

Tacchella, S., Finkelstein, S. L., Bagley, M., et al. 2022, ApJ, 927, 170, doi: `10.3847/1538-4357/ac4cad`

Tacconi, L. J., Genzel, R., Saintonge, A., et al. 2018, ApJ, 853, 179, doi: `10.3847/1538-4357/aaa4b4`

Tadaki, K.-i., Belli, S., Burkert, A., et al. 2020, ApJ, 901, 74, doi: `10.3847/1538-4357/abaf4a`

Tilvi, V., Malhotra, S., Rhoads, J. E., et al. 2020, ApJL, 891, L10, doi: `10.3847/2041-8213/ab75ec`

Tomczak, A. R., Quadri, R. F., Tran, K.-V. H., et al. 2016, ApJ, 817, 118, doi: `10.3847/0004-637X/817/2/118`

Topping, M. W., Stark, D. P., Endsley, R., et al. 2022a, ApJ, 941, 153, doi: `10.3847/1538-4357/aca522`

—. 2022b, MNRAS, 516, 975, doi: `10.1093/mnras/stac2291`

Trebitsch, M., Blaizot, J., Rosdahl, J., Devriendt, J., & Slyz, A. 2017, MNRAS, 470, 224, doi: `10.1093/mnras/stx1060`

Tremonti, C. A., Heckman, T. M., Kauffmann, G., et al. 2004, ApJ, 613, 898, doi: `10.1086/423264`

Treu, T., Roberts-Borsani, G., Bradac, M., et al. 2022, ApJ, 935, 110, doi: `10.3847/1538-4357/ac8158`

Vanzella, E., Loiacono, F., Bergamini, P., et al. 2023, arXiv e-prints, arXiv:2305.14413, doi: `10.48550/arXiv.2305.14413`

Walter, F., Decarli, R., Aravena, M., et al. 2016, ApJ, 833, 67, doi: `10.3847/1538-4357/833/1/67`

Wang, B., Fujimoto, S., Labbe, I., et al. 2023, arXiv e-prints, arXiv:2308.03745, doi: `10.48550/arXiv.2308.03745`

Wang, T., Schreiber, C., Elbaz, D., et al. 2019, Nature, 572, 211, doi: `10.1038/s41586-019-1452-4`

Weaver, J. R., Davidzon, I., Toft, S., et al. 2022a, arXiv e-prints, arXiv:2212.02512, doi: `10.48550/arXiv.2212.02512`

Weaver, J. R., Kauffmann, O. B., Ilbert, O., et al. 2022b, ApJS, 258, 11, doi: `10.3847/1538-4365/ac3078`

Werner, M. W., Roellig, T. L., Low, F. J., et al. 2004, ApJS, 154, 1, doi: `10.1086/422992`

Westera, P., Lejeune, T., Buser, R., Cuisinier, F., & Bruzual, G. 2002, A&A, 381, 524, doi: `10.1051/0004-6361:20011493`

Whitaker, K. E., van Dokkum, P. G., Brammer, G., & Franx, M. 2012, ApJL, 754, L29, doi: `10.1088/2041-8205/754/2/L29`

Whitaker, K. E., Franx, M., Leja, J., et al. 2014, ApJ, 795, 104, doi: `10.1088/0004-637X/795/2/104`

Whitler, L., Endsley, R., Stark, D. P., et al. 2022, arXiv e-prints, arXiv:2208.01599. `https://arxiv.org/abs/2208.01599`

—. 2023, MNRAS, 519, 157, doi: `10.1093/mnras/stac3535`

Wilkins, S. M., Stanway, E. R., & Bremer, M. N. 2014, MNRAS, 439, 1038, doi: `10.1093/mnras/stu029`

Wootten, A., & Thompson, A. R. 2009, IEEE Proceedings, 97, 1463, doi: `10.1109/JPROC.2009.2020572`

Yamaguchi, Y., Kohno, K., Hatsukade, B., et al. 2020, PASJ, 72, 69, doi: `10.1093/pasj/psaa057`

Zavala, J. A., Casey, C. M., Manning, S. M., et al. 2021, ApJ, 909, 165, doi: `10.3847/1538-4357/abdb27`

Zhu, Y., Becker, G. D., Bosman, S. E. I., et al. 2022, ApJ, 932, 76, doi: `10.3847/1538-4357/ac6e60`

2

INTERMEDIATE-REDSHIFT CONTAMINANTS IN THE SEARCH FOR $z > 6$ GALAXIES WITHIN THE *Euclid* DEEP SURVEY

Euclid Collaboration: S.E. van Mierlo, K.I. Caputi et al.
(203 additional authors not shown)

This chapter has been published as *Euclid preparation. XXI. Intermediate-redshift contaminants in the search for z > 6 galaxies within the Euclid Deep Survey* in Astronomy & Astrophysics **666**, A200, 2022. In order to recognize this research, I was awarded the Euclid Star Prize 2022 in the PhD student category.

ABSTRACT

The Euclid mission is expected to discover thousands of $z > 6$ *galaxies in three deep fields, which together will cover a ~50 deg*^{2} *area. However, the limited number of Euclid bands (four) and the low availability of ancillary data could make the identification of* $z > 6$ *galaxies challenging. In this work we assess the degree of contamination by intermediate-redshift galaxies (*$z = 1$*–5.8) expected for* $z > 6$ *galaxies within the Euclid Deep Survey. This study is based on ~176 000 real galaxies at* $z = 1$*–8 in a ~0.7 deg*^{2} *area selected from the UltraVISTA ultra-deep survey and ~96 000 mock galaxies with* $25.3 \leq H < 27.0$*, which altogether cover the range of magnitudes to be probed in the Euclid Deep Survey. We simulate Euclid and ancillary photometry from fiducial 28-band photometry and fit spectral energy distributions to various combinations of these simulated data.We demonstrate that identifying* $z > 6$ *galaxies with Euclid data alone will be very effective, with a* $z > 6$ *recovery of 91% (88%) for bright (faint) galaxies. For the UltraVISTA-like bright sample, the percentage of* $z = 1$*–5.8 contaminants amongst apparent* $z > 6$ *galaxies as observed with Euclid alone is 18 %, which is reduced to 4% (13%) by including ultra-deep Rubin (Spitzer) photometry. Conversely, for the faint mock sample, the contamination fraction with Euclid alone is considerably higher at 39 %, and minimised to 7 % when including ultra-deep Rubin data. For UltraVISTA-like bright galaxies, we find that Euclid* $(I_\mathrm{E} - Y_\mathrm{E}) > 2.8$ *and* $(Y_\mathrm{E} - J_\mathrm{E}) < 1.4$ *colour criteria can separate contaminants from true* $z > 6$ *galaxies, although these are applicable to only 54 % of the contaminants as many have unconstrained* $(I_\mathrm{E} - Y_\mathrm{E})$ *colours. In the best scenario, these cuts reduce the contamination fraction to 1 % whilst preserving 81 % of the fiducial* $z > 6$ *sample. For the faint mock sample, colour cuts are infeasible; we find instead that a* 5σ *detection threshold requirement in at least one of the Euclid near-infrared bands reduces the contamination fraction to 25 %.*

2.1. INTRODUCTION

Over more than a decade now, numerous works have investigated the presence of galaxies around the epoch of re-ionisation. In particular, photometric studies of various fields have identified many galaxies at $z > 6$, mostly through deep *Hubble Space Telescope* (HST) imaging (e.g. Bouwens et al. 2010; Ellis et al. 2013; Oesch et al. 2014; Atek et al. 2015; Finkelstein et al. 2015; Bowler et al. 2020; Salmon et al. 2020; Roberts-Borsani et al. 2022). These studies provide us with clues regarding the physical nature of the objects present in the early Universe, which is of key importance for constraining the early phases of galaxy evolution.

The number densities of low-luminosity $z > 6$ galaxies are relatively high, enabling a search for these sources in deep, small-area surveys, such as the Cosmic Assembly Near-infrared Deep Extragalactic Legacy Survey (CANDELS; Grogin et al. 2011; Koekemoer et al. 2011). Conversely, bright $z > 6$ galaxies ($M_{\rm UV} \lesssim -20.5$) are much rarer and, thus, are only likely to be found in wide-area surveys with reasonable depths at optical and near-infrared (NIR) wavelengths. For example, recent work from Bouwens et al. (2021) determined that the number density of $z \sim 6$ galaxies with rest-frame magnitudes $M_{1600} \sim -21$ is $1.4 \times 10^{-5}\,{\rm Mpc}^{-3}\,{\rm mag}^{-1}$, and increases by a factor of $\sim 10^3$ for sources with $M_{1600} \sim -17$. Consequently, only a minor fraction of $z > 6$ galaxy studies have been devoted to exploring the bright end of the galaxy luminosity function at these high redshifts (e.g. Willott et al. 2013; Duncan et al. 2014; Bowler et al. 2015; Song et al. 2016; Stefanon et al. 2019). It is around these brightest galaxies where re-ionisation was presumably completed first (Pentericci et al. 2014; Castellano et al. 2016).

To date, the necessary combination of area and depth to search for bright $z > 6$ sources is only available in a few fields (McCracken et al. 2012; Jarvis et al. 2013). However, the forthcoming *Euclid* mission (Laureijs et al. 2011) will open up a new era in the search of such objects by mapping a large area of the sky at NIR wavelengths. In addition to its main wide survey, *Euclid* will perform deep observations of three so-called Euclid Deep Fields, which will encompass a total area of ~50 deg^2 (Euclid Collaboration: Scaramella et al. 2022). *Euclid* carries four photometric bands: a visible imager (VIS; Cropper et al. 2016) that has an optical band $I_{\rm E}$ [1] at 5500–9000 Å and the Near-Infrared Spectrometer and Photometer (NISP; Maciaszek et al. 2016) that carries three NIR bands, that is, $Y_{\rm E}$, $J_{\rm E}$, and $H_{\rm E}$, which together cover the wavelength range 9000–20 000 Å (Euclid Collaboration: Schirmer et al. 2022). The expected 5σ depths (assuming point-like sources) for the Euclid Deep Fields are $I_{\rm E} = 28.2$ and $Y_{\rm E}J_{\rm E}H_{\rm E} \approx 26.4$ (AB magnitude). With these characteristics, the Euclid Deep Fields are expected to reveal thousands of $z > 6$ galaxies and therefore enable studies of early galaxy formation and evolution with unprecedented statistical significance.

Since *Euclid* has a limited number of photometric bands, enormous efforts are being made to provide additional, external coverage of the Euclid Deep Fields, both with ground-based facilities and the *Spitzer Space Telescope* (e.g. Euclid Collaboration: Moneti et al. 2022; McPartland et al., in prep). In the best-case scenario, Euclid Deep sources will have photometric coverage in at most 10–12 filters, and therefore deriving accurate photometric redshifts and galaxy physical parameters will be challenging. As such, a

---

[1] Originally referred to as the VIS band within the Euclid Consortium but recently renamed the $I_{\rm E}$ band.

pre-launch critical assessment of contamination in *Euclid* galaxy selections at different redshifts is of utmost importance.

Identifying $z > 6$ galaxies in particular is challenging for a number of reasons. Extreme emission line galaxies at intermediate redshifts can mimic Lyman-break galaxies due to a combination of large equivalent width emission lines and a faint continuum, therefore contaminating the selection of high-redshift objects (Atek et al. 2011; Huang et al. 2015). A second type of degeneracy arises from the blackbody spectra of cool, brown dwarf stars that have similar NIR colours to $z > 6$ galaxies (Stern et al. 2007; Bowler et al. 2015; Salmon et al. 2020). Finally, another main source of contamination in the selection of $z > 6$ sources are intermediate-redshift ($z \sim 1$–6) galaxies, for which the 4000 Å break can be misidentified as the Lyman-α break at $\lambda = 1216$ Å of a high-redshift object (Vulcani et al. 2017). This latter sort of contamination is the focus of this work. We note that the study of high-redshift contaminants to intermediate-z sources, especially dusty galaxies at $z = 4$–6, is an interesting complementary problem, but outside the scope of this paper.

Here we make use of galaxies selected from the third data release (DR3) of the UltraVISTA ultra-deep survey (McCracken et al. 2012) and the *Spitzer* Matching Survey of the UltraVISTA ultra-deep Stripes (SMUVS; Ashby et al. 2018) to assess the degree of contamination produced by intermediate-redshift galaxies in the selection of $z > 6$ galaxies in the Euclid Deep Survey. UltraVISTA and SMUVS are uniquely suited for this simulation because of their considerable common area ($\sim$0.66 deg^2) and depths ($\sim$25.5 AB mag). However, we emphasise that this analysis is only valid for galaxies at $z = 6$–8 due to the limitations of the fiducial sample, and as such we cannot study the photometric redshift recovery of *Euclid* $z > 8$ galaxies.

This paper is organised as follows. In Sect. 2.2 we briefly describe the datasets used in this work. In Sect. 2.3 we describe our source catalogue construction and how the *Euclid* and ancillary photometry were simulated. We present our estimates on the contamination fraction of bright $z > 6$ galaxies in the Euclid Deep Fields in Sect. 2.4, together with colour selection criteria to separate intermediate-z interlopers from true $z > 6$ galaxies. In addition, we analyse the degree of $z > 6$ contamination and the effectiveness of the colour criteria for a sample of faint ($25.3 \le H < 27.0$) mock galaxies in Sect. 2.5. In Sect. 2.6 we comment on the validity of our results and finally present our concluding remarks in Sect. 2.7. Throughout this paper we adopt a cosmology with $\mathrm{H}_0 = 70$ km s^{-1} Mpc^{-1}, $\Omega_\mathrm{m} = 0.3$, and $\Omega_\Lambda = 0.7$. All magnitudes and fluxes are total, with magnitudes referring to the AB system (Oke & Gunn 1983). Stellar masses correspond to a Chabrier (2003) initial mass function (IMF).

2.2. COSMOS AS A BASIS TO SIMULATE *Euclid* GALAXIES

2.2.1. ULTRAVISTA/SMUVS AND NON-SMUVS GALAXY CATALOGUES

As a basis to simulate *Euclid* (+ancillary) photometry, we use real, NIR galaxy surveys in the field of the Cosmic Evolution Survey (COSMOS; Scoville et al. 2007). Specifically, the ultra-deep UltraVISTA survey (McCracken et al. 2012) has provided Y, J, H, K_s images whose depth is relatively similar ($\sim$25–26 mag) to that expected for the Euclid Deep Fields, and therefore constitutes an excellent starting point to simulate *Euclid* galaxies. However, given that the Euclid Deep Survey will be 1.2 magnitude deeper in the H band than the UltraVISTA survey, we create a complementary catalogue of *Euclid*-like faint mock galaxies from scaled-down versions of the fiducial UltraVISTA spectral energy distributions (SEDs). This process is described in detail in Sect. 2.5; here we discuss the construction of the UltraVISTA galaxy catalogue that forms the basis for both the bright UltraVISTA-like sample and the faint mock sample.

In this work we only consider the three (out of four) UltraVISTA ultra-deep stripes with ultra-deep *Spitzer Space Telescope* (Werner et al. 2004) coverage from SMUVS (Ashby et al. 2018). This programme used the *Spitzer* Infrared Array Camera (IRAC; Fazio et al. 2004) to map the three UltraVISTA ultra-deep stripes with deepest ancillary data, reaching matching depths in the 3.6 and 4.5 μm bands, over a total area of $0.66\,\mathrm{deg}^2$.

Deshmukh et al. (2018; hereafter D18) presented a photometric catalogue of approximately 300 000 SMUVS sources with multi-wavelength ancillary data in COSMOS, for a total of 28 bands from Canada–France–Hawaii Telescope (CFHT) u through IRAC 4.5 μm. The SMUVS photometry has been obtained using sources detected in the UltraVISTA DR3 HK_s stack mosaic as priors, and by requiring that each source has a detection in at least one of the IRAC bands. Given that the SMUVS images suffer from severe source confusion, the IRAC photometry was measured using a point-spread-function (PSF) fitting technique from the Image Reduction and Analysis Facility (IRAF), using empirical images of the PSF as constructed from stars in the field. Using this method, $\sim 95\,\%$ of all UltraVISTA sources are detected in at least one IRAC band. In addition, the IRAC photometry of sources with bright IRAC neighbours was not utilised in the SED fitting to prevent contamination in these bands from affecting the best-fit SED.

D18 derived photometric redshifts and stellar masses for all these sources, based on SED analysis, as we explain in Sect. 2.2.2. We refer the reader to D18 for detailed information about the SMUVS catalogue. Here we use it as a basis to obtain our *Euclid* simulated data.

In addition, we considered a second, complementary catalogue consisting of all the UltraVISTA HK_s-stack sources that are not *Spitzer*-detected, in the same three UltraVISTA ultra-deep stripes 1, 2, and 3, to which we refer as non-SMUVS sources throughout this work. As in D18, we used the HK_s stack source positions to measure $2''$ diameter circular photometry, using the code `SourceExtractor` (Bertin & Arnouts 1996), on 26 bands in the COSMOS field: CFHT u; Subaru SuprimeCam $B, V, r, i^+, z^+, z^{++}$, *IA427, IA464, IA484, IA505, IA527, IA574, IA624, IA679, IA709, IA738, IA767, IA82, NB711*, and *NB816*; HST *F814W*; and UltraVISTA Y, J, H, and K_s.

The measured fluxes were corrected to total fluxes through point-source aperture corrections, based on the curves of growth of non-saturated stars in the field (as derived by D18). These corrections are consistent with those quoted in McCracken et al. (2012) and Laigle et al. (2016). For the *Spitzer* photometry, typical aperture corrections have been tabulated by Ashby et al. (2015). These authors have demonstrated that treating *Spitzer* sources as point-like is valid in virtually all cases at $z > 2$ and in a large fraction of sources at $z = 1$–2. Moreover, we note that our *Euclid* (+ancillary) photometry are simulated directly from our COSMOS photometry and therefore, the recovery fraction and contaminants of high-z sources studied in this paper are not influenced by the use of point-like photometry. This is confirmed by the results shown in Appendix 2.7, where we repeat our $z > 6$ recovery tests on the COSMOS2020 catalogue (Weaver et al. 2022), which contains independent photometric measurements of the same field.

The total fluxes were subsequently corrected for Galactic extinction using the dust maps from Schlafly & Finkbeiner (2011). We used the masks from D18 to mask regions of contaminated light surrounding the brightest sources. This removes $\sim 6\,\%$ of the considered UltraVISTA region; as a consequence, our masked catalogue covers a total area of ~ 0.7 deg^2. Following the method outlined in Caputi et al. (2006, Fig. 1), we cleaned the non-SMUVS catalogue for Galactic stars using the Subaru SuprimeCam $(i^+ - z^+)$ and UltraVISTA $(J - K_s)$ colour diagram. Sources that have an HK_s-based stellarity parameter greater than 0.8 and reside in the stellar locus were discarded from our non-SMUVS sample, where the stellar locus refers to sources that have $(J - K_s) \leq 0.1$. This approach is slightly different from D18, who used the $(J - [3.6])$ versus $(B - J)$ colour diagram to identify Galactic stars. Given that no IRAC 3.6 μm photometry is available for the non-SMUVS sources, we utilised this alternative colour diagnostic to clean the non-SMUVS catalogue from Galactic stars.

By including the non-SMUVS sources in our analysis, we gain approximately 19 700 additional sources. The majority of the additional sources ($\sim 70\,\%$) resides in the second ultra-deep stripe, as the northern part of it ($2.61° \leq \mathrm{Dec} \leq 2.76°$) is not covered by SMUVS.

Finally, for both the UltraVISTA SMUVS and non-SMUVS catalogues, we updated the UltraVISTA photometry using the DR4 mosaics to increase the sensitivity of our photometry, by running `SourceExtractor` on the DR4 images and matching the resulting source catalogue with our DR3 catalogue. We therefore emphasise that our final UltraVISTA catalogue consists exclusively of DR3-selected sources, of which the UltraVISTA Y, J, H, and K_s bands have been updated with the DR4 photometry. Between DR3 and DR4, the 5σ limiting magnitudes in the ultra-deep stripes increase by 0.1, 0.2, and 0.1 mag in the Y, J, and H bands, respectively, while the K_s band depth is unchanged.

2.2.2. GALAXY PHYSICAL PARAMETERS OBTAINED WITH SED FITTING

We derived photometric redshifts and main physical parameters for all the galaxies in the general (SMUVS and non-SMUVS) UltraVISTA catalogue with updated DR4 photometry, following a similar SED fitting methodology to that applied by D18, but with a few important changes more suitable for high-redshift sources, as follows. We made use of the χ^2-fitting routine `LePhare` (Arnouts et al. 1999; Ilbert et al. 2006), adopting a broader set of star formation histories (SFHs) than D18, that is, a single stellar population, an exponentially declining SFH, and a delayed exponentially declining SFH. For both declining models, we used the same range of star formation timescales $\tau = 0.01$, 0.1, 0.3, 1.0, 3.0, 5.0, 10.0, and 15 Gyr. We considered two metallicities: solar ($Z = \mathrm{Z}_\odot$) and sub-solar ($Z = 0.2\mathrm{Z}_\odot$). In total, we considered 36 templates of different combinations of SFH and metallicity. We also included empirical spectra of L, M, and T stars from the SpeX Prism Library (Burgasser 2014) to minimise the contamination of the high-z galaxy sample by dwarf stars. The effectiveness of this method in removing brown-dwarf contamination was demonstrated by Bowler et al. (2014) and Bowler et al. (2015). Finally, we used the redshift range $z = 0$–9 for our SED fitting, whereas D18 used the redshift range $z = 0$–7.

As in D18, each SED template was attenuated with the Calzetti et al. (2000) reddening law and the colour excess was left as a free parameter between $E(B-V)=0$ and 1, with a step of 0.1. We ran `LePhare` with emission lines (the recipe based on simple scaling relations from Kennicutt 1998 between the ultraviolet (UV) luminosity and O II line; see Ilbert et al. 2009) and multiplied the flux errors by a factor of 1.5 since, as shown by Dahlen et al. (2013), this choice improves photometric redshift estimation. We include a flat prior for the absolute magnitude in the Subaru r band such that $-10 < M_r < -26$. We adopted the same treatment for non-detections as in D18 and Caputi et al. (2015), that is, we substituted them with 3σ flux upper limits in the broad bands and simply ignored them in the intermediate- and narrow-band data. We then chose the option in `LePhare` that rejects any SED template that produces fluxes higher than the 3σ upper limits in the bands with non-detections. In order to improve the quality of the fit, we applied photometric zero-point corrections as in D18. These were derived as follows: after we obtained best-fit SEDs with `LePhare`, we calculated the mean offset between the observed and template fluxes in each band, which were subsequently applied to the photometric catalogue. We repeated this process until the offsets converged to obtain our final photometric redshifts. Averaged over all 28 bands, the offset between the observed and template fluxes is 0.06 mag.

We cleaned the output redshift catalogue returned by `LePhare` as follows: first, we removed sources that are best fit by stellar (rather than galaxy) templates. This was achieved by comparing the best-fit galaxy $\chi^2_{\nu,\mathrm{gal}}$ and stellar $\chi^2_{\nu,\mathrm{star}}$ values for any source with a HK_s-based stellarity parameter greater than 0.8 (as measured with `SourceExtractor` from the HK_s detection image); we removed these sources if $\chi^2_{\nu,\mathrm{star}} < \chi^2_{\nu,\mathrm{gal}}$ or if $|\chi^2_{\nu,\mathrm{gal}} - \chi^2_{\nu,\mathrm{star}}| < 4$.

Second, for all galaxies at $z > 3.6$, we checked if the high-redshift solution is compatible with their detection at short wavelengths, that is, we ensure galaxies with high-redshift solutions do not have flux bluewards of the Lyman break. Therefore, following Caputi et al. (2015), we discarded sources with $z_\mathrm{phot} > 3.6$ and a $> 2\sigma$ U-band detection; or with $z_\mathrm{phot} > 4.6$ and a $> 2\sigma$ B-band detection; or with $z_\mathrm{phot} > 5.6$ and a $> 2\sigma$ V-band detection; or with $z_\mathrm{phot} > 6.6$ and a $> 2\sigma$ r-band detection. To further clarify, these conditions are implemented such that any band bluewards of the Lyman break is checked, for instance, we ensured a $z_\mathrm{phot} > 6.6$ source also does not have significant detections in the U, B, and V bands. In addition, for $z_\mathrm{phot} > 7$ galaxies we do not expect any detection bluewards of the Lyman-α line, due to Lyman series absorption of neutral hydrogen in the intergalactic medium (Inoue et al. 2014). Therefore, we discarded sources with $z_\mathrm{phot} > 7.0$ and a $> 2\sigma$ z^{++}-band detection; or with $z_\mathrm{phot} > 8.0$ and a $> 2\sigma$ Y-band detection. Lastly, for all sources with $z_\mathrm{phot} \geq 6$, we performed rigorous visual inspection of their broad-band images and removed all sources that are for example contaminated by bright neighbours or appear artificial (e.g. they are aligned exactly on the diffraction spikes of bright stars).

In total, these measures removed < 0.5 % of the sources. The total (SMUVS and non-SMUVS), clean UltraVISTA catalogue in the three ultra-deep stripes 1, 2, and 3 contains ~ 306 000 galaxies, including ~ 176 000 with best photometric redshifts $z = 1$–8 (see Fig. 2.1). These latter objects constitute our fiducial intermediate-redshift ($z = 1$–6) and high-redshift ($z = 6$–8) galaxy samples.

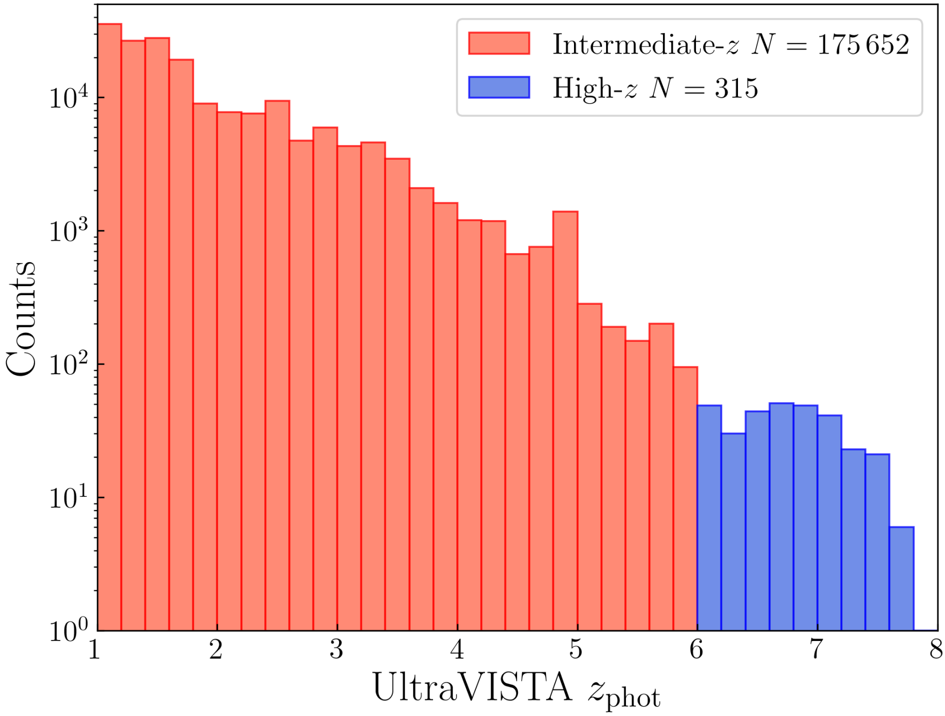

Figure 2.1 | Redshift distribution of the UltraVISTA DR4 $z = 1$–8 galaxies in the UltraVISTA ultra-deep stripes 1, 2, and 3. These galaxies constitute the fiducial intermediate ($z = 1$–6) and high-z ($z = 6$–8) samples in this work. The intermediate-z and high-z samples consist of 175652 and 315 galaxies, respectively.

2.3. SIMULATION OF *Euclid*, RUBIN-LSST, H20 SURVEY, AND *Spitzer* PHOTOMETRY OF $z = 1$–8 GALAXIES

The main goal of this analysis is to assess the identification of $z > 6$ and $z = 1$–6 galaxies based on the data that are (or will be) available in the Euclid Deep Fields. *Euclid* will observe the sky in four photometric bands: the $I_{\rm E}$, $Y_{\rm E}$, $J_{\rm E}$ and $H_{\rm E}$ bands, which together cover the wavelength range 5500–20 000 Å (Euclid Collaboration: Schirmer et al. 2022). Given that one of the aims of this research is to investigate how the inclusion of external data improves the photometric redshift of *Euclid* sources at $z > 6$, we considered additional Rubin, CFHT and Subaru Hyper Suprime Camera (HSC), and *Spitzer* photometry. To simulate photometry in the *Euclid* (+ancillary) bands, we made use of the above described SMUVS/UltraVISTA galaxy catalogue as a basis. In addition, as described in Appendix 2.7, we repeated our analysis based on the COSMOS2020 catalogue (Weaver et al. 2022), for which all photometric measurements have been obtained in an independent manner.

In this paper we consider complementary data from the Vera Rubin C. Observatory, which will sample the two southern Euclid Deep Fields in the Legacy Survey of Space and Time (LSST; Ivezić et al. 2019). The Rubin Observatory will observe in six photometric bands, *ugrizy*, which span the wavelength range 3200–11 000 Å. Given that the Euclid Deep Field North cannot be observed by Rubin, we also consider the ongoing Hawaii Two-0 Survey (H20), which is currently observing the Euclid Deep Field North and Euclid Deep Field Fornax (McPartland et al., in prep). The H20 survey will consist of deep optical data in the MegaCam *u* band of the CFHT and the Subaru HSC *g,r,i,z* bands, and will be available long before the Rubin full depth mosaics. Therefore, we consider both simulated Rubin- and H20-like photometry complementary to the *Euclid* bands. Lastly, *Spitzer*/IRAC observations of the Euclid Deep Fields were presented in Euclid Collaboration: Moneti et al. (2022), who combined new observations with all relevant archival IRAC data to produce very deep imaging of these fields in all four IRAC bands. Given that these *Spitzer* mosaics are very similar in depth to SMUVS (5σ mag = 24.8), we directly use the observed SMUVS photometry and therefore only consider the IRAC 3.6 and 4.5 μm bands. We note that our choice for including the H20 survey and IRAC bands is based on the Cosmic Dawn Survey (Toft et al., in prep), which is an ongoing effort to obtain multi-wavelength imaging for the Euclid Deep Fields to depths that will match the *Euclid* data.

In Table 2.1 we provide an overview of the expected 5σ point-like source depths, mean wavelengths and filter widths of *Euclid* (+ancillary) photometric bands considered in this work. Their corresponding transmission curves are shown in Fig. 2.2. The expected *Euclid* depths are taken from Euclid Collaboration: Scaramella et al. (2022), assuming that the Euclid Deep Survey will be two magnitudes deeper than the Euclid Wide Survey. For our tests we consider two different scenarios for the Rubin 5σ point source depth: one that is expected after 10 years of observing and one that is representative for the Rubin Deep Drilling Fields (DDF), which are likely to coincide with the two southern Euclid Deep Fields. We assumed approximate Rubin DDF depths from Foley et al. (2018). It is worth noting that the 5σ depths presented in Table 2.1 are estimates and may vary once all programmes are finalised, with the exception of the already completed *Spitzer* observations.

We considered our UltraVISTA galaxy catalogue with fiducial $z > 1$ redshifts and simulated their *Euclid* (+ancillary) photometry by convolving their best-fit SEDs based on the 28-band COSMOS photometry with the *Euclid* (+ancillary) filter curves, which can be easily done with `LePhare`. We modelled the flux errors following separate methods for each instrument. For the *Euclid* and H20 photometry, we followed the method presented in `LePhare` to simulate magnitude errors:

$$\sigma_m = \begin{cases} \sigma_{m_5} \times 10^{\,0.3\,(m-m_5)} & \text{if } m \leq m_5 \\ \sigma_{m_5} \times 0.37 \exp\left(10^{\,0.22\,(m-m_5)}\right) & \text{if } m > m_5 \end{cases}, \tag{2.1}$$

where m_5 is the 5σ point-source depth from Table 2.1 and σ_{m_5} is the corresponding magnitude error. In addition, we added a 0.03 systemic magnitude error to σ_m in quadrature. For the Rubin photometry, we used the formulae provided in Ivezić et al. (2019). The Rubin total photometric error has both a systematic and a random contribution, with the latter being dependent on the expected 5σ depth in each band. We refer the reader to Ivezić et al. (2019) for a detailed description of the Rubin flux error prescription. For the *Spitzer* photometry we adopted a strategy where the fluxes are sampled from the fiducial best-fit SED (as was done for the *Euclid*, H20, and Rubin photometry) and the flux errors

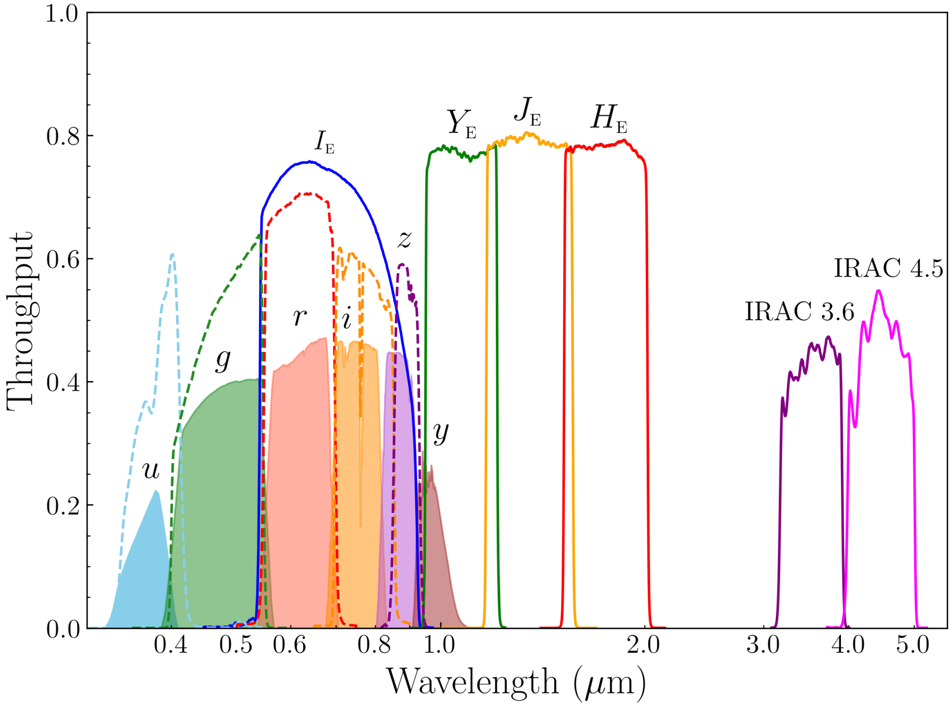

Figure 2.2 | Transmission curves of the *Euclid* I_E, Y_E, J_E, and H_E filters, the Rubin *u, g, r, i, z,* and *y* filters (filled-in, solid curves), the CFHT *u* and Subaru HSC *g,r,i,* and *z* filters (open, dashed curves), and the *Spitzer* IRAC 3.6 and 4.5 μm filters.

Table 2.1 | Expected 5σ depth (for point-like objects) in the Euclid Deep Fields, mean wavelength, and full width half maximum (FWHM) of the four *Euclid* filters, the Rubin $ugrizy$ filters, the CFHT u and Subaru/HSC $griz$ filters (McPartland et al., in prep), and the *Spitzer* IRAC 3.6 and 4.5 μm filters (Euclid Collaboration: Moneti et al. 2022).

Band	5σ depth [AB]	$\lambda_{\rm mean}$ [Å]	FWHM [Å]
$I_{\rm E}$	28.2	7140	3627
$Y_{\rm E}$	26.3	10 829	2667
$J_{\rm E}$	26.5	13 696	4053
$H_{\rm E}$	26.4	17 762	5032
Rubin/u	26.1 (26.8)[a]	3685	516
Rubin/g	27.4 (28.4)	4802	1461
Rubin/r	27.5 (28.5)	6231	1356
Rubin/i	26.8 (28.3)	7542	1248
Rubin/z	26.1 (28.0)	8690	1028
Rubin/y	24.9 (26.2)	9736	9699
CFHT/u	26.2	3832	3899
HSC/g	27.5	4816	4724
HSC/r	27.5	6234	6136
HSC/i	27.0	7741	7654
HSC/z	26.5	8911	8902
IRAC/3.6 μm	24.8	35 634	7444
IRAC/4.5 μm	24.7	45 110	10 119

a Rubin depth after 10 years of observing; in parentheses we show the depths expected for the Rubin DDF (Foley et al. 2018).

are simply set to the observed *Spitzer* flux errors from SMUVS, as the *Spitzer* observations of the Euclid Deep Fields are similar in depth to SMUVS. Given that not all sources in our UltraVISTA catalogue are *Spitzer*-detected, we only simulated *Spitzer* photometry for galaxies that have a detection in at least one IRAC band. All simulated magnitudes and magnitude errors were subsequently converted to flux space.

In total, we address eight scenarios of different combinations of *Euclid*, Rubin, H20, and *Spitzer* photometry, as summarised in Table 2.2. Throughout this paper, we globally refer to these combinations as *Euclid* (+ancillary) photometry. The number of final sources in the simulated *Euclid* photometric catalogues are listed in this table, where the distinction between intermediate-z and high-z galaxies is based on the fiducial redshift. We remind the reader that the number of sources in the catalogues including *Spitzer* photometry is lower as not all galaxies in our UltraVISTA DR4 catalogue are IRAC-detected. For each filter we randomised the simulated photometry of each galaxy by sampling a Gaussian distribution with mean μ equal to the modelled flux from the fiducial best-fit SED and standard deviation σ equal to the flux error, derived as explained above.

Since our simulated fluxes are directly sampled from the fiducial best-fit galaxy template, they are unaffected by exposure time limits, contrary to real, observed photometry. Therefore, to ensure our simulated photometry is realistically deep, we applied a 2σ flux limit to each filter, as derived from their expected 5σ survey depth. For *Euclid*, Rubin, and H20 bands with fluxes fainter than their 2σ detection limits, we adopted 2σ flux upper limits in the subsequent SED fitting process. For *Spitzer* fluxes fainter than the corresponding 2σ limits, we did not adopt 2σ upper limits, but rather excluded the band in the SED fitting process. We implemented this criterion because the χ^2-minimisation technique of the SED fitting naturally has most of its weight at the longest wavelength filters and could be confused rather than helped by the presence of flux upper limits.

In our analysis, we consider a single realisation of the randomly simulated photometry. We produced and analysed a few other realisations, but found no significant differences in the results discussed below.

2.4. RESULTS

2.4.1. PHOTOMETRIC REDSHIFTS BASED ON *Euclid* AND ANCILLARY DATA

We repeated the SED fitting of the sources with fiducial $z > 1$ redshifts, using `LePhare` again, but now considering only the simulated *Euclid* (+ancillary) data. We used exactly the same `LePhare` settings as for the UltraVISTA DR4 catalogue, described in Sect. 2.2.2 (the flat absolute magnitude prior is now applied to the H_E band). Despite the low number of photometric bands, `LePhare` finds a redshift solution for > 99 % of the sources from *Euclid* photometry alone. We did not repeat our checks for stellar solutions or compatibility with short wavelengths, but the latter is discussed in Sect. 2.6.1.

We aim to illustrate how the incorporation of ancillary data improves the performance of the photometric redshift recovery. Therefore, we compare the derived redshifts (to which we refer as simulated redshifts) with the fiducial redshifts obtained from our UltraVISTA and remaining COSMOS photometry (28 bands in total) in three scenarios: *Euclid*, *Euclid*+H20, and *Euclid*+Rubin DDF. The results are shown in Fig. 2.3. In each panel, we identify catastrophic outliers as sources satisfying the condition

$$\frac{|z_\mathrm{sim} - z_\mathrm{fid}|}{1 + z_\mathrm{fid}} > 0.15, \tag{2.2}$$

where z_sim is the simulated redshift and z_fid the fiducial redshift. We calculated the catastrophic outlier fraction (OLF) in two redshift bins separately, namely $z = 1$–6 (intermediate-z) and $z = 6$–8 (high-z). We note that the OLF only quantifies the quality of the photometric redshifts in these fiducial redshift bins; contamination of the intermediate-z bin to the high-z bin is addressed in Sect. 2.4.2.

From Fig. 2.3 it is evident that the addition of ancillary data improves the redshift estimation for both intermediate- and high-z galaxies. First, we discuss the photometric redshift quality when only the four *Euclid* bands are utilised. At $z_\mathrm{fid} > 6$, the redshifts are already quite accurate, with an OLF of 7.6 %. This is the result of the wavelength range covered by the *Euclid* bands, as for galaxies at $z = 6$–8, they sample the rest-frame UV and optical continuum, enabling the identification of $z > 6$ galaxies with the Lyman-break drop-out technique (Steidel et al. 1996). On the contrary, the redshift recovery at intermediate redshifts is considerably poorer. The majority (> 65 %) of the intermediate-z sample consists of $z_\mathrm{fid} = 1$–2 galaxies (see Fig. 2.1), and so the *Euclid* filters sample the rest-frame optical continuum redwards of the Lyman-α line. With no constraint on the Lyman break, galaxies with red UV slopes (either from dust attenuation or old age) are easily confused for higher-redshift objects. Simultaneously, young non-dusty sources at

Table 2.2 | Summary of the eight scenarios of combinations of *Euclid* and ancillary data considered in this work and the corresponding 2σ magnitude limits that were applied to the photometry. The number of intermediate-z and high-z galaxies that are inserted in our simulations (based on their fiducial redshift) is indicated in the last two columns.

Scenario	Description	$z = 1$–6	$z = 6$–8
Euclid	*Euclid* $I_{\mathrm{E}}, Y_{\mathrm{E}}, J_{\mathrm{E}}, H_{\mathrm{E}}$	175 652	315
Euclid + Rubin	*Euclid* $I_{\mathrm{E}}, Y_{\mathrm{E}}, J_{\mathrm{E}}, H_{\mathrm{E}}$; Rubin $ugrizy$ (depth after 10 years)	175 652	315
Euclid + Rubin DDF	*Euclid* $I_{\mathrm{E}}, Y_{\mathrm{E}}, J_{\mathrm{E}}, H_{\mathrm{E}}$; Rubin $ugrizy$ (Deep Drilling Fields depth)	175 652	315
Euclid + H20	*Euclid* $I_{\mathrm{E}}, Y_{\mathrm{E}}, J_{\mathrm{E}}, H_{\mathrm{E}}$; CFHT u and Subaru HSC $griz$	175 652	315
Euclid + *Spitzer*	*Euclid* $I_{\mathrm{E}}, Y_{\mathrm{E}}, J_{\mathrm{E}}, H_{\mathrm{E}}$; *Spitzer* IRAC 3.6 and 4.5 μm	134 562	203
Euclid + Rubin + *Spitzer*	*Euclid* $I_{\mathrm{E}}, Y_{\mathrm{E}}, J_{\mathrm{E}}, H_{\mathrm{E}}$; Rubin $ugrizy$ (depth after 10 years); *Spitzer* IRAC 3.6 and 4.5 μm	134 562	203
Euclid + Rubin DDF + *Spitzer*	*Euclid* $I_{\mathrm{E}}, Y_{\mathrm{E}}, J_{\mathrm{E}}, H_{\mathrm{E}}$; Rubin $ugrizy$ (Deep Drilling Fields depth); *Spitzer* IRAC 3.6 and 4.5 μm	134 562	203
Euclid + H20 + *Spitzer*	*Euclid* $I_{\mathrm{E}}, Y_{\mathrm{E}}, J_{\mathrm{E}}, H_{\mathrm{E}}$; CFHT u and Subaru HSC $griz$; *Spitzer* IRAC 3.6 and 4.5 μm	134 562	203

Photometry	2σ limiting magnitude [AB]
Euclid	$I_{\mathrm{E}} = 29.2$; $Y_{\mathrm{E}} = 27.3$; $J_{\mathrm{E}} = 27.5$; $H_{\mathrm{E}} = 27.4$
Rubin (10 yrs depth)	$u = 27.1$; $g = 28.4$; $r = 28.5$; $i = 27.8$; $z = 27.1$; $y = 25.9$
Rubin (DDF depth)	$u = 27.8$; $g = 29.4$; $r = 29.5$; $i = 29.3$; $z = 29.0$; $y = 27.2$
H20	$u = 27.2$; $g = 28.5$; $r = 28.5$; $i = 28.0$; $z = 27.5$
Spitzer	$[3.6] = 25.8$; $[4.5] = 25.7$

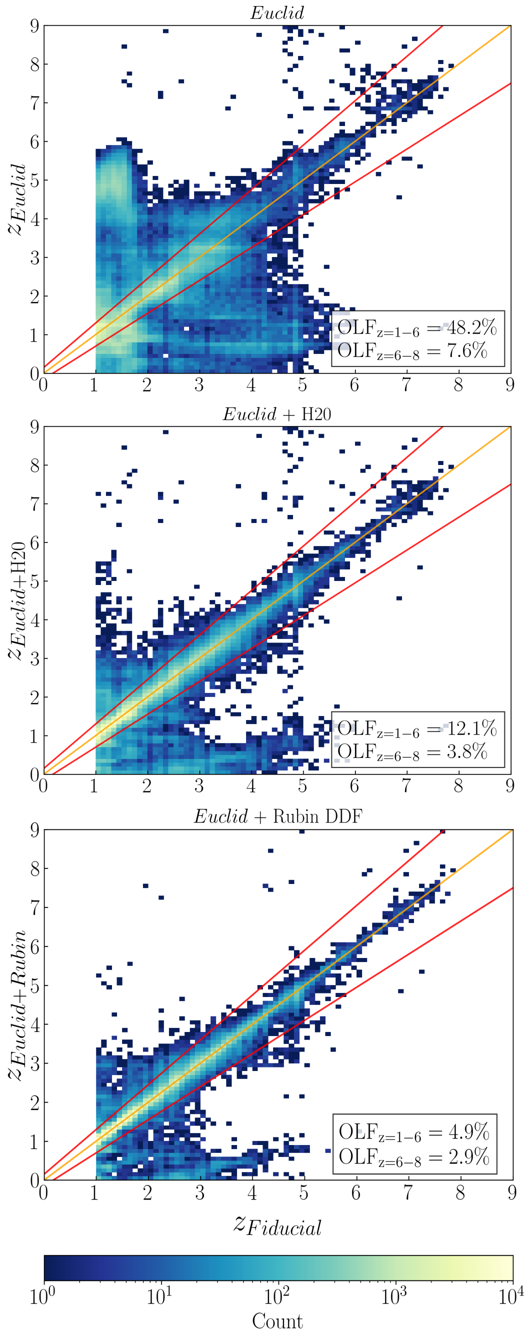

Figure 2.3 | Comparison of the fiducial photometric redshift to the photometric redshift obtained from three combinations of *Euclid* and ancillary photometry. In each panel, the catastrophic outlier fractions (OLFs) are reported for two fiducial redshift bins, $z = 1$–6 and $z = 6$–8. The OLF represents the fraction of sources with $|z_{\mathrm{sim}} - z_{\mathrm{fid}}|/(1 + z_{\mathrm{fid}}) > 0.15$. The outlier identification boundaries are indicated with solid red lines. The data points are presented as 2D histograms with bin size $\Delta z = 0.1$. The colour bar corresponds to the number of galaxies in each bin and is the same for all panels. The solid orange line is the identity curve. Data outside the two solid red lines are identified as catastrophic outliers.

Table 2.3 | Number of true $z > 6$ galaxies (that is, galaxies at fiducial $z_{\text{fid}} = 6$–8 that are recovered at $z_{\text{sim}} > 6$) and $z > 6$ contaminants (galaxies at fiducial $z_{\text{fid}} = 1$–5.8 recovered at $z_{\text{sim}} > 6$), from various combinations of *Euclid* and ancillary data. In addition, we report the fraction of contaminants amongst the total apparent $z > 6$ population, for which uncertainties from ten random realisations of the contaminant and true $z > 6$ source photometry. We also report the completeness, which represents the percentage of fiducial $z = 6$–8 galaxies that are correctly identified as $z > 6$ sources.

Filters	True $z > 6$	Contaminants	Contamination Fraction	Completeness
Euclid	287	65	$0.18^{+0.07}_{-0.06}$	91 %
Euclid + Rubin	291	71	$0.20^{+0.07}_{-0.09}$	92 %
Euclid + Rubin DDF	301	13	$0.04^{+0.03}_{-0.02}$	96 %
Euclid + H20	286	65	$0.19^{+0.07}_{-0.09}$	91 %
Euclid + *Spitzer*	188	27	$0.13^{+0.04}_{-0.05}$	93 %
Euclid + Rubin + *Spitzer*	193	26	$0.12^{+0.04}_{-0.04}$	95 %
Euclid + Rubin DDF + *Spitzer*	191	2	$0.01^{+0.0006}_{-0.0001}$	94 %
Euclid + H20 + *Spitzer*	186	23	$0.11^{+0.04}_{-0.04}$	92 %

$z_{\text{fid}} = 1$–2 that have a mostly flat UV and optical continuum become highly degenerate with $z \sim 5$ galaxies, as a flat SED without a strong 4000 Å break can be confused for a UV-bright high-redshift object. Interestingly, only the latter type of degeneracy is clearly present in Fig. 2.3; $z_{\text{fid}} = 1$–2 galaxies are predominately scattered between $z_{\text{sim}} = 4$ and $z_{\text{sim}} = 6$, with only a few sources at $z_{\text{sim}} > 7$.

We find that the inclusion of deep optical data, either from Rubin observations or the H20 survey, reduces the number of catastrophic outliers, especially at intermediate redshifts. At $z = 6$–8, this can be explained since the short-wavelength bands sample the spectrum bluewards and redwards of the Lyman-α break, such that the photometric redshift estimation becomes more precise. In addition, the inclusion of optical data rules out a low-redshift nature for nearly all $z_{\text{fid}} > 6$ galaxies. At intermediate redshifts, we see how the inclusion of optical data strongly improves the OLF. Moreover, with data from the Rubin DDF, which constitutes the deepest optical ancillary data considered in this work, the degeneracy between $z_{\text{fid}} = 4$–6 and $z_{\text{sim}} > 6$ galaxies is almost completely lifted in our analysis.

2.4.2. IDENTIFICATION OF $z > 6$ CONTAMINANTS

For each *Euclid* (+ancillary) data scenario, we identify three populations from the redshift comparison plots shown in Fig. 2.3: (i) galaxies with fiducial redshifts $z_{\text{fid}} = 1$–6 that stay in that same redshift bin when the photometric redshift is obtained with *Euclid* (+ancillary) photometry, to which we refer as the 'stable' intermediate-z galaxy population; (ii) galaxies with fiducial redshifts $z_{\text{fid}} > 6$ that stay at these high redshifts when the photometric redshift is obtained with *Euclid* (+ancillary) photometry, which are the 'true' $z > 6$ galaxies; and (iii) galaxies with fiducial redshifts $z_{\text{fid}} = 1$–5.8 and *Euclid* (+ancillary) redshifts $z > 6$, which we consider to be the intermediate-redshift contaminants to the high-z galaxy sample. The latter population constitutes the main subject of study in this paper. We set an upper redshift cut at a fiducial redshift $z_{\rm fid} = 5.8$ for the purpose of defining contaminants to avoid discussing sources that may end up populating the $z > 6$ regime simply due to a random error scattering of the photometric redshifts. Therefore, galaxies with $z_{\rm fid} = 5.8$–6 that are falsely recovered at $z > 6$ are discarded from our analysis, as they would constitute only 6 % the true $z > 6$ population (*Euclid* alone) and the majority are recovered at $z_{\rm sim} = 6$–6.2. Lastly, we acknowledge a fourth population consisting of galaxies with fiducial redshifts $z_{\rm fid} > 6$ that appear as intermediate-z galaxies when observed with *Euclid*. These sources constitute 9 % of the fiducial $z = 6$–8 galaxy sample (*Euclid* alone). The study of this population is outside the scope of this paper.

For each data scenario, in Table 2.3 we present the number of true $z > 6$ galaxies, the number of $z > 6$ contaminants and the following fraction of contaminants amongst the apparent $z > 6$ galaxy population. By apparent $z > 6$ galaxies we mean all the galaxies assigned a photometric redshift $z > 6$ based on the *Euclid* (+ancillary) simulated photometry, independently of being truly at these redshifts or not. We also report the completeness in Table 2.3, which represents the percentage of fiducial $z_{\rm fid} = 6$–8 galaxies that are correctly identified as $z_{\rm sim} > 6$ sources. The missing galaxies in our reported completeness are those with fiducial $z_{\rm fid} > 6$ redshifts, but which are falsely recovered at $z_{\rm sim} < 6$ with the *Euclid* (+ancillary) photometry. We remind the reader that not all galaxies in our fiducial $z = 1$–8 galaxy sample are IRAC-detected, explaining the lower numbers of $z > 6$ contaminants and true $z > 6$ galaxies in scenarios where *Spitzer* data are considered.

We calculated the uncertainties in the contamination fraction by producing ten randomised flux catalogues of the $z > 6$ contaminants and the true $z > 6$ galaxies, for which we derived the photometric redshifts with `LePhare`. Subsequently, we assigned a probability of correct identification to each source by counting in how many realisations the source is re-identified as a contaminant, and identically for the true $z > 6$ sample. Using the average probability of correct identification, we calculated upper and lower limits on both the number of contaminants and the number of true $z > 6$ galaxies, which were propagated into an upper and lower limit on the contamination fraction. We adopt this approach as a compromise because producing ten realisations of the entire $z = 1$–8 flux catalogue is too computationally expensive.

Our main findings on the contamination fraction are as follows. First, the fraction of contaminants amongst the apparent $z > 6$ population is already relatively low when only data from the four *Euclid* bands are available: 18 % of all apparent $z > 6$ galaxies are actually intermediate-z contaminants. In addition, the $z > 6$ completeness is very high in all data scenarios, even with *Euclid* photometry alone.

Second, for sources at the UltraVISTA depth, the inclusion of ancillary optical data produces a negligible effect in the fraction of contaminants and the $z > 6$ completeness level. This is because the Rubin and H20 surveys are both shallower in the optical regime than the Euclid Deep Survey (see Table 2.1), and as such their data are of little help in preventing intermediate-z galaxies from being misidentified as $z > 6$ galaxies. In fact, the contamination fractions from *Euclid*+Rubin and *Euclid*+H20 are slightly higher than that from *Euclid* photometry alone, although the difference is not significant within the uncertainties. We expect the H20 data to perform better in the redshift recovery compared to Rubin, even though the latter includes the additional y band coverage. This can be explained as the H20 data are slightly deeper, especially in the z band.

Only with the ultra-deep photometry from the Rubin DDF does the contamination fraction improve, as the Rubin DDF r and i data will be 0.3 and 0.1 mag deeper than the $I_{\rm E}$ photometry. Clearly, the Rubin DDF data provide such stringent constraints on the photometric depth that even the faintest intermediate-z galaxies in our sample cannot be confused for high-redshift sources. However, we note that this is the most idealised scenario we consider in this paper, and only with these data can the contamination fraction be taken to very low levels. As a safety measure, we tested the scenario where we combine simulated Rubin DDF and *Spitzer* data, without including *Euclid* photometry. In this case, we find a contamination fraction of 0.08 and a completeness of 92 %. This demonstrates that whereas the Rubin DDF photometry is incredibly effective at reducing the degree of contamination, *Euclid* photometry is essential to achieve virtually no contamination.

Third, *Spitzer* data are moderately helpful in preventing the incidence of intermediate-redshift contaminants to the $z > 6$ sample. The majority of contaminants are at $z_{\rm fid} = 4$–6, and produce redder fiducial $(H - [3.6])$ contaminants than actual $z > 6$ galaxies. Hence, IRAC detections enable one to distinguish between a red SED slope from intermediate-z interlopers and a flat SED slope that one would observe for young galaxies at high redshifts. However, using *Euclid*+*Spitzer* data, the contamination fraction is still 0.13, so the improvement is marginal compared to the *Euclid*+Rubin DDF scenario. We believe this is mostly due to the typical uncertainty of IRAC fluxes, given that *Spitzer* sources are severely blended in crowded fields such as COSMOS. In addition, we investigate the signal-to-noise ratio (S/N) in the simulated IRAC bands and conclude that 67 % of the contaminants identified from *Euclid*+*Spitzer* data have a $F_\nu/\sigma_{F_\nu} \geq 5$ detection in both IRAC bands.

It is possible that the particular de-blending treatment used to obtain IRAC photometry (see Deshmukh et al. 2018 for a detailed overview) leads to a slight underestimation of the flux errors. Given that in this scenario redshifts are based on only six bands, any uncertainties in the IRAC photometry carry more weight in the SED fitting as compared to the fit on the fiducial, 28-band photometry. We note that the limited effectiveness of the IRAC photometry is independent of our specific method for measuring the IRAC fluxes; when we estimate the contamination fractions using the COSMOS2020 catalogue as presented in Appendix 2.7, for which the IRAC photometry was derived in a completely independent manner, we find it has essentially no effect on the contamination fraction.

Finally, combining *Euclid* photometry with both optical and infrared data yields the best contamination fractions; evidently, with more photometric bands available for the SED fitting, the redshift recovery steadily improves. In the *Euclid*+Rubin DDF+*Spitzer* scenario, the deep, 11-band photometry is highly successful at correctly identifying $z > 6$ galaxies, and so contamination from intermediate-z interlopers is virtually non-existent and the $z > 6$ completeness is very high at 94 %.

Apart from the eight combinations of *Euclid* and ancillary bands considered throughout this work, we evaluate a few other scenarios to gain more insight into preventing intermediate-z interlopers.

First, we tested the importance of the Rubin y band for the selection of high-z galaxies, given that *Euclid* itself will create very deep imaging in the $Y_{\rm E}$ band (see Fig. 2.2 for the respective filter transmission curves). Presumably, y-band observations are of key importance to the $z > 7$ galaxy selection, since at $z = 7$–8 the Lyman-α break at 1216 Å is sampled by this band. In this paper we have assumed that the Rubin DDF will be 0.1 mag shallower in the y band as compared to the Euclid Deep Fields. We derive the contamination fraction from *Euclid*+Rubin DDF photometry whilst excluding the y band, and find that it is 0.07 as compared to 0.04 whilst including the y band (see Table 2.3). Simultaneously, we find that a 0.5 mag increase in the Rubin DDF y-band depth does not improve the contamination fraction any further. Therefore, we conclude that even though the central wavelengths and filter widths of the Rubin y and *Euclid* Y_{E} band differ, ultra-deep Rubin y-band photometry is only marginally effective when Y_{E}-band imaging is readily available.

Second, we tested how robust our results on the contamination fraction are when we vary the full final depth of the ancillary data. The magnitude limits adopted throughout this paper are, with the exception of the *Spitzer* data, not definite as the observations have not commenced or are not completed yet. Therefore, an assessment of how the degree of contamination is dependent on the final survey depths is important. We determine that if the H20 survey was 0.5 mag deeper across all five bands, the fraction of contaminants amongst the apparent $z > 6$ sample would decrease from 0.19 to 0.10. Simultaneously, by making the Rubin DDF 0.5 mag shallower across all six bands, the contamination fraction worsens from 0.04 to 0.08. Clearly, the final depth of the optical data has strong implications for the contamination fraction.

Finally, we investigated which optical band contributes the most to accurate $z > 6$ galaxy selection, using *Euclid*+H20 data. We increased the 5σ depth by 0.5 mag for each H20 band individually whilst the photometry in the other bands remains unchanged, creating five different flux catalogues. Subsequently, we derive the contamination fraction for all five realisations, and find the Subaru HSC i band is most important for excluding intermediate-z interlopers, reducing the contamination fraction to 0.14 (as compared to 0.19 from *Euclid*+H20 with no depth variations). This is unsurprising as the majority of our fiducial $z > 6$ sample is at $z = 6$–7 and so the i band provides a strong constraint on the Lyman-α break. The second most important band is the Subaru HSC z band (contamination fraction of 0.15). Conversely, we find that increasing the survey depth in the CFHT u band leaves the contamination fraction unimproved. We emphasise that these results on the importance of individual bands concern the contamination of $z > 6$ sources. In fact, the CFHT u band is most important for normal galaxies at lower-redshifts, that is, the OLF of stable intermediate-z galaxies as defined in Fig. 2.3 moderately improves to 11.2 % from increasing the u band depth.

Depending on the research purpose, certain detection threshold requirements may be imposed on potential *Euclid* high-redshift galaxies. Therefore, we explore how a 5σ detection threshold requirement in at least one of the NIR bands for *Euclid* high-redshift galaxies may result in lower degree of contamination by intermediate-z sources. Considering only *Euclid* data, the contamination fraction is reduced to $0.12^{+0.04}_{-0.04}$ with this measure. Generally, we find a moderate improvement in the contamination fraction in each *Euclid* (+ancillary) data scenario, but no significant differences within the error bars. We further explore the usefulness of S/N cuts in Sect. 2.4.3.

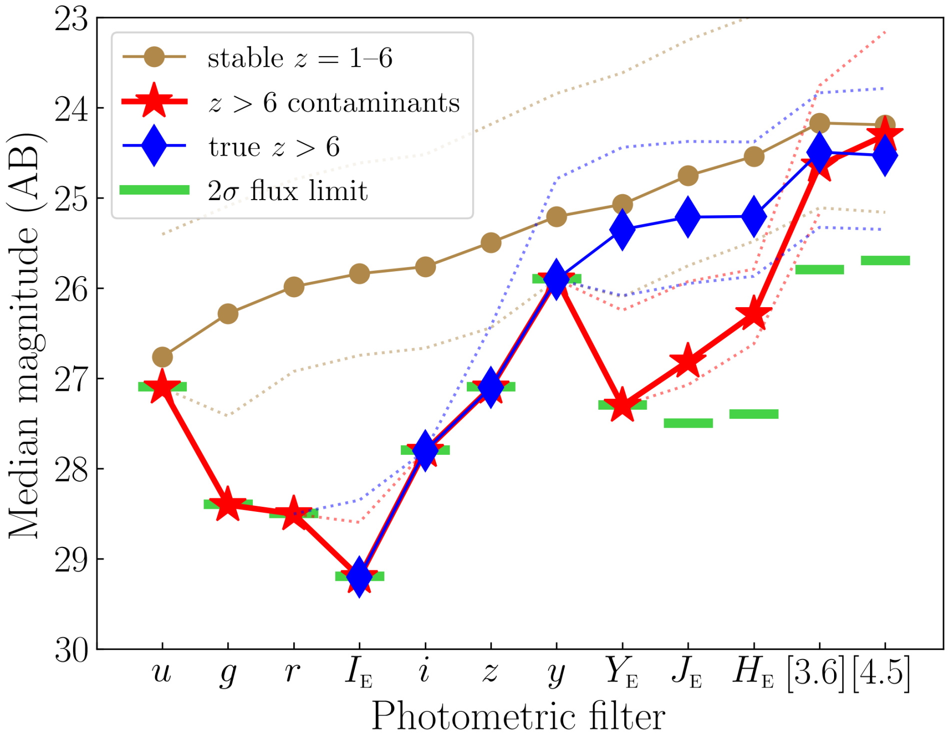

Figure 2.4 | Median magnitudes of our simulated sources in the *Euclid*, Rubin, and *Spitzer* filters. Light brown circles represent stable intermediate-z galaxies, red stars $z > 6$ contaminants, and blue diamonds true $z > 6$ galaxies. For each population, the dotted lines indicate the 16^{th} and 84^{th} percentiles. For each band, the 2σ flux limit is shown with a green bar. The selection of intermediate-z, contaminants, and $z > 6$ galaxies is based on *Euclid*+Rubin+*Spitzer* data. The median magnitudes for $z > 6$ galaxies in the Rubin u, g, r bands are equal to -99 (no intrinsic flux) and therefore omitted from this figure.

2.4.3. SEPARATION OF CONTAMINANTS FROM TRUE $z > 6$ GALAXIES

Having quantified the incidence of intermediate-redshift contaminants in the $z > 6$ sample, now we aim to develop a method to cleanly separate the contaminants from the true $z > 6$ galaxies, based on the photometry available in the Euclid Deep Fields. To achieve this, we investigate which photometric and SED properties can separate the two populations. Specifically, we investigate the usefulness of colour diagrams. For instance, Bisigello et al. (2020) already showed how *Euclid* colour-colour selection techniques can effectively separate star-forming and quiescent galaxies at $z = 0$–3.

Figure 2.4 shows the median observed magnitude in each filter for intermediate-z galaxies, $z > 6$ contaminants and true $z > 6$ galaxies identified from *Euclid*+Rubin+*Spitzer* photometry. This figure demonstrates that contaminants of $z > 6$ galaxies are the faintest amongst intermediate-redshift galaxies, that is, falsely identified $z > 6$ galaxies tend to be much fainter than secure $z = 1$–6 galaxies. On average, contaminants are ~ 1.9 mag fainter

Colour cut	Condition
$(I_E - Y_E) > 2.0$ & $(Y_E - J_E) < 1.4$	all true $z > 6$ galaxies with a I_E and/or Y_E detection included
$(I_E - Y_E) > 2.6$ & $(Y_E - J_E) < 1.4$	95 % of true $z > 6$ galaxies with a I_E and/or Y_E detection included
$(I_E - Y_E) > 2.8$ & $(Y_E - J_E) < 1.4$	90 % of true $z > 6$ galaxies with a I_E and/or Y_E detection included
$(I_E - Y_E) > 3.4$ & $(Y_E - J_E) < 0.9$	all contaminants with a I_E and/or Y_E detection excluded

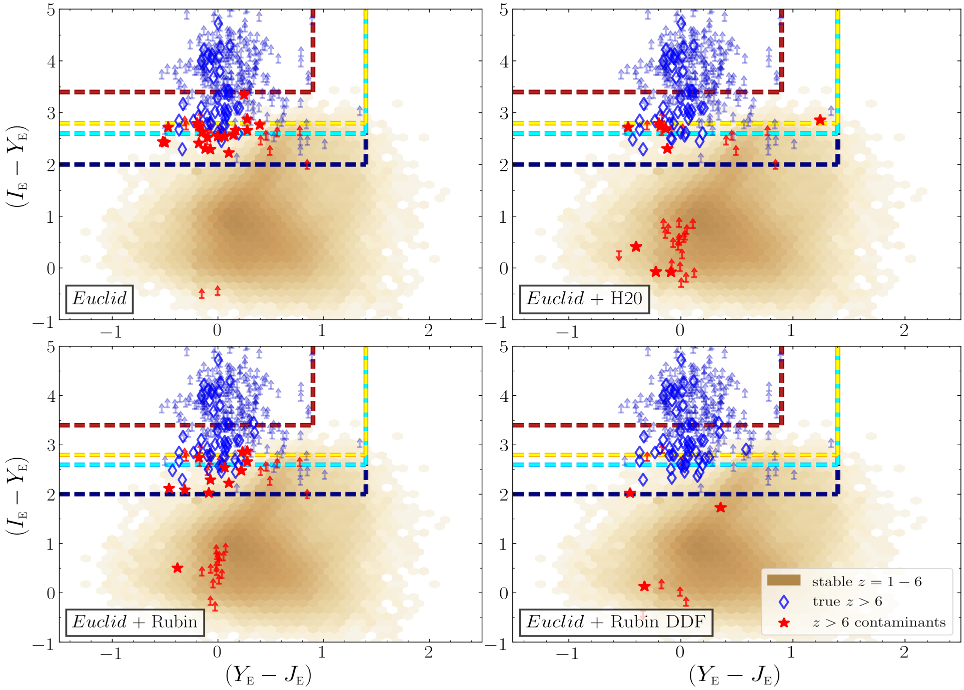

Figure 2.5 | $(I_E - Y_E)$ versus $(Y_E - J_E)$ colour diagrams in eight cases of combinations of *Euclid* and ancillary data, showing only sources with a flux measurement in the I_E and/or Y_E band. In the scenario of *Euclid* data only, this means that 1.4 % and 46 % of the true $z > 6$ sources and contaminants are left out of the colour-colour diagram. The $z > 6$ contaminants and true $z > 6$ galaxies are shown with red stars and blue diamonds, respectively (lower limits are shown with arrows in corresponding colours). The stable intermediate-z sources are shown in light brown hexagonal bins, where the colour intensity corresponds to the number of galaxies in each bin (darker colours correspond to more sources). The various colour selection criteria and the conditions they meet are listed at the top, and the criteria are indicated in the colour diagrams with dashed coloured lines.

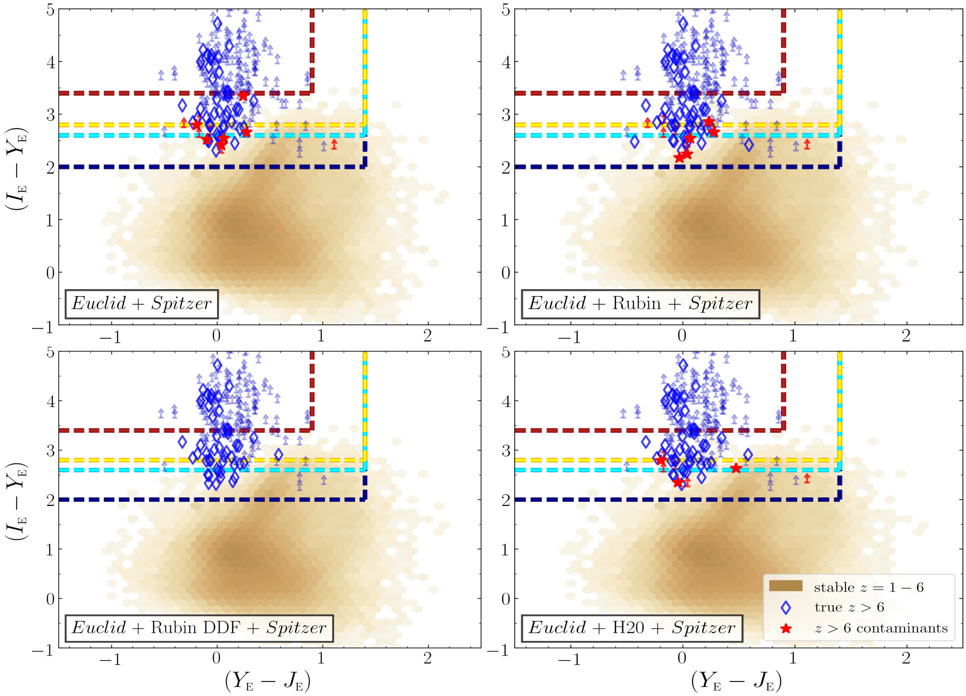

Figure 2.5 | Continued.

Table 2.4 | Contamination fraction and completeness for four different $(I_{\rm E} - Y_{\rm E})$ & $(Y_{\rm E} - J_{\rm E})$ colour cuts, in eight scenarios of *Euclid* (+ancillary) photometry, once applied to all sources that have a $I_{\rm E}$ and/or $Y_{\rm E}$ flux measurement. The colour cuts are listed in the first column, while the other columns correspond to the different data combinations. In these eight columns, we show the fraction of intermediate-z interlopers amongst the apparent $z > 6$ galaxy sample after applying the colour cut (on the left) and the percentage of fiducial $z > 6$ galaxies correctly identified as high-z sources that survive the cut (on the right). The colouring of the rows in this table is equal to how the colour selection criteria are plotted with coloured, dashed lines in Fig. 2.5.

Colour cut $(I_{\rm E} - Y_{\rm E})$ & $(Y_{\rm E} - J_{\rm E})$	*Euclid*	*Euclid* +H20	*Euclid* +Rubin	*Euclid* +Rubin DDF	*Euclid* +*Spitzer*	*Euclid* +Rubin +*Spitzer*	*Euclid* +Rubin DDF +*Spitzer*	*Euclid* +H20 +*Spitzer*
2.0 & 1.4	0.10 90%	0.05 90%	0.08 91%	0.01 94%	0.06 91%	0.05 94%	0.0 93%	0.04 90%
2.6 & 1.4	0.05 86%	0.03 85%	0.03 86%	0.01 89%	0.03 85%	0.03 86%	0.00 86%	0.03 85%
2.8 & 1.4	0.01 81%	0.01 81%	0.01 81%	0.00 82%	0.01 78%	0.01 79%	0.00 78%	0.01 77%
3.4 & 0.9	0.00 58%	0.00 59%	0.00 58%	0.00 59%	0.00 55%	0.00 55%	0.00 55%	0.00 55%

than stable intermediate-z galaxies in the *Euclid* and Rubin filters. Only in the IRAC bands are the contaminants similarly bright to the stable intermediate-z sources. The photometry of contaminants is dominated by 2σ flux upper limits. This is in agreement with Vulcani et al. (2017), who have shown that low-z contaminants of drop-out selected $z > 5$ galaxies are located near the detection limit of galaxy surveys. Because of the numerous upper limits, the SED fitting of the contaminants is poorly constrained, that is, their redshift parameter space becomes highly degenerate.

Moreover, Fig. 2.4 clearly shows how contaminants differ from true $z > 6$ galaxies based on their I_E, Y_E, J_E, and H_E photometry. True $z > 6$ galaxies have very red $(I_\mathrm{E} - Y_\mathrm{E})$ colours in addition to very flat $(Y_\mathrm{E} - J_\mathrm{E})$ and $(J_\mathrm{E} - H_\mathrm{E})$ colours. Conversely, $z > 6$ contaminants show on average a gradual brightening over the same wavelength range, with bluer $(I_\mathrm{E} - Y_\mathrm{E})$ colours than true $z > 6$ galaxies. The physical interpretation of this difference is straightforward. At $z_\mathrm{fid} = 6$–8, the I_E and Y_E bands sample the rest-frame spectrum blue- and redwards of Lyman-α line at $\lambda = 1216\,\mathrm{Å}$, resulting in a strong, red $(I_\mathrm{E} - Y_\mathrm{E})$ colour. On the contrary, at $z_\mathrm{fid} = 1$–5.8, the I_E and Y_E bands sample the UV continuum mostly redwards from the Lyman-α line. At this wavelength range, the fiducial SEDs of the $z > 6$ contaminants are particularly faint: they are below the assumed Euclid Survey depth and therefore have significantly different $(I_\mathrm{E} - Y_\mathrm{E})$ colours than true $z > 6$ galaxies.

For true $z > 6$ galaxies, we obtain median $(Y_\mathrm{E} - J_\mathrm{E}) = 0.14$ and $(J_\mathrm{E} - H_\mathrm{E}) = 0.01$ colours as the Y_E, J_E, and H_E filters sample the rest-frame UV and blue optical continuum. This is the result of our input fiducial $z = 6$–8 galaxies, which have similarly flat UltraVISTA $(Y - J)$ and $(J - H)$ colours and are typically UV bright (median $M_{1500\mathrm{Å}} = -21.7$ mag). Additionally, the majority of true $z > 6$ galaxies have fiducial redshift $z_\mathrm{fid} = 6$–7 (77 %), so the median $(Y_\mathrm{E} - J_\mathrm{E})$ colour is marginally influenced by the red $(Y_\mathrm{E} - J_\mathrm{E})$ colour caused by the Lyman-α break of $z_\mathrm{sim} > 7$ sources. The flat colour signature is typical for high-redshift Lyman-break galaxies (Salmon et al. 2020), as they have high specific star-formation rates (de Barros et al. 2014) and virtually no dust attenuation (Bouwens et al. 2012), resulting in flat UV spectra because of the dominance of young stellar populations.

Although Fig. 2.4 is based on *Euclid*+Rubin+*Spitzer* data, the observed general trends are present in all eight combinations of photometry. In all scenarios, we find that $z > 6$ contaminants comprise the faintest intermediate-redshift galaxies, and that contaminants have significantly different $(I_\mathrm{E} - Y_\mathrm{E})$ and $(Y_\mathrm{E} - J_\mathrm{E})$ colours from the true $z > 6$ galaxies.

These results clearly indicate the importance of the Y_E band in separating contaminants from the real $z > 6$ galaxies. Therefore, we construct colour-colour diagrams considering this band, namely $(I_\mathrm{E} - Y_\mathrm{E})$ versus $(Y_\mathrm{E} - J_\mathrm{E})$, which are shown in Fig. 2.5. We emphasise that these colour diagrams can only be constructed for galaxies up to $z_\mathrm{fid} = 8$, as sources beyond this redshift are Y_E dropouts and as such do not have a meaningful $(I_\mathrm{E} - Y_\mathrm{E})$ colour. Therefore, the below proposed colour criteria cannot be used to identify *Euclid* $z > 8$ galaxies.

Similarly, because the contaminants comprise the faintest galaxies in our sample, many have flux upper limits in both the I_E and Y_E band, so that their $(I_\mathrm{E} - Y_\mathrm{E})$ colour is meaningless. Therefore, this analysis considers only true $z > 6$ galaxies and $z > 6$ contaminants that have a detection in the I_E and/or Y_E band. In the scenario of *Euclid* data alone, this means that 1.4 % and 46 % of the true $z > 6$ galaxies and $z > 6$ contaminants are excluded, respectively. These numbers are representative for the other combinations of *Euclid* and ancillary photometry. Furthermore, the vast majority of true $z > 6$ galaxies in all scenarios have a detection in the Y_{E} band but a flux upper limit in the I_{E} band; as such, their $(I_{\mathrm{E}} - Y_{\mathrm{E}})$ colour is actually a lower limit and may be even redder in reality.

To separate the contaminants from the true $z > 6$ galaxies, we present an array of $(I_{\mathrm{E}}-Y_{\mathrm{E}})$ & $(Y_{\mathrm{E}}-J_{\mathrm{E}})$ colour criteria that produce different degrees of contamination and $z > 6$ completeness. The four colour cuts were derived using only *Euclid* data and are based on sources with a solid flux measurement in at least the I_{E} or Y_{E} band. The colour criteria and the conditions that they meet are listed in Fig. 2.5. We subsequently applied these colour cuts to the other *Euclid* (+ancillary) data scenarios, and derived the completeness and contamination fraction of the surviving galaxy sample. The results are presented in Table 2.4. The completeness is defined as the fraction of recovered $z_{\mathrm{fid}} = 6$–8 galaxies compared to the entire fiducial $z_{\mathrm{fid}} = 6$–8 sample, consisting of 315 galaxies.

First, we emphasise that the achieved contamination fractions from applying the colour criteria are lower limits, given that generally half of the $z > 6$ contaminants are not included in this analysis. For the true $z > 6$ galaxies and contaminants that have a I_{E} and/or Y_{E} detection, the colour criteria are highly successful at preventing the intermediate-z interlopers from entering the high-redshift galaxy sample. Specifically, the colour cut $(I_{\mathrm{E}} - Y_{\mathrm{E}}) > 2.8$ & $(Y_{\mathrm{E}} - J_{\mathrm{E}}) < 1.4$ (in yellow) reduces the contamination fraction to 0.01 while simultaneously preserving 90 % of the true $z > 6$ galaxies (*Euclid* alone); the resulting completeness of fiducial $z = 6$–8 galaxies is 81 %. When additional optical photometry, Spitzer data, or a combination of both are considered, this cut reduces the contamination fraction to ≤ 0.01, whilst still preserving ~ 80 % of the high-redshift galaxies.

Here we comment on the usability of these *Euclid* colour diagrams for the selection of $z = 6$–8 galaxies. In the case of *Euclid* data alone, 30 out of the 65 contaminants cannot be included in these diagrams because they do not have a well-constrained $(I_{\mathrm{E}} - Y_{\mathrm{E}})$ colour. Considering the colour criteria $(I_{\mathrm{E}} - Y_{\mathrm{E}}) > 2.8$ & $(Y_{\mathrm{E}} - J_{\mathrm{E}}) < 1.4$, this means that in the worst-case scenario, 30 additional contaminants could actually survive this selection, and so the contamination fraction would be 0.11 instead of 0.01. Therefore, the purity of the apparent $z > 6$ sample would still improve from applying colour selection criteria, although possibly not as drastically as presented in Table 2.4. On the contrary, given that the $(I_{\mathrm{E}} - Y_{\mathrm{E}})$ colour of most true $z > 6$ galaxies is a lower limit, the recovered completeness with the colour criteria may be higher in reality. In conclusion, the presented colour criteria in this work are useful for selecting a relatively pure sample of $z > 6$ galaxies whilst maintaining acceptable completeness, although it is not possible to exactly state to which degree.

As mentioned in Sect. 2.4.2, an alternative strategy that is often used to ensure that intermediate-z galaxies do not enter the high-redshift galaxy sample is to require a detection with a certain S/N for high-z candidates. Here we explore in depth how imposing a 3-, 5-, and 10σ detection threshold requirement on the apparent *Euclid* $z > 6$ sample could reduce the contamination fraction. Figure 2.6 shows the distribution of the H_{E}-band S/N for contaminants and true $z > 6$ galaxies, where the three S/N cuts are indicated with dashed lines. We imposed each S/N cut on the apparent $z > 6$ sample and subsequently recomputed the contamination fraction and $z > 6$ completeness. Ultimately, we find that even a 10σ S/N requirement merely reduces contamination to 5 % whilst preserving only 30 % of the actual high-z galaxies. For reference, the most stringent colour cut presented in Table 2.4 is able to maintain 58 % completeness. We find similar results for the Y_{E} and H_{E} bands. We conclude that for the UltraVISTA-like bright sample, the colour cuts are more effective for identifying intermediate-z interlopers than imposing a S/N requirement.

Finally, we explore how effective a combination of a S/N requirement with colour selection criteria would be. First, we applied a 5σ H_{E}-band S/N detection threshold requirement to the apparent $z > 6$ sample recovered with *Euclid* data alone. Subsequently, we applied the same colour criteria presented in this paragraph to the restricted sample, and highlight the results from the colour criteria $(I_{\mathrm{E}} - Y_{\mathrm{E}}) > 2.8$ & $(Y_{\mathrm{E}} - J_{\mathrm{E}}) < 1.4$. Imposing these criteria, the contamination fraction is reduced to 0.01 whilst preserving 70 % of the high-redshift sources. However, even with the detection threshold requirement, 5 out of 18 contaminants do not have a constraint $(I_{\mathrm{E}} - Y_{\mathrm{E}})$ colour and, therefore, cannot be included in the colour diagrams. Therefore, if all of these sources survived these colour criteria and continued to populate the recovered high-redshift sample, the contamination fraction would be 0.03. In summary, the combination of a S/N requirement and colour selection criteria is able to recover a high-redshift sample with very high purity, but at the cost of the $z > 6$ completeness; as such, whether or not this combination should be used will depend on the research purpose.

2.4.4. THE NATURE OF THE $z > 6$ CONTAMINANTS

Now that we have quantified the expected degree of contamination in the Euclid Deep $z > 6$ galaxy selection and showed how this can be reduced, we aim to understand the nature of the contaminant sources. We do this by inspecting the fiducial physical parameters of these galaxies, as obtained from `LePhare` in the original run based on COSMOS 28-band photometry. Subsequently, we compare the *Euclid*-derived SED properties of true $z > 6$ galaxies and contaminants, in order to investigate if the two populations can be further segregated based on their recovered physical parameters.

PHOTOMETRIC REDSHIFT DISTRIBUTIONS

Figure 2.7 shows the fiducial and simulated normalised redshift distribution of $z > 6$ contaminants and true $z > 6$ galaxies, in each *Euclid* (+ancillary) data scenario. Between the different photometric scenarios, the shape of the fiducial redshift distribution of the contaminants is roughly similar: we consistently identify broad peaks at $z_{\mathrm{fid}} \sim 1$–3 and $z_{\mathrm{fid}} \sim 4.0$–6, and typically very few sources at $z_{\mathrm{fid}} \sim 3$–4. In addition, for almost all scenarios, the majority of contaminants have $z_{\mathrm{fid}} \sim 4.0$–6. Therefore, we conclude that the underlying galaxy populations that are likely to be misidentified as high-z galaxies are similar, regardless of the external data available to complement *Euclid* data in the SED fitting analysis.

Figure 2.7 also shows the redshift distribution of $z > 6$ contaminants once constrained with simulated *Euclid* (+ancillary) photometry. Here we can see how the contaminants affect different redshift bins at $z > 6$, which varies according to the considered data combination. Generally we find that without constraints from *Spitzer* photometry, the contaminants are systematically placed at higher redshifts than in scenarios where *Spitzer* data are available. From Fig. 2.7 it is evident that the recovered redshift distributions of

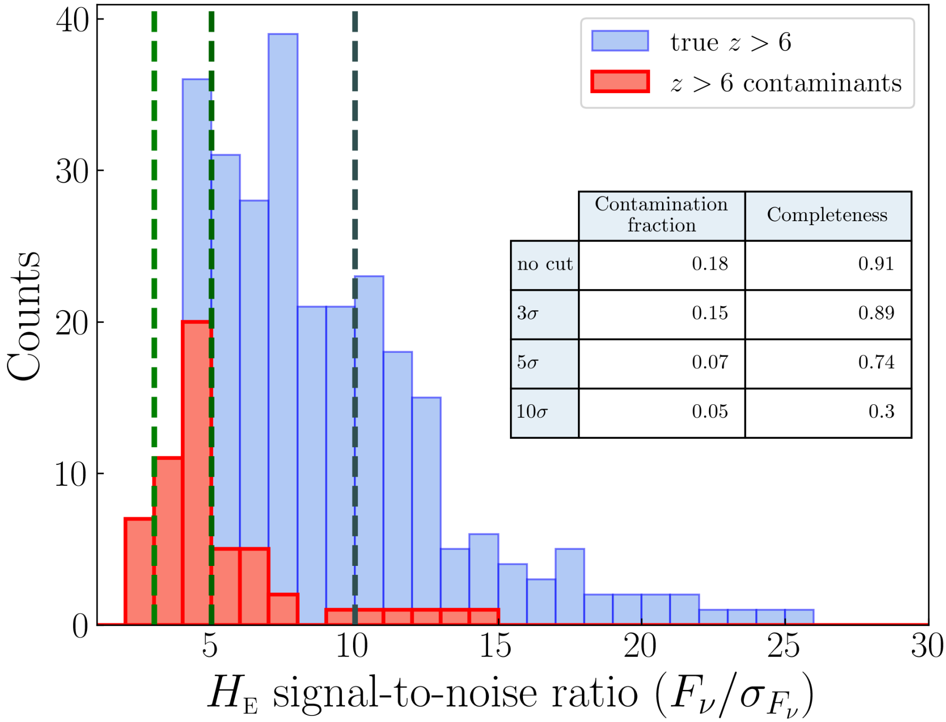

	Contamination fraction	Completeness
no cut	0.18	0.91
3σ	0.15	0.89
5σ	0.07	0.74
10σ	0.05	0.3

Figure 2.6 | Histogram of the H_E-band S/N. Contaminants and true $z > 6$ galaxies as identified from *Euclid* data alone are displayed in red and blue graphs, respectively. The vertical dashed lines indicate the 3σ, 5σ, and 10σ detection cutoffs. The contamination fraction and completeness computed for the three cuts are indicated in the table.

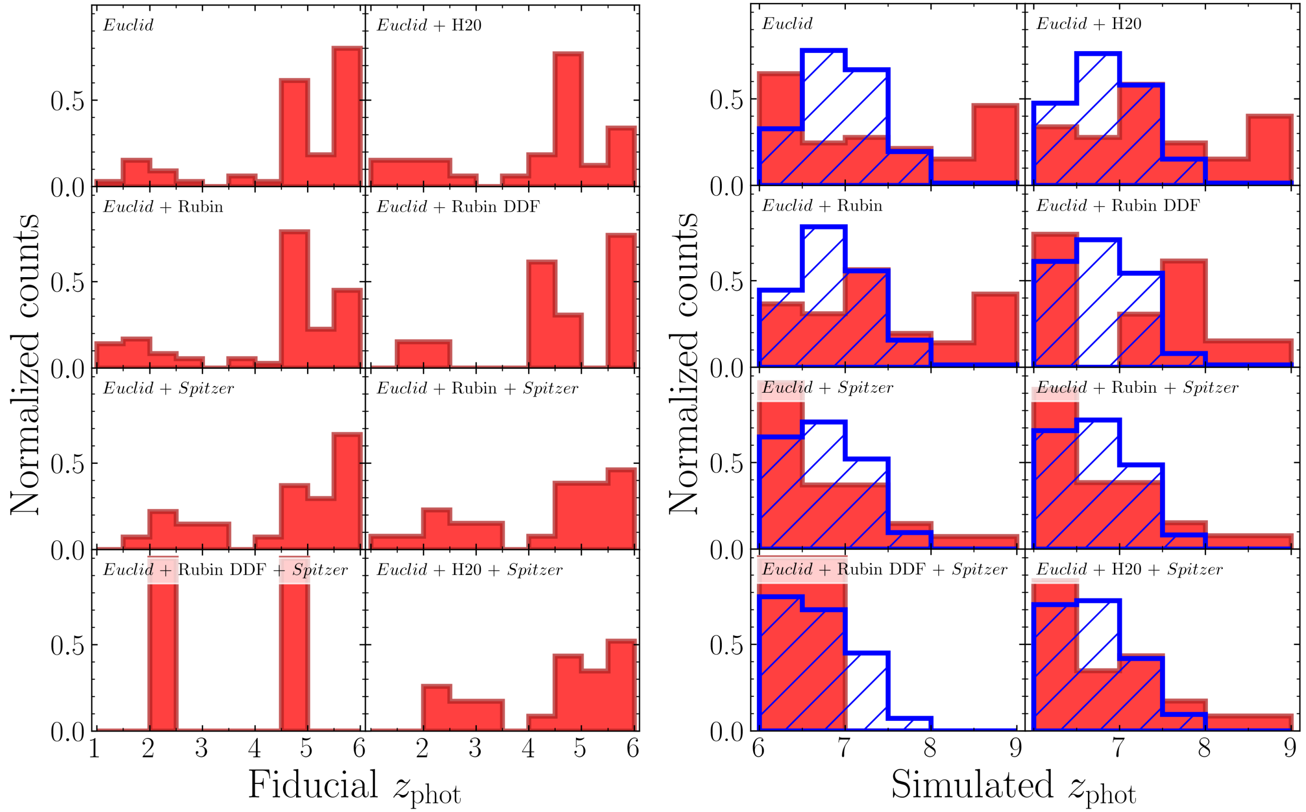

Figure 2.7 | Photometric redshifts distributions of the intermediate-z interlopers. (*Left panel*) Normalised fiducial redshift distribution of the $z > 6$ contaminants in each scenario of *Euclid* (+ancillary) photometry. (*Right panel*) Normalised *Euclid* (+ancillary) photometry-derived redshift distributions of the true $z > 6$ galaxies (in hatched blue) and $z > 6$ contaminants (in red).

true $z > 6$ galaxies and $z > 6$ contaminants are different but largely overlapping, and thus the $z > 6$ contaminants cannot be identified solely based on their recovered redshifts.

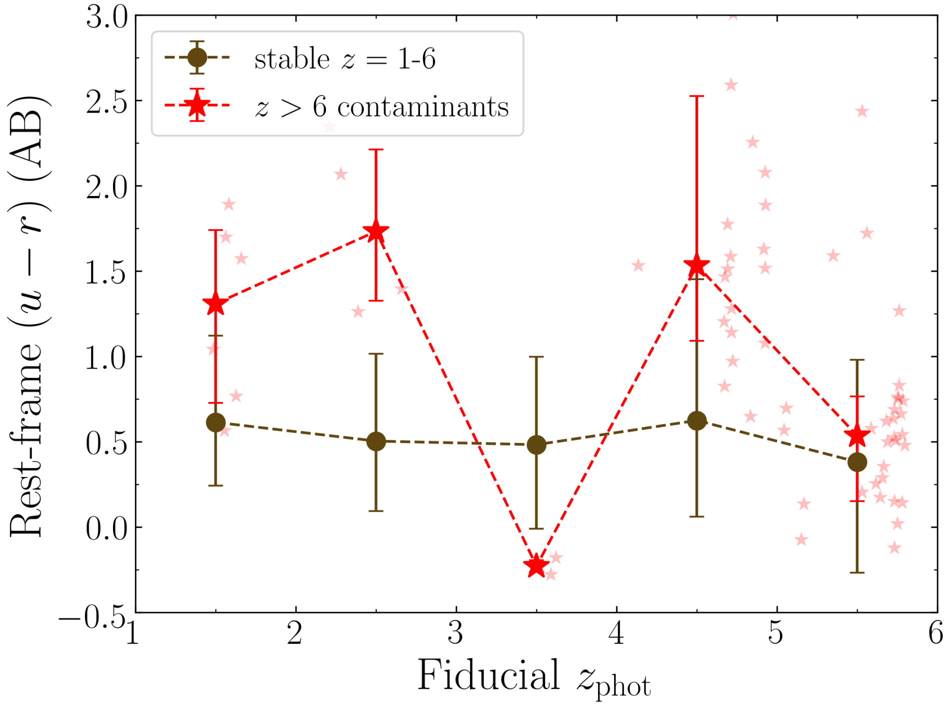

Figure 2.8 | Rest-frame $(u - r)$ colour of the $z > 6$ contaminants and stable intermediate-z galaxies against the fiducial redshift, based on real COSMOS photometry. The $z > 6$ contaminants and stable intermediate-z galaxies are identified through *Euclid* photometry alone. For both populations, we plot the median $(u - r)$ colour in $\Delta z = 1.0$ fiducial redshift bins, where the error bars represent the 16th and 84th percentiles. The individual data points of $z > 6$ contaminants are shown with small red stars.

PHYSICAL PARAMETERS

So far, we have established that, regardless of which ancillary data are added to the *Euclid* photometry, $z > 6$ contaminants are amongst the faintest sources in our intermediate-z galaxy sample and primarily correspond to galaxies with fiducial redshifts around $z_{\mathrm{fid}} \sim 2.5$ or $z_{\mathrm{fid}} \sim 5$. Here we analyse the physical properties of these galaxies, to better understand why specifically these populations are sensitive to the $z > 6$ degeneracy.

In Fig. 2.8 we show the rest-frame $(u - r)$ colour against the fiducial redshift for intermediate-z galaxies and $z > 6$ contaminants, as identified from *Euclid* photometry. The rest $(u - r)$ colour is derived from the fiducial COSMOS photometry and corresponding best-fit SED, and samples the rest-frame optical continuum at $\lambda \sim 3800$ Å (u) and $\lambda \sim 6300$ Å (r). First, we note that the blue $(u - r)$ colours of contaminants at $z_{\mathrm{fid}} = 3.0$–4.0 are a coincidence rather than a real degeneracy: there are only two galaxies in this bin that are both faint and have poorly constrained fiducial SEDs. Overall, we find that $z > 6$

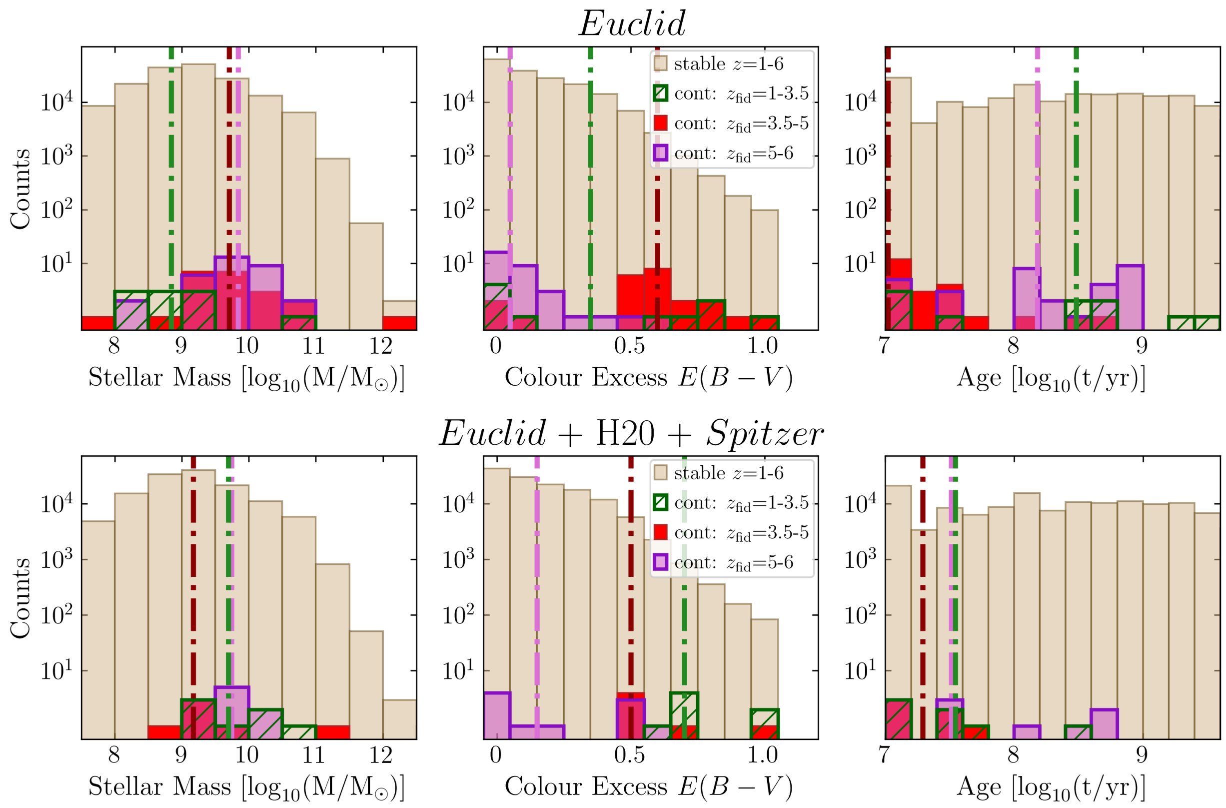

Figure 2.9 | Fiducial COSMOS photometry-derived stellar mass, colour excess, and age distributions of the stable intermediate-z galaxies (in light brown) and the $z > 6$ contaminants. The latter are divided into three samples: contaminants with fiducial $z = 1$–3.5 (in hatched green), contaminants with fiducial $z = 3.5$–5 (in red) and contaminants with fiducial $z = 5$–6 (in purple). The median of each distribution is indicated with a vertical line in a corresponding colour. The upper panels show contaminants identified from *Euclid* data alone, and the lower panels show contaminants identified from *Euclid*+H20+*Spitzer* data.

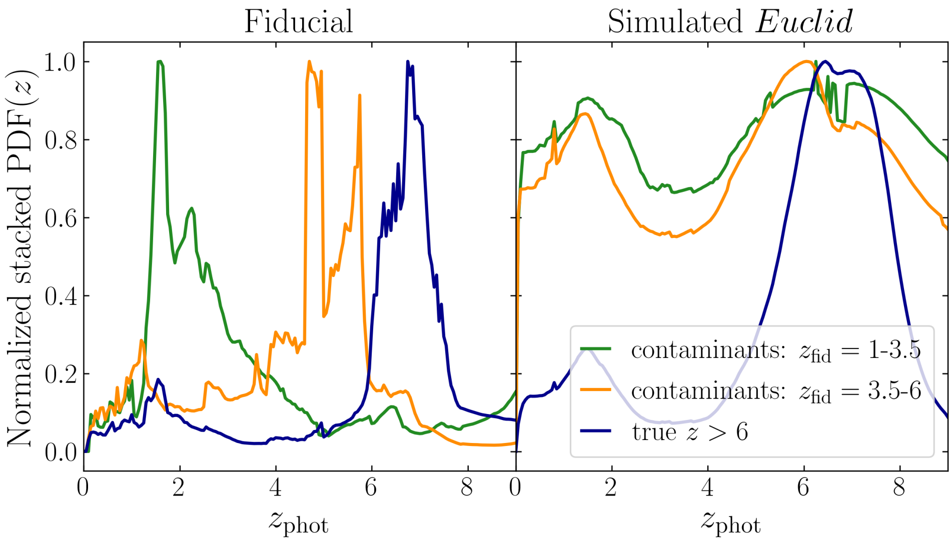

Figure 2.10 | Normalised, stacked probability distribution function of the redshift, PDF(z), of the $z > 6$ contaminants and true $z > 6$ galaxies identified from *Euclid* data. The fiducial PDF(z) derived from COSMOS 28-band photometry is shown in the left panel; the simulated PDF(z) derived from *Euclid* photometry is shown on the right.

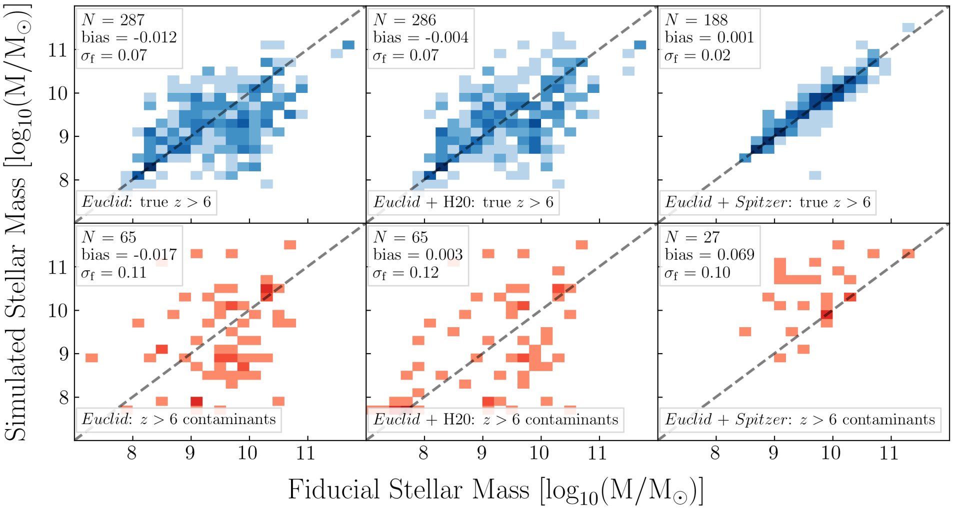

Figure 2.11 | Fiducial stellar mass versus *Euclid* (+ancillary) photometry-derived stellar mass for true $z > 6$ galaxies (upper panels) and $z > 6$ contaminants (lower panels), for three scenarios of *Euclid* and ancillary photometry. The number of galaxies shown is indicated in the upper-left corner of each panel, as is the bias and scatter $\sigma_{\rm f}$. The bias is defined as $mean[(\rm M_{sim} - M_{fid})/M_{fid}]$ and the scatter as $rms[(\rm M_{sim} - M_{fid})/M_{fid}]$. The colour intensity corresponds to the number of galaxies in each bin (darker colours correspond to more sources).

contaminants typically have redder $(u-r)$ colours than stable intermediate-z galaxies. Only at $z_{\text{fid}} = 5.5$–6.0 are the rest-frame optical colours of $z > 6$ contaminants similar to those of stable $z_{\text{fid}} = 5.5$–6.0 galaxies; the former are contaminants simply because they are much fainter compared to the latter. Lastly, for other combinations of *Euclid* and ancillary photometry, contaminants at $z_{\text{fid}} = 3.0$–4.0 display similarly red colours as those in other fiducial redshift bins. In conclusion, including the result from Fig. 2.4, the $z > 6$ contaminants are generally characterised as faint, systematically reddened, intermediate-z galaxies, in good agreement with previous studies (e.g. Oesch et al. 2012; Bowler et al. 2014).

In order to uncover what produces the redder optical colours of the contaminants, we inspect their fiducial stellar masses, dust extinctions and ages as derived from the original (COSMOS) photometry. We also investigate the *Euclid* (+ancillary) photometry-derived physical parameters of the contaminants, to see if these sources that appear as $z > 6$ galaxies occupy a different parameter space than the true $z > 6$ galaxies.

In Fig. 2.9 we show the fiducial stellar mass, colour excess, and age distributions of the $z > 6$ contaminants and the stable intermediate-z galaxies, as derived from the original SED fitting with COSMOS photometry. We show the comparison for two scenarios: one where interlopers are identified from *Euclid* photometry alone, and one where they are identified from *Euclid*+H20+*Spitzer* data. Furthermore, the contaminants are split into three samples based on their fiducial redshift, that is, $z_{\text{fid}} = 1$–3.5, $z_{\text{fid}} = 3.5$–5 and $z_{\text{fid}} = 5$–6, following the typical redshift distinction we observed in Fig. 2.7, and considering that contaminants at $z_{\text{fid}} = 3.5$–5 and $z_{\text{fid}} = 5$–6 display different $(u-r)$ colours. Apart from the three physical properties investigated in Fig. 2.9, we also inspect the characteristics of the best-fit SEDs of these sources, that is, their metallicity and SFH.

First and foremost, it is clear from Fig. 2.9 that the $z > 6$ contaminants and stable intermediate-z galaxies occupy the same parameter space for any property investigated in this paper. Therefore, we conclude from this that the galaxies driving the *Euclid* $z > 6$ contamination are not part of some specific population, but are primarily interlopers because of their faintness.

When we investigate the three samples of $z > 6$ contaminants as identified from *Euclid* photometry, we find that contaminants at $z_{\text{fid}} = 1$–3.5 are typically moderately massive galaxies that have red optical colours either because they are young with considerable dust attenuation, or because they are old with well established stellar populations. Towards higher redshifts, we observe that contaminants at $z_{\text{fid}} = 3.5$–5 are constituted almost solely of young, massive galaxies that are strongly affected by dust. Finally, contaminants at $z_{\text{fid}} = 5$–6 are comparably massive, typically not dusty and of average age. Summarising, the sources that produce similar *Euclid* colours to actual $z > 6$ galaxies are either intermediate-z galaxies that become degenerate through typical confusion of the Lyman-α and 4000 Å breaks (either due to strong dust attenuation or old age), or faint galaxies with flat SEDs bordering $z \sim 6$ that become degenerate because of the limited measurements available to properly constrain them.

Given that we have demonstrated how the inclusion of ancillary photometry reduces the number of intermediate-z interlopers, we also inspect the physical parameters of contaminants identified from *Euclid*+H20+*Spitzer* data. These surviving galaxies constitute the core of the $z > 6$ contamination, since they produce similar colours as high-redshift galaxies in not just the four *Euclid* bands, but in seven ancillary optical and infrared filters as well. As shown in the lower panels of Fig. 2.9, the remainder of $z > 6$ contaminants show a similar albeit narrower mass distribution compared to the scenario with only *Euclid* photometry. Conversely, contaminants at $z_{\rm fid} = 1$–3.5 and $z_{\rm fid} = 3.5$–5.0 are now solely young and dusty galaxies. Apparently, the degeneracy between older, intermediate-z galaxies with well-developed 4000 Å breaks and actual $z > 6$ galaxies is at least partially broken through the addition of ancillary photometry, whereas the degeneracy between dust-reddened galaxies and $z > 6$ galaxies mostly remains.

We show the normalised, stacked probability distribution function of the redshift, PDF(z), of the $z > 6$ contaminants and true $z > 6$ galaxies in Fig. 2.10. For clarity, we divide the contaminants into only two redshift bins, namely $z_{\rm fid} = 1$–3.5 and $z_{\rm fid} = 3.5$–6. Interestingly, although their fiducial PDF(z) is generally broad considering it was derived from 28-band photometry, the $z > 6$ contaminants do not show significant probability for secondary redshift solutions at $z > 6$. When observed with *Euclid* alone, the PDF(z) of any $z > 6$ contaminant is highly degenerate. This means that even though the contaminants are falsely identified as high-redshift galaxies with *Euclid*, one cannot possibly exclude a low-redshift nature based on the PDF(z) that is recovered. Upon further inspection, we find that even with additional H20 and *Spitzer* photometry, the majority of contaminants produce highly degenerate results for the PDF(z); only with the ultra-deep photometry from the Rubin DDF do we retrieve $z > 6$ contaminants that have a PDF(z) solely defined at $z > 6$. Therefore, one would never know from the PDF(z) that these sources are actually misidentified intermediate-z galaxies.

Now that we have characterised the galaxy population that drives the $z > 6$ contamination, we inspect the physical properties as derived with *Euclid* (+ancillary) photometry of the true $z > 6$ galaxies and $z > 6$ contaminants. Since the stellar mass is the most important physical parameter second to the photometric redshift, we first inspect the stellar-mass recovery in Fig. 2.11. It is clear that in the scenarios of *Euclid* and *Euclid*+H20 data, where the true $z > 6$ galaxies are unconstrained in the NIR, the stellar-mass recovery is poor. Conversely, when IRAC photometry is available, the recovery of the stellar mass from only the six *Euclid* and *Spitzer* bands is very efficient. In addition, when we inspect the age and SFH recovery of the true $z > 6$ galaxies, we see (not shown in this paper) a similar trend. *Spitzer* photometry is therefore far more effective than optical data for the recovery of these parameters. Without IRAC data, the rest-frame stellar continuum beyond the 4000 Å break of an apparent $z > 6$ source is completely unconstrained, and so physical parameters directly related to the older stellar population (the stellar mass and age of the galaxy) are unfounded.

Figure 2.11 also shows the stellar-mass recovery of the $z > 6$ contaminants. Naturally, we do not expect a tight correlation, as the contaminants are by definition misidentified as vastly different galaxies from *Euclid* (+ancillary) photometry. However, the abundant scatter in the distribution is noteworthy; we have established that distinct populations of galaxies cause the $z > 6$ contamination, but we see no signs of bimodal behaviour in the stellar-mass recovery. By including *Spitzer* photometry, the light from the older stellar populations is actually constrained: for 74 % of the contaminants, their recovered stellar mass is higher than their fiducial stellar mass. This is expected, as even though we know the contaminants are relatively faint compared to their stable intermediate-

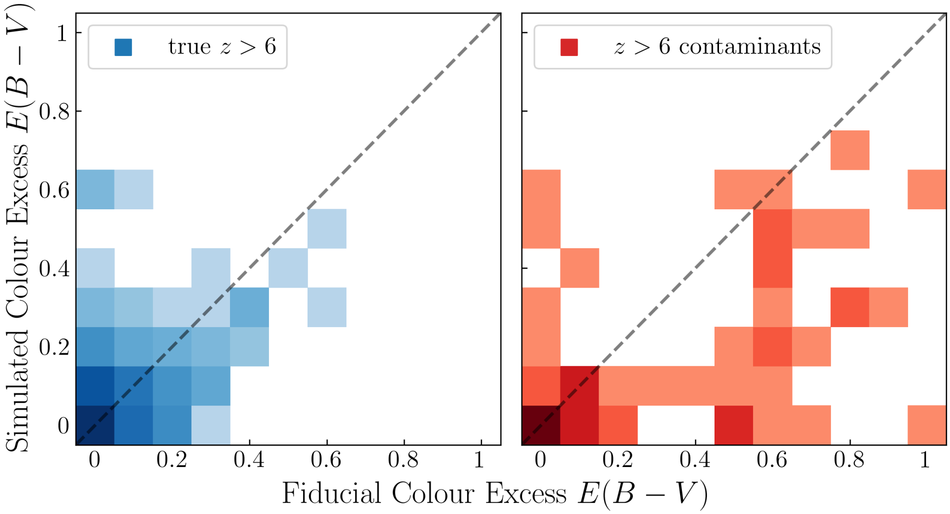

Figure 2.12 | Fiducial colour excess versus *Euclid* photometry-derived colour excess for true $z > 6$ galaxies (left panel) and $z > 6$ contaminants (right panel). The colour intensity corresponds to the number of galaxies in each bin (darker colours correspond to more sources).

z counterparts, their fluxes can only be attributed to massive $z > 6$ galaxies since the stellar mass is directly derived from the SED normalisation. Unfortunately, the simulated stellar mass distributions of true $z > 6$ galaxies and intermediate-z interlopers overlap considerably, and so we cannot further separate these populations based on their stellar masses, nor on their ages or SFH models.

Figure 2.12 shows the colour excess recovery for $z > 6$ contaminants and intermediate-z galaxies derived from *Euclid* data alone. We do not show any other combination of *Euclid* and ancillary photometry, as the results are universal. The vast majority of true $z > 6$ galaxies (93 %) have very low fiducial dust extinction, $E(B-V) \leq 0.2$. These values are well recovered once observed with *Euclid*. This is different for the $z > 6$ contaminants; as expected, dusty intermediate-z galaxies are mistaken for high-redshift sources with considerably less dust attenuation. Unfortunately, the colour excess cannot be employed to separate interlopers from actual $z > 6$ galaxies; 72 % of the $z > 6$ contaminants have recovered dust extinction $E(B-V) \leq 0.2$.

We employ the two-parameter Kolmogorov-Smirnov test (Smirnov 1939) to compare the parameter distributions of $z > 6$ contaminants and true $z > 6$ galaxies. In virtually all scenarios of data availability, the test shows that the stellar mass and colour excess values of contaminants and actual $z > 6$ galaxies are unlikely to come from the same parent distribution, with p-values generally below 0.01 (in the scenarios with Rubin DDF photometry we cannot properly compare the distributions due to the low number of contaminants). The age distributions of interlopers and actual $z > 6$ galaxies are more similar. Still, the parameter spaces of each physical property significantly overlap for the two populations. Therefore, we conclude that there exists no obvious separation between intermediate-z contaminants and true $z > 6$ galaxies based on their recovered stellar mass, dust extinction and age parameters.

2.5. COMPLEMENTARY TESTS BASED ON A FAINT MOCK GALAXY SAMPLE

In this work we used real data from the COSMOS field to investigate the expected contamination of $z > 6$ galaxies in the Euclid Deep Fields. However, especially in the optical regime, the Euclid Deep Fields will be considerably deeper than our fiducial UltraVISTA catalogue. In fact, the 5σ limiting magnitude of the UltraVISTA H-band photometry included in our fiducial UltraVISTA catalogue is 25.2, whereas the expected 5σ depth in *Euclid* H_{E} band is 26.4 magnitude. Therefore, our results on the contamination fraction in Table 2.3 are biased towards the brightest and most massive galaxies at $z_{\mathrm{fid}} = 6$–8, and therefore possibly too optimistic.

To uncover how successful *Euclid* data will be at identifying faint high-redshift galaxies, we created a sample of faint mock galaxies from our fiducial UltraVISTA catalogue and repeated our analysis of the contamination fraction with this sample. To create the mocks, we shifted the entire fiducial best-fit SEDs of our UltraVISTA galaxies at $z_{\mathrm{fid}} = 1$–8 by 1.2 magnitude, which is the difference in depth between the UltraVISTA H- and *Euclid* H_{E}-band images. From these modified SEDs, we selected all galaxies with $25.3 \leq H < 27.0$ magnitude, since sources with $H < 25.3$ are already discussed in the bright UltraVISTA-like sample and $H = 27.0$ corresponds to the H-band 3σ flux limit in the Euclid Deep Survey.

To ensure the faint mock sample follows a realistic photometric redshift distribution, especially at $z_{\mathrm{fid}} = 6$–8, we made use of the CANDELS photometric redshift catalogue in the COSMOS field produced by Nayyeri et al. (2017), which consists of 38 671 sources identified with the HST and contains photometric data in 42 bands. This catalogue is approximately 2.4 magnitudes deeper in the H band than our UltraVISTA catalogue. From this CANDELS catalogue, we selected all galaxies with $z = 1$–8 and $25.3 \leq H < 27.0$, the latter based on the *HST*/WFC3 F160W band at 1.6 μm. Subsequently, in $\Delta z = 0.2$ bins, we selected galaxies from our constructed faint mock galaxy sample at random to replicate the re-normalised CANDELS redshift distribution in that bin. Within each redshift bin, we also altered the scaling of the modified SEDs of individual sources such that their H magnitude distribution (in $\Delta \mathrm{m} = 0.1$ mag bins) is identical to the re-normalised CANDELS H magnitude distribution in the same redshift bin. This method ensures that our faint mock sample follows quite closely the CANDELS luminosity functions at $z = 6$–8.

We note that the CANDELS $z = 7.8$–8.0 redshift distribution cannot be reproduced, as our UltraVISTA catalogue does not contain sources in that redshift bin. However, for simplicity, we globally refer to the faint mock high-redshift sample as mock galaxies with $z_{\mathrm{fid}} = 6$–8 redshifts. Therefore, the final faint mock sample contains 96 084 sources, of which 936 are at $z_{\mathrm{fid}} = 6$–8. Out of this sample, 41 775 sources are detected in at least IRAC channel 1 or channel 2, and 408 of these sources are at fiducial $z_{\mathrm{fid}} = 6$–8. The fiducial photometric redshift and H magnitude distribution of the faint mock sample are shown in Fig. 2.13, together with the corresponding re-normalised CANDELS distributions.

We sampled the *Euclid* (+ancillary) fluxes directly from the modified SEDs of the

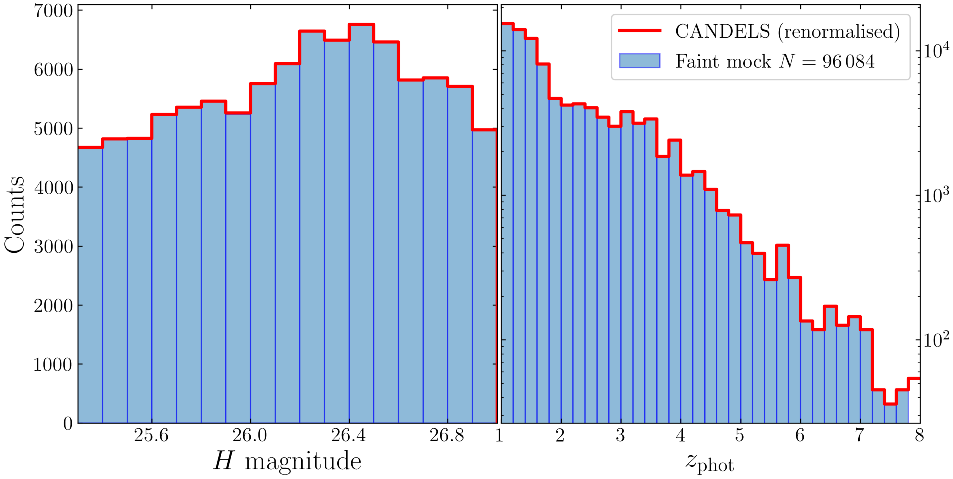

Figure 2.13 | Template UltraVISTA H magnitude distribution in $\Delta m = 0.1$ mag bins (left panel) and fiducial photometric redshift distribution in $\Delta z = 0.2$ bins (right panel) of the faint mock sample. In both panels, the corresponding re-normalised CANDELS distributions are shown in red outlines.

faint mock galaxies, and obtained the final, randomised *Euclid* (+ancillary) photometry following the methods described in Sect. 2.3, except for the simulated *Spitzer* flux errors. Instead, these were not taken directly from the observed UltraVISTA/SMUVS photometry, but scaled along with the fiducial SEDs to preserve the S/N and subsequently adopted as the simulated *Spitzer* flux errors.

We note that some of the UltraVISTA sources, especially at $z_{\rm fid} = 6$–8, are included in the faint mock sample multiple times, as there are relatively more high-redshift sources in the CANDELS catalogue than in the scaled-down UltraVISTA catalogue. However, fiducial duplicates can be considered as individual sources for the purpose of this analysis, as the simulated Euclid (+ ancillary) photometry is independently randomised for each instance.

We derive the contamination fraction and $z > 6$ completeness of the mock sample in all eight *Euclid* (+ancillary) data scenarios, which are shown in Table 2.5. The uncertainties on the contamination fraction were derived in the same manner for the UltraVISTA-like bright sample (see Sect. 2.4.2). First and foremost, the $z > 6$ completeness ranges from 87 % to 93 % (in the most optimistic scenario *Euclid*+Rubin DDF+*Spitzer*), which is lower than the 91-96 % completeness obtained with the bright UltraVISTA-like sample. This is unsurprising, since we have demonstrated how the $z_{\rm fid} = 6$–8 galaxies are characterised by having very red $(I_{\rm E} - Y_{\rm E})$ colours and 2σ flux upper limits in the $I_{\rm E}$ band. By shifting the fiducial SED downwards, the simulated $Y_{\rm E}$ fluxes of $z_{\rm fid} = 6$–8 are fainter and the $(I_{\rm E} - Y_{\rm E})$ colours not as red, which makes identification of these sources more difficult. This is illustrated in Fig. 2.14, where we show the median magnitude in the *Euclid*, Rubin and *Spitzer* bands of the faint mock galaxies. Nonetheless, a completeness of > 80 % for faint high-redshift sources identified with *Euclid* will be excellent for most astronomy science purposes.

Table 2.5 | Number of true $z > 6$ galaxies and $z > 6$ contaminants, from various combinations of *Euclid* and ancillary data, based on the faint mock sample. As in Table 2.3, we report the contamination fraction and completeness for each data availability scenario.

Filters	True $z > 6$	Contaminants	Contamination Fraction	Completeness
Euclid	824	523	$0.39^{+0.10}_{-0.11}$	88 %
Euclid + Rubin	824	540	$0.40^{+0.10}_{-0.12}$	88 %
Euclid + Rubin DDF	863	63	$0.07^{+0.03}_{-0.03}$	92 %
Euclid + H20	831	489	$0.37^{+0.10}_{-0.11}$	89 %
Euclid + *Spitzer*	355	201	$0.36^{+0.09}_{-0.09}$	87 %
Euclid + Rubin + *Spitzer*	358	191	$0.35^{+0.08}_{-0.10}$	88 %
Euclid + Rubin DDF + *Spitzer*	378	24	$0.06^{+0.03}_{-0.02}$	93 %
Euclid + H20 + *Spitzer*	357	181	$0.34^{+0.08}_{-0.09}$	88 %

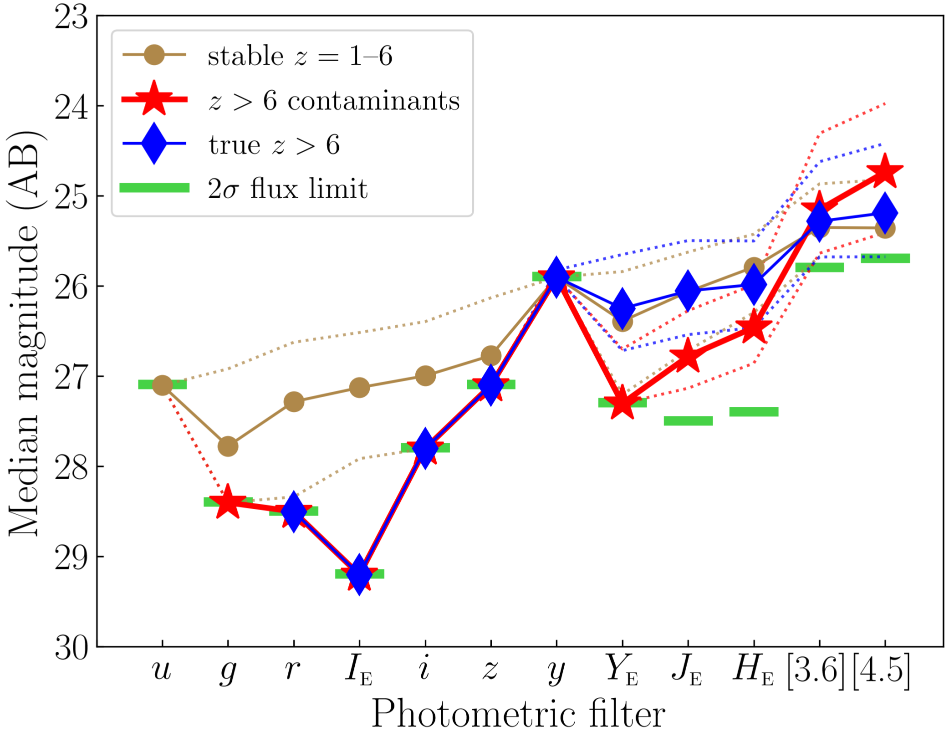

Figure 2.14 | Median simulated magnitudes of the faint mock sample in the *Euclid*, Rubin, and *Spitzer* filters. Light brown circles represent stable intermediate-z galaxies, red stars $z > 6$ contaminants, and blue diamonds true $z > 6$ galaxies. For each population, the dotted lines indicate the 16th and 84th percentiles. The 2σ flux limits are shown with green bars. The selection of intermediate-z, contaminants, and $z > 6$ galaxies from the faint mock sample is based on *Euclid*+Rubin+*Spitzer* data. The median magnitudes for $z > 6$ galaxies in the Rubin u and g bands and for contaminants in the Rubin u band are equal to −99 (no intrinsic flux) and therefore omitted from this figure.

Simultaneously, we find that the contamination fraction of the mock sample is 0.39 with *Euclid* photometry alone, compared to 0.18 with the bright UltraVISTA-like sample. Again, this stark increase is not surprising, as we have demonstrated how intermediate-z interlopers are primarily characterised by their faintness. By shifting the UltraVISTA photometry downwards, intermediate-z galaxies that previously remained at the same redshifts when observed with *Euclid* are now assigned *Euclid* (+ancillary) fluxes much closer to their respective 2σ flux limits, and therefore are more likely to be mistaken for $z > 6$ galaxies.

With the faint mock sample, we find similar trends regarding the usefulness of ancillary optical data; only the ultra-deep Rubin DDF photometry truly improves the contamination fraction, reducing it to 0.07. In addition, we find that including the simulated *Spitzer* photometry of the mock galaxies barely improves the contamination fraction, contrary to the moderate improvement obtained with the regular UltraVISTA sample. We explain this from the average $(Y_{\rm E} - [3.6])$ colour of $z > 6$ contaminants and true $z > 6$ galaxies. As can be seen in Fig. 2.14, contaminants identified in the faint mock sample do not produce the extremely red $(Y_{\rm E} - [3.6])$ colours of contaminants in the bright UltraVISTA-like sample. Because of this, the $(Y_{\rm E} - [3.6])$ colours of $z > 6$ contaminants and true $z > 6$ galaxies are more similar, meaning *Spitzer* photometry barely helps in distinguishing between these sources.

As was done for the UltraVISTA-like bright sample, we explore what happens to the contamination fraction once we impose a NIR detection threshold requirement for the source selection. This should be especially relevant for the faint mock sample, given that many of these sources have flux measurements close to the 2σ flux limits in each band. If we require that faint mock sources have a 5σ detection in at least one of the *Euclid* NIR bands, 70 831 sources (74 % of the sample) survive, of which 669 galaxies have fiducial $z_{\rm fid} = 6$–8. We recalculate the contamination fraction and $z > 6$ completeness on this restricted sample for all eight data combinations, and show the results in Table 2.6. We emphasise that the completeness is calculated as the fraction of all fiducial $z_{\rm fid} = 6$–8 galaxies that satisfy the detection threshold requirement; otherwise, variations in the completeness could be simply attributed to the restriction imposed on the sample.

From Table 2.6, it is clear that a NIR detection threshold requirement for faint, apparent $z > 6$ galaxies considerably reduces contamination from intermediate-z sources. In any data scenario, the $z > 6$ completeness is comparable to that of the UltraVISTA-like bright sample. This is expected, as the faintest and therefore most poorly constrained high-redshift sources do not survive the detection threshold requirement. Between the different combinations of *Euclid* and ancillary photometry, we find that including *Spitzer* photometry does not improve the redshift recovery, nor is it able to distinguish contaminants from true $z > 6$ sources. Again, the only truly valuable addition to *Euclid* data is ultra-deep photometry from Rubin DDF.

To conclude, the high level of $z > 6$ galaxy recovery together with the low contamination fraction are only representative of bright galaxies equivalent to those in the UltraVISTA catalogue. As we showed here, the $z > 6$ completeness level becomes lower and the contamination fraction significantly higher for fainter sources, which will be part of the Euclid Deep Survey as well. Although we have shown that a NIR detection threshold requirement only moderately reduces the degree of contamination in the UltraVISTA-like

Table 2.6 | Number of true $z > 6$ galaxies and $z > 6$ contaminants, from various combinations of *Euclid* and ancillary data, based on the restricted faint mock sample. The restricted faint mock sample consists of sources that have a 5σ flux measurement in at least one the *Euclid* NIR bands. We report the contamination fraction and $z > 6$ completeness, where the latter is calculated as the fraction of all fiducial $z_{\mathrm{fid}} = 6$–8 sources that satisfy the detection threshold requirement.

Filters	True $z > 6$	Contaminants	Contamination Fraction	Completeness
Euclid	609	204	$0.25^{+0.07}_{-0.07}$	91 %
Euclid + Rubin	609	202	$0.25^{+0.07}_{-0.07}$	91 %
Euclid + Rubin DDF	636	28	$0.04^{+0.02}_{-0.01}$	95 %
Euclid + H20	617	172	$0.22^{+0.06}_{-0.06}$	92 %
Euclid + *Spitzer*	312	107	$0.26^{+0.06}_{-0.07}$	91 %
Euclid + Rubin + *Spitzer*	315	97	$0.24^{+0.06}_{-0.07}$	92 %
Euclid + Rubin DDF + *Spitzer*	329	18	$0.05^{+0.02}_{-0.02}$	96 %
Euclid + H20 + *Spitzer*	309	94	$0.23^{+0.06}_{-0.06}$	90 %

bright sample, it is very useful for the faint mock sample.

2.6. DISCUSSION

2.6.1. VALIDITY OF THE SIMULATED HIGH-z SOLUTIONS

We present numbers of $z > 6$ contaminants for each scenario of simulated photometry in Table 2.3. These contaminants are identified from their simulated redshift, with no further checks on the compatibility of the photometry and the best-fit photometric redshifts. Therefore, we explore if additional validation of their redshift could reduce the fraction of contaminants amongst $z > 6$ galaxies.

We checked if the photometric redshifts are compatible with detections at short wavelengths. At $z_{\mathrm{sim}} > 6$, the Lyman limit at $\lambda = 912$ Å is redwards of the Rubin u and g filters, and CFHT u and HSC g filters. Therefore, any apparent $z > 6$ galaxy with a $> 2\sigma$ detection limit in these bands can be ruled out. Similarly, at $z_{\mathrm{sim}} > 6.5$ the Lyman limit is redwards of the Rubin r and HSC r bands, so a detection in said bands should not exceed its 2σ limit. Additionally, due to Lyman series absorption of neutral hydrogen in the intergalactic medium (Inoue et al. 2014), the Lyman break of a galaxy spectrum shifts to the Lyman-α line at $\lambda = 1216$ Å; as such, sources at $z_{\mathrm{sim}} > 7$ with Rubin r and i, HSC r and i, and I_{E} detections exceeding their 2σ limit are ruled out, as are $z_{\mathrm{sim}} > 8.1$ galaxies with a $> 2\sigma$ detection in the Y_{E} band.

Based on the bright UltraVISTA-like sample, imposing these conditions on the $z > 6$ contaminant sample has strongly varying consequences depending on the photometric availability: 2.0 % of the *Euclid*-observed contaminants are discarded; 20% of the *Euclid*+Rubin-observed contaminants are discarded; 38 % of the *Euclid*+Rubin DDF-observed contaminants are discarded; 28 % of the *Euclid*+H20-observed contaminants are discarded; and 0 % of the *Euclid*+*Spitzer*-observed contaminants are discarded. We find considerably lower values for the faint mock sample; between 0.2 and 4 % of contaminants can be discarded from these checks, depending on the combination of *Euclid* and ancillary data. Clearly, it is useful to compare the best-fit photometric redshifts with their detections in ancillary optical bands, as it will improve the contamination fraction. Nonetheless, we conclude that $z > 6$ contaminants generally are assigned valid redshifts by the SED fitting based on their simulated photometry. Therefore, the majority of contaminants are not the result of poor SED fitting in which short-wavelength photometry is ignored by the algorithm.

2.6.2. INDEPENDENT CHECK OF CONTAMINATION FRACTION WITH COSMOS2020

We verified our estimates of the contamination amongst *Euclid* $z > 6$ galaxies by repeating our analysis of the bright UltraVISTA-like sources using a different photometric catalogue and other SED fitting codes. We used the COSMOS2020 catalogue (Weaver et al. 2022) to simulate *Euclid* (+ancillary photometry) following the same method presented in Sect. 2.3. The COSMOS2020 catalogue contains the latest updated data in the COSMOS field (Scoville et al. 2007), with photometry for over 1.7 million sources in 44 optical and infrared bands. In this work we have made use of the so-called COSMOS2020 Classic catalogue, which contains aperture photometry performed on PSF-homogenised images in all bands, except for the IRAC photometry, which was derived from PSF-fitting with the `IRACLEAN` software (Hsieh et al. 2012). We provide a detailed description on how we selected a sample of $z = 1$–8 galaxies from this catalogue in Appendix 2.7.

Using the COSMOS2020 Classic photometry, we performed three independent tests to derive the contamination fraction in various *Euclid* (+ancillary) data scenarios. Here we briefly list our tests for which fitting codes were used (detailed descriptions of the tests are provided in Appendix 2.7): (i) The new `C++` version of `LePhare` (`LePhare++`), following the two-step SED fitting strategy used in Weaver et al. (2022, see our Appendix 2.7). (ii) The conventional `LePhare` algorithm, adopting the photometric redshifts from Weaver et al. (2022) but deriving their corresponding best-fit templates using the SED fitting parameters from this paper (see Appendix 2.7). (iii) The new `Python` version of the `EAZY` template fitting algorithm (version `0.5.2.dev7`; Brammer et al. 2008; see our Appendix 2.7).

Using these photometric redshift codes, we simulated *Euclid* (+ancillary) photometry from the COSMOS2020 catalogue. For each test, we recomputed the photometric redshifts based on this photometry and tabulated the resulting estimates of the contamination fraction and $z > 6$ completeness in Appendix 2.7.

Here we reflect on the reproducibility and the resultant validity of our *Euclid* $z > 6$ galaxy sample contamination estimates. We find generally good agreement between the contamination fractions derived from our own UltraVISTA catalogue and from the COSMOS2020 catalogue processed by either version of the `LePhare` code. Therefore, we conclude that regardless of the fiducial photometry, between 15 and 20 % of apparent $z > 6$ galaxies identified from *Euclid* photometry with `LePhare` are actually intermediate-z interlopers. As we have shown in Sect. 2.5, this number is likely too optimistic, since *Euclid* will probably detect fainter $z > 6$ galaxies than what is currently possible with

COSMOS. The contamination is neither surprising nor unanticipated, as huge efforts are being made to collect ancillary photometry in all three Euclid Deep Fields. Overall, this result emphasises how we should be careful with *Euclid* high-redshift candidates for which ancillary photometry is not available.

Between the `LePhare` strategies, the contamination fractions with *Euclid* data alone agree well, although those derived from the COSMOS2020 photometry are slightly smaller. Interestingly, we find conflicting results regarding the importance of ancillary data for preventing $z > 6$ contamination. Overall, *Spitzer* photometry simulated from COSMOS2020 data barely contributes to reducing the contamination fraction, contrary to the moderate improvement achieved with our own UltraVISTA photometry, whereas the COSMOS2020 catalogue actually contains the deepest possible IRAC photometry over the COSMOS field. In addition, ancillary optical photometry from the H20 survey improves the contamination fraction in the test with `LePhare++`. We believe this is possible given that the COSMOS2020 catalogue contains very deep optical imaging from the Subaru HSC. However, we do not find the same improvement from the H20 survey data in the test with `LePhare`. Nonetheless, we observe the same general trend that optical imaging from the Rubin DDF is most effective at distinguishing intermediate-z interlopers from actual $z > 6$ galaxies, which confirms that the relative depth of the ancillary optical data is of key importance.

We used `EAZY` to reproduce our results in three data scenarios: *Euclid*, *Euclid*+H20, and *Euclid*+Rubin DDF. These scenarios were chosen as they summarise the different levels of expected depths of the ancillary data. Interestingly we find that the contamination fractions as derived with `EAZY` are extremely low in all three scenarios. In addition, the redshift recovery of actual $z > 6$ galaxies is poorer than when using `LePhare`, with a completeness of 81 % with *Euclid* alone. Contrary to what is expected, the level of completeness drops considerably from adding ancillary data: in the *Euclid*+H20 scenario, the $z > 6$ completeness is only 45 %. In all three scenarios, the missing $z_{\rm fid} = 6$–8 galaxies are misidentified as $z_{\rm sim} = 1$–2 and $z_{\rm sim} = 5.5$–6 galaxies, which is in accordance with the typical redshift degeneracies we identified for the intermediate-z contaminants. These results demonstrate how our `EAZY` routine appears reluctant to assign high-redshift solutions at all, which is remarkable, as we did not employ an apparent magnitude prior for the SED fitting of the *Euclid* (+ancillary) photometry. The lower $z > 6$ completeness may be partially due to the different flux upper-limit strategies between `LePhare` and `EAZY`. With the former code, 2σ upper limits in the optical bands impose very strong constraints on the photometric redshift of a true $z > 6$ galaxy; `LePhare` will outright reject most intermediate-z solutions as they produce higher fluxes than the upper limits in optical bands. With `EAZY`, the upper limits are less constraining as they are treated as actual detections with large flux errors that reflect the 2σ detection level. Therefore, false intermediate-z solutions for actual $z > 6$ galaxies may be unlikely, but not immediately rejected.

In conclusion, our tests using different SED fitting codes on the same dataset demonstrate that the choice of code could have strong implications for both the degree of contamination and the redshift recovery of $z > 6$ galaxies.

2.6.3. IDENTIFICATION OF $z > 6$ GALAXIES FROM COLOUR-COLOUR DIAGRAMS ALONE

We showed how, once the photometric redshifts are determined, a simple $(I_\mathrm{E} - Y_\mathrm{E})$ & $(Y_\mathrm{E} - J_\mathrm{E})$ colour cut can weed out $z > 6$ contaminants from true $z > 6$ galaxies in all scenarios of photometric availability, but only for sources that have a flux measurement in at least the I_E or Y_E band. Regardless, it makes sense to wonder to what degree it is possible to use directly this colour-colour plot for a $z > 6$ galaxy selection in *Euclid*, without the need for photometric redshifts in the first place. In fact, based on the bright UltraVISTA-like sample, we find that not any $z_\mathrm{fid} = 1$–6 galaxy (with a detection in I_E and/or Y_E), contaminant or not, populates the $(I_\mathrm{E} - Y_\mathrm{E}) > 3.4$ and $(Y_\mathrm{E} - J_\mathrm{E}) < 0.9$ colour box (*Euclid* data alone). Compared to 184 true $z > 6$ galaxies that do, this means one can potentially obtain a pure sample whilst preserving 58 % of the fiducial $z > 6$ galaxies. This suggests that direct selection of $z > 6$ galaxies may be possible from *Euclid* colours alone, circumventing the need for photometric redshifts.

However, once we take into account the faint mock sample, it becomes clear that photometric redshifts are absolutely necessary. In the scenario of *Euclid* data alone, 66 % of contaminants in the faint mock sample have an unconstrained $(I_\mathrm{E} - Y_\mathrm{E})$ colour. If we would apply the colour criteria $(I_\mathrm{E} - Y_\mathrm{E}) > 3.4$ and $(Y_\mathrm{E} - J_\mathrm{E}) < 0.9$ to the faint mock sample, virtually none of the contaminants that have a $(I_\mathrm{E} - Y_\mathrm{E})$ colour survive, but neither do the actual high-redshift galaxies: the completeness drops to 13 %. In addition, considering that more than half of the contaminants cannot be included in this analysis at all, we can conclude that using colour cuts to identify faint high-redshift sources with *Euclid* is unfeasible.

For the bright UltraVISTA-like sample, we explore if combining the $(I_\mathrm{E} - Y_\mathrm{E})$ and $(Y_\mathrm{E} - J_\mathrm{E})$ colours with additional criteria can achieve pure $z > 6$ galaxy selection with acceptable completeness. Based on the *Euclid* photometry, we inspect the $(Y_\mathrm{E} - J_\mathrm{E})$ versus $(J_\mathrm{E} - H_\mathrm{E})$ colour diagrams for all sources that survive the $(I_\mathrm{E} - Y_\mathrm{E}) > 2.8$ & $(Y_\mathrm{E} - J_\mathrm{E}) < 1.4$ colour cut, including all galaxies with an unconstrained $(I_\mathrm{E} - Y_\mathrm{E})$ colour. We find that the true $z > 6$ galaxies are well-separated from stable intermediate-z galaxies, but not from contaminants. Additionally, many contaminants that have no $(I_\mathrm{E} - Y_\mathrm{E})$ colour actually have $(Y_\mathrm{E} - J_\mathrm{E})$ and $(J_\mathrm{E} - H_\mathrm{E})$ colours similar to true $z > 6$ galaxies, so applying a succeeding colour cut in this colour space is mostly unhelpful for weeding out contaminants.

Finally, before we can draw conclusions on the feasibility of *Euclid* $z > 6$ galaxy selection from colours alone, we have to address a caveat in our analysis: we have not inspected the colours of fiducial $z_\mathrm{fid} = 0$–1 galaxies, given that by definition our intermediate-z sample spans $z_\mathrm{fid} = 1$–6. Upon inspection of the *Euclid* colours of UltraVISTA galaxies at $z = 0$–1, virtually none of these sources survive the $(I_\mathrm{E} - Y_\mathrm{E})$ & $(Y_\mathrm{E} - J_\mathrm{E})$ colour criterion, and therefore contamination of $z > 6$ galaxies by $z = 0$–1 galaxies is negligible.

To summarise, our results demonstrate that one should not select a $z > 6$ galaxy sample from *Euclid* colours alone, as the colours $z > 6$ contaminants are poorly constrained, especially in the faint regime. Accurate knowledge of photometric redshifts cannot be circumvented, as even the most stringent colour cut presented in this work is not guaranteed to eliminate intermediate-z contamination, while it strongly sacrifices the $z > 6$ completeness.

In general, we note that photometric redshift algorithms are by nature more efficient than colours alone for accurate selection of galaxy samples. As an alternative to the proposed colour selection criteria, one could make efforts to fine-tune `LePhare` (or any other SED fitting tool) to assign more weight to the $Y_{\rm E}$ band or the $(Y_{\rm E} - J_{\rm E})$ colour, thereby optimising the algorithm to further lift the degeneracy between intermediate- and high-redshift galaxies. More work is warranted to investigate how to optimise SED fitting codes to improve the discrimination between true $z > 6$ and intermediate-z interlopers.

In addition, machine learning methods as alternatives to traditional SED fitting are becoming increasingly popular, especially with the advent of large sky surveys such as the Euclid Survey. Recent works using mock *Euclid* photometry have demonstrated how machine learning approaches typically outperform template-fitting algorithms to retrieve the photometric redshift and galaxy classification at $z < 1$ (Euclid Collaboration: Desprez et al. 2020; Humphrey et al. 2021 in prep). At higher redshifts, machine learning methods become increasingly unreliable because extensive spectroscopic training samples are lacking. However, *Euclid* will obtain spectroscopy and high-quality photometry in several reference fields that already contain deep ancillary data. Therefore, machine learning methods for selecting $z > 6$ galaxies are likely to become more viable in the future and will possibly reduce contamination of intermediate-z galaxies further.

2.6.4. POSSIBLE CAVEATS IN THIS WORK

As a few final words of caution, a possible caveat in this work is how the *Euclid* (+ancillary) photometry is simulated from best-fit SED templates, as compared to extracting fluxes from real *Euclid* (+ancillary) images or even simulated images that emulate the real data more directly. By sampling the photometry directly from models, we do not take into account factors that could degrade the quality of the photometric measurements, such as telescope defects and source confusion. We do note, however, that *Euclid* will have an excellent (HST-like) angular resolution, and, thus, source blending is unlikely to be a major problem, considering the depths of the Euclid Deep Fields. Nonetheless, the simulated data in this work are idealised to a certain degree, and as such photometric redshift degeneracies could be more prevalent for the real data. Moreover, we used the same template set to simulate the *Euclid* (+ancillary) photometry and to recompute the photometric redshifts based on these simulated data. The template fluxes were randomised as we described in Sect. 2.3, but nonetheless, our results on the contamination fractions could be affected by this.

Second, throughout this work we have not distinguished between normal galaxies and galaxies that host an active galactic nucleus (AGN), even though we know that these types of galaxies are present in the COSMOS field (Brusa et al. 2010; Delvecchio et al. 2017; Chang et al. 2017). We cross-correlated our UltraVISTA DR4 catalogue with the C-COSMOS X-ray catalogue (Civano et al. 2016) and identified 996 X-ray AGN sources with host galaxy redshifts between $z = 1$–5.3. These sources are rare, as they constitute only 0.6 % of the total galaxy population between $z = 1$–5.3. Moreover, we find that the simulated redshifts of these sources lie below $z = 6$ in any scenario of *Euclid* (+ancillary) data. Therefore, we conclude that our X-ray selected AGNs do not contaminate the *Euclid* high-redshift galaxy sample. However, alternative methods to identify AGNs exist, so more work regarding this AGN contamination of $z > 6$ galaxies is desired.

Lastly, throughout this work we have assumed the expected full depths for the *Euclid* and Rubin photometry, finalised once the nominal missions have been completed. With this assumption, we have demonstrated how ancillary photometry is only marginally helpful to prevent intermediate-z contaminants from entering the high-redshift sample, and how $z > 6$ galaxies are well-recovered from *Euclid* data alone for both bright and faint galaxies. This does not imply that the ancillary data have an insignificant role in the study of high-z galaxies. The efforts to gather ancillary imaging in the Euclid Deep Fields are very important. For a long time the ancillary data in the optical bands will be deeper than that provided by *Euclid* I_{E}. In fact, the final I_{E} depth assumed here will not be achieved until late stages of the *Euclid* operations. Given that the *Euclid* and Rubin missions will run over many years, interim datasets at intermediate depths will be released. Therefore, ancillary imaging will be very important for all the studies of high-z galaxies performed in the first years of *Euclid* data analysis. In general, we conclude that more work is required to analyse the contamination fraction estimates at intermediate *Euclid* and Rubin depths.

2.7. SUMMARY AND CONCLUSIONS

We have investigated the contamination from intermediate-z interlopers ($z = 1$–5.8) of the $z > 6$ galaxy population as expected for the Euclid Deep Fields. Our tests are based on ~176 000 real galaxies at $z = 1$–8 in a ~0.7 deg^2 area selected from the UltraVISTA ultra-deep survey in the COSMOS field and an additional sample of ~96 000 mock galaxies with $25.3 \leq H < 27.0$ that follow a CANDELS-like photometric redshift and H magnitude distribution. For both datasets, we simulated *Euclid* and ancillary photometry from fiducial 28-band photometry and subsequently re-derived photometric redshifts for eight scenarios of data availability: (i) *Euclid* data only; (ii) *Euclid* and Rubin $ugrizy$ data; (iii) *Euclid* and ultra-deep Rubin $ugrizy$ data from the Rubin DDF; (iv) *Euclid* and CFHT u and Subaru HSC $griz$ data from the H20 survey; (v) *Euclid* and *Spitzer* IRAC 3.6 and 4.5 μm data; (vi) *Euclid*, Rubin, and *Spitzer* data; (vii) *Euclid*, Rubin DDF, and *Spitzer* data; and (viii) *Euclid*, H20, and *Spitzer* data. We emphasise that the findings presented below are only representative of galaxies up to $z = 8$ due to the limitations of our fiducial sample and that we cannot assess the photometric redshift recovery of *Euclid* $z > 8$ galaxies.

1. We determined the fraction of intermediate-z contaminants (fiducial $z = 1$–5.8) amongst the apparent $z > 6$ population as identified from *Euclid* (+ancillary) data. Based on the bright UltraVISTA-like sample, we estimate the contamination fraction of $z > 6$ galaxies observed with *Euclid* to be $0.18^{+0.07}_{-0.06}$. Contrarily, when we consider the faint mock sample, the contamination fraction of $z > 6$ galaxies with *Euclid* is significantly higher at $0.39^{+0.10}_{-0.11}$.

2. Based on the bright UltraVISTA-like sample, we find that the contamination fraction is reduced to $0.13^{+0.04}_{-0.05}$ when including *Spitzer* IRAC photometry, and to $0.04^{+0.03}_{-0.02}$ when including Rubin DDF photometry. In our most optimistic scenario, where we combined *Euclid*, Rubin DDF, and *Spitzer* photometry, virtually any possible contamination from intermediate-z interlopers is ruled out; the contamination fraction is $0.01^{+0.0006}_{-0.0001}$. Conversely, when we consider the faint mock sample, the

contamination fraction is only significantly reduced once we include the ultra-deep Rubin DDF photometry, to $0.07^{+0.03}_{-0.03}$.

3. We replicated our analysis of the bright UltraVISTA-like sample on the COSMOS2020 galaxy catalogue, which contains independent photometry over the same field, in combination with various SED fitting routines. We find generally good agreement between the contamination fraction estimated from our own photometry and those derived using `LePhare`/`LePhare++` with the COSMOS2020 catalogue. However, we obtain different results using the `EAZY` code, which returns a lower fraction of contaminants as well as a lower completeness in the recovery of $z > 6$ galaxies.

4. The contaminants of $z > 6$ galaxies have distinctly different $(I_\mathrm{E} - Y_\mathrm{E})$ colours from true $z > 6$ galaxies, so colour selection criteria can be used to separate these populations a posteriori of obtaining the *Euclid*-like photometric redshifts. However, many contaminants have unconstrained $(I_\mathrm{E} - Y_\mathrm{E})$ colours and as such cannot be included in this analysis. Regardless, we have presented a grid of $(I_\mathrm{E} - Y_\mathrm{E})$ & $(Y_\mathrm{E} - J_\mathrm{E})$ colour cuts that balance the contamination fraction and $z > 6$ galaxy completeness. For the bright UltraVISTA-like sample, the colour cut $(I_\mathrm{E} - Y_\mathrm{E}) > 2.8$ & $(Y_\mathrm{E} - J_\mathrm{E}) < 1.4$ when applied to the apparent $z > 6$ galaxies (that have a flux measurement in the I_E and/or Y_E bands; identified from *Euclid* data) reduces the contamination fraction to 0.01 while preserving 81 % of the fiducial $z > 6$ galaxies (i.e. galaxies at fiducial $z = 6$–8 that are recovered at $z > 6$ from *Euclid* photometry). Considering the faint mock sample, these proposed colour selection criteria are not useful, given that the majority of contaminants are undetected in both the I_E and Y_E bands.

5. Alternatively, we find that imposing a 5σ detection threshold requirement in at least one of the *Euclid* NIR bands is useful for obtaining a purer apparent $z > 6$ sample, specifically for the faint mock sample. By employing this detection threshold requirement, the contamination fraction of the faint mock $z > 6$ galaxies is $0.25^{+0.07}_{-0.07}$ (*Euclid* data alone), and we maintain a $z > 6$ completeness of 91 %. As such, the identification of faint high-redshift sources in the Euclid Deep Fields will be very efficient, with a moderate contamination of intermediate-z galaxies.

6. We investigated if one can select a pure sample of $z > 6$ galaxies from *Euclid* colours alone. Based on the bright UltraVISTA-like sample, we have shown how a strict colour cut at $(I_\mathrm{E} - Y_\mathrm{E}) > 3.4$ & $(Y_\mathrm{E} - J_\mathrm{E}) < 0.9$ could possibly select a pure sample of high-redshift galaxies, whilst maintaining a $z > 6$ completeness of 58 %. However, this cannot be achieved for the faint mock sample at all, and therefore we conclude that deriving photometric redshifts cannot be circumvented.

7. We compared the fiducial physical properties (based on 28 bands in COSMOS) of the intermediate-redshift galaxies that are $z > 6$ contaminants and stable intermediate-z galaxies (i.e. $z = 1$–6 galaxies that stay in the same redshift bin when observed with *Euclid* (+ancillary) data). The analysis of the physical parameters is solely based on the bright UltraVISTA-like sample. We find that the $z > 6$ contaminants reside primarily at fiducial redshifts $z_\mathrm{fid} \sim 1$–3 and $z_\mathrm{fid} \sim 4.5$–6 and are primarily faint, regardless of which ancillary data are added to the *Euclid* photometry. We identify

three distinct populations: (i) moderately reddened galaxies at $z_{\rm fid}$ =1–3.5 that are misidentified through the typical confusion of the Lyman-α break at $\lambda = 1216$ Å and the 4000 Å break; (ii) a group of contaminants at $z_{\rm fid} = 3.5$–5 that are strongly dust-reddened; and (iii) a group at $z_{\rm fid} = 5$–6 that have typically ill-defined, flat, fiducial SEDs and are mistaken for $z \sim 6$ galaxies.

8. Moreover, we compared the physical properties as derived with *Euclid* (+ancillary) photometry of $z > 6$ contaminants and true $z > 6$ galaxies. We have demonstrated how *Spitzer* photometry is essential for recovering the stellar masses of $z > 6$ galaxies. The $z > 6$ contaminants are most separated from true $z > 6$ galaxies based on their colour excess, as the latter have virtually no dust attenuation. Although the parameter distributions of true $z > 6$ galaxies and $z > 6$ contaminants are generally statistically different, we find no selection criteria that effectively separate them based on their physical parameters.

Overall, we conclude that the *Euclid* high-redshift recovery will be excellent for bright $z = 6$–8 galaxies, and successful for faint galaxies as well. In addition, ultra-deep ancillary photometry is highly effective at reducing contamination from intermediate-z interlopers to the $z > 6$ galaxy sample.

ACKNOWLEDGEMENTS
Based on data products from observations conducted with ESO Telescopes at the Paranal Observatory under ESO program ID 179.A-2005 and on data products produced by TERAPIX and the Cambridge Astronomy Survey Unit on behalf of the UltraVISTA consortium. Also based in part on observations carried out with the *Spitzer* Space Telescope, which is operated by the Jet Propulsion Laboratory, California Institute of Technology under a contract with NASA. Also based on observations carried out by NASA/ESA Hubble Space Telescope, obtained and archived at the Space Telescope Science Institute; and the Subaru Telescope, which is operated by the National Astronomical Observatory of Japan. This research has made use of the NASA/IPAC Infrared Science Archive, which is operated by the Jet Propulsion Laboratory, California Institute of Technology, under contract with NASA.
SvM and KC acknowledge funding from the European Research Council through the award of the Consolidator Grant ID 681627-BUILDUP. PD acknowledges support from the European Research Council's starting grant ERC StG-717001 (DELPHI), from the NWO grant 016.VIDI.189.162 (ODIN) and the European Commission's and University of Groningen's CO-FUND Rosalind Franklin program. The Euclid Consortium acknowledges the European Space Agency and a number of agencies and institutes that have supported the development of *Euclid*, in particular the Academy of Finland, the Agenzia Spaziale Italiana, the Belgian Science Policy, the Canadian Euclid Consortium, the French Centre National d'Etudes Spatiales, the Deutsches Zentrum für Luft- und Raumfahrt, the Danish Space Research Institute, the Fundação para a Ciência e a Tecnologia, the Ministerio de Economia y Competitividad, the National Aeronautics and Space Administration, the National Astronomical Observatory of Japan, the Netherlandse Onderzoekschool Voor Astronomie, the Norwegian Space Agency, the Romanian Space Agency, the State Secretariat for Education, Research and Innovation (SERI) at the Swiss Space Office (SSO),

and the United Kingdom Space Agency. A complete and detailed list is available on the *Euclid* web site (`http://www.euclid-ec.org`). We thank Smaran Deshmukh for useful discussions on the SMUVS catalogue photometry. We thank Marc Sauvage for carefully reading the manuscript and providing constructive comments for the Euclid Consortium internal review.

REFERENCES

Aihara, H., AlSayyad, Y., Ando, M., et al. 2019, PASJ, 71, 114, doi: `10.1093/pasj/psz103`

Arnouts, S., Cristiani, S., Moscardini, L., et al. 1999, MNRAS, 310, 540, doi: `10.1046/j.1365-8711.1999.02978.x`

Arnouts, S., Le Floc'h, E., Chevallard, J., et al. 2013, A&A, 558, A67, doi: `10.1051/0004-6361/201321768`

Ashby, M. L. N., Willner, S. P., Fazio, G. G., et al. 2015, ApJS, 218, 33, doi: `10.1088/0067-0049/218/2/33`

Ashby, M. L. N., Caputi, K. I., Cowley, W., et al. 2018, ApJS, 237, 39, doi: `10.3847/1538-4365/aad4fb`

Atek, H., Siana, B., Scarlata, C., et al. 2011, ApJ, 743, 121, doi: `10.1088/0004-637X/743/2/121`

Atek, H., Richard, J., Kneib, J.-P., et al. 2015, ApJ, 800, 18, doi: `10.1088/0004-637X/800/1/18`

Bertin, E., & Arnouts, S. 1996, A&AS, 117, 393, doi: `10.1051/aas:1996164`

Bisigello, L., Kuchner, U., Conselice, C. J., et al. 2020, MNRAS, 494, 2337, doi: `10.1093/mnras/staa885`

Bouwens, R. J., Illingworth, G. D., Oesch, P. A., et al. 2010, ApJL, 709, L133, doi: `10.1088/2041-8205/709/2/L133`

—. 2012, ApJ, 754, 83, doi: `10.1088/0004-637X/754/2/83`

Bouwens, R. J., Oesch, P. A., Stefanon, M., et al. 2021, AJ, 162, 47, doi: `10.3847/1538-3881/abf83e`

Bowler, R. A. A., Jarvis, M. J., Dunlop, J. S., et al. 2020, MNRAS, 493, 2059, doi: `10.1093/mnras/staa313`

Bowler, R. A. A., Dunlop, J. S., McLure, R. J., et al. 2014, MNRAS, 440, 2810, doi: `10.1093/mnras/stu449`

—. 2015, MNRAS, 452, 1817, doi: `10.1093/mnras/stv1403`

Brammer, G. B., van Dokkum, P. G., & Coppi, P. 2008, ApJ, 686, 1503, doi: `10.1086/591786`

Brusa, M., Civano, F., Comastri, A., et al. 2010, ApJ, 716, 348, doi: `10.1088/0004-637X/716/1/348`

Bruzual, G., & Charlot, S. 2003, MNRAS, 344, 1000, doi: `10.1046/j.1365-8711.2003.06897.x`

Burgasser, A. J. 2014, in Astronomical Society of India Conference Series, Vol. 11, Astronomical Society of India Conference Series, 7–16. `https://arxiv.org/abs/1406.4887`

Calzetti, D., Armus, L., Bohlin, R. C., et al. 2000, ApJ, 533, 682, doi: `10.1086/308692`

Caputi, K. I., McLure, R. J., Dunlop, J. S., Cirasuolo, M., & Schael, A. M. 2006, MNRAS, 366, 609, doi: `10.1111/j.1365-2966.2005.09887.x`

Caputi, K. I., Ilbert, O., Laigle, C., et al. 2015, ApJ, 810, 73, doi: `10.1088/0004-637X/810/1/73`

Castellano, M., Dayal, P., Pentericci, L., et al. 2016, ApJL, 818, L3, doi: `10.3847/2041-8205/818/1/L3`

Chabrier, G. 2003, PASP, 115, 763, doi: `10.1086/376392`

Chang, Y.-Y., Le Floc'h, E., Juneau, S., et al. 2017, ApJS, 233, 19, doi: `10.3847/1538-4365/aa97da`

Civano, F., Marchesi, S., Comastri, A., et al. 2016, ApJ, 819, 62, doi: `10.3847/0004-637X/819/1/62`

Conroy, C., & Gunn, J. E. 2010, ApJ, 712, 833, doi: `10.1088/0004-637X/712/2/833`

Conroy, C., Gunn, J. E., & White, M. 2009, ApJ, 699, 486, doi: `10.1088/0004-637X/699/1/486`

Cropper, M., Pottinger, S., Niemi, S., et al. 2016, in Society of Photo-Optical Instrumentation Engineers (SPIE) Conference Series, Vol. 9904, Space Telescopes and Instrumentation 2016: Optical, Infrared, and Millimeter Wave, ed. H. A. MacEwen, G. G. Fazio, M. Lystrup, N. Batalha, N. Siegler, & E. C. Tong, 99040Q, doi: `10.1117/12.2234739`

Dahlen, T., Mobasher, B., Faber, S. M., et al. 2013, ApJ, 775, 93, doi: `10.1088/0004-637X/775/2/93`

de Barros, S., Schaerer, D., & Stark, D. P. 2014, A&A, 563, A81, doi: `10.1051/0004-6361/201220026`

Delvecchio, I., Smolčić, V., Zamorani, G., et al. 2017, A&A, 602, A3, doi: `10.1051/0004-6361/201629367`

Deshmukh, S., Caputi, K. I., Ashby, M. L. N., et al. 2018, ApJ, 864, 166, doi: `10.3847/1538-4357/aad9f5`

Duncan, K., Conselice, C. J., Mortlock, A., et al. 2014, MNRAS, 444, 2960, doi: `10.1093/mnras/stu1622`

Ellis, R. S., McLure, R. J., Dunlop, J. S., et al. 2013, ApJL, 763, L7, doi: `10.1088/2041-8205/763/1/L7`

Euclid Collaboration: Desprez, G., Paltani, S., Coupon, J., et al. 2020, A&A, 644, A31, doi: `10.1051/0004-6361/202039403`

Euclid Collaboration: Moneti, A., McCracken, H. J., Shuntov, M., et al. 2022, A&A, 658, A126, doi: `10.1051/0004-6361/202142361`

Euclid Collaboration: Scaramella, R., Amiaux, J., Mellier, Y., et al. 2022, A&A, 662, A112, doi: `10.1051/0004-6361/202141938`

Euclid Collaboration: Schirmer, M., Jahnke, K., Seidel, G., et al. 2022, A&A, 662, A92, doi: `10.1051/0004-6361/202142897`

Fazio, G. G., Hora, J. L., Allen, L. E., et al. 2004, ApJS, 154, 10, doi: `10.1086/422843`

Finkelstein, S. L., Ryan, Russell E., J., Papovich, C., et al. 2015, ApJ, 810, 71, doi: `10.1088/0004-637X/810/1/71`

Foley, R. J., Koekemoer, A. M., Spergel, D. N., et al. 2018, arXiv e-prints, arXiv:1812.00514. `https://arxiv.org/abs/1812.00514`

Grogin, N. A., Kocevski, D. D., Faber, S. M., et al. 2011, ApJS, 197, 35, doi: `10.1088/0067-0049/197/2/35`

Hsieh, B.-C., Wang, W.-H., Hsieh, C.-C., et al. 2012, ApJS, 203, 23, doi: `10.1088/0067-0049/203/2/23`

Huang, X., Zheng, W., Wang, J., et al. 2015, ApJ, 801, 12, doi: `10.1088/0004-637X/801/1/12`

Ilbert, O., Arnouts, S., McCracken, H. J., et al. 2006, A&A, 457, 841, doi: `10.1051/0004-6361:20065138`

Ilbert, O., Capak, P., Salvato, M., et al. 2009, ApJ, 690, 1236, doi: `10.1088/0004-637X/690/2/1236`

Inoue, A. K., Shimizu, I., Iwata, I., & Tanaka, M. 2014, MNRAS, 442, 1805, doi: `10.1093/mnras/stu936`

Ivezić, Ž., Kahn, S. M., Tyson, J. A., et al. 2019, ApJ, 873, 111, doi: `10.3847/1538-4357/ab042c`

Jarvis, M. J., Bonfield, D. G., Bruce, V. A., et al. 2013, MNRAS, 428, 1281, doi: `10.1093/mnras/sts118`

Kennicutt, R. C. 1998, ApJ, 498, 541, doi: `10.1086/305588`

Koekemoer, A. M., Faber, S. M., Ferguson, H. C., et al. 2011, ApJS, 197, 36, doi: `10.1088/0067-0049/197/2/36`

Laigle, C., McCracken, H. J., Ilbert, O., et al. 2016, ApJS, 224, 24, doi: `10.3847/0067-0049/224/2/24`

Laureijs, R., Amiaux, J., Arduini, S., et al. 2011, arXiv e-prints, arXiv:1110.3193. `https://arxiv.org/abs/1110.3193`

Maciaszek, T., Ealet, A., Jahnke, K., et al. 2016, in Society of Photo-Optical Instrumentation Engineers (SPIE) Conference Series, Vol. 9904, Space Telescopes and Instrumentation 2016: Optical, Infrared, and Millimeter Wave, ed. H. A. MacEwen, G. G. Fazio, M. Lystrup, N. Batalha, N. Siegler, & E. C. Tong, 99040T, doi: `10.1117/12.2232941`

McCracken, H. J., Milvang-Jensen, B., Dunlop, J., et al. 2012, A&A, 544, A156, doi: `10.1051/0004-6361/201219507`

Nayyeri, H., Hemmati, S., Mobasher, B., et al. 2017, ApJS, 228, 7, doi: `10.3847/1538-4365/228/1/7`

Oesch, P. A., Bouwens, R. J., Illingworth, G. D., et al. 2012, ApJ, 745, 110, doi: `10.1088/0004-637X/745/2/110`

Oesch, P. A., Bouwens, R. J., Illingworth, G. D., et al. 2014, ApJ, 786, 108, doi: `10.1088/0004-637x/786/2/108`

Oke, J. B., & Gunn, J. E. 1983, ApJ, 266, 713, doi: `10.1086/160817`

Pentericci, L., Vanzella, E., Fontana, A., et al. 2014, ApJ, 793, 113, doi: `10.1088/0004-637X/793/2/113`

Polletta, M., Tajer, M., Maraschi, L., et al. 2007, ApJ, 663, 81, doi: `10.1086/518113`

Prevot, M. L., Lequeux, J., Maurice, E., Prevot, L., & Rocca-Volmerange, B. 1984, A&A, 132, 389

Roberts-Borsani, G., Morishita, T., Treu, T., Leethochawalit, N., & Trenti, M. 2022, ApJ, 927, 236, doi: `10.3847/1538-4357/ac4803`

Salmon, B., Coe, D., Bradley, L., et al. 2020, ApJ, 889, 189, doi: `10.3847/1538-4357/ab5a8b`

Schlafly, E. F., & Finkbeiner, D. P. 2011, ApJ, 737, 103, doi: `10.1088/0004-637X/737/2/103`

Scoville, N., Aussel, H., Brusa, M., et al. 2007, ApJS, 172, 1, doi: `10.1086/516585`

Smirnov, N. V. 1939, Bull. Math. Univ. Moscou, 2, 3

Song, M., Finkelstein, S. L., Ashby, M. L. N., et al. 2016, ApJ, 825, 5, doi: `10.3847/0004-637X/825/1/5`

Stefanon, M., Labbé, I., Bouwens, R. J., et al. 2019, ApJ, 883, 99, doi: `10.3847/1538-4357/ab3792`

Steidel, C. C., Giavalisco, M., Pettini, M., Dickinson, M., & Adelberger, K. L. 1996, ApJL, 462, L17, doi: `10.1086/310029`

Stern, D., Kirkpatrick, J. D., Allen, L. E., et al. 2007, ApJ, 663, 677, doi: `10.1086/516833`

van Mierlo, S. E., Caputi, K. I., Ashby, M., et al. 2022, A&A, 666, A200, doi: `10.1051/0004-6361/202243950`

Vulcani, B., Trenti, M., Calvi, V., et al. 2017, ApJ, 836, 239, doi: `10.3847/1538-4357/aa5caf`

Weaver, J. R., Kauffmann, O. B., Ilbert, O., et al. 2022, ApJS, 258, 11, doi: `10.3847/1538-4365/ac3078`

Werner, M. W., Roellig, T. L., Low, F. J., et al. 2004, ApJS, 154, 1, doi: `10.1086/422992`

Willott, C. J., McLure, R. J., Hibon, P., et al. 2013, AJ, 145, 4, doi: `10.1088/0004-6256/145/1/4`

APPENDIX: COSMOS2020

In order to verify the validity of our estimates on the fraction of intermediate-z interlopers amongst the *Euclid*-observed $z > 6$ galaxy population, we have repeated our analysis of the bright UltraVISTA-like sources on a different photometric catalogue and different SED fitting codes.

We have used photometry from the COSMOS2020 catalogue (Weaver et al. 2022; version of December 2020; hereafter W21), which comprises the latest data release of COSMOS (Scoville et al. 2007). This catalogue includes new ultra-deep optical data from DR2 of the HSC Subaru Strategic Program (Aihara et al. 2019), infrared data from the fourth release of the UltraVISTA survey (McCracken et al. 2012), and all *Spitzer* data in four IRAC channels ever obtained in the COSMOS field (Euclid Collaboration: Moneti et al. 2022). Two independent versions of the COSMOS2020 catalogue using different techniques of measuring photometry were constructed, and in this work we made use of the so-called Classic catalogue. For this version, source detection was performed with `SourceExtractor` on the combined $izYJHK_s$ detection image, after which photometry was measured in $2''$ and $3''$ diameter apertures on the PSF-homogenised images in 40 optical and NIR bands. The IRAC fluxes were extracted separately using the `IRACLEAN` software (Hsieh et al. 2012). The final catalogue consists of roughly 1 700 000 sources. We refer the reader to W21 for a complete description of the COSMOS2020 Classic photometric catalogue. Throughout this paper we globally refer to the COSMOS2020 Classic photometry as the COSMOS2020 aperture photometry.

In addition, W21 presented two independent sets of photometric redshifts for all sources in the COSMOS2020 Classic catalogue, derived from two different template-fitting routines, namely `LePhare` and `EAZY` (again, we refer the reader to the original publication for the full details on their methodology). Here we make use of both sets of photometric redshifts.

For our tests, we only considered sources classified as galaxies (type=0) from this catalogue. In addition, we considered only the very deepest parts of COSMOS2020 catalogue and therefore cut the catalogue to ensure its area overlaps exactly with our own UltraVISTA catalogue (which comprises three out of the four ultra-deep stripes). These measures reduced the sample to 316 698 galaxies. We used the aperture and Galactic extinction corrections from W21 (the latter based on dust maps from Schlafly & Finkbeiner 2011, consistent with our own analysis) to obtain total, dust-corrected photometry.

Our goal is to derive *Euclid*-like photometry and photometric redshifts based on the COSMOS2020 catalogue, in three independent tests where we use different SED fitting algorithms.

COSMOS2020 WITH THE LEPHARE++ ROUTINE

For our first test, we simply replicated the SED fitting process with `LePhare` as described in W21 to the best of our ability. We used an updated version of `LePhare` called `LePhare++`, which is based on the `Fortran` version of the code but has been migrated to `C++`. The set of galaxy templates included 19 empirical elliptical and spiral templates from Polletta et al. (2007), 12 star-forming galaxy models from the Bruzual & Charlot (2003, hereafter BC03) library and two BC03 templates with exponentially declining star-formation rates. The considered attenuation curves are from Calzetti et al. (2000), Prevot et al. (1984), and two realisations of the Calzetti law including the 2175 Å bump (Prevot et al. 1984) at different strengths. Dust extinction was varied between $E(B-V)=0.0$ and 0.5 in 0.05 steps and the considered redshift range was $z=0$–10 with $\Delta z=0.01$ increments. Emission lines were included in the fit following the original recipe from LePhare (Ilbert et al. 2009), but using a new functionality in `LePhare++`, we allowed the modelled O III $\lambda\lambda 4931, 5007$ flux to vary between 50 % and 150 % (in 25 % steps) of the theoretical line flux.

This run was based on 34 bands from the COSMOS2020 photometric catalogue: GALEX NUV; CFHT MegaCam u and u*; Subaru HSC g, r, i, z, and y; Subaru Suprime-Cam B, V, r^+, i^+, z^{++}, and 14 intermediate- and narrow bands; VISTA Y, J, H, K_s, and $NB118$; and IRAC channels 1 and 2. We applied photometric offsets as presented in Table 2 in W21 to the fluxes and added 0.02 mag errors in quadrature to the photometric errors in the optical bands, 0.05 mag errors to the VISTA J, H, and K_s bands and IRAC channel 1 and the three narrow bands, and 0.1 mag to IRAC channel 2.

Once we derived the photometric redshifts for the COSMOS2020 galaxies in this way, we fixed their redshifts to these values and used `LePhare++` with an alternate template library to derive their physical properties and best-fit SEDs from which we measure *Euclid*-like photometry. The two-step strategy follows W21 and is necessary as the empirical galaxy templates cannot be used to derive physical parameters. In this second run, we used a set of 11 BC03 templates with nine exponentially declining and two delayed exponentially declining SFHs, assuming a Chabrier (2003) IMF. We adopted two metallicities: solar ($Z=0.02$) and half-solar ($Z=0.008$). The dust extinction was allowed to vary between $E(B-V)=0.0$ and 0.7 in 0.1 steps. The extinction laws used were the Calzetti et al. (2000) law and a curve that has a slope in between the Calzetti et al. (2000) law and the Prevot et al. (1984) curve ($\lambda^{0.9}$; Appendix A of Arnouts et al. 2013). Again, we add emission lines using the recipe from Ilbert et al. (2009), but employ no dispersion of the OIII doublet. We emphasise again that this two-step method is directly taken from W21.

Once we obtained the best-fit SEDs, we derived the *Euclid* (+ancillary) photometry in precisely the same manner as presented in Sect. 2.3. An important caveat is that the source detection of the COSMOS2020 catalogue was performed using the UltraVISTA DR4 mosaics, which means the catalogue is deeper than our own DR3-derived UltraVISTA catalogue. Given that we want to exclude sources that lie beyond the detection abilities of *Euclid*, we restrained the COSMOS2020 sample to sources that have at least a 3σ detection in both the simulated J_{E} and H_{E} bands.

In total, the COSMOS2020 photometry processed with the above described SED fitting routine, after applying the J_{E}- and H_{E}-band requirements, yields 164 800 galaxies with fiducial redshifts $z_{\mathrm{fid}} = 1$–8, of which 598 are at $z_{\mathrm{fid}} = 6$–8. Out of this sample, 127 985 galaxies are detected in at least IRAC channel 1 or channel 2, and 342 of these sources are at $z_{\mathrm{fid}} = 6$–8.

For each of the eight *Euclid* and ancillary data availability scenarios, we re-derived the photometric redshifts of the COSMOS2020 galaxies from their simulated *Euclid* (+ancillary) photometry alone, using `LePhare++` with the same set of empirical and BC03 templates as described above in the first step of the two-step SED fitting strategy. Following the method outlined in Sect. 2.4.2, we calculated the high-redshift completeness and fraction of intermediate-z interlopers amongst $z > 6$ galaxies. The results are shown in Table 2.7.

COSMOS2020 WITH THE `LEPHARE` ROUTINE USED IN THIS PAPER

For our second test, we used the COSMOS2020 aperture photometry in combination with `LePhare` (the `Fortran` version), using the SED fitting settings we adopted for our own UltraVISTA catalogue (Sect. 2.2). As a reminder, our SED fitting routine considers among others a smaller redshift range ($z = 0$–9), templates from the BC03 library only and a broader dust extinction range, that is, $E(B-V) = 0$–1 with the Calzetti et al. (2000) reddening law. We based this test on the same 34 optical and infrared band as listed for the previous test. We did not derive the fiducial photometric redshifts from scratch, instead fixing the redshift to those derived by W21 with `LePhare`. However, given that for this test, our `LePhare` parameters are not identical to those of W21, we minimised any discrepancies between our resulting best-fit SED and the fixed photometric redshift by deriving photometric offsets. This was done iteratively, until the difference between the input photometry and template fluxes converged. Subsequently, we sample the *Euclid* (+ancillary) photometry from the final best-fit SED.

With this second SED fitting method, the COSMOS2020 photometry yields 165 190 galaxies at fiducial redshifts $z_{\mathrm{fid}} = 1$–8 that exceed the 3σ flux in the J_{E} and H_{E} bands, of which 466 are at $z_{\mathrm{fid}} = 6$–8. Out of this sample, 124 520 galaxies are detected in at least IRAC channel 1 or channel 2, and 253 of these are at $z_{\mathrm{fid}} = 6$–8.

Subsequently, photometric redshifts based on the *Euclid* (+ancillary) photometry were recomputed using our own `LePhare` fitting routine. We derived the contamination fraction and $z > 6$ completeness for each combination of *Euclid* and ancillary photometry based on this second test with the COSMOS2020 catalogue, and show the results in Table 2.8.

COSMOS2020 WITH THE EAZY CODE

For our third test, we used the COSMOS2020 aperture photometry but now with another SED fitting code, that is, the newly updated version of the `EAZY` code (Brammer et al. 2008), which has been migrated to `Python` (version `0.5.2.dev7`). Similar to `LePhare`, `EAZY` is a template-fitting algorithm that assigns photometric redshifts to multi-wavelength photometry. This code was used by W21 to provide a second set of photometric redshifts based on the COSMOS2020 data. Therefore, we reproduce their process as closely as possible in order to recover the `EAZY` best-fit templates for the COSMOS2020 Classic catalogue.

Following W21, `EAZY` uses a set of 17 templates derived from the Flexible Stellar Population Synthesis models (Conroy et al. 2009; Conroy & Gunn 2010) with a range of dust attenuations and SFHs, and fits linear combinations of these templates to the observed photometry. The redshift is allowed to range from $z = 0$–12 and a K_s apparent magnitude prior is applied in the process. We include the photometric offsets computed by W21 in the fit, derived iteratively from a subsample of sources with spectroscopic redshifts. Multiplicative factors as presented in W21 were applied to the photometric errors, and the same magnitude errors as used for LePhare were added in quadrature. We selected a sample of $z = 1$–8 galaxies from the EAZY COSMOS2020 catalogue and derived our own fiducial photometric redshifts with this method. `EAZY` was used to retrieve the observed frame fluxes in the *Euclid* (+ancillary) filters.

Our strategy to ensure realistic depths for the simulated photometry is slightly different. With `LePhare`, one is able to set flux upper limits such that any template that produces fluxes higher than the upper limits in bands with non-detections is immediately discarded. `EAZY` performs the template fitting in linear flux density units, so it naturally accounts for the σ flux limits we derive from the expected *Euclid* (+ancillary) depths when we set the flux uncertainty in each band to half the 2σ flux. Subsequently, we re-derived the photometric redshifts based on the simulated photometry using the templates and settings as used for the COSMOS2020 photometry, although we did not employ the apparent magnitude prior.

The COSMOS2020 photometry with `EAZY` yields 160 260 galaxies at fiducial $z_{\rm fid} = 1$–8 that satisfy the $J_{\rm E}$- and $H_{\rm E}$-band criteria we imposed, of which 369 are at $z_{\rm fid} = 6$–8. We calculated the contamination fraction and high-redshift completeness for three scenarios of *Euclid* and ancillary photometry: *Euclid*, *Euclid*+H20, and *Euclid*+Rubin DDF. The results are shown in Table 2.9. For our test with `EAZY`, we chose to investigate only these three scenarios as they reflect well the different levels of depth expected from the ancillary data.

Lastly, we note that uncertainties on the contamination fraction were derived for all three tests, using the exact same method adopted for our photometric catalogue (see Sect. 2.4.2).

Table 2.7 | Number of true $z > 6$ galaxies and $z > 6$ contaminants, using the COSMOS2020 Classic catalogue from Weaver et al. (2022). The fiducial photometric redshifts and *Euclid* (+ancillary) photometry were derived using the methods described in Weaver et al. (2022). Only sources with a 3σ detection in both the J_E and H_E bands are considered here.

Filters	True $z > 6$	Contaminants	Contaminant Fraction	Completeness
Euclid	527	90	$0.15^{+0.03}_{-0.04}$	88 %
Euclid + Rubin	531	98	$0.16^{+0.05}_{-0.06}$	89 %
Euclid + Rubin DDF	561	30	$0.05^{+0.02}_{-0.02}$	94 %
Euclid + H20	541	86	$0.14^{+0.04}_{-0.04}$	90 %
Euclid + *Spitzer*	292	55	$0.16^{+0.05}_{-0.05}$	85 %
Euclid + Rubin + *Spitzer*	301	57	$0.16^{+0.04}_{-0.04}$	88 %
Euclid + Rubin DDF + *Spitzer*	317	18	$0.05^{+0.02}_{-0.01}$	93 %
Euclid + H20 + *Spitzer*	300	54	$0.15^{+0.04}_{-0.04}$	88 %

Table 2.8 | Number of true $z > 6$ galaxies and $z > 6$ contaminants, using the COSMOS2020 Classic catalogue from Weaver et al. (2022). The fiducial photometric redshifts and *Euclid* (+ancillary) photometry were derived using the same method adopted for the UltraVISTA/SMUVS photometry, described in Sect. 2.2.2. Only sources with a 3σ detection in both the J_E and H_E bands are considered here.

Filters	True $z > 6$	Contaminants	Contaminant Fraction	Completeness
Euclid	418	82	$0.16^{+0.05}_{-0.04}$	90 %
Euclid + Rubin	414	81	$0.16^{+0.06}_{-0.05}$	89 %
Euclid + Rubin DDF	424	18	$0.04^{+0.02}_{-0.02}$	91 %
Euclid + H20	418	58	$0.12^{+0.04}_{-0.04}$	90 %
Euclid + *Spitzer*	227	43	$0.16^{+0.06}_{-0.06}$	90 %
Euclid + Rubin + *Spitzer*	227	47	$0.17^{+0.06}_{-0.05}$	88 %
Euclid + Rubin DDF + *Spitzer*	228	8	$0.03^{+0.01}_{-0.01}$	90 %
Euclid + H20 + *Spitzer*	228	28	$0.11^{+0.05}_{-0.04}$	90 %

Table 2.9 | Number of true $z > 6$ galaxies and $z > 6$ contaminants, using the COSMOS2020 Classic catalogue from Weaver et al. (2022). The fiducial photometric redshifts and *Euclid* (+ ancillary) photometry were derived with `EAZY`, following the methods outlined in Weaver et al. (2022). Only sources with a 3σ detection in both the J_E and H_E bands are considered here.

Filters	True $z > 6$	Contaminants	Contaminant Fraction	Completeness
Euclid	299	30	$0.09^{+0.05}_{-0.05}$	81 %
Euclid + Rubin DDF	263	2	$0.01^{+0.002}_{-0.006}$	71 %
Euclid + H20	165	0	$0.0^{+0.00}_{-0.00}$	45 %

3

NO NEED FOR EXTREME STELLAR MASSES AT $z \sim 7$: A TEST-CASE STUDY OF COS-87259

S.E. van Mierlo, K.I. Caputi, and V. Kokorev

This chapter has been published as *No need for extreme stellar masses at z ∼ 7: a test-case study of COS-87259* in The Astrophysical Journal Letters **945**, L21, 2023.

ABSTRACT

Recent controversy regarding the existence of massive ($\log(M_*/M_\odot) \gtrsim 11$*) galaxies at* $z > 6$ *poses a challenge for galaxy formation theories. Hence, it is of critical importance to understand the effects of SED fitting methods on stellar mass estimates of Epoch of Re-ionisation galaxies. In this work, we perform a case study on the AGN-host galaxy candidate COS-87259 with spectroscopic redshift* $z_{\rm spec} = 6.853$*, that is claimed to have an extremely high stellar mass of* $\log(M_*/M_\odot) \sim 11.2$*. We test a suite of different SED fitting algorithms and stellar population models on our independently measured photometry in 17 broad bands for this source. Between five different code set-ups, the stellar mass estimates for COS-87259 span* $\log(M_*/M_\odot) = 10.24$*–11.00, whilst the reduced* χ^2 *values of the fits are all close to unity within* $\Delta\chi^2_\nu = 1.2$*, so that the quality of the SED fits is basically indistinguishable. Only when we adopt a non-parametric star formation history model within* PROSPECTOR *do we retrieve a stellar mass exceeding* $\log(M_*/M_\odot) = 11$*. Although the derived stellar masses change when using previously reported photometry for this source, the non-parametric SED-fitting method always yields the highest values. As these models are becoming increasingly popular for James Webb Space Telescope high-redshift science, we stress the absolute importance to test various SED fitting routines particularly on apparently very massive galaxies at such high redshifts.*

3.1. INTRODUCTION

Over the past two decades, many examples of galaxies with stellar masses $\log(M_*/M_\odot) \gtrsim 11$ out to redshift $z \sim 6$ have been found (e.g., Caputi et al. 2011; Stefanon et al. 2015; Deshmukh et al. 2018; Marsan et al. 2022). However, towards the Epoch of Re-ionisation (EoR; $z \gtrsim 6$), such massive galaxies become increasingly rarer (e.g., Stefanon et al. 2021). For instance, Caputi et al. (2015) found virtually no galaxy with stellar mass $\log(M_*/M_\odot) > 11.0$ at such high redshifts over $0.8\,\mathrm{deg}^2$ within the COSMOS field (Scoville et al. 2007). This result has been recently challenged by the apparent discovery of unusually massive galaxies at $z > 6$ (Endsley et al. 2022a; Labbé et al. 2023). The existence of these sources would be in tension with galaxy formation theories assuming ΛCDM cosmology (e.g., Behroozi & Silk 2018; Boylan-Kolchin 2022; Menci et al. 2022).

Galaxy stellar masses are usually estimated through spectral energy distribution (SED) fitting of photometric data. Many different SED fitting codes exists, which can lead to significantly different stellar mass estimates of the same object, especially for apparently faint galaxies (e.g., Dahlen et al. 2013; Weaver et al. 2022). Therefore, a critical study of the effects of SED fitting approaches on the derived stellar masses at $z > 6$ is of utmost importance.

For example, recent works have demonstrated that SED models assuming a non-parametric star formation history (SFH) yield higher stellar masses compared to traditional parametric descriptions (Tacchella et al. 2022; Topping et al. 2022; Whitler et al. 2022), although Stefanon et al. (2022) found identical stellar masses between a constant and non-parametric SFH fit of a stacked sample of $z \sim 10$ galaxies. In addition, the choice of initial mass function (IMF) also affects the derived stellar mass, and a Galactic IMF might not be the most suitable at $z > 6$ (Steinhardt et al. 2023).

In this letter, we present a case study of the source COS-87259, located in the third ultra-deep stripe of the UltraVISTA survey in COSMOS. This galaxy was originally identified as a $z_{\rm phot} \approx 6.6$–6.9 Lyman Break galaxy in Endsley et al. (2021). Subsequently, Endsley et al. (2022b) identified radio and X-ray emission coming from this source, concluding that this galaxy likely harbors an active galactic nucleus (AGN). Finally, Endsley et al. (2022a) conducted follow-up spectroscopy with ALMA, identifying strong [CII]158 μm and dust continuum emission, establishing a precise spectroscopic redshift of $z_{\rm phot} = 6.853 \pm 0.002$. Endsley and collaborators obtained different stellar mass estimates for COS-87259 in their different works, with the study based on optical to far-infrared photometry including the ALMA measurement claiming that its best-estimate stellar mass is $\log(M_*/M_\odot) = 11.2 \pm 0.2$.

By using different SED fitting codes, in this work we assess whether this extremely high stellar mass value is necessarily the most accurate estimate for COS-87259. We adopt a cosmology with $\mathrm{H}_0 = 70$ km s^{-1} Mpc^{-1}, $\Omega_{\rm m} = 0.3$, and $\Omega_\Lambda = 0.7$. All magnitudes and fluxes are total, with magnitudes referring to the AB system (Oke & Gunn 1983). Stellar masses correspond to a Chabrier (2003) IMF.

Table 3.1 | Optical and NIR flux density measurements for COS-87259, as obtained in this work. For non-detections, 3σ upper limits are reported.

Telescope/Instrument	Band	Flux (μJy)
CFHT/MegaCam	u	< 0.0039
Subaru/Suprime-Cam	B	< 0.0050
Subaru/HSC	g	< 0.0045
Subaru/Suprime-Cam	V	< 0.014
Subaru/HSC	r	< 0.0067
Subaru/Suprime-Cam	r^+	< 0.013
Subaru/Suprime-Cam	i^+	< 0.013
Subaru/HSC	i	< 0.0079
Subaru/HSC	z	< 0.0098
Subaru/Suprime-Cam	z^{++}	0.007 ± 0.025
Subaru/HSC	y	0.097 ± 0.053
VISTA/VIRCAM	Y	0.214 ± 0.035
VISTA/VIRCAM	J	0.391 ± 0.043
VISTA/VIRCAM	H	0.577 ± 0.051
VISTA/VIRCAM	K_S	0.837 ± 0.081
Spitzer/IRAC	[3.6]	1.90 ± 0.17
Spitzer/IRAC	[4.5]	1.91 ± 0.18

3.2. PHOTOMETRY

COS-87259 is part of the UltraVISTA ultra-deep catalogue presented in van Mierlo et al. (2022). Based on the photometry in this catalogue, our initial photometric redshift for COS-87259 is $z_{\rm phot} = 6.87^{+0.08}_{-0.07}$, in excellent agreement with the spectroscopic redshift from Endsley et al. (2022a). To obtain more precise flux measurements for this analysis, we redid the photometry for COS-87259, using the PYTHON modules ASTROPY (version 5.0.4; Astropy Collaboration et al. 2022) and PHOTUTILS (version 1.4.1; Bradley et al. 2022).

We included ultra-deep optical data from Data Release (DR) 3 of the Subaru Hyper Suprime-Cam (HSC) Strategic Program (Aihara et al. 2022) in the g, r, i, z, and y bands. In addition, we consider CFHT Megacam u and Subaru Suprime-Cam broad-band data, namely the B, V, r^+, i^+, and z^{++} bands (Ilbert et al. 2009; Taniguchi et al. 2015). We also included the UltraVISTA DR4 VIRCAM Y,J,H, and $K_{\rm s}$ data (McCracken et al. 2012) and IRAC 3.6 and 4.5 μm imaging from the SMUVS programme (Ashby et al. 2018; Deshmukh et al. 2018). In total, we consider imaging in 17 rest-frame optical to near-infrared (NIR) broad bands, which together probe the rest-frame wavelength range 450–6390 Å at $z_{\rm spec} = 6.853$.

We measured the photometry in 2" circular diameters at the position of COS-87259 measured from the $HK_{\rm s}$ stack, i.e., right ascension $\alpha = 149h44m34s.06$ and declination $\delta = +01d39m20s.10$. COS-87259 has only two faint low-redshift neighbours in a 5" radius that are both undetected in IRAC, such that we are not worried about flux contamination. Assuming a point-source morphology, aperture flux corrections were derived for each band individually using the curve-of-growths of nearby bright stars, and used to correct the fluxes to total.

To derive the flux errors in all but the IRAC bands, we measured the background fluxes in 2" empty apertures over a 30 by 30" region around the source, and calculated the flux error as the standard deviation of the flux distribution that was 3σ-clipped over five iterations. As the IRAC images suffer from source confusion, for the IRAC flux errors instead, we adopted a SOURCEEXTRACTOR-like approach (Bertin & Arnouts 1996) meaning that we derive the flux errors from the local background measurement in a 4 to 8” diameter annulus surrounding the source.

Finally, all fluxes and error measurements were corrected for Galactic dust extinction using the Schlafly & Finkbeiner (2011) dust maps with the Fitzpatrick (1999) reddening law. In bands with non-detections, we adopt 3σ flux upper limits derived from the empty aperture fluxes. We present an overview of our flux measurements in each band in Table 3.1.

We compare our photometric measurements of COS-87259 to those by Endsley et al. (2022b), presented in their Table 1. Between the bands that overlap in both samples, our flux upper limits in non-detected bands are systematically lower, by at most a factor ~ 6 in HSC g. Our VISTA Y, J, and H measurements all agree within the flux uncertainty, but most importantly, our $K_{\rm s} - [3.6]$ colour of 0.9 is significantly bluer than $K_{\rm s} - [3.6] = 1.5$ from Endsley et al. (2022b). In Sect. 3.4 we demonstrate how the photometric differences between our work and theirs affect our stellar mass comparison for COS-87259.

Table 3.2 | Resulting fit parameters from various SED fitting runs on the optical to NIR broad-band photometry of COS-87259.

Code	Stellar Population Models	SFH	χ^2_ν	M_* (log[$M/M_\odot$])
LePhare	BC03	Parametric	0.66	$10.42^{+0.22}_{-0.05}$
Prospector	FSPS	Parametric	1.11	$11.00^{+0.05}_{-0.07}$
Prospector	FSPS	Binned SFH	2.20	$11.16^{+0.05}_{-0.06}$
LePhare	STARBURST99	Parametric	1.19	$10.24^{+0.18}_{-0.05}$
EAZY	FSPS/Carnall et al. (2022)	Parametric	1.55	$10.53^{+0.09}_{-0.12}$

3.3. SED FITTING

In this section, we describe the different SED fitting approaches we took to derive the physical properties of COS-87259. We ran each code on the 17-band photometry, with the redshift fixed to the spectroscopic redshift $z_{\text{spec}} = 6.853$ from Endsley et al. (2022a).

3.3.1. LEPHARE WITH BC03

As a first code, we used the traditional, well-tested algorithm LEPHARE (Arnouts et al. 1999; Ilbert et al. 2006). The galaxy models were sampled from the GALAXEV library (Bruzual & Charlot 2003; BC03 hereafter).

We adopted different SFHs: a single stellar population and two parametric SFHs, i.e., an exponentially declining SFH (SFR $\propto$ $\mathrm{e}^{-t/\tau}$) and a delayed exponentially declining (SFR $\propto$ $t\mathrm{e}^{-t/\tau}$), using star formation timescales $\tau = 0.01, 0.1, 0.3, 1.0, 3.0, 5.0, 10.0$, and 15 Gyr. We considered solar ($Z = Z_\odot$) and sub-solar ($Z = 0.2 Z_\odot$) metallicities.

We adopted the Calzetti et al. (2000) reddening law and left the colour excess free between $E(B-V) = 0$–1. Emission lines were incorporated following the scaling relations from Kennicutt (1998) (see Ilbert et al. 2009 for a detailed description). Absorption of emission at wavelengths shorter than rest-frame 912 Å by the intergalactic medium (IGM) was implemented following Madau (1995). LEPHARE rejects any modelled SED that produces fluxes higher the 3σ upper limits in the non-detected bands.

3.3.2. LEPHARE WITH STARBURST99

Young galaxies with strong nebular line and continuum emission can have significantly boosted broad-band flux measurements, so that their stellar masses may be overestimated by up to a factor 10 (Bisigello et al. 2019). Therefore, we performed a separate SED fitting run with LEPHARE using stellar population models from the STARBURST99 library (Leitherer et al. 1999), which include both stellar emission and nebular line and continuum emission. We considered five templates with sub-solar metallicity of $Z = 0.05 Z_\odot$, ages spanning 10^6 to 10^8 years, and constant SFRs between 0.01–10 $M_\odot \mathrm{yr}^{-1}$. These templates were compiled into SED models and fitted to the photometry following the LEPHARE approach described in Sect. 3.3.1.

3.3.3. PROSPECTOR

The second code we considered is the Bayesian inference code PROSPECTOR (Johnson et al. 2021). This relatively new code has been extensively tested on low-redshift galaxies (e.g., Leja et al. 2017, 2019), but more recently has been used in numerous works to model the properties of very high-redshift galaxies, including *James Webb* Space Telescope (*JWST*)-observed sources (e.g. Naidu et al. 2022; Tacchella et al. 2022; Whitler et al. 2022).

PROSPECTOR uses the Flexible Stellar Population Synthesis code (FSPS; Conroy et al. 2009; Conroy & Gunn 2010). We tested both a delayed exponentially declining SFH and a flexible, non-parametric SFH.

Our parametric model involves six free parameters, using the default prior shapes with the following ranges: the formed stellar mass $M_* = 10^9$–$10^{12} M_\odot$, the metallicity $\log(Z/Z_\odot) = -2$–0.19, the e-folding time $\tau_{\rm SF} = 0.001$–15 Gyr, and the age $t_{age} = 0.001$–13.8 Gyr. We modelled diffuse dust attenuation following Calzetti et al. (2000) with $\tau_{dust} = 0$–4. Lastly, we implemented IGM absorption following Madau (1995) and nebular emission, using the default parameters.

In the non-parametric model ("continuity prior"), the SFH history is described by N temporal bins, with a constant SFR in each bin, and PROSPECTOR fits the ratio between these bins. We largely adopted the approach outlined in Tacchella et al. (2022), modelling six time bins, where the first bin spans 0–10 Myr in lookback time, and the remaining five bins are spaced equally in logarithmic time space up to $z = 20$. In addition, we fitted the formed stellar mass, metallicity, diffuse dust attenuation, IGM absorption factor, and gas ionisation parameter, following the PROSPECTOR parametric model.

Lastly, PROSPECTOR treats non-detections by utilizing the 1σ flux limit as the flux error.

3.3.4. EAZY

As a third SED fitting model, we used the PYTHON version of EAZY (Brammer et al. 2008). EAZY utilises a series of non-negative linear combinations of basis-set templates constructed with the FSPS models. Specifically, we used the CORR_SFHZ_13 subset of models within EAZY. These models contain redshift-dependent SFHs, which, at a given redshift, exclude the SFHs that start earlier than the age of the Universe. The maximum allowed attenuation is also tied to a given epoch. Additionally, we included the best-fit template to the *JWST*-observed extreme emission line galaxy at $z = 8.5$ (ID4590) from Carnall et al. (2022), which has been rescaled to match the normalization of the FSPS models. This was done to adequately model potential emission lines with large equivalent widths.

To fit our object, we adopted the EAZY template error function, to account for any additional uncertainty related to unusual stellar populations, using the default value of 0.2 for the template error. For non-detected bands, EAZY utilises the 1σ flux upper limit in the fit.

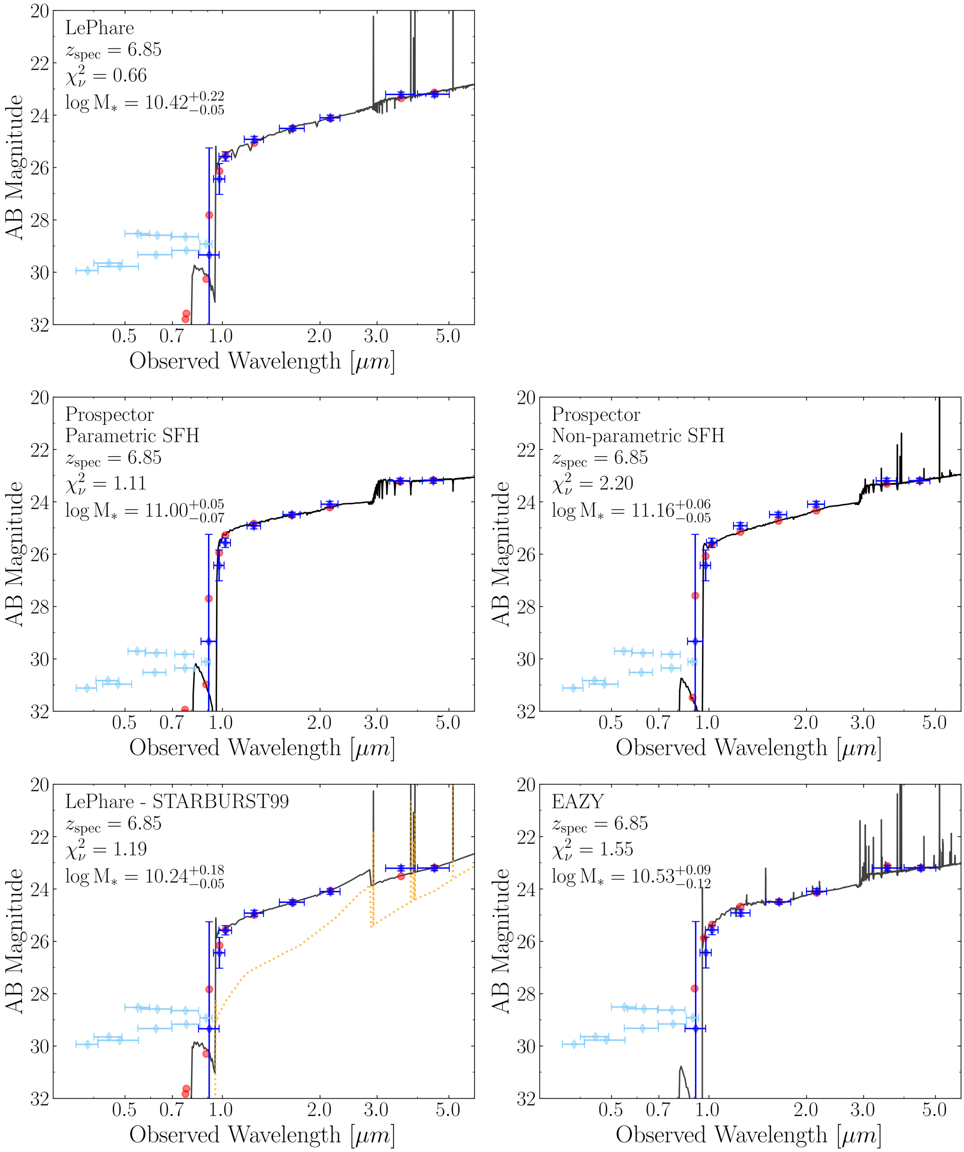

Figure 3.1 | Best-fit SEDs corresponding to the five SED fitting set-ups presented in Table 3.2. In each panel, the SED is shown in a black line. The observed fluxes and flux upper limits are shown in dark and light blue diamonds respectively. The template fluxes in each band are shown in red points. Each panel reports the SED fitting set-up, the spectroscopic redshift from Endsley et al. (2022a), the reduced χ^2 value of the fit, and the stellar mass. For the LEPHARE run using STARBURST99 models, shown in the lower left panel, the yellow dotted line represents the contribution of nebular emission to the total SED.

3.4. RESULTS

Here we compare the best-fit SEDs and associated stellar masses of COS-87259 obtained with the approaches outlined in Sect. 3.3.

For each SED fitting code and choice of stellar population models, we report the reduced χ^2 and stellar mass in Table 3.2. The corresponding best-fit SEDs are shown in Fig. 3.1. Each code has their own metric to determine the best-fit SED, so we explain them as follows. With LEPHARE, the best-fit SED simply minimises the χ^2 value compared to the observed photometry, and the stellar mass uncertainties reflect the 34th and 66th percentiles of the maximum likelihood distribution. The resulting SEDs and stellar masses obtained with PROSPECTOR correspond to the median of the posterior SED, and the errors on the stellar represent the 34th and 66th percentiles of the stellar mass posterior distribution. Finally, EAZY returns the best-fit SED based on the linear combination of templates that maximises the posterior probability distribution, with the errors on the stellar mass derived as the 16th and 84th percentiles. The non-homogeneous error recipes between the codes should be taken into account account upon comparing the stellar mass errors in Table 3.2, as it makes our reported EAZY stellar mass error inherently larger.

To compare the goodness of fit for each model, we use the reduced χ^2 metric calculated from comparing the observed and modelled photometry (including contribution from emission lines) in all bands excluding flux upper limits, where the number of degrees of freedom is simply the number of secure detections minus one, i.e., seven (see Table 3.1). For the stellar mass estimates presented in Table 3.2, we imposed a minimum error of 0.05 (10σ), which was derived from the signal-to-noise ratio in the observed band that samples the SED most closely to the rest-frame K-band, i.e., the IRAC 4.5 μm band. At $z \sim 7$, the IRAC 4.5 μm band samples the rest-frame ~ 5500 Å continuum and should be free from strong emission lines, such that it provides the best assessment of the stellar mass uncertainty given the our photometric data set for this source.

Our most important result is that between the five set-ups of codes and stellar population models, the resulting stellar masses differ by up to 0.9 dex, whereas it is virtually impossible to determine which of these fits is most representative of the truth: the χ^2_ν values are all close to one and differ by 1.54 at most.

Between the runs performed with LEPHARE using the BC03 models and the PROSPECTOR parametric set-up, their best-fit SEDs shown in the upper and central left panels of Fig. 3.1 respectively, the stellar masses differ by 0.6 dex and do not agree within the errors, even though we chose the run parameters to be as similar as possible. We believe this is partially because of the different templates sets, but also because of the actual SED fitting prescriptions (even if the stellar mass is derived directly from the template normalisation), given that stellar mass difference between the LEPHARE+BC03 and LEPHARE+STARBURST99 runs is only 0.18 dex.

According to the LEPHARE+BC03 result, this galaxy would be of solar metallicity, young at 0.01 Gyr old, actively undergoing star formation with $\tau = 15$ Gyr, and quite dusty with $A_V = 2.03$. Instead, PROSPECTOR finds that this source would be metal-poor with $Z = 0.014 Z_\odot$, relatively old with an age of 0.18 Gyr and less dusty with $A_V = 0.80$. Most importantly, its SFH e-folding time of only 0.003 Gyr and lack of nebular emission lines suggests that this galaxy would have undergone a short burst of SF upon creation and evolved relatively passively afterwards. Based on χ^2_ν values of these different fits, it is impossible to say with confidence which result is most likely between these two conflicting descriptions of of COS-87259's nature.

Using PROSPECTOR, we explicitly assess the dependency of stellar mass on the assumed SFH. We find a moderate difference of 0.12 dex in stellar mass between the two models, such that the stellar mass of $\log(M_*/M_\odot) = 11.16$ from the non-parametric SFH exceeds the parametric estimate of $\log(M_*/M_\odot) = 11.00$, even within the uncertainty. This effect has been observed in other works at similar redshift (Topping et al. 2022; Whitler et al. 2022). The non-parametric fit has the highest associated $\chi^2_\nu = 2.20$, explained by the underestimation of rest-frame UV fluxes due to moderate dust attenuation of $A_V = 1.44$. When we inspect our non-parametric SFH fit, we find that more than 80 % of the stellar mass was formed between lookback times of 0.18 Gyr and 0.042 Gyr, with a constant SFR of $1166\,M_\odot\mathrm{yr}^{-1}$. After this initial burst, the star formation rate falls off and continues at $42\,M_\odot\mathrm{yr}^{-1}$. This could explain the slightly higher stellar mass as compared to the parametric SFH, for which star formation ceases completely in the last $\sim 10^7$ years.

We find that stellar mass estimate from LEPHARE using the STARBURST99 templates is the lowest of our considered set-ups, at $\log(M_*/M_\odot) = 10.24$ with $\chi^2_\nu = 1.19$. The best-fit SED is shown in the lower left panel of Fig. 3.1, and corresponds to a 0.01 Gyr old galaxy with a constant SFR of $10\,M_\odot\mathrm{yr}^{-1}$ and sub-solar metallicity $Z = 0.05Z_\odot$. Upon decomposition of the SED, we find that 52 % of the integrated light is in fact nebular emission, resulting in a correct stellar mass of only $\log(M_*/M_\odot) = 9.91$.

Finally, we show the best-fit SED obtained with EAZY in the lower right panel of Fig. 3.1. The stellar mass from this fit is $\log(M_*/M_\odot) = 10.53$, with an associated $\chi^2_\nu = 1.55$, which makes the EAZY SED the worst fit out of the five code set-ups considered here. EAZY identifies COS-87259 as a 0.05 Gyr old galaxy, with moderate dust content so that $A_V = 0.87$ and a strong presence of emission lines.

We have demonstrated how different SED fitting approaches applied to independent photometric data produce strongly varying stellar mass estimates for COS-87259. Moreover, our estimates are all lower than the $\log(M_*/M_\odot) = 11.2 \pm 0.2$ value from Endsley et al. (2022a), although, given the uncertainty on their stellar mass estimate, it is not significantly different from our PROSPECTOR results.

The stellar mass discrepancy might to some extent be explained by different photometric values: we measure a significantly bluer $K_\mathrm{s} - [3.6] = 0.9$ colour than $K_\mathrm{s} - [3.6] = 1.5$ from Endsley et al. (2022b). At $z \sim 7$, the $K_\mathrm{s} - [3.6]$ colour is sensitive to the 4000Å break, but also to $O[III] + H\beta$ emission which can boost the IRAC 3.6 μm flux.

As a sanity check, we have run all codes discussed in Sect. 3.3 on the optical and NIR photometry (HSC g up to IRAC 4.5μm) from Table 1 in Endsley et al. (2022b), again fixing the redshift to $z_\mathrm{spec} = 6.853$. With our LEPHARE+BC03 set-up, we retrieve a stellar mass estimate of $\log(M_*/M_\odot) = 10.87^{+0.16}_{-0.13}$. This is 0.45 dex higher than the LEPHARE+BC03 stellar mass derived from our own photometry, and the values do not agree within the error bars. Surprisingly, the HSC IB945 flux upper limit strongly affects the stellar mass: if we change the significance of this constraint from 2σ to 3σ, the best-fit SED changes to a $\log(M_*/M_\odot) = 10.58^{+0.15}_{-0.10}$ result. Furthermore, from our other code set-ups, we retrieve systematically higher stellar mass for COS-87259 compared to our own results, but the

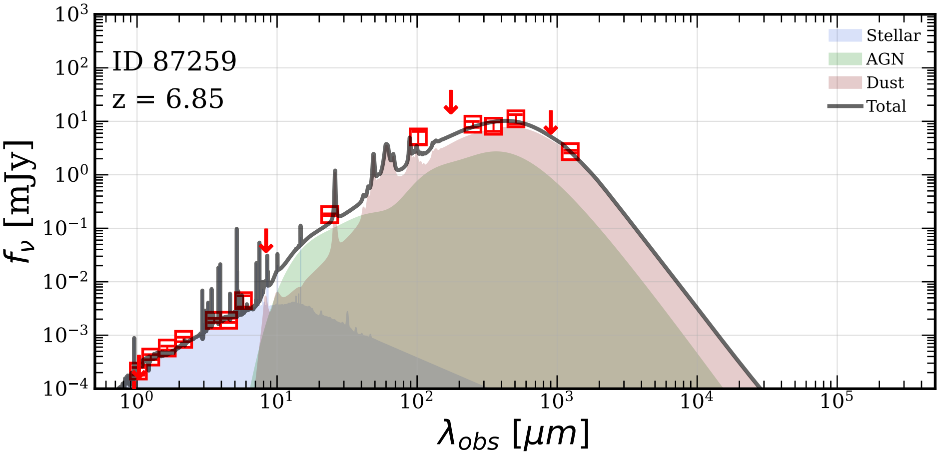

Figure 3.2 | Best-fit SED of COS-87259 obtained with STARDUST on the observed UV to millimeter photometry from Endsley et al. (2022b) and Endsley et al. (2022a). The flux measurements are shown in red, where the arrows correspond to flux upper limits. The individual components of the stellar, AGN and dust emission are shown in blue, green and red curves respectively.

same spread in masses of 0.9 dex. Therefore, we conclude our lower stellar mass estimate for COS-87259 is partially driven by our photometry, but the discrepancies between the results of our considered SED fitting routines are not.

3.5. COMBINED STELLAR AND DUST EMISSION SED FITTING

Another key difference with respect to our analysis that could explain the $\log(M_*/M_\odot) = 11.2 \pm 0.2$ result from Endsley et al. (2022a) is the inclusion of FIR to millimeter data, especially given that COS-87259 likely harbors an AGN. In fact, Endsley et al. (2022a) have fitted the full optical to millimeter wavelength photometry with a custom Bayesian SED fitting package, which includes AGN and galaxy dust emission components, as well as stellar emission using the FSPS code under the PROSPECTOR framework. So far we have only fitted the optical to NIR regime, so here we adopted the 5.8 μm to 1.4 mm photometry for COS-87259 from Endsley et al. (2022a) and Table 1 in Endsley et al. (2022b).

This combined suite of photometry is fitted with the SED-fitting code STARDUST (Kokorev et al. 2021), again fixing the redshift to $z_{\rm spec} = 6.853$. STARDUST models light from stars, AGN and infrared emission arising from the dust reprocessed stellar continuum. Similarly to EAZY, STARDUST fits independent linear combinations of templates, however with one key advantage of not assuming the energy balance between stellar and dust emission. For our fit we utilised UV-NIR templates adopted from EAZY, empirically derived AGN templates of Mullaney et al. (2011) and the dust models from Draine & Li (2007). For the latter, the minimum radiation fields intensity spans $U_{\rm min} = 40$–50, and fraction of dust contained in the photo-dissociation regions (PDRs) spans $\gamma = 0.01$–0.3. When combined, these correspond to a range of luminosity weighted dust temperatures

(T_{dust}) from 35–45 K.

The best-fit SED obtained from STARDUST is shown in Fig. 3.2. We note that STARDUST treats any flux measurement with confidence level $< 3\sigma$ as an upper limit instead, which brings the the total number of secure detections to 14. The χ^2_ν value for this fit is 1.90, and the resulting stellar mass is $\log(M_*/M_\odot) = 10.81^{+0.05}_{-0.05}$, which is over 0.4 dex lower than the $\log(M_*/M_\odot) = 11.2 \pm 0.2$stellar mass from Endsley et al. (2022a), and does not agree within the error bars. When we run STARDUST on the exact photometry from Endsley et al. (2022b), we retrieve a stellar mass of $\log(M_*/M_\odot) = 11.02^{+0.05}_{-0.05}$. These results with STARDUST reinforce our previous conclusion obtained with the SED fitting of only the source stellar emission: the stellar mass of COS-87259 is most likely $< 10^{11.2}\,M_\odot$.

3.6. CONCLUSION

In this letter, we reassessed the stellar mass of $z_{\text{spec}} = 6.853$ AGN-host galaxy candidate COS-87259, located in the UltraVISTA ultra-deep region in the COSMOS field. This source has been extensively studied in previous works: its most recent stellar mass estimate is unexpectedly high with $\log(M_*/M_\odot) = 11.2 \pm 0.2$ (Endsley et al. 2022a). Here, we took this galaxy as a case study to compare the best-fit SEDs and physical parameters obtained with different SED fitting routines. We measured independent photometry from 17 rest-frame optical to NIR broad-band images for COS-87259. These data were fitted with SED fitting codes LEPHARE, PROSPECTOR, EAZY, and STARDUST, including 5.8 μm to 1.4 mm photometry from Endsley et al. (2022a) for the latter fit.

Between six set-ups of codes and stellar population models, we find that the resulting stellar masses span $\log(M_*/M_\odot) = 10.24$–$11.16$. Contrarily, the reduced χ^2 values of the fits are all close to unity within $\Delta\chi^2_\nu = 1.2$. Therefore, all SED fits are of comparable quality, making is virtually impossible to decide which stellar mass estimate is most representative of the truth.

We find that the combination of PROSPECTOR and a non-parametric description of the SFH (which has been frequently used to fit newly *JWST*-discovered high-redshift galaxies) yields the highest stellar mass estimate in this work, $\log(M_*/M_\odot) = 11.16$. Moreover, even when adopting a traditional parametric SFH, PROSPECTOR yields significantly higher stellar masses than any of the other considered codes. Lastly, by considering very young galaxy templates that have strong nebular line and continuum emission, we obtain our lowest stellar mass estimate of $\log(M_*/M_\odot) = 10.24$ with $\chi^2_\nu = 1.19$.

We emphasise that none of our six considered SED fitting routines can replicate the extremely high stellar mass result from Endsley et al. (2022a), although this is partially explained by our bluer $K_s - [3.6]$ colour measurement. It should be noted however that a $\log(M_*/M_\odot) \geq 11$ solution for COS-87259 does not violate ΛCDM number density upper limit (Boylan-Kolchin 2022), even when other $z \sim 7$ galaxies of such stellar masses may be discovered in the COSMOS field in the future (Lovell et al. 2023).

In conclusion, in light of the recent discoveries of very massive EoR galaxies with *JWST*, we emphasise the absolute importance of testing various SED fitting routines on these seemingly massive galaxies to obtain a confident stellar mass estimate. Otherwise, we may falsely conclude that *JWST* is allowing us to probe an unexpectedly numerous population of massive galaxies, whereas in fact overestimation from novel SED fitting approaches is the main driver behind these results. As for the specific instance of COS-87259, this source will be observed with *JWST* in the near future, hopefully bringing us yet again closer to a consensus on the nature of this undoubtedly interesting galaxy.

ACKNOWLEDGEMENTS
We thank Ryan Endsley, Joel Leja, Chris Lovell, and Mara Salvato for useful discussions. We are also grateful to the anonymous referee for a careful reading of the manuscript and a constructive report. KIC and SvM acknowledge funding from the European Research Council through the award of the Consolidator Grant ID 681627-BUILDUP. KIC and VK acknowledge funding from the Dutch Research Council (NWO) through the award of the Vici Grant VI.C.212.036.

REFERENCES

Aihara, H., AlSayyad, Y., Ando, M., et al. 2022, PASJ, 74, 247, doi: `10.1093/pasj/psab122`

Arnouts, S., Cristiani, S., Moscardini, L., et al. 1999, MNRAS, 310, 540, doi: `10.1046/j.1365-8711.1999.02978.x`

Ashby, M. L. N., Caputi, K. I., Cowley, W., et al. 2018, ApJS, 237, 39, doi: `10.3847/1538-4365/aad4fb`

Astropy Collaboration, Price-Whelan, A. M., Lim, P. L., et al. 2022, ApJ, 935, 167, doi: `10.3847/1538-4357/ac7c74`

Behroozi, P., & Silk, J. 2018, MNRAS, 477, 5382, doi: `10.1093/mnras/sty945`

Bertin, E., & Arnouts, S. 1996, A&AS, 117, 393, doi: `10.1051/aas:1996164`

Bisigello, L., Caputi, K. I., Colina, L., et al. 2019, ApJS, 243, 27, doi: `10.3847/1538-4365/ab2911`

Boylan-Kolchin, M. 2022, arXiv e-prints, arXiv:2208.01611. `https://arxiv.org/abs/2208.01611`

Bradley, L., Sipőcz, B., Robitaille, T., et al. 2022, astropy/photutils:, 1.4.0, Zenodo, doi: `10.5281/zenodo.6385735`

Brammer, G. B., van Dokkum, P. G., & Coppi, P. 2008, ApJ, 686, 1503, doi: `10.1086/591786`

Bruzual, G., & Charlot, S. 2003, MNRAS, 344, 1000, doi: `10.1046/j.1365-8711.2003.06897.x`

Calzetti, D., Armus, L., Bohlin, R. C., et al. 2000, ApJ, 533, 682, doi: `10.1086/308692`

Caputi, K. I., Cirasuolo, M., Dunlop, J. S., et al. 2011, MNRAS, 413, 162, doi: `10.1111/j.1365-2966.2010.18118.x`

Caputi, K. I., Ilbert, O., Laigle, C., et al. 2015, ApJ, 810, 73, doi: `10.1088/0004-637X/810/1/73`

Carnall, A. C., Begley, R., McLeod, D. J., et al. 2022, arXiv e-prints, arXiv:2207.08778. `https://arxiv.org/abs/2207.08778`

Chabrier, G. 2003, PASP, 115, 763, doi: `10.1086/376392`

Conroy, C., & Gunn, J. E. 2010, FSPS: Flexible Stellar Population Synthesis, Astrophysics Source Code Library, record ascl:1010.043. `http://ascl.net/1010.043`

Conroy, C., Gunn, J. E., & White, M. 2009, ApJ, 699, 486, doi: `10.1088/0004-637X/699/1/486`

Dahlen, T., Mobasher, B., Faber, S. M., et al. 2013, ApJ, 775, 93, doi: `10.1088/0004-637X/775/2/93`

Deshmukh, S., Caputi, K. I., Ashby, M. L. N., et al. 2018, ApJ, 864, 166, doi: `10.3847/1538-4357/aad9f5`

Draine, B. T., & Li, A. 2007, ApJ, 657, 810, doi: `10.1086/511055`

Endsley, R., Stark, D. P., Chevallard, J., & Charlot, S. 2021, MNRAS, 500, 5229, doi: `10.1093/mnras/staa3370`

Endsley, R., Stark, D. P., Lyu, J., et al. 2022a, arXiv e-prints, arXiv:2206.00018. `https://arxiv.org/abs/2206.00018`

Endsley, R., Stark, D. P., Fan, X., et al. 2022b, MNRAS, 512, 4248, doi: `10.1093/mnras/stac737`

Fitzpatrick, E. L. 1999, PASP, 111, 63, doi: `10.1086/316293`

Ilbert, O., Arnouts, S., McCracken, H. J., et al. 2006, A&A, 457, 841, doi: `10.1051/0004-6361:20065138`

Ilbert, O., Capak, P., Salvato, M., et al. 2009, ApJ, 690, 1236, doi: `10.1088/0004-637X/690/2/1236`

Johnson, B. D., Leja, J., Conroy, C., & Speagle, J. S. 2021, ApJS, 254, 22, doi: `10.3847/1538-4365/abef67`

Kennicutt, R. C. 1998, ApJ, 498, 541, doi: `10.1086/305588`

Kokorev, V. I., Magdis, G. E., Davidzon, I., et al. 2021, ApJ, 921, 40, doi: `10.3847/1538-4357/ac18ce`

Labbé, I., van Dokkum, P., Nelson, E., et al. 2023, Nature, 616, 266, doi: `10.1038/s41586-023-05786-2`

Leitherer, C., Schaerer, D., Goldader, J. D., et al. 1999, ApJS, 123, 3, doi: `10.1086/313233`

Leja, J., Johnson, B. D., Conroy, C., van Dokkum, P. G., & Byler, N. 2017, ApJ, 837, 170, doi: `10.3847/1538-4357/aa5ffe`

Leja, J., Johnson, B. D., Conroy, C., et al. 2019, ApJ, 877, 140, doi: `10.3847/1538-4357/ab1d5a`

Lovell, C. C., Harrison, I., Harikane, Y., Tacchella, S., & Wilkins, S. M. 2023, MNRAS, 518, 2511, doi: `10.1093/mnras/stac3224`

Madau, P. 1995, ApJ, 441, 18, doi: `10.1086/175332`

Marsan, Z. C., Muzzin, A., Marchesini, D., et al. 2022, ApJ, 924, 25, doi: `10.3847/1538-4357/ac312a`

McCracken, H. J., Milvang-Jensen, B., Dunlop, J., et al. 2012, A&A, 544, A156, doi: `10.1051/0004-6361/201219507`

Menci, N., Castellano, M., Santini, P., et al. 2022, ApJL, 938, L5, doi: `10.3847/2041-8213/ac96e9`

Mullaney, J. R., Alexander, D. M., Goulding, A. D., & Hickox, R. C. 2011, MNRAS, 414, 1082, doi: `10.1111/j.1365-2966.2011.18448.x`

Naidu, R. P., Oesch, P. A., Dokkum, P. v., et al. 2022, ApJL, 940, L14, doi: `10.3847/2041-8213/ac9b22`

Oke, J. B., & Gunn, J. E. 1983, ApJ, 266, 713, doi: `10.1086/160817`

Schlafly, E. F., & Finkbeiner, D. P. 2011, ApJ, 737, 103, doi: `10.1088/0004-637X/737/2/103`

Scoville, N., Aussel, H., Brusa, M., et al. 2007, ApJS, 172, 1, doi: `10.1086/516585`

Stefanon, M., Bouwens, R. J., Labbé, I., et al. 2021, ApJ, 922, 29, doi: `10.3847/1538-4357/ac1bb6`

—. 2022, arXiv e-prints, arXiv:2206.13525. `https://arxiv.org/abs/2206.13525`

Stefanon, M., Marchesini, D., Muzzin, A., et al. 2015, ApJ, 803, 11, doi: `10.1088/0004-637X/803/1/11`

Steinhardt, C. L., Kokorev, V., Rusakov, V., Garcia, E., & Sneppen, A. 2023, ApJL, 951, L40, doi: `10.3847/2041-8213/acdef6`

Tacchella, S., Finkelstein, S. L., Bagley, M., et al. 2022, ApJ, 927, 170, doi: `10.3847/1538-4357/ac4cad`

Taniguchi, Y., Kajisawa, M., Kobayashi, M. A. R., et al. 2015, PASJ, 67, 104, doi: `10.1093/pasj/psv106`

Topping, M. W., Stark, D. P., Endsley, R., et al. 2022, MNRAS, 516, 975, doi: `10.1093/mnras/stac2291`

van Mierlo, S. E., Caputi, K. I., & Kokorev, V. 2023, ApJL, 945, L21, doi: `10.3847/2041-8213/acb773` van Mierlo, S. E., Caputi, K. I., Ashby, M., et al. 2022, A&A, 666, A200, doi: `10.1051/0004-6361/202243950`

Weaver, J. R., Kauffmann, O. B., Ilbert, O., et al. 2022, ApJS, 258, 11, doi: `10.3847/1538-4365/ac3078`

Whitler, L., Endsley, R., Stark, D. P., et al. 2022, arXiv e-prints, arXiv:2208.01599. `https://arxiv.org/abs/2208.01599`

4

A HIGH INCIDENCE OF DUSTY Hα EMITTERS AT $z > 3$ AMONG ULTRAVISTA DROPOUT GALAXIES IN COSMOS REVEALED BY JWST

S.E. van Mierlo, K.I. Caputi, M.L.N. Ashby, V. Kokorev, R. Navarro-Carrera, and P. Rinaldi

---

This chapter has been submitted as *A high incidence of dusty Hα emitters at $z > 3$ among UltraVISTA dropout galaxies in COSMOS revealed by JWST* to The Astrophysical Journal, and is under review.

ABSTRACT

We have characterized 26 Spitzer/IRAC-selected sources from the SMUVS program that are undetected in the UltraVISTA DR5 H- and/or K_s-band images, covering 94 square arcmin of the COSMOS field which have deep multi-wavelength JWST photometry. We analyzed the JWST/NIRCam imaging from the PRIMER survey and ancillary HST data to reveal the properties of these galaxies from spectral energy distribution (SED) fitting. We find that the majority of these galaxies are detected by NIRCam at $\lambda < 2\,\mu\mathrm{m}$*, with only four remaining as near-infrared dropouts in the deeper JWST images. Our results indicate that the UltraVISTA dropouts candidates are primarily located at* $z > 3$ *and are characterized by high dust extinctions, with a typical colour excess* $E(B-V) = 0.5 \pm 0.3$ *and stellar mass* $\log(M_* / M_\odot) = 9.5 \pm 1.0$*. Remarkably,* ~ 75 *% of these sources show a flux enhancement between the observed photometry and modelled continuum SED that can be attributed to Hα emission in the corresponding NIRCam bands. The derived (Hα + N[II] + S[II]) rest-frame equivalent widths and Hα star formation rates (SFRs) span values* ~ 100*–2200 Å and* ~ 5*–375* $M_\odot\,\mathrm{yr}^{-1}$*, respectively. The locations of these sources on the SFR-*M_* *plane indicates that 35 % of them are starbursts, 40 % are main-sequence galaxies and the remaining 25 % are located in the star-formation valley. Our sample includes one AGN and six sub-millimeter sources, as revealed from ancillary X-ray and sub-mm photometry. The high dust extinctions combined with the flux boosting from Hα emission explain why these sources are relatively bright Spitzer galaxies and yet unidentified in the ultra-deep UltraVISTA near-infrared images.*

4.1. INTRODUCTION

Over the past decade, deep near-/mid-infrared galaxy surveys have been used to study galaxy evolution up to high redshifts with ever increasing statistics (e.g., Laigle et al. 2016; Deshmukh et al. 2018; Weaver et al. 2022). A number of these galaxy surveys have been conducted with the Infrared Array Camera (IRAC; Fazio et al. 2004) on board the *Spitzer Space Telescope* (Werner et al. 2004), in different cosmological fields (e.g., Ashby et al. 2015, 2018). Other galaxy surveys have been carried out from the ground at near-infrared wavelengths, with infrared telescopes such as the VISTA telescope (e.g. McCracken et al. 2012; Jarvis et al. 2013). A key factor to make these galaxy surveys successful has been the availability of ancillary photometry of matching depth at optical wavelengths, either from the *Hubble Space Telescope* (HST) or ground-based telescopes. This multi-wavelength coverage allow for properly constraining the galaxy spectral energy distribution (SED) properties and particularly deriving secure photometric redshifts.

Not all infrared galaxies are detected at optical wavelengths, though, even when deep images are available (for recent studies on this population, see e.g., Barrufet et al. 2023; Pérez-González et al. 2023; Smail et al. 2023). Some galaxies can be relatively bright in the Spitzer mid-infrared images ($\lambda > 3\,\mu$m), but faint even at near-infrared ($\lambda = 1-3\,\mu$m) wavelengths. A number of studies have been devoted to study the nature of these very red sources. They concluded that these galaxies are mostly at $z = 3-6$, with a subset of candidates for higher redshifts (e.g., Caputi et al. 2012; Wang et al. 2019). Although a minority amongst all high-redshift galaxies, mid-infrared-bright, near-infrared-faint galaxies account for a half of the most massive galaxies at $z = 4-6$ (Caputi et al. 2015). From their follow up at sub-/millimeter wavelengths, some of these galaxies have been found to be dusty star-forming galaxies (Ikarashi et al. 2017; Shu et al. 2022; Smail et al. 2023; Zavala et al. 2023), which contribute significantly more to the cosmic star-formation-rate density than equally massive UV-bright galaxies at $z > 3$ (Zavala et al. 2021).

More difficult to constrain are the small percentage of Spitzer sources for which no counterpart at all has been found in deep near-infrared images. The advent of the *James Webb Space Telescope* (JWST) allows us now to investigate the nature of these sources by providing, for the first time, ultra-deep multi-wavelength coverage at infrared wavelengths. Recent results have shown that in these red sources with have no optical counterparts, the enhanced mid-infrared with respect to near-infrared flux is explained by a combination of factors, typically high dust extinction combined with an intermediate/high redshift (Barrufet et al. 2023; Pérez-González et al. 2023).

Previous to the launch of the JWST, it has been demonstrated how the presence of emission lines can also potentially produce such red colours, although only a few cases of this kind have been found to date (Alcalde Pampliega et al. 2019). Indeed emission lines can produce a significant enhancement even in broad-band fluxes if their equivalent widths are sufficiently high. This is particularly the case for Hα (λ6563 Å). A number of works have successfully exploited the Spitzer/IRAC images to identify intense Hα-emitters at $z \approx 4$–5 from flux excess in the IRAC 3.6 μm band (Smit et al. 2016; Caputi et al. 2017; Faisst et al. 2019), with rest-frame equivalent widths (EW_0) ranging from ~ 100–10000 Å. These studies are biased towards galaxies well detected in the near-infrared, as good constraints on the continuum bluewards of the 3.6μm band are necessary to identify any flux excess. No particular connection between line emitters and dropout galaxies has been derived from these studies.

In this work, we exploit the JWST/NIRCam imaging in the PRIMER survey together with ancillary HST/ACS and HST/WFC3 imaging, to follow up IRAC-selected galaxies from the Spitzer Matching survey of the UltraVISTA ultra-deep Stripes (SMUVS) (Ashby et al. 2018) that are undetected in the UltraVISTA DR5 H- and K_s bands. The improved depth and wavelength coverage of the new JWST data enables us to reveal the true nature of these so far elusive galaxies.

This paper is organized as follows. In Sect. 4.2 we describe the ground- and space-based imaging used in this work, and Sect. 4.3 describes our initial selection of dropout candidates. In Sect. 4.4, we describe the derived HST and JWST aperture photometry for the JWST-detected counterparts of the dropout candidates. In Sect. 4.5.1, we describe the subsequent SED fitting of our sample, and present their general properties. In Sect. 4.5.2 we present our results on the Hα line-complex equivalent widths and SFRs. Finally, in Sect. 4.6 we summarize our findings and discuss our conclusions. We adopt a cosmology with $H_0 = 70$ km s^{-1} Mpc^{-1}, $\Omega_m = 0.3$, and $\Omega_\Lambda = 0.7$. All magnitudes and fluxes are total, with magnitudes referring to the AB system (Oke & Gunn 1983). Stellar masses correspond to a Chabrier (2003) initial mass function (IMF).

4.2. DATA

4.2.1. GROUND-BASED AND SPITZER/IRAC IMAGING

Our initial search for $H-$ and K_s-band dropout galaxies is based on the UltraVISTA VIRCAM imaging (McCracken et al. 2012) and Spitzer (Werner et al. 2004) IRAC (Fazio et al. 2004) 3.6 and 4.5 μm imaging from the SMUVS program (Ashby et al. 2018) in the COSMOS field (Scoville et al. 2007).

The UltraVISTA data considered in this work correspond to the fifth data release (DR5), which contain ultra-deep imaging in three stripes on the sky taken with the VIRCAM instrument on the VISTA telescope. Over the considered PRIMER region in this work, the data reach average 5σ depths of ~ 26–27 mag in the Y, J, H, K_s and $NB118$ bands. We performed source extraction on these data ourselves as described in Sect. 4.3.

The SMUVS program conducted observations to map three UltraVISTA ultra-deep stripes, over a total area of 0.66 deg^2. We make use of the existing IRAC 3.6 and 4.5 μm catalog from Ashby et al. (2018). Source detection and aperture photometry measurements for this catalog were conducted using point spread function (PSF)-fitting techniques implemented with STARFINDER (Diolaiti et al. 2000). Source positions were identified on both IRAC mosaics separately, and subsequently combined into a single two-band catalog using a $1''$ matching radius, whilst retaining single-detected sources as well for completeness. Finally, the catalog contains a total of ~ 350 000 galaxies down to 4σ limits of roughly 25.0 AB mag in both IRAC bands. Over the PRIMER area, the IRAC data reach average 5σ depths of ~ 26 mag.

4.2.2. HST AND JWST IMAGING

In this work, we made use of archival HST and newly obtained JWST imaging to uncover the true nature of potential HK_s-dropout galaxies. We have used the JWST/NIRCam data collected during the recent GO Cycle 1 program PRIMER (PID: 1837; PI: James Dunlop). PRIMER observations are conducted in eight NIRCam broad and medium bands, - F090W, F115W, F150W, F200W, F277W, F356W, F410M, and F444W, and two MIRI bands, i.e. F770W and F1800W, over two CANDELS legacy fields (Grogin et al. 2011; Koekemoer et al. 2011) in COSMOS and UDS (Lawrence et al. 2007; Cirasuolo et al. 2007). Here, we consider all observations of target COSMOS-2 , the first-released subsection of the full PRIMER target area, taken up until January 6 2023, with a total integration time of 36.1 hours covering an area of ~94 square arcminutes. We did not utilize the available MIRI data as they are offset from the NIRCam data, nor did we use NIRCam/F150W-band imaging as it had not been taken yet.

We have processed the *JWST*/NIRCam data in the following way. First, we retrieved the level-2 data products from the MAST archive [1] and processed them with the GRIZLI pipeline (version 1.7.7; Brammer 2023). We took particular care when introducing additional corrections for the NIRCam photometric zeropoints relative to the Calibration Reference Data System pipeline mapping (CRDS; pmap) 1041, including variations across the detector itself (Brammer 2022). These were found to be consistent with the efforts by other groups (Boyer et al. 2022; Nardiello et al. 2022). We additionally introduce corrections and masking to account for the detrimental effect of the cosmic rays and stray light in the detector (see Bradley et al. 2022). More detailed descriptions of this procedure are presented in Kokorev et al. (2023) and Valentino et al. (2023), and will be further expanded upon in Brammer et al. (in prep.).

We supplement the JWST observations with the available HST optical and near-infrared data available in the Complete *Hubble* Archive for Galaxy Evolution (CHArGE; Kokorev et al. 2022). These data include imaging in the HST/WFC3 F125W, F140W, F160W, and HST/ACS F435W, F606W, F814W bands. We do not include the available data in WFC3/F105W and ACS/F475W bands as these cover only a small fraction of the PRIMER region. All available JWST and HST exposures were aligned to the Gaia DR3 (Gaia Collaboration et al. 2023) astrometry, co-added, and drizzled (Fruchter & Hook 2002) onto two sets of grids. We used $0\farcs02$ pixel scale for the Short Wavelength (SW) NIRCam bands and $0\farcs04$ for all the remaining JWST and HST filters. For comparison, the Full Width at Half Maximum (FWHM) of the NIRCAM PSF adopted in this work is $0\farcs03$ in the F090W band.

The depth in each band considered throughout this work is shown in Fig. 4.1, measured from 2" empty apertures in the field.

4.3. INITIAL SAMPLE SELECTION FROM IRAC AND VIRCAM IMAGING

Our analysis is based on a selection of IRAC-detected sources in the PRIMER region that are undetected in the UltraVISTA DR5 VIRCAM H- and/or K_s-band images.

---

[1] Data available at 10.17909/bysp-ds64

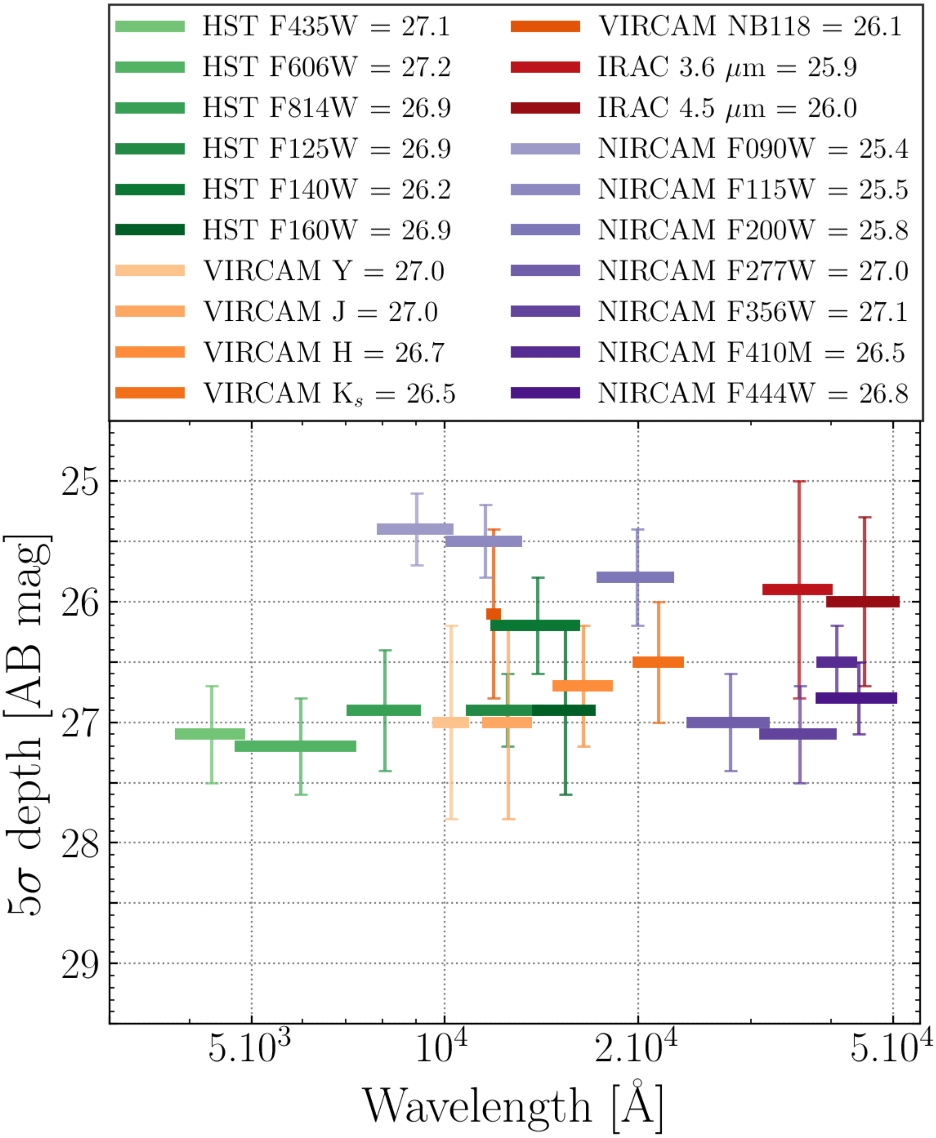

Figure 4.1 | Depth (5σ) and associated uncertainty in each filter considered throughout this work, measured as the median and standard deviation of the local background in 30 by 30$''$ regions over the PRIMER field respectively. In each region, the local background is the standard deviation of the flux measurement in empty 2$''$ circular diameter apertures. The horizontal width of each datapoint indicates the Full Width at Half Maximum (FWHM) for the filter.

We created from scratch an initial UltraVISTA DR5 catalog to cross-match with the IRAC combined 3.6 and 4.5 μm catalog from Ashby et al. (2018). We performed source detection on the UltraVISTA H- and $K_{\rm S}$-band DR5 images separately using SOURCEEXTRACTOR (Bertin & Arnouts 1996). We adopted a 1.5σ detection threshold over 5 contiguous pixels. We used SOURCEEXTRACTOR in dual-image mode to measure supporting Y, J, and NB118 fluxes at the locations of the H- and $K_{\rm S}$-detected sources. To ensure we catch all the light for the flux measurements, we extracted both the SOURCEEXTRACTOR 'mag_auto' and the aperture magnitude measured from 2$''$ apertures. Subsequently, for each band individually, we chose between these those flux measurements based on the local 10σ depth, such that we favour aperture fluxes for faint sources. The UltraVISTA images are not PSF-matched, but this poses no concern as we derive aperture flux corrections for each filter separately from the curve-of-growth of bright stars in the field. We applied corrections for galactic dust extinction using the Schlafly & Finkbeiner (2011) dust maps with the Fitzpatrick (1999) reddening law.

In total, the PRIMER region as considered in this work contains 11 651 and 10 633 H- and $K_{\rm S}$-detected sources respectively, and 7057 IRAC-detected galaxies from the Ashby et al. (2018) catalog. We cross-matched all UltraVISTA sources that have $> 2\sigma$ flux detections in the Y, J, H, $K_{\rm S}$, and NB118 bands with the IRAC galaxies within a 1$''$ search radius. We kept all IRAC sources that are unmatched with any UltraVISTA source within this search radius, yielding 1441 potential $K_{\rm S}$-dropout candidates and 148 potential H-dropout candidates.

We proceeded to carefully inspect these candidates through various measures. First, we used the JWST/NIRCam F444W imaging to check the validity of the IRAC sources, as any IRAC source is expected to be visible in these data of superior depth and resolution. We identified the JWST sources by running SOURCEEXTRACTOR on the F444W image with a detection threshold of 1.5σ over 3 contiguous pixels and a `gauss_3.0_3x3.conv` convolution mask. The IRAC sources were cross-matched with the F444W-detected sources in a 1$''$ search radius, and any IRAC source with no JWST source located in its aperture was removed from the sample, that being 32 and 3 % of the initial $K_{\rm S}$- and H-dropout candidate samples respectively. From visual inspection, we determined that 93 % of these removed candidates are falsely-detected residuals of bright IRAC galaxies.

Our second check was to cross-match the dropout candidates with the HSC bright star masks (Aihara et al. 2022) and Gaia DR3 star catalog (Gaia Collaboration et al. 2023). Any IRAC source located within the HSC masks or within a 3$''$ radius of a Gaia source was removed from the sample, that being 16 and 41 % of the initial $K_{\rm S}$- and H-dropout candidate samples respectively. This was done to avoid flux contamination from the bright, nearby star due to the broad IRAC PSF.

For our third and final check, we removed any dropout candidate that has significant UltraVISTA fluxes. For example, an intrinsically faint galaxy with strong emission lines may be undetected in the $K_{\rm S}$ image, but be perfectly visible in the Y or J band. To measure the VIRCAM fluxes of the dropout candidates, we performed forced aperture photometry on the VIRCAM images at the IRAC positions, using the PYTHON modules ASTROPY (version 5.0.4; Astropy Collaboration et al. 2022) and PHOTUTILS (version 1.4.1; Bradley et al. 2022), as contrary to SOURCEEXTRACTOR, one can directly supply a list of source locations to these software. The photometry was measured on the Y, J, H, $K_{\rm S}$, and

NB118 bands in 2″ apertures. We derived the flux errors as the standard deviation of the 3σ-clipped (five iterations) background flux distribution, measured from empty apertures placed over a 10 by 10″ region around the source. We required a minimum error of 0.1 magnitude error, corrected the fluxes to total, and applied galactic extinction corrections.

In principle, we discarded all K_s-dropout candidates that have $> 2\sigma$ flux measurements in any of the Y, J, H, K_s, and NB118 bands. Similarly, we considered the Y, J, H, and NB118 flux measurements for the H-dropout candidates. However, we carefully visually inspected every dropout candidates discarded by this measure, as the flux errors can be affected by a crowded background, and decided to keep 4 K_s- 4 and H-dropout candidates in our final dropout candidate sample for this reason. Moreover, upon visual inspection of the dropout candidates with no significant VIRCAM fluxes, we find that between both the K_s- and $H-$ dropout candidates, roughly a third are IRAC residual detections. These detections survived our earlier checks, because they coincidentally match with a very faint F444W-detected source. However, the focus of our work are isolated IRAC galaxies with a direct correspondence to a JWST-detected source, so that we discard these residual detections from the final sample. In addition, we discarded another ~ 20 % of the galaxies with no significant VIRCAM flux measurements because we visually confirmed the presence of a convincing source in these bands, and another 10 % because the VIRCAM and IRAC imaging are highly contaminated by the presence of a nearby bright source.

After implementing the above-mentioned checks, our final sample consists of 18 and 8 K_s- and H-band dropout candidates respectively. This amounts to 0.4 % of all IRAC-detected sources in PRIMER from the Ashby et al. (2018) catalog. The IRAC magnitudes of the final dropouts range between 23.1-27.0 mag, with the signal-to-noise ratio (SNR) varying between 3.5 and 10.9. For comparison, considering all IRAC-detected sources over the PRIMER field, the median 3.6 and 4.5 μm magnitudes are 23.6 and 23.7 with typical SNRs of ~ 40.

4.4. HST AND JWST PHOTOMETRY OF THE DROPOUT CANDIDATES

Now that we have selected a sample of apparent dropout galaxies from VIRCAM and IRAC data, we turn to the JWST and HST imaging to study these sources in detail.

Given the superior resolution of the JWST imaging, instead of using the IRAC priors to measure the NIRCam aperture photometry, we detected sources directly on the F277W/F356W/F444W stacked image using SOURCEEXTRACTOR. Similar to the extraction of sources on the singular F444W image in the previous section, we required a detection threshold of 1.5σ over 3 contiguous pixels and convolved the data with a `gauss_3.0_3x3.conv` mask. In addition, we performed identical runs on the F200W and F277W images alone, as some of the dropout candidates suffer from source blending in the longest wavelength JWST channels. We cross-matched our JWST-detected sources with the IRAC positions of the dropout candidates, and retained all within a 1″ radius of the candidates, i.e., all that would fall within the IRAC 2″ apertures adopted throughout this work. In 11 out of the 26 UltraVISTA dropout candidates, the JWST imaging shows multiple counterparts. For each counterpart, we measure the HST and *JWST* apertures fluxes individually. In total, the cross-matching with the IRAC priors yields 51 JWST-detected galaxies.

To measure the HST and JWST photometry of the cross-matched galaxies, we again performed forced aperture photometry with ASTROPY and PHOTUTILS. We emphasize that we did not create a fully realized JWST-detected source catalog over the PRIMER field for this study. We measured fluxes in both $0.''5$ and $1''$ diameter circular apertures at the positions of the JWST-detected sources on the following 13 optical and near-infrared bands, that together span the wavelength range 0.4–4.4 μm: JWST/NIRCAM F090W, F115W, F200W, F277W, F356W, F410M, F444W, and HST/WFC3 F125W, F140W, F160W, and HST/ACS F435W, F606W, F814W. We decided between the $0.''5$ and $1''$ diameter apertures on a source-by-source basis from careful visual inspection of the NIRCam images. Similar to the routine described in the previous section, we derived the flux errors as the standard deviation of the 3σ-clipped (five iterations) background flux distribution, measured from empty apertures placed over a 10 by 10" region around the source. We required a minimum error of 0.05 magnitude error for both the HST and JWST photometry. Assuming a point-source morphology, the HST aperture fluxes were corrected to total using the median curve-of-growth of stars in the field. Aperture corrections for the JWST fluxes were estimated using the WEBBPSF [2] software instead, as virtually all stars in PRIMER-COSMOS are saturated in the NIRCam imaging. We applied corrections for galactic dust extinction. In bands with non-detections, we adopted 3σ flux upper limits derived from the empty aperture fluxes.

4.5. RESULTS

4.5.1. SED FITTING BASED ON *HST* AND *JWST* PHOTOMETRY

In this section, we describe how we derived redshifts and physical parameters based on the HST and JWST photometry of the 26 dropout candidates. To ensure the validity of the photometric redshifts for these sources, we ran three separate redshifts codes: LEPHARE, EAZY, and PROSPECTOR. The latter two codes are strictly used to verify the redshift results produced by LEPHARE. We describe the routines adopted for the three codes in the following paragraphs.

First, the χ^2-fitting algorithm LEPHARE (Arnouts et al. 1999; Ilbert et al. 2006) uses a set of galaxy templates created from stellar population synthesis to find the best-fit galaxy solution to the observed photometry using a χ^2-minimisation technique, thereby deriving the physical parameters of the observed source. The galaxy models adopted in this work were sampled from the GALAXEV library (Bruzual & Charlot 2003), which consists of evolutionary stellar population synthesis models constructed with isochrones and a collection of theoretical and (semi-)empirical stellar spectra.

To compile our galaxy models, we adopt different star formation histories (SFHs): a single stellar population and two parametric SFHs, i.e. the star formation rate (SFR) is an analytical function of time. For the latter, we adopted an exponentially declining SFH

---

[2] WebbPSF is available at `https://webbpsf.readthedocs.io/en/latest/`

(SFR $\propto$ $e^{-t/\tau}$) and a delayed exponentially declining (SFR $\propto$ $te^{-t/\tau}$), using the range of star formation timescales $\tau = 0.01, 0.1, 0.3, 1.0, 3.0, 5.0, 10.0$, and 15 Gyr. We considered two metallicities: solar ($Z = Z_{\odot}$) and sub-solar ($Z = 0.2Z_{\odot}$). This results in 36 different combinations of SFH and metallicity for our considered SED models.

For dust attenuation, we adopted the Calzetti et al. (2000) reddening law and left the color excess as a free parameter between $E(B-V) = 0$ and 1, with a step of 0.1. For the galaxy ages, we adopted a grid of values spanning 0.01–13.5 Gyr. We applied emission lines to the galaxy templates using LePhare, which are modelled using scaling relations from Kennicutt (1998) between the UV luminosity and [OII] line. In this treatment, the following emission lines are considered with individual ratios compared to the O[II] line: Lyα, Hα, Hβ, [OIII], and O[II] (λ4959, λ5007 Å). The intensity of the lines is scaled with the intrinsic UV luminosity of the galaxy. We refer the reader to (Ilbert et al. 2009) for a detailed description of the emission line implementation in LePhare. Absorption of emission at wavelengths shorter than rest-frame 912 Å by the intergalactic medium (IGM) was implemented following Madau (1995). Finally, any templates that produce fluxes exceeding the 3σ flux upper limits in non-detected bands are rejected by LePhare.

If our candidates drop out of the UltraVISTA bands because these sample the Lyman break, the sources could be at redshifts as high as $z \sim 17$. Therefore, we performed two runs with different redshift ranges: one spanning $z = 0$–9 and one extending to $z = 17$. Similarly, the dropout nature could be caused by extreme dust reddening, such that we ran one additional SED fit with $z = 0$–9 but $E(B-V)$ extending to 1.5. We subsequently compared the reduced χ^2 of the three fits for each source, where we adopt the results from the run that yields the smallest χ^2_{ν} value. We adopted this approach in an effort to mitigate the effects of photometric redshifts degeneracy, which red galaxies are particularly prone to.

Second, we used the Python version of EAZY (Brammer et al. 2008). EAZY employs a set of non-negative linear combinations of basic templates constructed with the Flexible Stellar Population Synthesis models (FSPS; Conroy et al. 2009; Conroy & Gunn 2010). Specifically, this analysis used the corr_sfhz_13 subset of models. These contain redshift-dependent SFHs, which at a given redshift are restricted by the age of the Universe. In addition, the maximum allowed dust attenuation is tied to a given epoch. We also included the best-fit template to the JWST-observed extreme emission line galaxy at $z = 8.5$ (ID4590) from Carnall et al. (2022), which was re-normalized in alignment with the FSPS models. This was done in order to model potentially large equivalent width emission lines.

We adopted the EAZY template error function, to accommodate additional uncertainty related to unusual stellar populations, using the default value of 0.2 for the template error. We considered a redshift range of $z = 0.01$–17 for this run. Because EAZY does not allow for the same treatment of non-detected bands as LePhare, we instead adopted the 1σ flux upper limit as a flux measurement for the non-detected bands in the fitting process.

Lastly, we made use of the Bayesian inference code `Prospector` (Johnson et al. 2021). Similarly to EAZY, its stellar population models are based on the FSPS code, but Prospector rather builds the galaxy SED models on the fly using the Python-FSPS bindings. Prospector is well-known for its ability to model complex, non-parametric SFHs (see e.g. Leja et al. 2017; Tacchella et al. 2022). However, given that our intend is to generate a photometric redshift with PROSPECTOR in order to verify our LEPHARE results, we stick to a simple delayed exponentially declining parametric SFH.

The parametric model involves seven free parameters, for which we chose broad priors comparable to the LEPHARE run. For each parameter, we used the default prior shapes with the following ranges: the redshift $z = 0$–17, the formed stellar mass $M_* = 10^6$–$10^{12}\,M_\odot$, the metallicity $\log(Z/Z_\odot) = -2$–0.19, the e-folding time $\tau_{\rm SF} = 0.001$–15 Gyr, and the age $t_{age} = 0.001$–13.8 Gyr. We modelled diffuse dust attenuation following Calzetti et al. (2000) with $\tau_{dust} = 0$–4. Lastly, we implemented IGM absorption following Madau (1995) and nebular emission, using the default parameters. Finally, PROSPECTOR also treats non-detections differently, such that we set the flux to zero and the flux uncertainty as the 1σ upper limit in the corresponding bands.

ONE-TO-ONE COMPARISON BETWEEN IRAC- AND JWST-DETECTED GALAXIES

In Sect. 4.5.1, we discuss the results from our SED fitting on the HST and JWST photometry of all JWST-detected galaxies that are counterparts to our 26 UltraVISTA dropout candidates. As we remind the reader, the dropout candidates cross-match with 51 JWST-detected galaxies. Therefore, for each system, the one-to-one correspondence between the IRAC- and JWST-detected galaxies varies, as we discover from the combined inspection of the JWST source detection, the LEPHARE-derived photometric redshifts, and the image cutouts of the 26 UltraVISTA dropout candidates in the HST, JWST, IRAC, and ancillary ground-based bands (VIRCAM and HSC). In the interest of clarity and structure, we therefore first discuss the sub-classification of the 26 dropout candidates before we present the photometric redshift evaluation in the next section.

The dropout image cutouts of the candidates can be found in Appendix 4.6, in Figures 4.10, 4.11, and 4.12.

First, we have checked if the UltraVISTA dropout candidates are true dropout galaxies. Following the strategy applied on the VIRCAM photometry, we checked if the JWST-detected counterparts have $> 2\sigma$ flux measurements in the HST and JWST bands blueward of the NIRCAM/F200W and WFC3/F160W bands for the $K_{\rm s}$- and H-dropout candidates respectively. We find that out of the 26 dropout candidates, 4 systems display no significant flux in these bands; 2 $K_{\rm s}$- and 2 H-band dropout candidates are true dropout galaxies.

Second, in 15 out of the 26 candidates, the superior resolution of the HST and JWST imaging compared to the IRAC data enables us to identify multiple sources residing in the 2" diameter IRAC apertures. In fact, only 11 out of 26 candidates appear as one galaxy in JWST, i.e., there is a one-to-one correspondence with the IRAC detection. The other 15 candidates are composed of multiple sources. Among these systems, 10 cases consist of a primary galaxy with one or more non-associated foreground sources contaminating the aperture photometry, boosting the flux of the primary source. We identify the primary galaxy as the brightest source in the system considering the NIRCAM/F444W flux, which coincidentally is also closest in angular separation to the IRAC source position. The contaminating sources in each system emit less than 10% of the F444W flux of the primary galaxy, which the exception of two systems. However, in these two systems, the F444W fluxes and photometric redshifts of the contaminates are significantly lower than those of the main galaxy considering the error bars, such that we can safely deem them to be not associated. By contrast, the remaining 5 candidates are systems of galaxies that are partially associated with each other. This means that multiple individual components in these systems have closely related redshifts and/or comparable F444W fluxes (i.e. $> 10\%$ of the F444W flux of the brightest galaxy in the system), so that their appearance in the IRAC aperture is either not simply the result of superposition, or their contribution to the IRAC flux cannot be dismissed. Throughout this paper, we refer to these categories as (11) secure galaxies, (10) deboosted galaxies, and (5) associated galaxies.

As mentioned before, the cross-matching with the IRAC priors yields 51 JWST-detected galaxies, although the contaminating sources of the deboosted sample are omitted from our analysis, as these low-redshift foreground galaxies are beyond the focus of our work. Therefore, the total number of JWST-detected galaxies we discuss throughout this work is 35.

EVALUATION OF THE HST- AND JWST-DERIVED PHOTOMETRIC REDSHIFTS

Now that we have explained how the UltraVISTA dropout candidates are classified in different categories based on their JWST-detected counterparts, we discuss the redshift results from the three separate SED fitting routines performed with LEPHARE, EAZY, and PROSPECTOR.

Table 4.1 shows the best-fit photometric redshifts obtained for each of the relevant 35 JWST-detected galaxies, as well as the source position, [F160W-F444W] color and size of the aperture used to measure the HST and JWST photometry. We distinguish between candidates originally identified as H- and $K_{\rm s}$-dropouts candidates by means of their ID. We note that due to the close proximity and therefore overlap in sources of systems PD-H-a-1 and PD-H-a-2, we consider them together as one system PD-H-a-1/2 throughout this work. We also group the sources in Table 4.1 by their respective classes (secure, deboosted, and associated) for clarity. The LEPHARE and EAZY photometric redshifts corresponds to the model that minimizes the χ^2_ν; for PROSPECTOR, the median of the probability distribution function of the redshift, PDF(z), is reported. In all three cases, the uncertainty on the photometric redshift correspond to the 16th and 84th percentiles.

We visualize our redshift results in Fig. 4.2, where we show for each JWST-detected galaxy the PDF(z) from PROSPECTOR, as well as the best-fit redshifts and uncertainty ranges from LEPHARE and EAZY. We also indicate the secondary redshift form LEPHARE, i.e., the competing model that minimizes the χ^2_ν second-best.

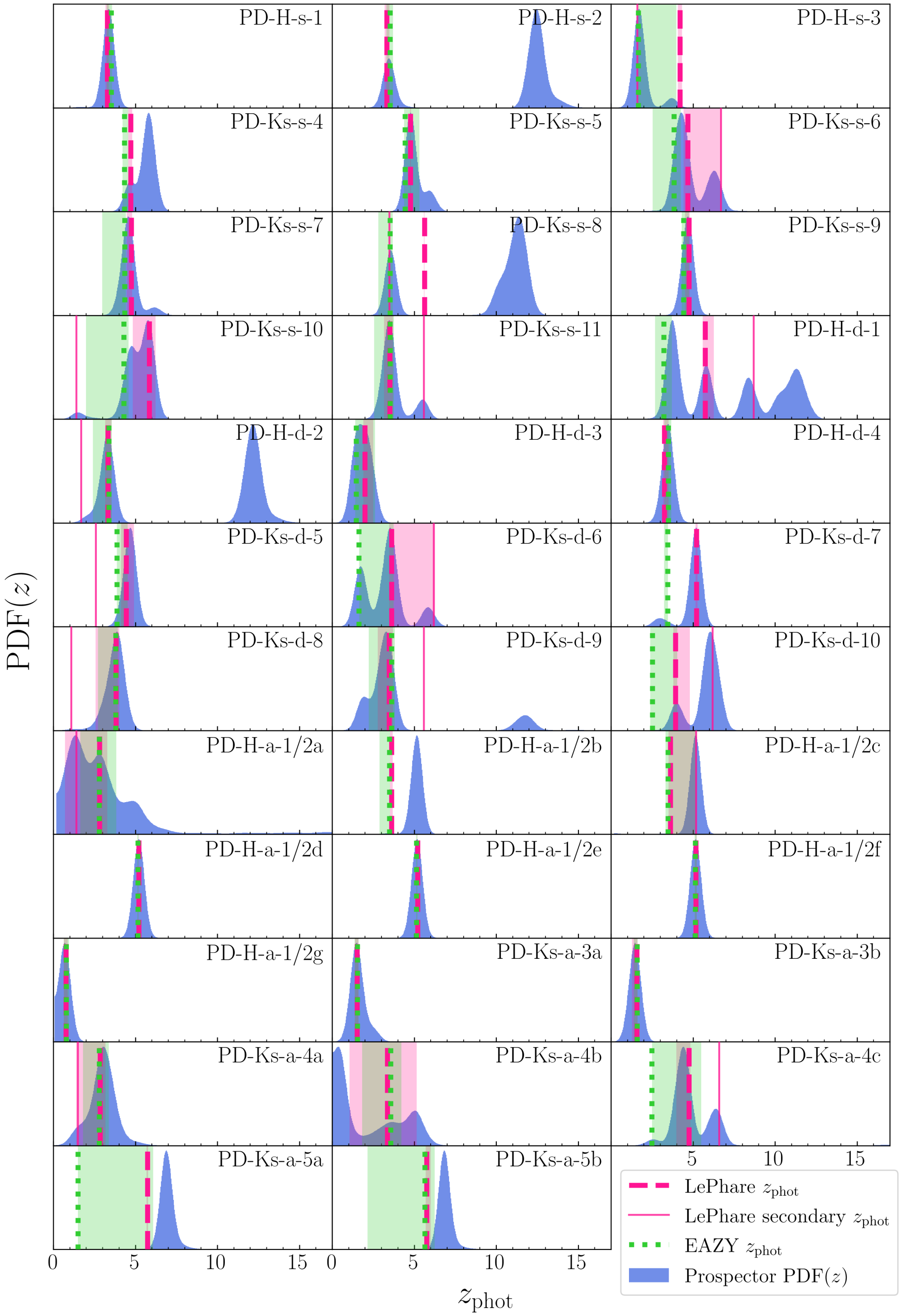

Figure 4.2 | Photometric redshift distribution of the dropout candidates derived from SED fitting the HST and JWST photometry. Each panel shows one of the 35 JWST-detected counterparts to the UltraVISTA dropout candidates considered in this work, depicting the probability density function of the redshift produced by PROSPECTOR in blue. The best-fit photometric redshift solutions from LEPHARE and EAZY are shown with pink dashed and green dotted vertical lines respectively. We also show for the LEPHARE and EAZY redshift solutions the 16th and 84th percentiles by means of correspondingly colored shaded regions. Finally, the secondary redshift from LEPHARE when available is shown in a solid pink vertical line.

Table 4.1 | Photometric redshifts of JWST-detected galaxies located within the IRAC apertures

ID		RA	Dec	[F160W-F444W]	Aperture	Photometric redshift		
				(AB mag)	"	LePhare	EAZY	Prospector
PD-H-s-1		10:00:30.42	+02:26:17.16	3.6 ± 0.2	0.5	$3.28^{+0.10}_{-0.10}$	$3.53^{+0.06}_{-0.28}$	$3.39^{+0.09}_{-0.12}$
PD-H-s-2		10:00:27.98	+02:25:29.62	3.8 ± 0.6	1.0	$3.32^{+0.17}_{-0.13}$	$3.53^{+0.18}_{-0.22}$	$12.34^{+0.38}_{-8.84}$
PD-H-s-3		10:00:47.04	+02:19:56.52	1.5 ± 0.2	0.5	$4.21^{+0.12}_{-0.13}$	$1.67^{+2.33}_{-0.01}$	$1.73^{+0.11}_{-0.09}$
PD-Ks-s-4		10:00:36.19	+02:15:50.76	2.4 ± 0.5	0.5	$4.71^{+0.09}_{-0.15}$	$4.34^{+0.22}_{-0.13}$	$5.74^{+0.26}_{-0.1.00}$
PD-Ks-s-5		10:00:33.86	+02:20:18.15	2.4 ± 0.2	0.5	$4.78^{+0.04}_{-0.02}$	$4.45^{+0.87}_{-0.07}$	$4.80^{+0.95}_{-0.06}$
PD-Ks-s-6 [b]		10:00:24.15	+02:20:05.40	4.1 ± 1.8	1.0	$4.68^{+2.03}_{-0.25}$	$3.83^{+0.42}_{-1.29}$	$4.48^{+1.78}_{-0.46}$
PD-Ks-s-7		10:00:40.80	+02:26:37.37	3.5 ± 0.8	0.5	$4.75^{+0.06}_{-0.28}$	$4.35^{+0.07}_{-1.37}$	$4.62^{+0.15}_{-0.26}$
PD-Ks-s-8		10:00:35.34	+02:28:26.63	2.9 [a]	1.0	$5.63^{+0.00}_{-0.04}$	$3.53^{+0.16}_{-0.73}$	$10.97^{+0.66}_{-7.37}$
PD-Ks-s-9		10:00:28.73	+02:16:01.25	4.9 ± 2.6	0.5	$4.75^{+0.06}_{-0.24}$	$4.42^{+0.33}_{-0.11}$	$4.71^{+0.08}_{-0.17}$
PD-Ks-s-10		10:00:48.53	+02:27:48.77	2.2 ± 0.3	0.5	$5.85^{+0.39}_{-1.00}$	$4.30^{+0.28}_{-2.32}$	$5.47^{+0.47}_{-0.90}$
PD-Ks-s-11 [b]		10:00:27.03	+02:24:24.03	3.8 ± 0.5	1.0	$3.51^{+0.19}_{-0.35}$	$3.53^{+0.23}_{-0.97}$	$3.54^{+0.90}_{-0.27}$
PD-H-d-1		10:00:41.83	+02:25:47.02	3.2 [a]	1.0	$5.73^{+0.54}_{-0.14}$	$3.23^{+0.48}_{-0.54}$	$6.00^{+5.16}_{-2.28}$
PD-H-d-2[b]		10:00:22.44	+02:23:40.99	2.9 ± 0.5	0.5	$3.32^{+0.23}_{-0.16}$	$3.39^{+0.18}_{-0.97}$	$11.74^{+0.66}_{-8.52}$
PD-H-d-3		10:00:38.31	+02:25:44.22	1.8 ± 0.2	1.0	$1.99^{+0.51}_{-0.09}$	$1.45^{+1.16}_{-0.04}$	$1.91^{+0.45}_{-0.50}$
PD-H-d-4 [b]		10:00:28.94	+02:25:05.13	6.2 ± 3.8	1.0	$3.25^{+0.26}_{-0.07}$	$3.50^{+0.18}_{-0.24}$	$3.49^{+0.12}_{-0.15}$
PD-Ks-d-5		10:00:37.48	+02:15:57.82	2.7 ± 0.7	1.0	$4.44^{+0.47}_{-0.30}$	$3.88^{+0.66}_{-0.00}$	$4.75^{+0.08}_{-0.30}$
PD-Ks-d-6		10:00:45.86	+02:22:02.26	2.0 ± 0.3	0.5	$3.62^{+2.64}_{-0.16}$	$1.63^{+2.11}_{-0.02}$	$3.43^{+0.32}_{-1.67}$
PD-Ks-d-7		10:00:31.20	+02:25:04.07	1.6 ± 0.2	1.0	$5.21^{+0.06}_{-0.06}$	$3.46^{+0.01}_{-0.22}$	$5.19^{+0.07}_{-0.12}$
PD-Ks-d-8		10:00:26.31	+02:19:38.36	0.6 ± 0.4	0.5	$3.82^{+0.20}_{-1.23}$	$3.80^{+0.12}_{-1.08}$	$3.83^{+0.34}_{-0.58}$
PD-Ks-d-9		10:00:45.96	+02:18:52.85	2.7 ± 0.4	0.5	$3.47^{+0.24}_{-0.69}$	$3.62^{+0.21}_{-1.38}$	$3.22^{+0.51}_{-1.02}$
PD-Ks-d-10		10:00:27.78	+02:25:52.04	2.9 [b]	1.0	$3.93^{+0.87}_{-0.13}$	$2.51^{+1.52}_{-0.12}$	$5.97^{+0.47}_{-1.72}$
PD-H-a-1/2	a	10:00:37.73	+02:16:55.07	0.0 ± 1.2	0.5	$2.82^{+0.48}_{-2.11}$	$2.79^{+1.04}_{-1.15}$	$2.47^{+2.14}_{-1.36}$
	b	10:00:37.78	+02:16:54.53	2.2 ± 1.1	0.5	$3.61^{+0.09}_{-0.09}$	$3.48^{+0.05}_{-0.60}$	$5.17^{+0.03}_{-0.04}$
	c	10:00:37.75	+02:16:54.42	0.7 ± 0.5	0.5	$3.61^{+1.59}_{-0.11}$	$3.47^{+1.68}_{-0.14}$	$5.16^{+0.03}_{-0.04}$
	d	10:00:37.72	+02:16:54.34	1.3 ± 0.5	0.5	$5.21^{+0.00}_{-0.02}$	$5.16^{+0.04}_{-0.03}$	$5.20^{+0.06}_{-0.04}$
	e	10:00:37.71	+02:16:54.01	2.3 ± 0.6	0.5	$5.21^{+0.00}_{-0.01}$	$5.14^{+0.05}_{-0.02}$	$5.18^{+0.03}_{-0.03}$
	f	10:00:37.69	+02:16:53.56	2.3 ± 0.2	0.5	$5.18^{+0.04}_{-0.01}$	$5.14^{+0.08}_{-0.04}$	$5.16^{+0.05}_{-0.05}$
	g	10:00:37.68	+02:16:52.74	-0.3 ± 0.4	0.5	$0.77^{+0.11}_{-0.13}$	$0.79^{+0.16}_{-0.14}$	$0.70^{+0.13}_{-0.13}$
PD-Ks-a-3	a	10:00:40.04	+02:23:16.75	-0.1 ± 0.3	0.5	$1.52^{+0.10}_{-0.13}$	$1.53^{+0.08}_{-0.17}$	$1.52^{+0.19}_{-0.18}$
	b	10:00:40.02	+02:23:16.57	0.0 ± 0.3	0.5	$1.57^{+0.05}_{-0.29}$	$1.59^{+0.04}_{-0.20}$	$1.47^{+0.13}_{-0.14}$
PD-Ks-a-4	a	10:00:45.05	+02:24:41.74	0.6 ± 0.4	0.5	$2.86^{+0.33}_{-1.46}$	$2.80^{+0.59}_{-0.98}$	$3.02^{+0.61}_{-0.76}$
	b	10:00:45.10	+02:24:41.38	0.2 ± 0.7	0.5	$3.36^{+1.81}_{-2.30}$	$3.56^{+0.66}_{-1.73}$	$1.38^{+3.55}_{-0.99}$
	c	10:00:45.07	+02:24:40.66	1.8 [a]	0.5	$4.76^{+0.09}_{-0.77}$	$2.49^{+3.02}_{-0.02}$	$4.55^{+1.76}_{-0.49}$
PD-Ks-a-5	a	10:00:31.03	+02:16:56.00	1.5 ± 0.3	0.5	$5.74^{+0.03}_{-0.05}$	$1.50^{+4.59}_{-0.01}$	$6.89^{+0.14}_{-0.10}$
	b	10:00:31.03	+02:16:55.77	2.3 ± 0.3	0.5	$5.75^{+0.27}_{-0.05}$	$5.65^{+0.59}_{-3.50}$	$6.82^{+0.09}_{-0.05}$

[a] The [F160W-F444W] color of this source is a based on a flux upper limit in F160W so it represents a lower limit on the redness of this color.

[b] This source qualifies as a true dropout galaxy, such that it has no significant flux detections in the short-wavelength HST and JWST channels.

We consider the LEPHARE best-fit redshift valid if it satisfies the criterion

$$\frac{|z - z_{\rm LePhare}|}{1 + z_{\rm LePhare}} < 0.15\,, \tag{4.1}$$

where z corresponds to either the EAZY or PROSPECTOR photometric redshift. This is the case for the vast majority of our sample, with the exception of the following four sources: PD-H-s-3, PD-Ks-s-8, PD-Ks-d-10, and PD-Ks-a-5a. Given that their photometric redshifts and therefore physical parameters are unreliable, we would discard them from any further analysis. However, PD-H-s-3 and PD-K-s-8 have secondary LEPHARE redshifts coinciding with the EAZY results, so we adopt the LEPHARE physical parameters associated with the secondary redshift solution. PD-Ks-d-10 is adjusted in a similar way, as its secondary redshift coincides with the PROSPECTOR solution. Lastly, PD-Ks-a-5a may have conflicting redshift results between the three SED fitting routines, but this is not the case for companion galaxy PD-Ks-a-5b, for which the LEPHARE redshift is backed up by the EAZY result. Given the similarity between the two sources and the large uncertainty on the EAZY redshift of PD-Ks-a-5a, we decide to keep the LEPHARE redshift for PD-Ks-a-5a. Therefore, none of the four JWST-detected galaxies with uncertain redshifts are discarded from the sample, but their LEPHARE-based physical parameters are modified accordingly.

GENERAL SED-DERIVED PROPERTIES OF THE JWST-DETECTED GALAXIES

In this section, we qualitatively analyze the physical parameters of the 35 JWST-detected counterparts to the UltraVISTA dropout candidates as derived with LEPHARE. We show the finalized LEPHARE photometric redshift distribution as discussed in the previous section in Fig. 4.3. The vast majority of our sample is located between $z = 3$–6. Moreover, the galaxies are relatively grouped in redshift space at $z \sim 3.3$, $z \sim 4.8$, and $z \sim 5.7$.

The physical parameters as determined with LEPHARE are shown in Table 4.2, including the photometric redshift, χ^2_ν, color excess, stellar mass, and age. The errors all parameters but the color excess represent the 16th and 84th percentiles. For the color excess instead, LEPHARE does not provide an error analysis for this parameter, such that we derived its uncertainty from the difference in $E(B-V)$ values between the best-fit SEDs at the lower and upper redshift error for each source. A subset of our galaxies are identified in other works, as indicated in Table 4.2; we discuss these individual sources in more detail in Sect. 4.5.2.

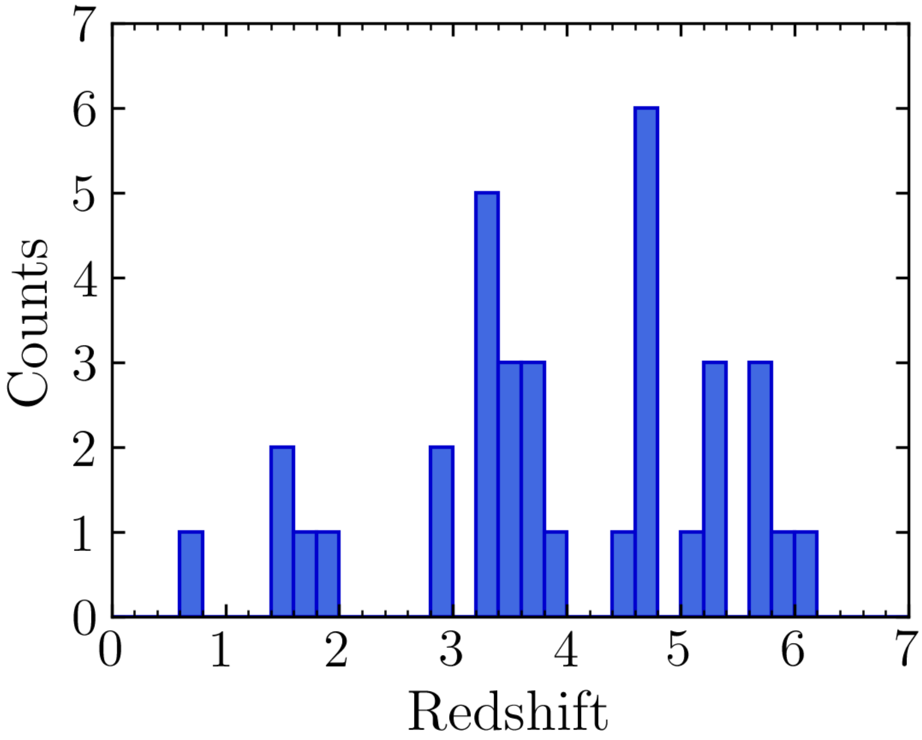

Figure 4.3 | Photometric redshift distribution of the dropout candidates derived from the LEPHARE SED fitting the HST and JWST photometry.

Table 4.2 | Physical parameters of JWST-detected galaxies located within the IRAC apertures

ID		Redshift	χ^2_ν	Color Excess $E(B-V)$	Stellar Mass ($\log[M/M_\odot]$)	Age ($\times 10^7$ yr)	F356W (AB mag)	F444W (AB mag)
PD-H-s-1		$3.28^{+0.10}_{-0.10}$	0.97	0.7 ± 0.0	$10.02^{+0.14}_{-0.18}$	$4.0^{+50.7}_{-0.0}$	24.09 ± 0.05	23.33 ± 0.05
PD-H-s-2 [a]		$3.32^{+0.17}_{-0.13}$	0.96	0.9 ± 0.0	$9.99^{+0.13}_{-0.14}$	$3.5^{+15.0}_{-0.7}$	24.07 ± 0.05	23.48 ± 0.05
PD-H-s-3 [c]		$1.61^{+0.00}_{-0.02}$	1.29	0.7 ± 0.0	$8.39^{+0.29}_{-0.08}$	$1.0^{+70.0}_{-0.0}$	25.22 ± 0.05	25.12 ± 0.05
PD-Ks-s-4		$4.71^{+0.09}_{-0.15}$	1.50	0.5 ± 0.0	$9.48^{+0.10}_{-0.09}$	$5.7^{+11.4}_{-1.2}$	25.14 ± 0.05	25.21 ± 0.05
PD-Ks-s-5		$4.78^{+0.04}_{-0.02}$	2.70	0.6 ± 0.0	$10.19^{+0.09}_{-0.10}$	$29.0^{+13.3}_{-18.6}$	24.24 ± 0.05	24.27 ± 0.05
PD-Ks-s-6 [b]		$4.68^{+2.03}_{-0.25}$	0.16	0.7 ± 0.7	$9.66^{+0.23}_{-0.28}$	$1.0^{+38.6}_{-0.0}$	24.88 ± 0.05	24.49 ± 0.05
PD-Ks-s-7		$4.75^{+0.06}_{-0.28}$	0.36	0.7 ± 0.0	$9.98^{+0.14}_{-0.15}$	$16.0^{+6.3}_{-12.4}$	24.85 ± 0.05	24.73 ± 0.05
PD-Ks-s-8 [b,c]		$3.48^{+0.23}_{-0.13}$	0.69	0.8 ± 0.1	$9.90^{+0.24}_{-0.25}$	$2.1^{+47.5}_{-0.0}$	24.40 ± 0.05	23.59 ± 0.05
PD-Ks-s-9		$4.75^{+0.06}_{-0.24}$	2.84	0.7 ± 0.0	$10.10^{+0.12}_{-0.12}$	$18.0^{+14.5}_{-12.5}$	24.56 ± 0.05	24.51 ± 0.05
PD-Ks-s-10		$5.85^{+0.39}_{-1.00}$	0.22	0.3 ± 0.1	$10.12^{+0.09}_{-0.11}$	$16.0^{+64.7}_{-0.0}$	25.01 ± 0.05	24.80 ± 0.05
PD-Ks-s-11 [b]		$3.51^{+0.19}_{-0.35}$	0.31	0.8 ± 0.1	$9.96^{+0.25}_{-0.21}$	$1.5^{+41.8}_{-0.0}$	23.92 ± 0.05	23.19 ± 0.05
PD-H-d-1 [b]		$5.73^{+0.54}_{-0.14}$	0.88	0.7 ± 0.0	$10.35^{+0.19}_{-0.18}$	$1.0^{+14.8}_{-0.0}$	24.45 ± 0.05	23.63 ± 0.05
PD-H-d-2		$3.32^{+0.23}_{-0.16}$	0.23	0.5 ± 0.0	$9.78^{+0.17}_{-0.24}$	$12.8^{+62.8}_{-7.3}$	24.78 ± 0.05	24.31 ± 0.05
PD-H-d-3		$1.99^{+0.51}_{-0.09}$	1.23	0.2 ± 0.2	$9.93^{+0.10}_{-0.24}$	$300.0^{+0.0}_{-274.6}$	24.03 ± 0.05	23.80 ± 0.05
PD-H-d-4 [b]		$3.25^{+0.26}_{-0.07}$	0.88	1.0 ± 0.0	$10.27^{+0.17}_{-0.22}$	$3.5^{+51.4}_{-1.2}$	23.77 ± 0.05	23.01 ± 0.05
PD-Ks-d-5		$4.44^{+0.47}_{-0.30}$	1.3	0.5 ± 0.1	$9.22^{+0.19}_{-0.15}$	$1.0^{+40.2}_{-0.0}$	25.33 ± 0.05	25.23 ± 0.05
PD-Ks-d-6		$3.62^{+2.64}_{-0.16}$	0.49	0.4 ± 0.1	$9.13^{+0.23}_{-0.24}$	$2.5^{+37.7.4}_{-0.0}$	25.54 ± 0.05	25.15 ± 0.05
PD-Ks-d-7		$5.21^{+0.06}_{-0.06}$	0.90	0.2 ± 0.0	$9.47^{+0.13}_{-0.13}$	$4.0^{+33.9}_{-0.0}$	25.03 ± 0.05	24.69 ± 0.05
PD-Ks-d-8		$3.82^{+0.20}_{-1.23}$	0.20	0.1 ± 0.3	$8.53^{+0.21}_{-0.26}$	$36.0^{+22.4}_{-31.2}$	26.60 ± 0.09	26.63 ± 0.13
PD-Ks-d-9		$3.47^{+0.24}_{-0.69}$	0.14	0.6 ± 0.1	$9.46^{+0.25}_{-0.22}$	$3.0^{+48.9}_{-0.0}$	25.18 ± 0.05	24.66 ± 0.05
PD-Ks-d-10 [b,c]		$6.17^{+0.11}_{-0.18}$	0.84	0.4 ± 0.0	$10.70^{+0.09}_{-0.11}$	$28.6^{+33.3}_{-19.4}$	24.26 ± 0.05	23.89 ± 0.05
PD-H-a-1/2	a	$2.82^{+0.48}_{-2.11}$	0.53	0.2 ± 0.1	$7.28^{+0.32}_{-0.31}$	$1.0^{+92.9}_{-0.0}$	28.17 ± 0.31	28.27 ± 0.47
	b	$3.61^{+0.09}_{-0.09}$	2.11	0.3 ± 0.1	$8.41^{+0.11}_{-0.08}$	$3.5^{+7.8}_{-0.8}$	26.50 ± 0.07	26.11 ± 0.06
	c	$3.61^{+1.59}_{-0.11}$	2.54	0.4 ± 0.1	$8.24^{+0.10}_{-0.10}$	$2.1^{+2.3}_{-0.6}$	27.25 ± 0.13	26.72 ± 0.13
	d	$5.21^{+0.00}_{-0.02}$	1.22	0.5 ± 0.0	$8.82^{+0.04}_{-0.04}$	$1.0^{+0.5}_{-0.0}$	26.82 ± 0.09	25.99 ± 0.06
	e	$5.21^{+0.00}_{-0.01}$	1.36	0.4 ± 0.0	$8.89^{+0.10}_{-0.08}$	$1.0^{+2.1}_{-0.0}$	26.11 ± 0.05	25.50 ± 0.05
	f	$5.18^{+0.04}_{-0.01}$	1.16	0.5 ± 0.0	$9.65^{+0.28}_{-0.14}$	$1.0^{+29.5}_{-0.0}$	24.50 ± 0.05	23.98 ± 0.05
	g	$0.77^{+0.11}_{-0.13}$	0.12	0.1 ± 0.1	$7.39^{+0.17}_{-0.22}$	$11.4^{+150.3}_{-5.5}$	26.84 ± 0.09	27.10 ± 0.19
PD-Ks-a-3	a	$1.52^{+0.10}_{-0.13}$	0.63	0.1 ± 0.1	$7.09^{+0.16}_{-0.15}$	$1.5^{+20.6}_{-0.0}$	27.37 ± 0.11	27.08 ± 0.12
	b	$1.57^{+0.05}_{-0.29}$	0.80	0.3 ± 0.3	$7.58^{+0.16}_{-0.15}$	$1.0^{+60.6}_{-0.0}$	26.91 ± 0.07	26.86 ± 0.09
PD-Ks-a-4	a	$2.86^{+0.33}_{-1.46}$	0.47	0.0 ± 0.2	$8.47^{+0.27}_{-0.33}$	$200.0^{+0.0}_{-196.1}$	26.78 ± 0.13	26.58 ± 0.17
	b	$3.36^{+1.81}_{-2.30}$	0.17	0.0 ± 0.0	$7.39^{+0.16}_{-0.15}$	$3.0^{+13.3}_{-0.6}$	28.32 ± 0.53	27.64 ± 0.42
	c	$4.76^{+0.09}_{-0.77}$	0.94	0.6 ± 0.4	$9.19^{+0.29}_{-0.23}$	$1.0^{+34.3}_{-0.0}$	25.74 ± 0.05	25.51 ± 0.07
PD-Ks-a-5	a	$5.74^{+0.03}_{-0.05}$	1.66	0.2 ± 0.0	$9.13^{+0.19}_{-0.18}$	$3.5^{+55.3}_{-0.1}$	26.25 ± 0.05	25.31 ± 0.05
	b	$5.75^{+0.27}_{-0.05}$	3.84	0.5 ± 0.0	$9.41^{+0.19}_{-0.17}$	$1.0^{+33.0}_{-0.0}$	25.82 ± 0.05	24.81 ± 0.05

a Detected at X-ray wavelengths in Chandra/XMM-Newton (Cappelluti et al. 2009; Civano et al. 2016)

b Detected at sub-mm wavelengths with ALMA/SCUBA/VLA (Liu et al. 2019; Simpson et al. 2020; Koprowski et al. 2016; Simpson et al. 2019; Smolčić et al. 2017)

c The redshift and physical parameters presented for this source are based on the second best-fit model from LEPHARE, which does agree with the redshift results from EAZY and/or PROSPECTOR.

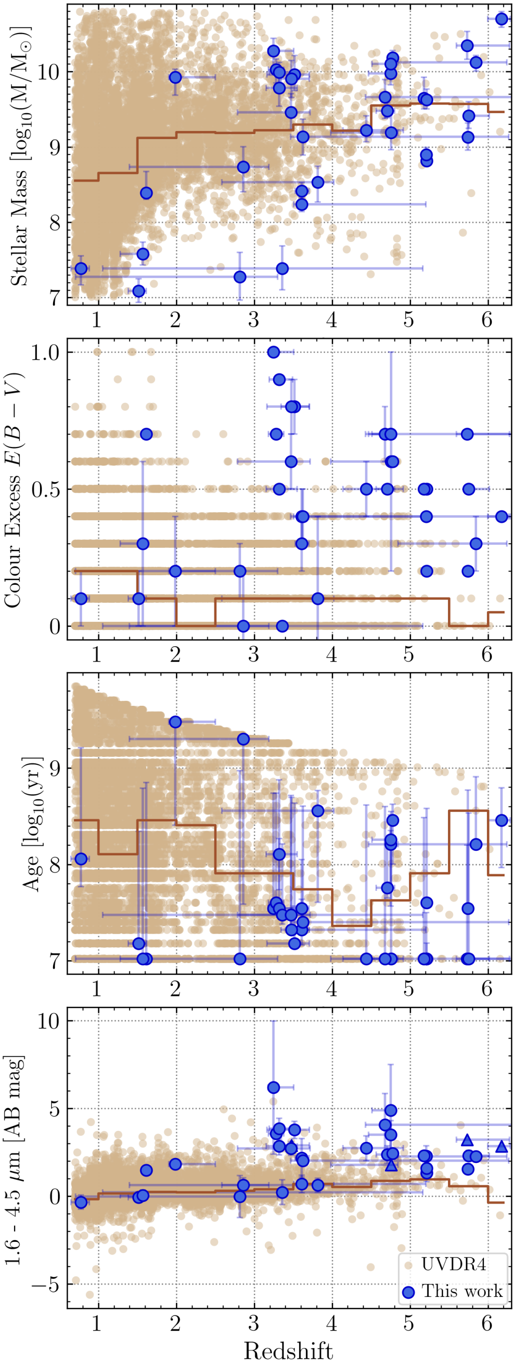

Figure 4.4 | Stellar mass, color excess, age and 1.6-4.5 μm color against redshift for our JWST-detected sample in blue. Ancillary UltraVISTA DR4 galaxies within the same redshift and mass range as the dropout candidates are shown in tan data points, with their median value derived in $dz = 0.5$ bins indicated by the brown line. The 1.6-4.5 μm color for the dropout candidates is based on the WFC3/F160W and NIRCam/F444W bands, and on the VIRCAM H and IRAC 4.5 μm bands for the ancillary sample. Upper and lower limits on the redness of this color are indicated with downwards- and upwards-pointing triangles respectively.

Fig. 4.4 shows the stellar mass, color excess, age, and observed [F160W-F444W] color against redshift for our JWST-detected sample. To put these special galaxies into the context of the general population, we compare them to the UltraVISTA DR4 catalog from van Mierlo et al. (2022). This catalog contains physical parameters for UltraVISTA HK_s-detected galaxies at $z_\mathrm{phot} = 0$–9, derived from SED fitting on multi-wavelength photometry spanning optical to IRAC imaging. To ensure a fair comparison, the catalog has been cut to the PRIMER area, such that it contains 10 272 galaxies. The UltraVISTA DR4 galaxies shown in Fig. 4.4 are matched to the redshift and stellar mass range of the JWST-detected sample, i.e. $z = 0.7$–6.2 and $\log(M_*/M_\odot) = 7.0$–10.8.

We find that ~ 70 % of our JWST-detected sample is defined as $z = 3$–6 galaxies of intermediate stellar mass $\log(M_*/M_\odot) \sim 8.2$–10.3, that have red [F160W-F444W] colors explained by their dusty nature. In fact, for the secure and deboosted samples (where there is good correspondence between the IRAC- and JWST-detected sources), 95% of the galaxies are dusty with $E(B-V) \geq 0.2$, and moreover, 71% are highly dusty with $E(B-V) \geq 0.5$. Their corresponding red colors explain straightforwardly why these sources were initially identified as dropouts in UltraVISTA imaging.

Although our sample consists mostly of these dusty intermediate-z sources, the remaining JWST-detected galaxies display a variety in behavior. For example, source PD-H-d-3, with $z = 1.99$ and $E(B-V) = 0.2$, appears to be an H-dropout galaxy in the UltraVISTA imaging. The HST and JWST photometry reveal that PD-H-d-3 is in fact not a dropout galaxy, but that its red color can be attributed to its age of 3.0 Gyr. In addition, system PD-Ks-a-3 is very different from any of the other dropout candidates we study throughout this paper (see Fig. 4.12 for the image cutouts). It is in fact the faintest IRAC source in our sample, with magnitude 27.0 (3.5σ) in the IRAC 4.5 μm band and no detection at all in the 3.6 μm band. HST and JWST imaging reveal that this IRAC source is made up out of two young galaxies at $z \sim 1.5$, that have very flat SEDs and low stellar masses of $\log(M_*/M_\odot) = 7.1$ and 7.6. To understand why this duo enters our dropout candidate sample, we search for galaxies of comparable redshift and IRAC brightness in the UltraVISTA DR4 catalog. This yields only six galaxies, all which have 3–22σ detections in the VIRCAM H, K_s and IRAC 3.6 μm bands. Given that the IRAC and VIRCAM imaging considered in this work are of comparable depths, it is unclear why PD-Ks-a-3-a and -b are absent from the VIRCAM imaging. Finally, we note the arc-like spatial alignment as seen in PD-H-a-1/2, which are two IRAC-detected galaxies at $1\farcs4$ angular separation, that both drop out in the VIRCAM H band. However, the HST and JWST imaging reveal that these two IRAC sources are in fact made up out of seven distinct galaxies that are partially spatially aligned, two of them at $z = 3.6$ and three at $z = 5.2$, although PD-H-a-1/2-c has a significant secondary solution at $z = 5.2$ too.

In the context of the general galaxy population, Fig. 4.4 clearly shows that the JWST-detected galaxies in this work are amongst the reddest and dustiest intermediate-mass sources at $z \simeq 3-6$. However, there are several UltraVISTA DR4 galaxies with similarly red colors, i.e. $[H-4.5] \gtrsim 2$, which do not drop out of the VIRCAM images, despite being of comparable brightness in the IRAC bands as our JWST-detected sample. Upon further inspection, these UltraVISTA DR4 galaxies are mostly old galaxies with ages exceeding 1 Gyr, such that given their redshift, the well-developed Balmer break is located in between the H and K_s bands, explaining their red $[H-4.5]$ color and simultaneous presence in the UltraVISTA DR4 catalog (which was detected on the stacked HK_s image). In addition, a small sample of the red UltraVISTA DR4 galaxies are dusty with $E(B-V) = 0.3$–0.7, but overall brighter than our JWST-detected galaxies (∼ 1.2 mag in the IRAC bands), such that they are just bright enough to be detected in the UltraVISTA imaging.

We show the normalized color excess distributions of our JWST-detected galaxies and the UltraVISTA DR4 galaxies in three redshift bins between $z = 3$–6 in Fig. 4.5. In each redshift bin, we find that the color excess distribution between the UltraVISTA DR4 galaxies and our sample are distinctly different, as confirmed by performing the two-sample Kolmogorov-Smirnov test (Smirnov 1939), which yields p-values $< 3 \times 10^{-3}$. The JWST-detected galaxies are consistently significantly dustier, even though Deshmukh et al. (2018) already showed that the fraction of $E(B-V) \geq 0.2$ galaxies at the epoch $z = 3$–6 is considerate at ∼ 30–40%. Especially at $z = 4$–5, all of the JWST-detected galaxies are highly dusty, with $E(B-V) \geq 0.5$. Our results imply these dust-reddened galaxies are a special population of galaxies that were not characterized by previous wide-area near-infrared surveys.

4.5.2. Hα EMISSION IN THE ULTRAVISTA DROPOUT GALAXIES

From inspection of the LEPHARE best-fit SEDs, some of the JWST-detected galaxies appear to have excess flux in bands coinciding with the (Hα+ N[II] + S[II]) line complex considering their photometric redshifts. Following Caputi et al. (2017), we set a minimum condition of $\Delta\text{mag} = \text{mag}_{\text{obs}} - \text{mag}_{\text{synth}} < -0.1$ in the band to consider the flux excess significant. Here, $\text{mag}_{\text{synth}}$ is the continuum emission in the band, which we obtain by re-modelling the SEDs with LEPHARE whilst excluding the affected band and emission line modelling, and adopting the fixed photometric redshift obtained from the original LEPHARE run (with all bands and emission lines). In addition, to ensure that flux excess is not the result of a poorly constrained continuum, we imposed the condition that $\Delta\text{mag} \leq 2 \times \text{mag}_{\text{err}}$ in at least one adjacent observed band.

For all galaxies where the Hα line coincides with one of the HST and JWST bands, we calculated the rest-frame equivalent width (EW_0) of the (Hα+ N[II] + S[II]) line following the approach outlined in Rinaldi et al. (2023) (which is in turn based on Mármol-Queraltó et al. 2016), such that

$$\text{EW}_0 = \frac{\text{W}_{\text{rec}}}{1+\text{z}}(10^{-0.4\Delta\text{mag}} - 1), \tag{4.2}$$

where W_{rec} is the FWHM of the filter containing the emission line of interest. We propagate the redshift error and the flux error into the EW_0 error. Subsequently, we converted the flux excess into an Hα emission line flux using the modelled continuum flux, such that

$$f(\text{H}\alpha + \text{N[II]} + \text{S[II]}) = 10^{-0.4\Delta\text{mag}} \times f_{\text{obs}} - f_{\text{synth}}, \tag{4.3}$$

where f_{obs} and f_{synth} are the observed and modelled fluxes respectively in the filter containing the emission line, where we again propagate the flux error. We corrected for dust extinction using the color excess from the original SED fitting and assuming a Calzetti et al. (2000) dust reddening law. Here, we assumed that the extinction is the same for both the lines and the continuum. We also propagated the error on the dust extinction, which was derived from the difference in $E(B-V)$ values between the best-fit SEDs at the

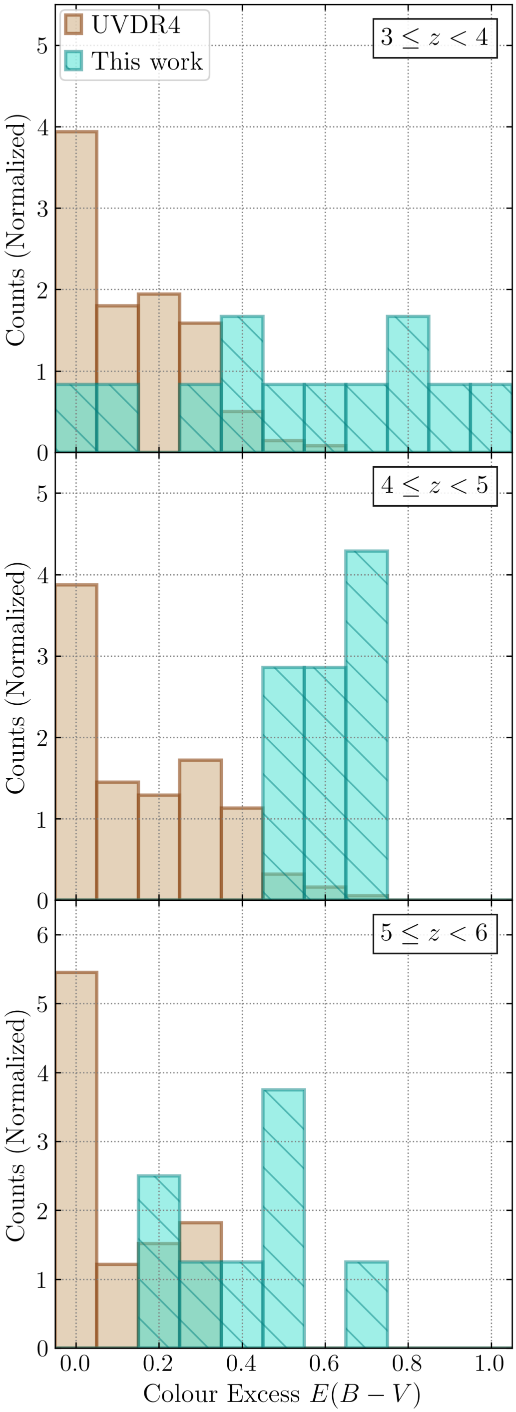

Figure 4.5 | Normalized color excess distribution of the JWST-detected galaxies in this work (turquoise) and the UltraVISTA DR4 galaxies (tan), in three redshifts bins $z = 3$–4, $z = 4$–5, and $z = 5$–6.

lower and upper redshift error for each source. We obtained the net Hα flux considering that $f(\mathrm{H}\alpha)$=0.63$f(\mathrm{H}\alpha$+N[II]+S[II]) (Anders & Fritze-v. Alvensleben 2003), and converted it to a SFR following Kennicutt (1998):

$$\mathrm{SFR(H}\alpha)(M_\odot\,\mathrm{yr}^{-1}) = 7.936 \times 10^{-42} \times L_{\mathrm{H}\alpha}(\mathrm{erg\,s}^{-1}), \tag{4.4}$$

where we divide the resulting SFRs by a factor 1.69 to re-scale them from a Salpeter (1955) IMF over (0.1–100) $M_\odot$ to a Chabrier (2003) IMF. We calculate the specific SFR (sSFR) by dividing the SFR by the stellar mass. We propagate the uncertainties on the SFR and stellar mass into a sSFR uncertainty. However, propagating the asymmetric uncertainty on the stellar mass is not trivial, such that we determine an average error on the stellar mass from its uncertainty limits and propagate that instead. Therefore, we warn the reader that the reported values on the sSFR uncertainty are only approximate.

Not all galaxies in our JWST-detected sample display flux excess at the location of the Hα line-complex; for those which do not, we calculated upper limits on their Hα properties from the minimum line-complex EW$_0$ that would produce $\Delta\mathrm{mag} = \mathrm{mag_{obs}} - \mathrm{mag_{synth}} = -0.1$ in the band containing the emission line-complex. Only for source PD-H-s-3 are we unable to calculate information on the Hα emission; due to its redshift, the line does not fall into any of the HST and *JWST* filters considered in this study.

Table 4.3 | Hα EW$_0$, L and SFR of JWST-detected galaxies located within the IRAC apertures, including upper limits for sources that display no flux excess.

ID		Redshift	Band	(Hα+ N[II] + S[II]) EW$_0$ (Å)	$L_{\mathrm{H}\alpha}$ (10^{42} erg s^{-1})	SFR ($M_\odot$yr^{-1})	sSFR (log(yr^{-1}))
PD-H-s-1		3.28	F277W	326^{+15}_{-15}	3.2 ± 0.1	15 ± 6	-8.8 ± 0.2
PD-H-s-2 [a]		3.32	F277W	722^{+34}_{-32}	3.8 ± 0.2	-	-
PD-H-s-3 [d]		1.61	-	-	-	-	-
PD-Ks-s-4		4.71	F356W	667^{+32}_{-30}	13.9 ± 0.6	65 ± 27	-7.7 ± 0.2
PD-Ks-s-5		4.78	F356W	617^{+29}_{-28}	23.2 ± 1.1	109 ± 46	-8.1 ± 0.2
PD-Ks-s-6		4.68	F356W	622^{+30}_{-21}	9.0 ± 2.8	42 ± 25	-8.0 ± 0.4
PD-Ks-s-7		4.75	F356W	594^{+29}_{-27}	9.4 ± 0.4	44 ± 18	-8.3 ± 0.2
PD-Ks-s-8		3.48	F277W	395^{+19}_{-17}	2.0 ± 0.6	9 ± 5	-8.9 ± 0.4
PD-Ks-s-9		4.75	F356W	538^{+26}_{-25}	11.4 ± 0.5	54 ± 22	-8.4 ± 0.2
PD-Ks-s-10 [b]		5.85	F444W	155	18.6	87	-8.2
PD-Ks-s-11		3.51	F277W	653^{+33}_{-29}	4.7 ± 1.5	22 ± 13	-8.6 ± 0.3
PD-H-d-1		5.73	F444W	400^{+19}_{-17}	30.4 ± 1.4	143 ± 59	-8.2 ± 0.3
PD-H-d-2 [b]		3.32	F277W	158	1.7	8	-8.9
PD-H-d-3 [b]		1.99	F200W	229	2.7	13	-8.8
PD-H-d-4		3.25	F277W	437^{+20}_{-19}	1.8 ± 0.1	8 ± 3	-9.4 ± 0.3
PD-Ks-d-5		4.44	F356W	358^{+17}_{-15}	6.2 ± 1.9	29 ± 17	-7.8 ± 0.3
PD-Ks-d-6		3.62	F277W	311^{+17}_{-11}	3.1 ± 0.9	14 ± 9	-8.0 ± 0.4
PD-Ks-d-7		5.23	F410M	484^{+26}_{-25}	74.2 ± 3.9	349 ± 146	-6.9 ± 0.2
PD-Ks-d-8 [b]		3.82	F356W	169	2.1	10	-7.5
PD-Ks-d-9 [b]		3.47	F277W	153	0.9	4	-8.8
PD-Ks-d-10		6.17	F444W	318^{+15}_{-14}	62.2 ± 2.9	292 ± 122	-8.2 ± 0.2
PD-H-a-1/2	a	2.82	F277W	1602^{+675}_{-268}	1.4 ± 0.5	7 ± 4	-6.5 ± 0.4
	b	3.61	F277W	1091^{+51}_{-49}	7.7 ± 2.4	36 ± 21	-6.9 ± 0.3
	c [c]	3.61	F277W	2169^{+147}_{-105}	5.4 ± 1.7	26 ± 15	-6.8 ± 0.3
	d	5.21	F410M	1171^{+64}_{-64}	23.9 ± 1.3	112 ± 47	-6.8 ± 0.2
	e	5.21	F410M	811^{+37}_{-37}	39.6 ± 1.8	186 ± 77	-6.6 ± 0.2
	f	5.18	F410M	515^{+24}_{-24}	79.8 ± 3.7	375 ± 156	-7.1 ± 0.3
	g [b]	0.77	F115W	460	0.04	0.2	-8.1
PD-Ks-a-3	a	1.52	F160W	115	0.2	0.8	-7.2
	b [b]	1.57	F160W	113	0.1	0.6	-7.8
PD-Ks-a-4	a	2.86	F277W	355^{+72}_{-41}	2.4 ± 1.5	11 ± 12	-7.7 ± 0.5
	b [b]	3.36	F277W	157	0.6	3	-7.0
	c	4.76	F356W	446^{+24}_{-20}	4.5 ± 5.6	21 ± 55	-7.9 ± 1.1
PD-Ks-a-5	a	5.74	F444W	1641^{+76}_{-75}	76.9 ± 3.5	361 ± 151	-6.6 ± 0.3
	b	5.75	F444W	1577^{+73}_{-70}	50.0 ± 2.2	225 ± 94	-7.1 ± 0.3

a This source is likely an AGN because of ancillary X-ray emission, such that the SFR conversion from Kennicutt (1998) is not applicable.

b No flux excess in the band where the Hα line should be observed for this source. The EW_0, $L_{\mathrm{H}\alpha}$ and SFR are upper limits assuming Δmag = 0.1.

c This source has poorly constrained continuum in bands F356W and F410M, and a significant secondary solution at $z = 5.2$, such that the Hα properties listed are uncertain at best.

d Due to its redshift, the Hα emission line falls outside any of the bands considered in this work, such that estimating its flux excess is not possible.

Table 4.3 lists the (Hα+ N[II] + S[II]) EW$_0$, the Hα luminosity and derived SFR for each JWST-detected counterpart to the UltraVISTA dropout candidates, including the upper limits for the sources which show no flux excess. We also list the band in which the flux excess is observed, and the specific star formation rate (sSFR). For this and any further plots involving the stellar mass, we consider the stellar mass as reported in Table 4.4, i.e., derived from the original SED fitting with emission lines and the filter containing the Hα line. In total, we identify Hα-emitters from the HST and JWST photometry amongst 19 of the 26 IRAC-selected dropout candidates, such that ~ 75 % of the sources that enter our original dropout candidate selection are boosted redwards of K_s band due to the presence of Hα line-complex emission.

Fig. 4.6 shows the derived (Hα+ N[II] + S[II]) EW$_0$ versus stellar mass for our JWST-detected sample. We exclude here and from any further plots the sources PD-H-s-2 and PD-H-a-1/2 c; the former because its detection at X-ray wavelengths means it is most likely an AGN, such that the SFR conversion from Kennicutt (1998) cannot be applied. The latter we exclude as both its redshift and the continuum in the bands redwards to the Hα line-complex are poorly constrained, such that its listed Hα properties in Table 4.3 are uncertain at best. We highlight in our plots three sources that are detected at sub-/millimeter wavelengths and are all Hα emitters, namely PD-Ks-s-6, PD-Ks-s-8, and PD-H-d-1, which we discuss further in Sect. 4.5.2. The rest-frame EWs span values between ~ 100–2200 Å. We find a general decline in the median EW$_0$ values with stellar mass: they are ~ 950 Å for galaxies with $\log(M_*/M_\odot) = 8.0$–9.0,but only ~ 440 Å for galaxies with $\log(M_*/M_\odot) = 10.0$–10.5. The anti-correlation between the main optical emission lines and stellar mass is well known at different redshifts (e.g, Reddy et al. 2018; Endsley et al. 2021; Rinaldi et al. 2023; Caputi et al. 2023). This trend is shown in Fig. 4.6, including the median (Hα+ N[II] + S[II]) EW$_0$ measurements from Smit et al. (2016) (the photometric–z sample) and Caputi et al. (2017), for galaxies at $z = 3.8$–5.0 and $z = 3.9$–4.9 respectively. We also show the empirical relation between (Hα+ N[II]) EW$_0$ and M_* from Reddy et al. (2018), derived from spectroscopic line measurements for galaxies at $z = 1.0$–2.6. The difference in EW$_0$ between the (Hα+ N[II]+S[II]) and (Hα+ N[II]) line-complex is on average only 0.09 dex, such that we can safely include their result in our plot. The EW$_0$ measurements in this work are located above this empirical relation, as expected given that emission line equivalent widths increase with redshift at fixed stellar mass (Reddy et al. 2018). We attribute the difference between the results from Smit et al. (2016) and Caputi et al. (2017) to cosmic variance and a different level of statistics, as the latter study covers a field that is ~ 7 times larger than that of the former. Finally, we note that the observed negative EW$_0$-M_* correlation for our JWST-detected galaxies makes sense from the perspective that these are IRAC-selected sources with no UltraVISTA H- and/or K_s-band counterparts; the less massive galaxies require significant flux boosting from Hα emission to enter our sample.

We show the best-fit SEDs (derived from the original LEPHARE run) for three of the most prominent Hα-emitters in our sample in Fig. 4.7. We show the SED for PD-Ks-a-5-b, which together with its associated galaxy are amongst the highest redshift galaxies in our sample that display flux excesses, with $z = 5.75$ and EW$_0$ ~ 1600 Å. In addition, we show the SED of PD-H-a-1/2-d, that is the brightest in this system of sources, where all but the one contaminating foreground galaxy are strong Hα-emitters, with mean EW$_0$ ~ 1040 Å.

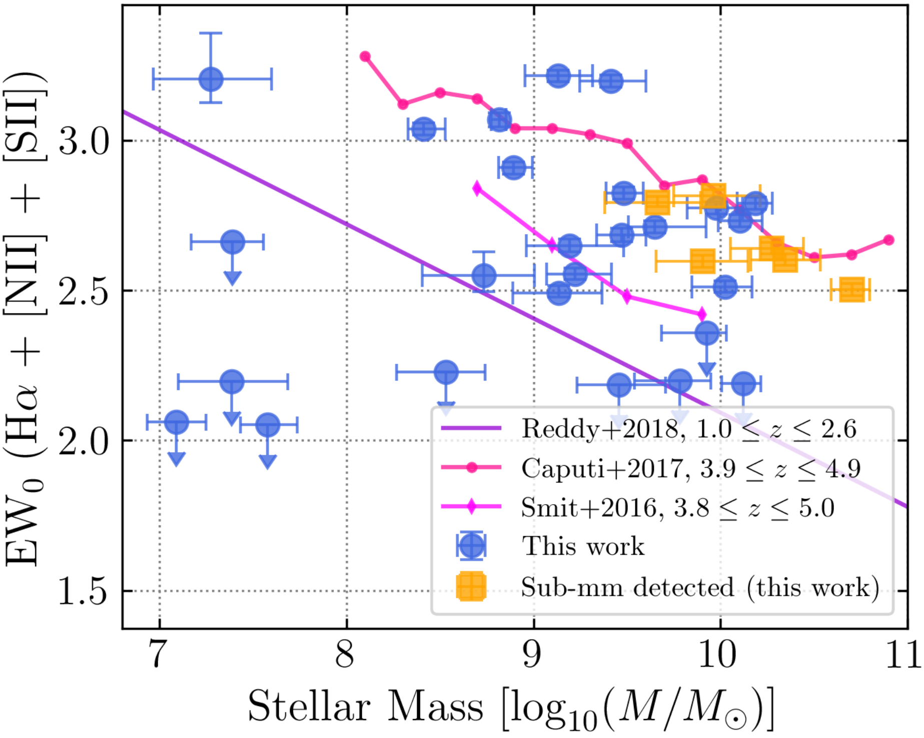

Figure 4.6 | (Hα+ N[II] + S[II]) rest-frame equivalent width versus stellar mass for all JWST-detected galaxies in our JWST-detected sample. EW$_0$ upper limits are indicated with downwards-pointing arrows. The orange data points represent the three sub-mm detected galaxies in the sample. We also show the median (Hα+ N[II] + S[II]) EW$_0$ results from Smit et al. (2016) (photometric–z sample) and Caputi et al. (2017), from galaxies at $z = 3.8$–5.0 and $z = 3.9$–4.9, in pink circles and magenta diamonds respectively. The purple line shows the empirical relation between (Hα+ N[II]) and M_* from Reddy et al. (2018), derived from spectroscopic line measurements for galaxies at $z = 1.0$–2.6.

Lastly, we include the SED of one of the sources detected at sub-mm wavelengths, i.e. PD-Ks-s-6, which due to extreme dust content combined with its Hα excess, has a red slope perfectly demonstrating why this relatively IRAC-bright galaxy is undetected in the ground-based VIRCAM imaging.

Finally, we show the Hα emitters on the SFR-M_* plane in Fig. 4.8. We also indicate the main sequence (MS) and starburst (SB) SFR-$M*$ relations from Caputi et al. (2017) and Rinaldi et al. (2022), the former derived from Hα emitters at $3.9 \leq z \leq 4.9$, the latter from star-forming galaxies in COSMOS at $2.8 \leq z \leq 6$. We also show the MS relation for galaxies at $z = 3$–6 from Speagle et al. (2014) and Santini et al. (2017), although neither of these works separate starburst and main sequence galaxies as done in Caputi et al. (2017) and Rinaldi et al. (2022). The Hα SFRs span values between ~ 5–400 $M_\odot\,\mathrm{yr}^{-1}$, and as expected, broadly increase with stellar mass. We find that the our Hα-emitters are scattered over the SFR-$M*$ plane: out of the 23 JWST-detected galaxies with secure Hα SFRs (that is, excluding upper limit estimates and the aforementioned poorly constrained source PD-H-a-1/2 c), 8 are starbursts with sSFR ≥ -7.1, and 9 are main-sequence galaxies with sSFR ≤ -8.1. The remaining 6 sources have sSFRs between -8.0 and -7.7, which following the classification from Caputi et al. (2017) places them in the so-called star formation valley, such that they are likely transitioning from starbursts into main-sequence galaxies. We point out that other works exploring the star formation valley at high-redshift (e.g., Caputi et al. 2017; Rinaldi et al. 2022) typically describe this region as an underdensity. In our work instead, these galaxies constitute 25% of the Hα-emitters, although it is difficult to derive any conclusions from this given the very specific source selection method employed in this paper, compared to the blind source analysis conducted in Caputi et al. (2017) and Rinaldi et al. (2022).

X-RAY AND SUB-MM COUNTERPARTS TO THE DROPOUT GALAXIES

Given the highly dusty nature of many of our JWST-detected galaxies, we search for counterparts in the literature specifically at X-ray and sub-mm wavelengths. We find that source PD-H-s-2 has a $0\farcs7$ offset X-ray association from both the Chandra-COSMOS Legacy Survey (Civano et al. 2016) and the XMM-Newton Wide-Field Survey (Cappelluti et al. 2009). Interestingly, as shown in Fig. 4.9, the optical and near-infrared continuum of PD-H-s-2 is well-fitted by stellar population templates, with $\chi^2_\nu = 0.96$ and no preference from LePhare for an AGN solution. Compared to the best-fit SED, the photometry of PD-H-s-2 shows flux excess in the F200W and F356W bands, which sample the (Hβ+O[III]) and (Hα+ N[II] + S[II]) lines respectively. Finally, we notice that PD-H-s-2 and PD-H-s-1 have very similar SED properties and brightness (F444W ~ 23.4 mag), but PD-H-s-1 lacks any ancillary detections at X-ray or radio wavelengths nor does it have similarly broad emission lines.

At the sub-mm regime, we find that sources PD-Ks-s-6, PD-Ks-s-8, PD-Ks-s-11, PD-H-d-1, PD-H-d-4, and PD-Ks-d-10 (all of which are Hα emitters as shown in the previous section) are detected at sub-mm wavelengths with ALMA from the A3COSMOS catalog (Liu et al. 2019), with ~ 1–2 mJy fluxes from Band 6 (~ 1.2 mm). In addition, PD-Ks-s-6, PD-Ks-s-8, and PD-H-d-10 were observed with SCUBA-2 at 850 μm and followed up at 870 μm with ALMA from the S2COSMOS study (Simpson et al. 2019) and the AS2COSMOS pilot study respectively (Simpson et al. 2020). PD-Ks-s-8 is also detected at 450 and

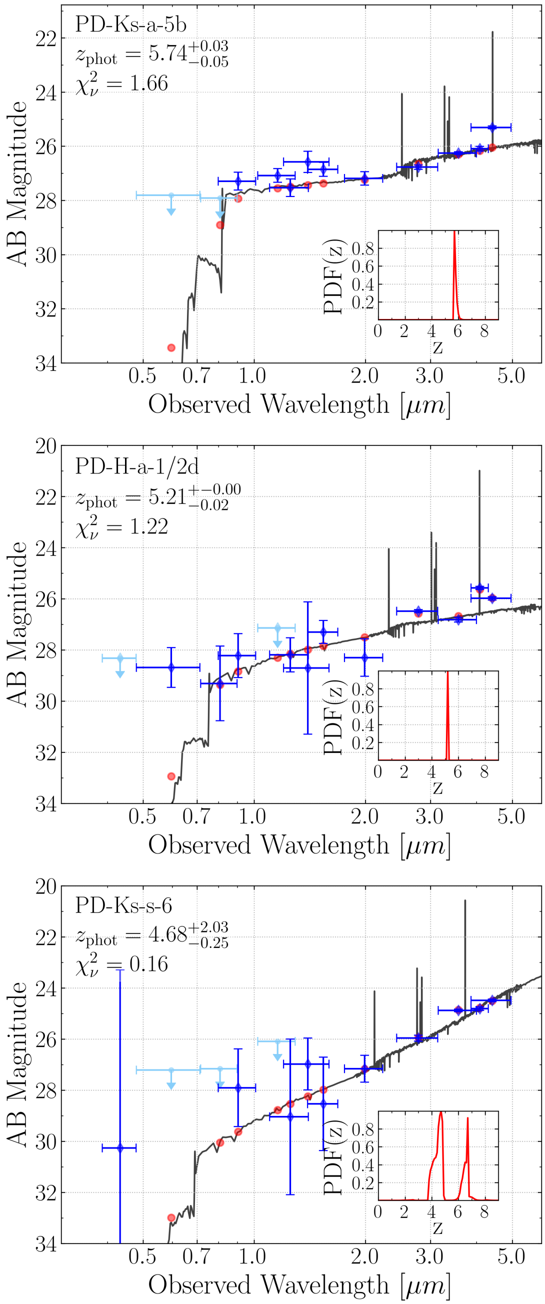

Figure 4.7 | Best-fit SED obtained with LEPHARE on HST and JWST photometry for three of the most prominent Hα-emitters among the JWST-detected galaxies. Photometric measurements are shown in blue diamonds, flux upper limits in cyan with downward-pointing arrows and the template fluxes (with emission line contributions) with red circles.

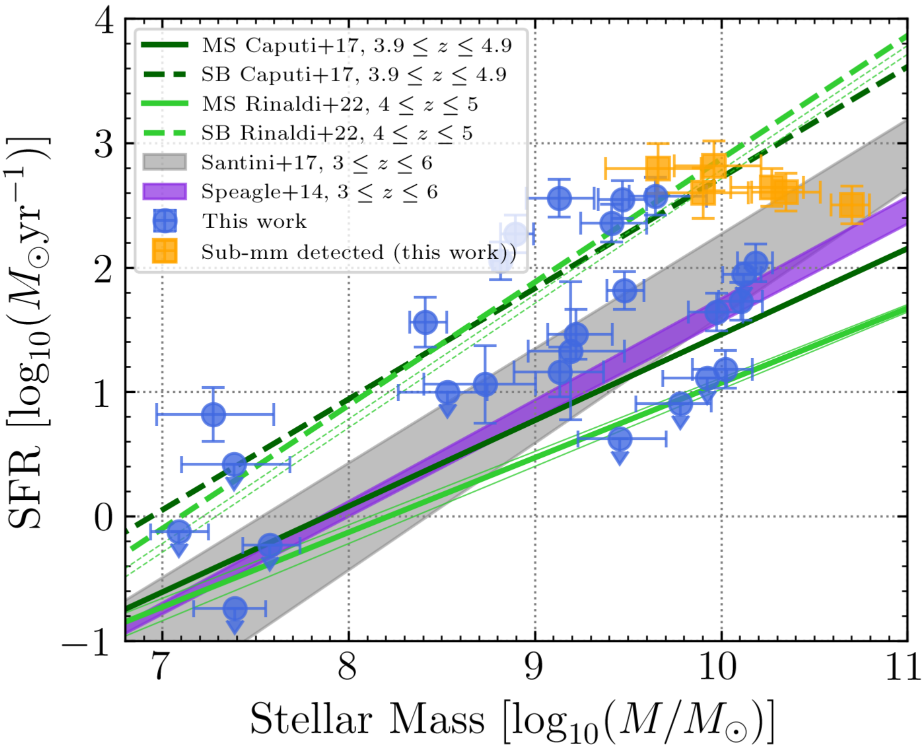

Figure 4.8 | SFR derived from the Hα luminosity versus stellar mass for all JWST-detected galaxies in our sample. SFR upper limits are indicated with downwards-pointing arrows. The orange data points represent the three sub-mm detected galaxies in the sample. The solid and dotted lines display the main sequence and starburst SFR-M_* relations respectively, taken from Caputi et al. (2017) in dark green and Rinaldi et al. (2022) in light green respectively. The faint, light green lines correspond to the SFR-M_* relations at $z = 2.8$–4 and $z = 5$–6 from Rinaldi et al. (2022). The MS relations between $z = 3$–6 from Speagle et al. (2014) and Santini et al. (2017) are shown in violet and grey shaded regions respectively.

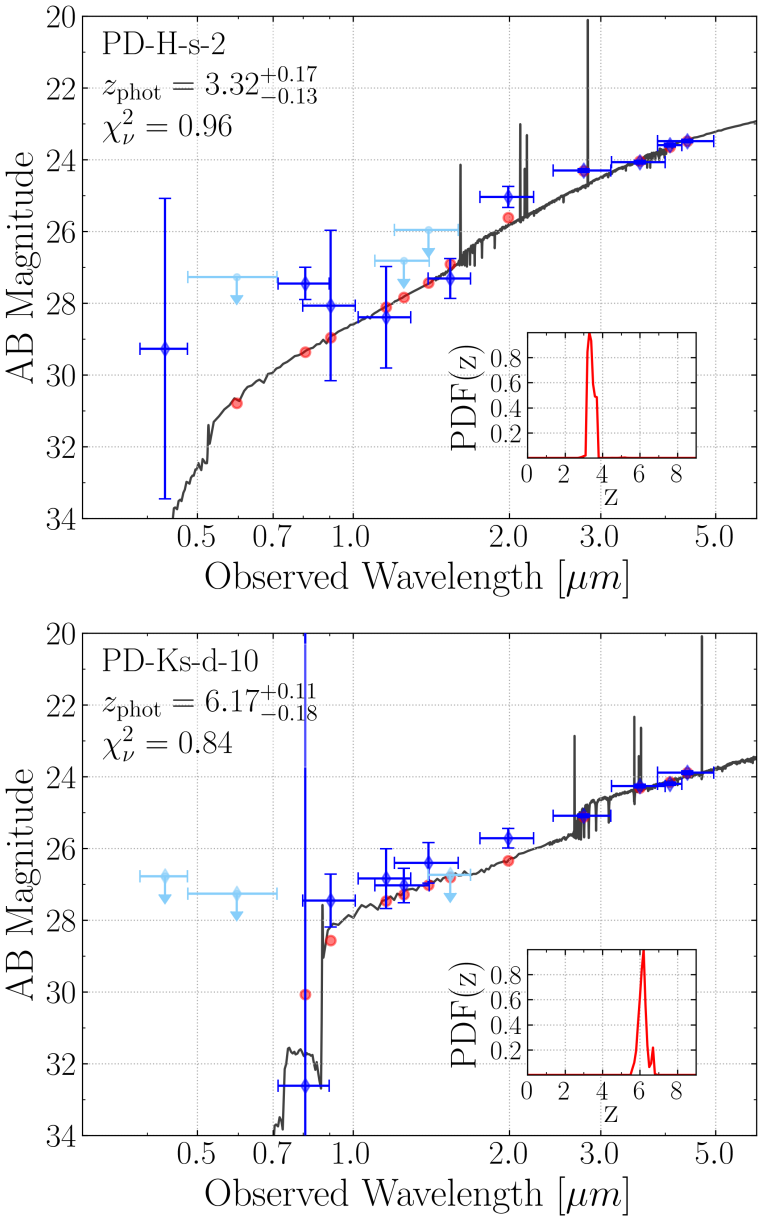

Figure 4.9 | Best-fit SED obtained with LEPHARE on HST and JWST photometry for PD-H-s-2 and PD-Ks-d-10. Photometric measurements are shown in blue diamonds, flux upper limits in cyan with downward-pointing arrows and the template fluxes (with emission line contributions) with red circles.

850 μm from the SCUBA-2 Cosmology Legacy Survey (Koprowski et al. 2016). Finally, PD-H-d-1 is detected with the VLA at 3 GHz (Smolčić et al. 2017).

Liu et al. (2019) report photometric redshifts of $z = 5.9$ and $z = 6.4$ and stellar masses of $\log(M_*/M_\odot) \sim 11.2$ for sources PD-Ks-s-6 and PD-H-d-1 respectively. These parameters are discrepant with our own solutions for these galaxies, although the probability distribution function of PD-Ks-s-6's redshift, PDF(z), is degenerate with a secondary solution at $z \sim 6.7$. Even when we re-run LEPHARE on our photometry with the redshift fixed to $z = 5.9$, we only retrieve a stellar mass of $\log(M_*/M_\odot) = 10.4$ for this source. The Liu et al. (2019) photometric redshifts for these two sources were actually taken from the superdeblended COSMOS catalog from Jin et al. (2018), who derived these redshifts from SED fitting FIR to sub-mm data. We therefore credit the discrepancy in redshifts to the different methodologies employed and different SED regime considered for the SED fitting between their work and ours.

We show the SED for PD-Ks-d-10 in Fig. 4.9. With its photometric redshift $z = 6.2$ and stellar mass of $\log(M_*/M_\odot) = 10.7$, it is amongst the highest redshift, most massive galaxies in our dropout sample. We have already shown the best-fit SED of PD-Ks-s-6 in Fig. 4.7. This source is amongst the four galaxies in our sample that would qualify as a true K_s-band dropouts, given that it has flux detections of at most $\sim 1\sigma$ significance in any of the bands redwards of the F200W band, nor is it visibly by eye in said bands. Although its nature is not particularly different from the other $z \sim 4.7$ galaxies in our sample, PD-Ks-s-6 is highly dusty with $E(B-V) = 0.7$ and the third reddest source in the sample with [F160W-F444W]=4.1.

4.6. DISCUSSION AND CONCLUSIONS

In this work we have studied a sample of Spitzer IRAC-detected galaxies that are part of the SMUVS program in the COSMOS field, but which are completely undetected in the latest data release (DR5) of the UltraVISTA VIRCAM H- and K_s-band imaging. These sources are rare, as we identify only 26 over an area of 94 square arcminutes (i.e., the area with multi-wavelength JWST coverage considered in this work). We used the available JWST/NIRCam data in 7 bands from the PRIMER program, together with ancillary HST/ACS and HST/WFC3 data, to study the properties of these galaxies, with vastly improved angular resolution and sensitivity with respect to the original Spitzer and ground-based data. We find that more than half of the IRAC sources are in fact systems of multiple galaxies: 10 consisting of a so-called deboosted galaxy that is accompanied by a low-redshift, faint foreground contaminant; and another 5 consisting of associated galaxies at similar redshifts. In addition, the majority of the dropout candidates display flux in the short-wavelength JWST channels, such that only two K_s-band dropout candidates and two H_s-band dropout candidates qualify as true dropout galaxies.

We find that our JWST-detected galaxies display a variety of properties, with redshifts between $z = 0.8$–6.2, stellar masses $\log(M_*/M_\odot) = 7.0$–10.7, and color excess between $E(B-V) = 0.0$ and 1.0. Most of the sample consists of intermediate-mass galaxies that are red because of dust attenuation, with median values of $z = 3.6$, $\log(M_*/M_\odot) = 9.5$, [F160W-F444W]= 2.2, and $E(B-V) = 0.5$. We compared the properties of our JWST-detected galaxies at $z = 3$–6 with those of UltraVISTA DR4 HK_s-detected galaxies in the same region. We find that our JWST-detected galaxies are amongst the dustiest galaxies at this epoch; in fact, ~ 65 % of our sample at $z = 3$–6 has $E(B-V) \geq 0.5$, compared to 7% at most amongst the UltraVISTA DR4 galaxies.

For ~ 75% of our IRAC-selected dropout candidates, the JWST photometry shows flux excess in bands encompassing the Hα emission line-complex, which enabled us to calculate (Hα+ N[II] + S[II]) rest-frame equivalent widths and Hα star formation rates. The (Hα+ N[II] + S[II]) EW$_0$ span values between ~ 100–2200 Å, and the SFRs between ~ 5–375 $M_\odot\,\mathrm{yr}^{-1}$. We studied them in the SFR-M_* plane, and found 35 % of the JWST-detected galaxies with secure Hα SFRs to be starbursts, 40 % to be main-sequence galaxies and the remaining 25 % to be located in the star-formation valley. Given their redshifts, the Hα emission contributes strongly to the continuum measurements redwards of the K_s band, explaining, together with their dusty nature, why these galaxies enter our initial dropout sample.

We checked if the Hα-emitting nature of our sample is apparent from the IRAC photometry as well. For seven dropout candidates, the Hα line falls in the 3.6 μm band, such that we would expect to see a flux excess with respect to the 4.5 μm band. However, for only three of these galaxies do we observe $\mathrm{m}_{3.6} - \mathrm{m}_{4.5} < 0$, such that we conclude the presence of Hα emission is not obvious from the IRAC bands alone. We note that although there are multiple dropout candidates for which the Hα line is observed with the 4.5μm band, we cannot perform a similar check, as a flux excess in this band with respect to the 3.6μm band can be explained by red continuum emission just as well.

We have cross-matched our sources with ancillary data at X-ray and sub-mm wavelengths, and find one AGN candidate and six ALMA-detected galaxies amongst them. For the ALMA-detected sources we obtained photometric redshifts between $z \sim 3.3$ and 6.2 and stellar masses $\log(M_*/M_\odot) = 9.7$–10.7 from the HST and JWST photometry. These sources are among the (Hα+ N[II] + S[II]) line emitters discussed above.

Our galaxies are not as *Spitzer*/IRAC-bright and massive as other studies targeting optically faint sources. The brightest IRAC source in our sample is 23.9 and 23.1 mag in the 3.6μm and 4.5μm bands respectively, and the median IRAC magnitude of our dropout candidates is ~ 24.6 mag. In addition, the most massive galaxy in our sample is $\log(M_*/M_\odot) = 10.7$ and the median stellar mass of the sample is $\log(M_*/M_\odot) = 9.5$. Similar endeavors to ours have been focused mostly on bright IRAC sources ([4.5] < 24 mag), finding them to be massive $\log(M_*/M_\odot) > 10.5$ star-forming galaxies at $z \sim 3$–6. Alcalde Pampliega et al. (2019) do find Hα emitters among relatively Spitzer-bright ([4.5] < 24.5 mag) HST/F160W-band dropout sources, although their incidence is only a third in their sample, versus our finding of Hα-emitters among ~ 75 % of our dropout candidates. More recently, Barrufet et al. (2023) looked for JWST-detected HST-dropout galaxies in CEERS. Their sample spans a similar NIRCam/F444W magnitude range as our JWST-detected galaxies (23 – 28 mag), which they find to be dusty $E(B-V) \sim 0.5$, relatively massive $\log(M_*/M_\odot) \sim 10$ star-forming galaxies at $z \sim 2$–8. The presence of Hα line emission is unfortunately not discussed in their work.

Lastly, our dropout candidates, with an observed surface density of ~ 0.3 arcmin^{-2}, appear to be relatively rare. Their incidence is comparable to that of mid-IR bright, true HST-dropout galaxies, for which studies have found typical surface densities of ~ 0.1 arcmin^{-2} (e.g., Alcalde Pampliega et al. 2019; Wang et al. 2019). However, a recent study by Barrufet et al. (2023) reported a surface density of ~ 0.8 arcmin^{-2} for JWST-detected, HST-dark galaxies.

In summary, we have revealed the nature of a representative sample of the IRAC sources that were left unidentified from the Spitzer era. In the future, once JWST/NIRCam imaging becomes available for other well-studied extra-galactic fields on the sky, we will be able to follow up more of these sources and characterize the overall population of emission-line galaxies with significant dust extinction at intermediate/high redshifts.

ACKNOWLEDGEMENTS

We thank the anonymous referee for a constructive report. We thank Ian Smail for updating our information on the presence of sub-millimetre sources within our galaxy sample, and Matt Jarvis for their useful feedback. KIC and VK acknowledge funding from the Dutch Research Council (NWO) through the award of the Vici Grant VI.C.212.036. This work is based on observations made with the NASA/ESA/CSA James Webb Space Telescope. The data were obtained from the Mikulski Archive for Space Telescopes at the Space Telescope Science Institute, which is operated by the Association of Universities for Research in Astronomy, Inc., under NASA contract NAS 5-03127 for JWST. All the JWST data used in this paper can be found in MAST: 10.17909/bysp-ds64.

REFERENCES

Aihara, H., AlSayyad, Y., Ando, M., et al. 2022, PASJ, 74, 247, doi: `10.1093/pasj/psab122`

Alcalde Pampliega, B., Pérez-González, P. G., Barro, G., et al. 2019, ApJ, 876, 135, doi: `10.3847/1538-4357/ab14f2`

Anders, P., & Fritze-v. Alvensleben, U. 2003, A&A, 401, 1063, doi: `10.1051/0004-6361:20030151`

Arnouts, S., Cristiani, S., Moscardini, L., et al. 1999, MNRAS, 310, 540, doi: `10.1046/j.1365-8711.1999.02978.x`

Ashby, M. L. N., Willner, S. P., Fazio, G. G., et al. 2015, ApJS, 218, 33, doi: `10.1088/0067-0049/218/2/33`

Ashby, M. L. N., Caputi, K. I., Cowley, W., et al. 2018, ApJS, 237, 39, doi: `10.3847/1538-4365/aad4fb`

Astropy Collaboration, Price-Whelan, A. M., Lim, P. L., et al. 2022, ApJ, 935, 167, doi: `10.3847/1538-4357/ac7c74`

Barrufet, L., Oesch, P. A., Weibel, A., et al. 2023, MNRAS, 522, 449, doi: `10.1093/mnras/stad947`

Bertin, E., & Arnouts, S. 1996, A&AS, 117, 393, doi: `10.1051/aas:1996164`

Boyer, M. L., Anderson, J., Gennaro, M., et al. 2022, Research Notes of the American Astronomical Society, 6, 191, doi: `10.3847/2515-5172/ac923a`

Bradley, L., Sipőcz, B., Robitaille, T., et al. 2022, astropy/photutils:, 1.4.0, Zenodo, doi: `10.5281/zenodo.6385735`

Bradley, L. D., Coe, D., Brammer, G., et al. 2022, arXiv e-prints, arXiv:2210.01777, doi: `10.48550/arXiv.2210.01777`

Brammer, G. 2022, Preliminary updates to the NIRCam photometric calibration, Zenodo, doi: `10.5281/zenodo.7143382`

—. 2023, grizli, 1.7.9, Zenodo, doi: `10.5281/zenodo.7649159`

Brammer, G. B., van Dokkum, P. G., & Coppi, P. 2008, ApJ, 686, 1503, doi: `10.1086/591786`

Bruzual, G., & Charlot, S. 2003, MNRAS, 344, 1000, doi: `10.1046/j.1365-8711.2003.06897.x`

Calzetti, D., Armus, L., Bohlin, R. C., et al. 2000, ApJ, 533, 682, doi: `10.1086/308692`

Cappelluti, N., Brusa, M., Hasinger, G., et al. 2009, A&A, 497, 635, doi: `10.1051/0004-6361/200810794`

Caputi, K. I., Dunlop, J. S., McLure, R. J., et al. 2012, ApJL, 750, L20, doi: `10.1088/2041-8205/750/1/L20`

Caputi, K. I., Ilbert, O., Laigle, C., et al. 2015, ApJ, 810, 73, doi: `10.1088/0004-637X/810/1/73`

Caputi, K. I., Deshmukh, S., Ashby, M. L. N., et al. 2017, ApJ, 849, 45, doi: `10.3847/1538-4357/aa901e`

Caputi, K. I., Rinaldi, P., Iani, E., et al. 2023, arXiv e-prints, arXiv:2311.12691, doi: `10.48550/arXiv.2311.12691`

Carnall, A. C., Begley, R., McLeod, D. J., et al. 2022, arXiv e-prints, arXiv:2207.08778. `https://arxiv.org/abs/2207.08778`

Chabrier, G. 2003, PASP, 115, 763, doi: `10.1086/376392`

Cirasuolo, M., McLure, R. J., Dunlop, J. S., et al. 2007, MNRAS, 380, 585, doi: `10.1111/j.1365-2966.2007.12038.x`

Civano, F., Marchesi, S., Comastri, A., et al. 2016, ApJ, 819, 62, doi: `10.3847/0004-637X/819/1/62`

Conroy, C., & Gunn, J. E. 2010, ApJ, 712, 833, doi: `10.1088/0004-637X/712/2/833`

Conroy, C., Gunn, J. E., & White, M. 2009, ApJ, 699, 486, doi: `10.1088/0004-637X/699/1/486`

Deshmukh, S., Caputi, K. I., Ashby, M. L. N., et al. 2018, ApJ, 864, 166, doi: `10.3847/1538-4357/aad9f5`

Diolaiti, E., Bendinelli, O., Bonaccini, D., et al. 2000, A&AS, 147, 335, doi: `10.1051/aas:2000305`

Endsley, R., Stark, D. P., Chevallard, J., & Charlot, S. 2021, MNRAS, 500, 5229, doi: `10.1093/mnras/staa3370`

Faisst, A. L., Capak, P. L., Emami, N., Tacchella, S., & Larson, K. L. 2019, ApJ, 884, 133, doi: `10.3847/1538-4357/ab425b`

Fazio, G. G., Hora, J. L., Allen, L. E., et al. 2004, ApJS, 154, 10, doi: `10.1086/422843`

Fitzpatrick, E. L. 1999, PASP, 111, 63, doi: `10.1086/316293`

Fruchter, A. S., & Hook, R. N. 2002, PASP, 114, 144, doi: `10.1086/338393`

Gaia Collaboration, Vallenari, A., Brown, A. G. A., et al. 2023, A&A, 674, A1, doi: `10.1051/0004-6361/202243940`

Grogin, N. A., Kocevski, D. D., Faber, S. M., et al. 2011, ApJS, 197, 35, doi: `10.1088/0067-0049/197/2/35`

Ikarashi, S., Caputi, K. I., Ohta, K., et al. 2017, ApJL, 849, L36, doi: `10.3847/2041-8213/aa9572`

Ilbert, O., Arnouts, S., McCracken, H. J., et al. 2006, A&A, 457, 841, doi: `10.1051/0004-6361:20065138`

Ilbert, O., Capak, P., Salvato, M., et al. 2009, ApJ, 690, 1236, doi: `10.1088/0004-637X/690/2/1236`

Jarvis, M. J., Bonfield, D. G., Bruce, V. A., et al. 2013, MNRAS, 428, 1281, doi: `10.1093/mnras/sts118`

Jin, S., Daddi, E., Liu, D., et al. 2018, ApJ, 864, 56, doi: `10.3847/1538-4357/aad4af`

Johnson, B. D., Leja, J., Conroy, C., & Speagle, J. S. 2021, ApJS, 254, 22, doi: `10.3847/1538-4365/abef67`

Kennicutt, R. C. 1998, ApJ, 498, 541, doi: `10.1086/305588`

Koekemoer, A. M., Faber, S. M., Ferguson, H. C., et al. 2011, ApJS, 197, 36, doi: `10.1088/0067-0049/197/2/36`

Kokorev, V., Brammer, G., Fujimoto, S., et al. 2022, ApJS, 263, 38, doi: `10.3847/1538-4365/ac9909`

Kokorev, V., Jin, S., Magdis, G. E., et al. 2023, ApJL, 945, L25, doi: `10.3847/2041-8213/acbd9d`

Koprowski, M. P., Dunlop, J. S., Michałowski, M. J., et al. 2016, MNRAS, 458, 4321, doi: `10.1093/mnras/stw564`

Laigle, C., McCracken, H. J., Ilbert, O., et al. 2016, ApJS, 224, 24, doi: 10.3847/0067-0049/224/2/24

Lawrence, A., Warren, S. J., Almaini, O., et al. 2007, MNRAS, 379, 1599, doi: 10.1111/j.1365-2966.2007.12040.x

Leja, J., Johnson, B. D., Conroy, C., van Dokkum, P. G., & Byler, N. 2017, ApJ, 837, 170, doi: 10.3847/1538-4357/aa5ffe

Liu, D., Lang, P., Magnelli, B., et al. 2019, ApJS, 244, 40, doi: 10.3847/1538-4365/ab42da

Madau, P. 1995, ApJ, 441, 18, doi: 10.1086/175332

Mármol-Queraltó, E., McLure, R. J., Cullen, F., et al. 2016, MNRAS, 460, 3587, doi: 10.1093/mnras/stw1212

McCracken, H. J., Milvang-Jensen, B., Dunlop, J., et al. 2012, A&A, 544, A156, doi: 10.1051/0004-6361/201219507

Nardiello, D., Bedin, L. R., Burgasser, A., et al. 2022, MNRAS, 517, 484, doi: 10.1093/mnras/stac2659

Oke, J. B., & Gunn, J. E. 1983, ApJ, 266, 713, doi: 10.1086/160817

Pérez-González, P. G., Barro, G., Annunziatella, M., et al. 2023, ApJL, 946, L16, doi: 10.3847/2041-8213/acb3a5

Reddy, N. A., Shapley, A. E., Sanders, R. L., et al. 2018, ApJ, 869, 92, doi: 10.3847/1538-4357/aaed1e

Rinaldi, P., Caputi, K. I., van Mierlo, S. E., et al. 2022, ApJ, 930, 128, doi: 10.3847/1538-4357/ac5d39

Rinaldi, P., Caputi, K. I., Costantin, L., et al. 2023, ApJ, 952, 143, doi: 10.3847/1538-4357/acdc27

Salpeter, E. E. 1955, ApJ, 121, 161, doi: 10.1086/145971

Santini, P., Fontana, A., Castellano, M., et al. 2017, ApJ, 847, 76, doi: 10.3847/1538-4357/aa8874

Schlafly, E. F., & Finkbeiner, D. P. 2011, ApJ, 737, 103, doi: 10.1088/0004-637X/737/2/103

Scoville, N., Aussel, H., Brusa, M., et al. 2007, ApJS, 172, 1, doi: 10.1086/516585

Shu, X., Yang, L., Liu, D., et al. 2022, ApJ, 926, 155, doi: 10.3847/1538-4357/ac3de5

Simpson, J. M., Smail, I., Swinbank, A. M., et al. 2019, ApJ, 880, 43, doi: 10.3847/1538-4357/ab23ff

Simpson, J. M., Smail, I., Dudzevičiūtė, U., et al. 2020, MNRAS, 495, 3409, doi: `10.1093/mnras/staa1345`

Smail, I., Dudzeviciute, U., Gurwell, M., et al. 2023, arXiv e-prints, arXiv:2306.16039, doi: `10.48550/arXiv.2306.16039`

Smirnov, N. V. 1939, Bull. Math. Univ. Moscou, 2, 3

Smit, R., Bouwens, R. J., Labbé, I., et al. 2016, ApJ, 833, 254, doi: `10.3847/1538-4357/833/2/254`

Smolčić, V., Novak, M., Bondi, M., et al. 2017, A&A, 602, A1, doi: `10.1051/0004-6361/201628704`

Speagle, J. S., Steinhardt, C. L., Capak, P. L., & Silverman, J. D. 2014, ApJS, 214, 15, doi: `10.1088/0067-0049/214/2/15`

Tacchella, S., Finkelstein, S. L., Bagley, M., et al. 2022, ApJ, 927, 170, doi: `10.3847/1538-4357/ac4cad`

Valentino, F., Brammer, G., Gould, K. M. L., et al. 2023, ApJ, 947, 20, doi: `10.3847/1538-4357/acbefa`

van Mierlo, S. E., Caputi, K. I., Ashby, M., et al. 2022, A&A, 666, A200, doi: `10.1051/0004-6361/202243950`

Wang, T., Schreiber, C., Elbaz, D., et al. 2019, Nature, 572, 211, doi: `10.1038/s41586-019-1452-4`

Weaver, J. R., Kauffmann, O. B., Ilbert, O., et al. 2022, ApJS, 258, 11, doi: `10.3847/1538-4365/ac3078`

Werner, M. W., Roellig, T. L., Low, F. J., et al. 2004, ApJS, 154, 1, doi: `10.1086/422992`

Zavala, J. A., Casey, C. M., Manning, S. M., et al. 2021, ApJ, 909, 165, doi: `10.3847/1538-4357/abdb27`

Zavala, J. A., Buat, V., Casey, C. M., et al. 2023, ApJL, 943, L9, doi: `10.3847/2041-8213/acacfe`

APPENIDX: *HST* AND *JWST* IMAGE CUTOUTS OF 20 DROPOUT CANDIDATES

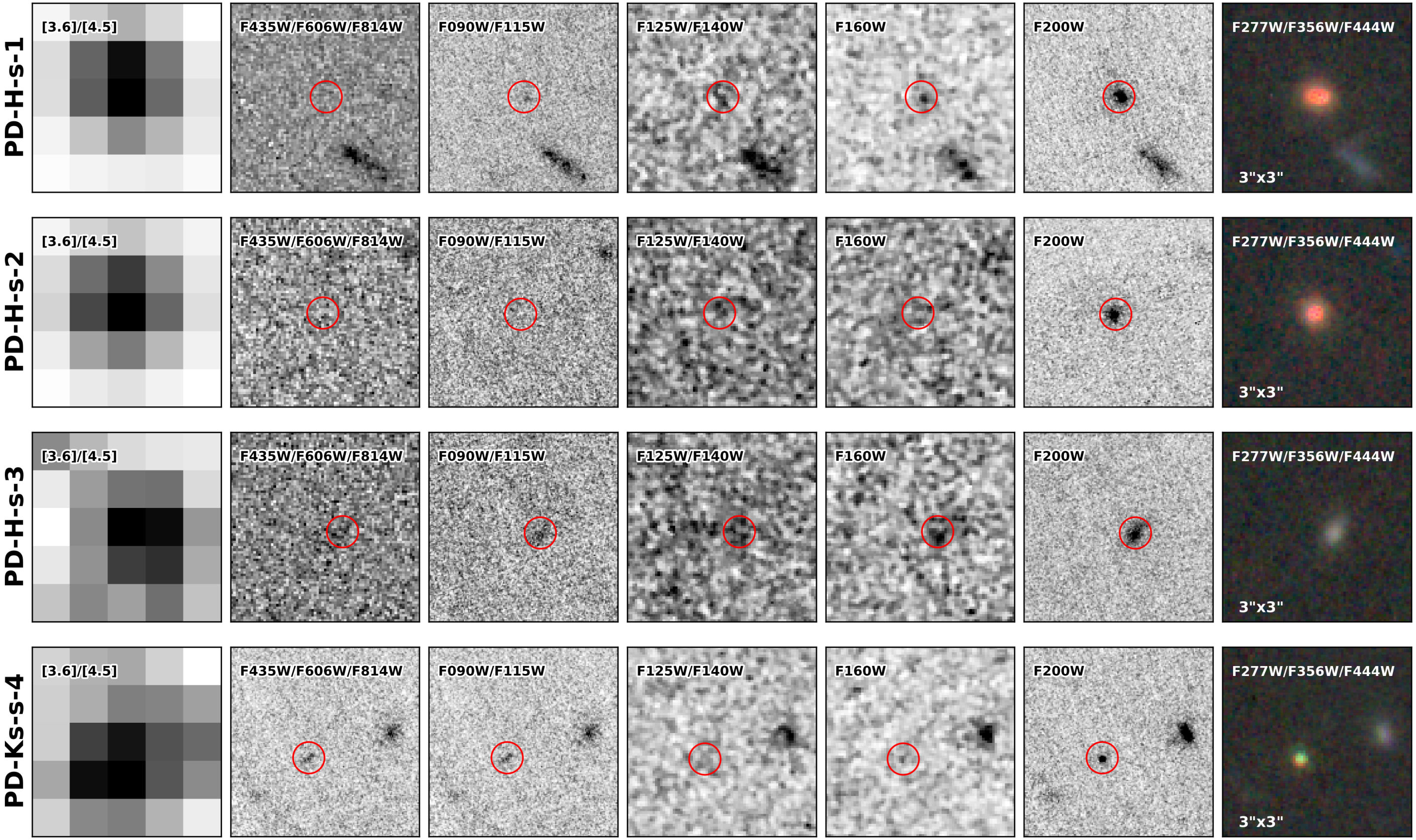

Figure 4.10 | Image cutouts for the ten secure dropout candidates. From left to right, the horizontal panels show the following imaging in 3 by 3" windows: IRAC 3.6 and 4.5 μm average; *HST*/ACS F435W, F606W, and F814W average; *JWST*/NIRCam F090W and F115W average; *HST*/WFC3 F125W and F140W average; *JWST*/NIRCam F200W; *JWST*/NIRCam F277W, F356W, and F444W rgb image. The red circle represents the $0\farcs5$ diameter circular aperture at the position of the *JWST*-detected galaxy.

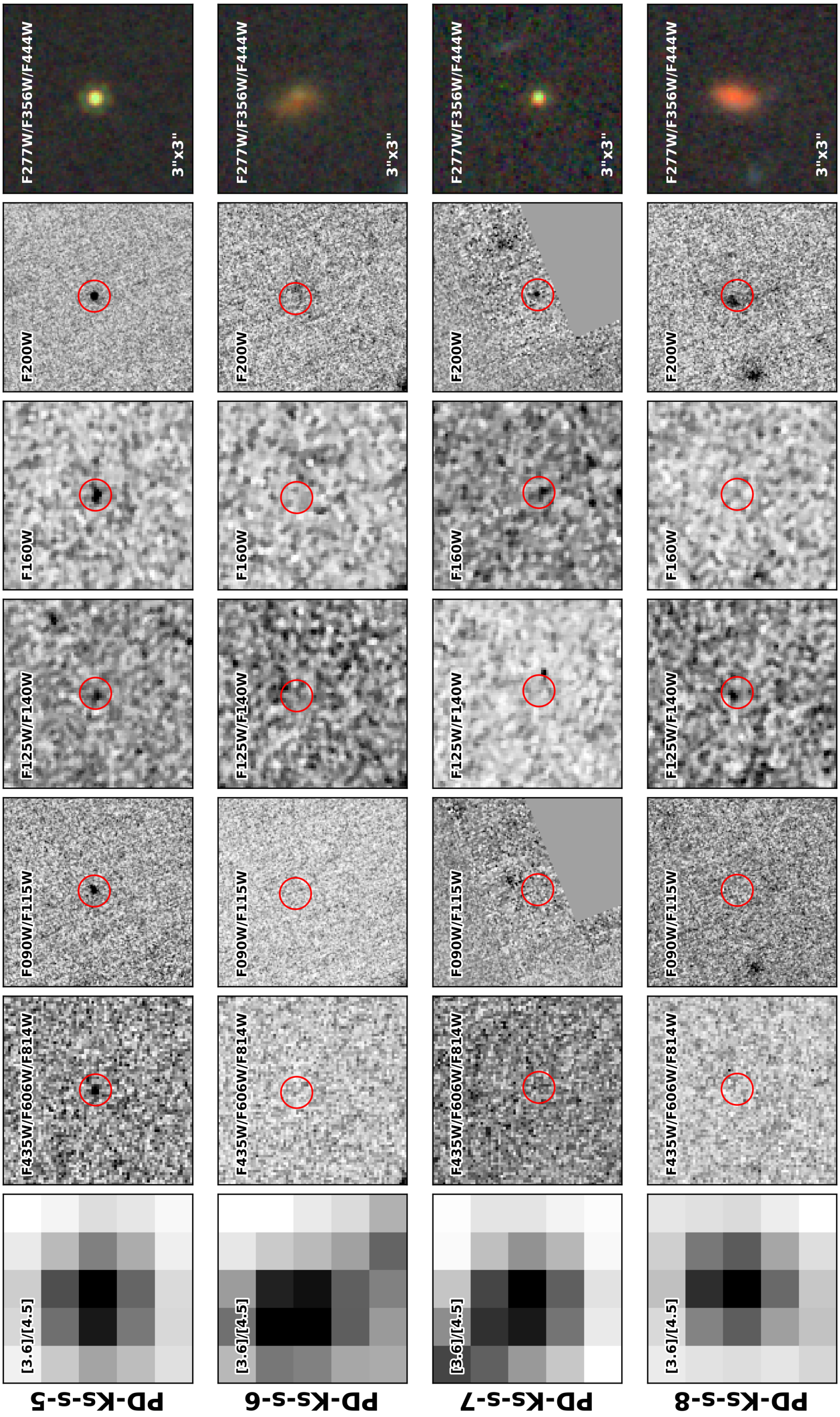

Figure 4.10 | Figure 4.10 continued.

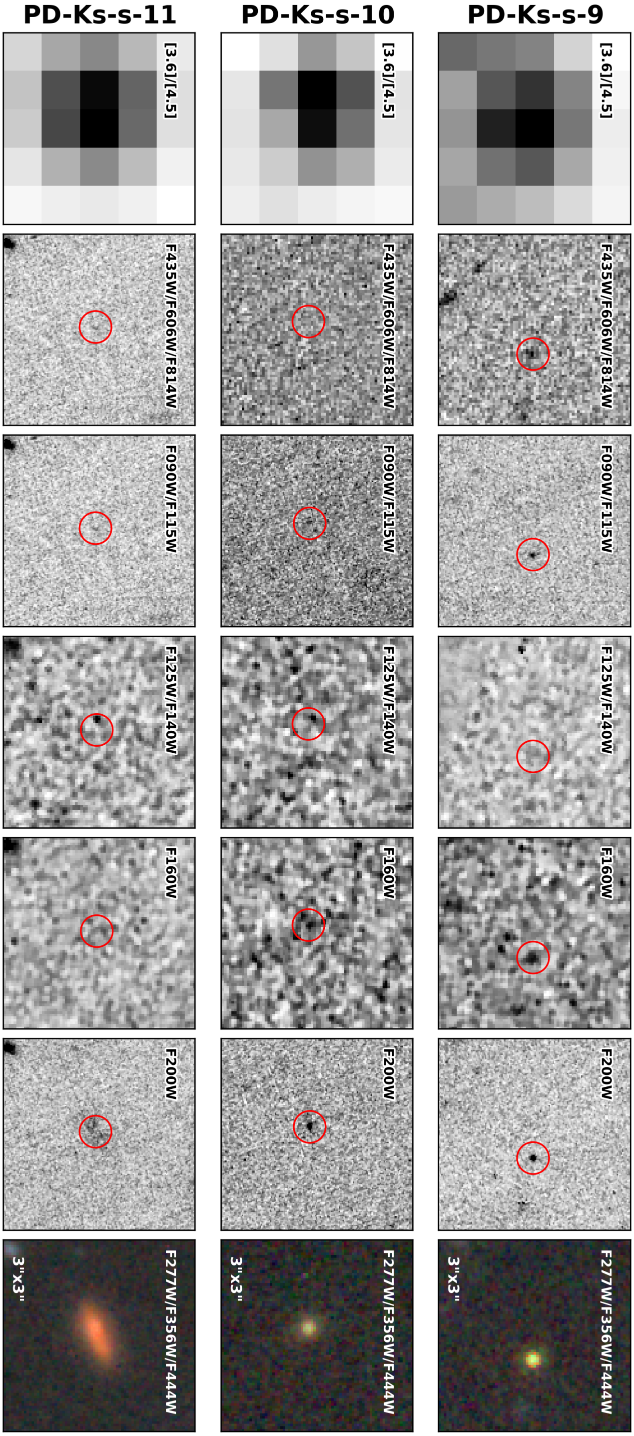

Figure 4.10 | Figure 4.10 continued.

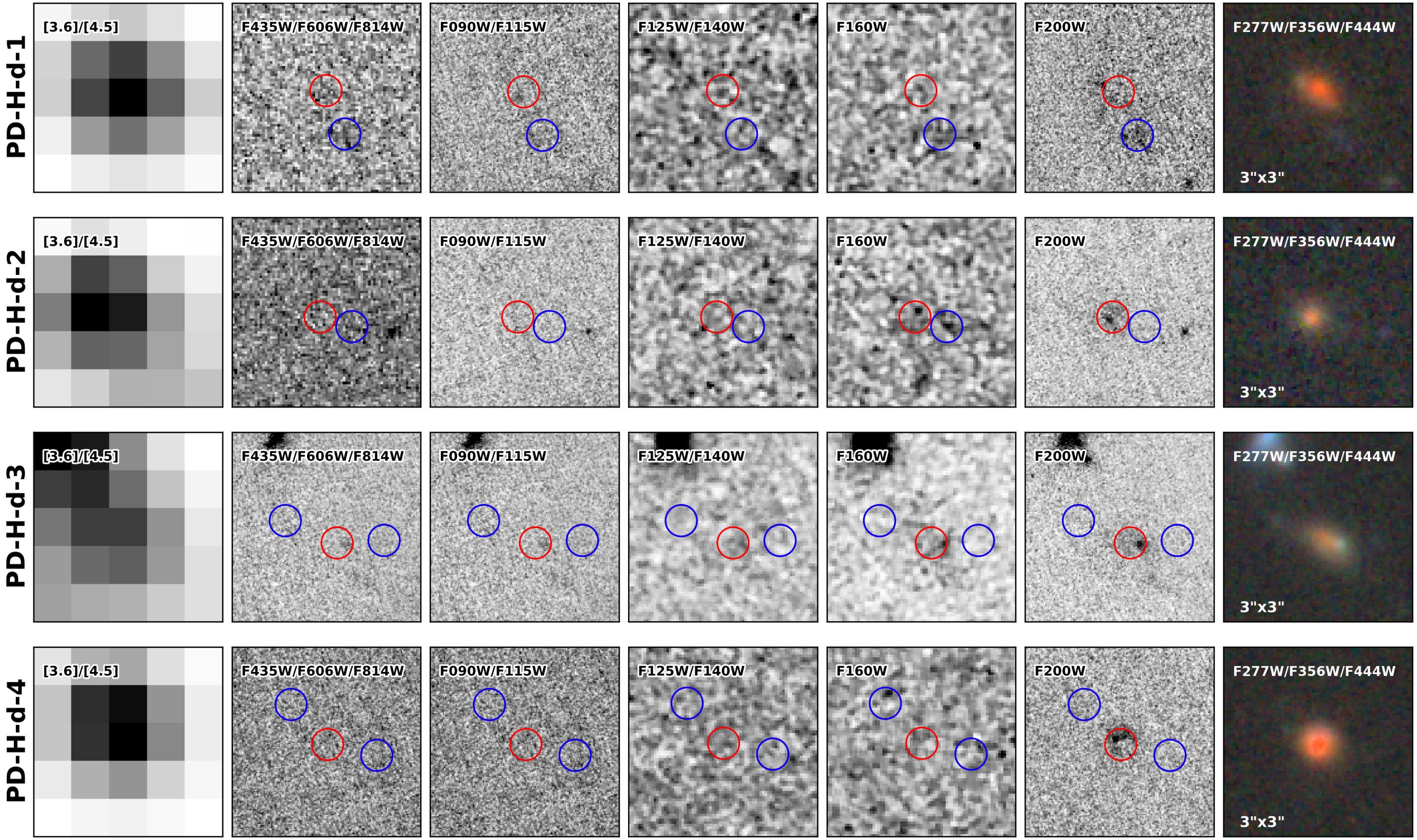

Figure 4.11 | Image cutouts for the five deboosted dropout candidates. The horizontal panels for each source show the same imaging as in Fig. 4.10. The circles represent the $0\overset{''}{.}5$ diameter circular aperture at the positions of the *JWST*-detected galaxies, showing the deboosted source in red and the contaminating foreground galaxies in blue.

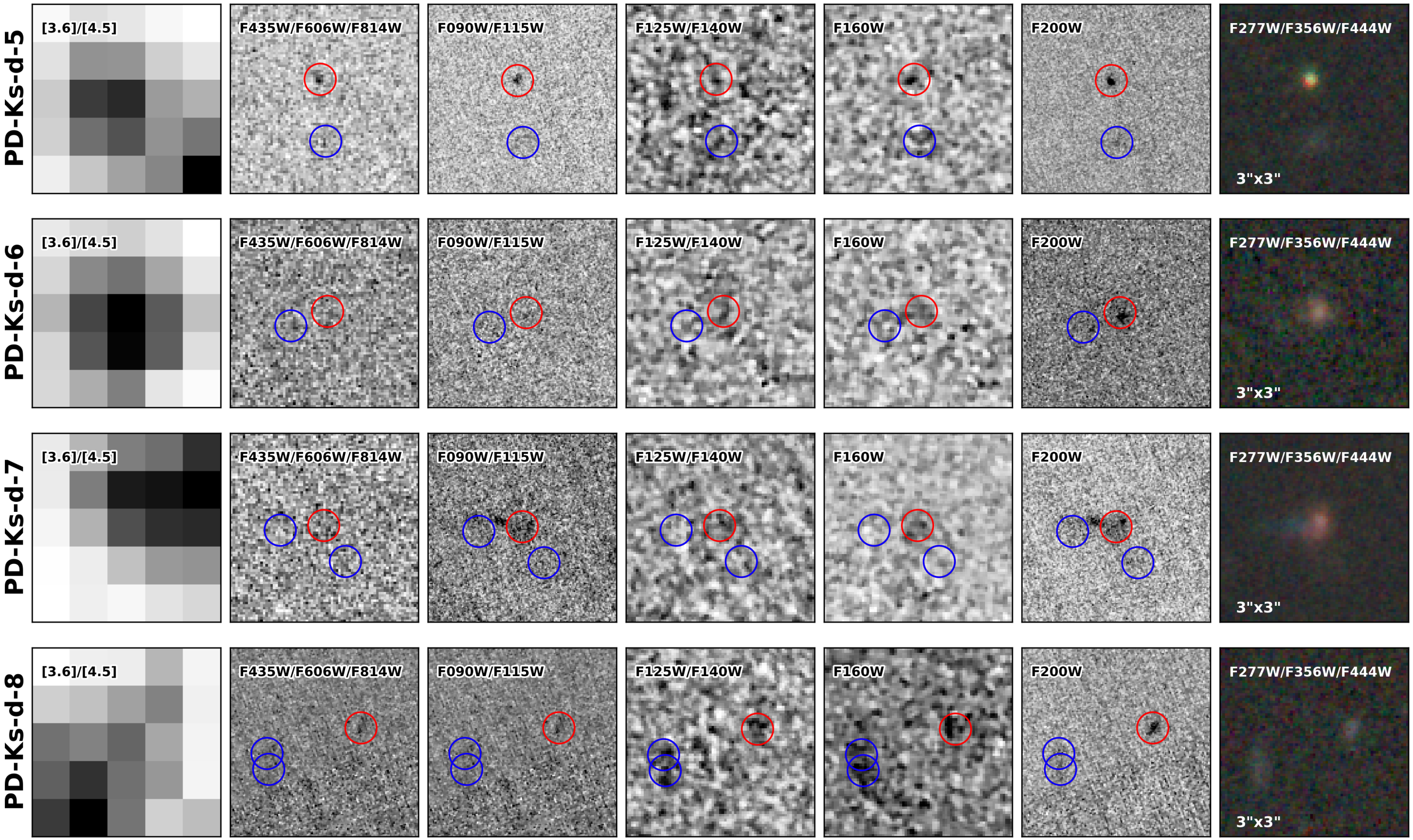

Figure 4.11 | Figure 4.11 continued.

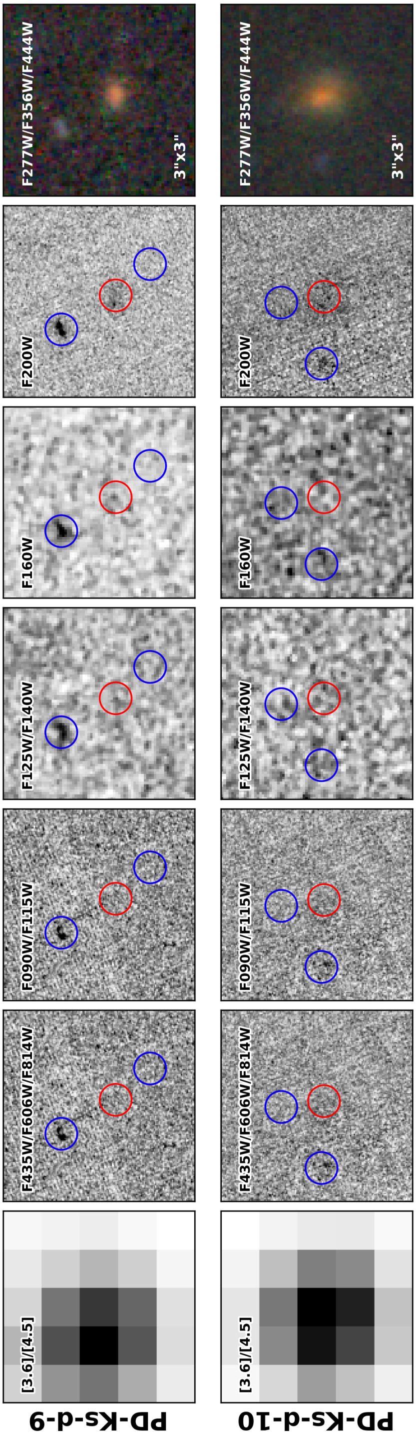

Figure 4.11 | Figure 4.11 continued.

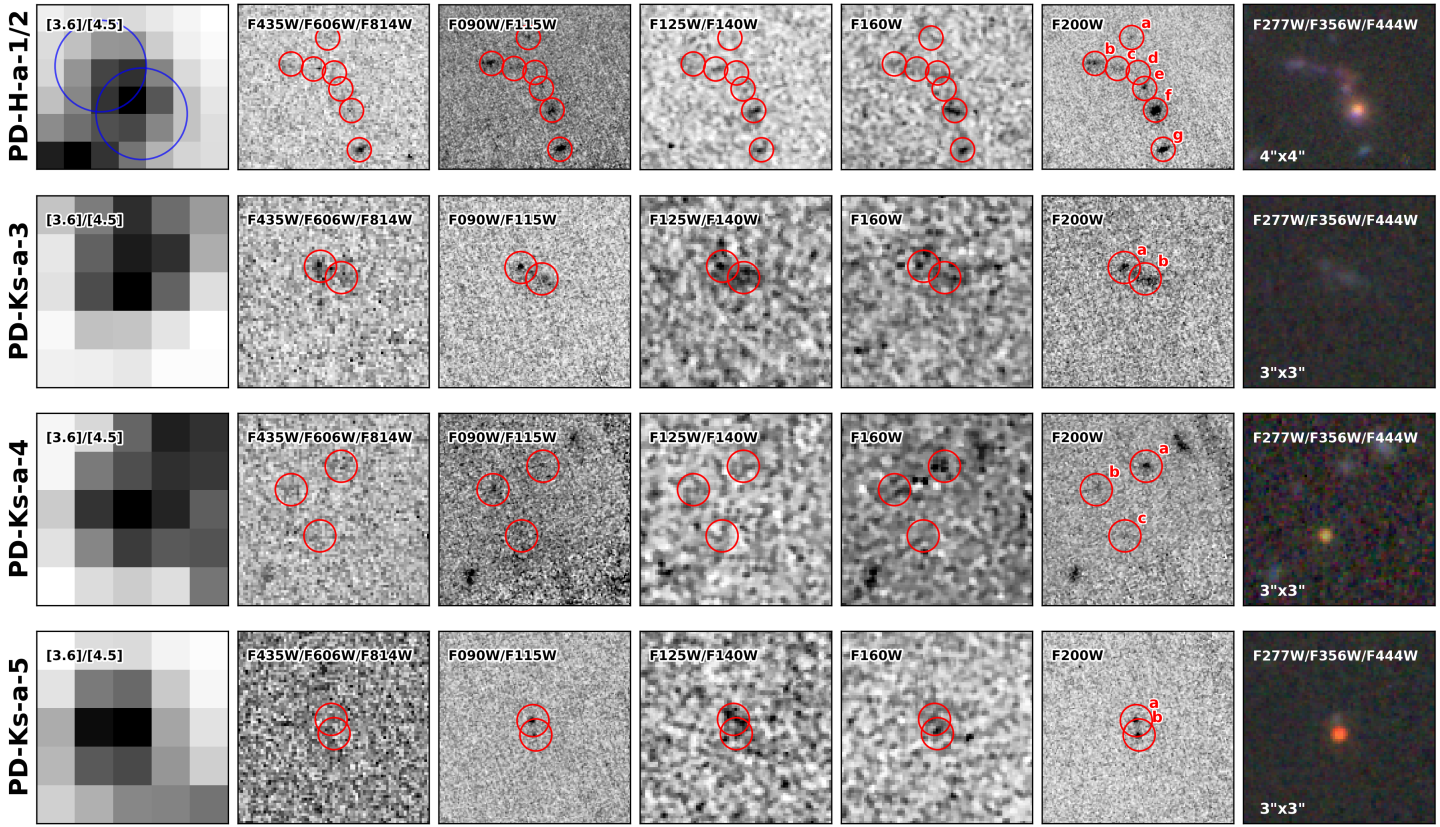

Figure 4.12 | Image cutouts for the five associated dropout candidates. The horizontal panels for each source show the same imaging as in Fig. 4.10. The red circles represent the $0\farcs5$ diameter circular aperture at the positions of the *JWST*-detected galaxies, which are annotated with their IDs on the F200W image cutout. As PD-H-a-1/2 is a system consisting of two IRAC detections, we indicate the $2''$ IRAC apertures on the 3.6 and 4.5 μm image stack in blue.

5

ALMA SUB-/MILLIMETER SOURCES AMONG *Spitzer* SMUVS GALAXIES AT $z > 2$ IN THE COSMOS FIELD

T.L. Suzuki, S.E. van Mierlo, and K.I. Caputi

This chapter has been accepted as *ALMA sub-/millimeter sources among Spitzer SMUVS galaxies at* $z > 2$ *in the COSMOS field* by The Astrophysical Journal.

ABSTRACT

Sub-millimeter observations reveal the star-formation activity obscured by dust in the young Universe. It still remains unclear how galaxies detected at sub-millimeter wavelengths are related to ultraviolet/optical-selected galaxies in terms of their observed quantities, physical properties, and evolutionary stages. Deep near- and mid-infrared observational data are crucial to characterize the stellar properties of galaxies detected with sub-millimeter emission. In this study, we make use of a galaxy catalog from the Spitzer Matching Survey of the UltraVISTA ultra-deep Stripes. By cross-matching with a sub-millimeter source catalog constructed with the archival data of the Atacama Large Millimeter/submillimeter Array (ALMA), we search for galaxies at $z > 2$ *with a sub-millimeter detection in our galaxy catalog. We find that the ALMA-detected galaxies at* $z > 2$ *are systematically massive and have redder* K_s*–[4.5] colors than the non-detected galaxies. The redder colors are consistent with the larger dust reddening values of the ALMA-detected galaxies obtained from SED fitting. We also find that the ALMA-detected galaxies tend to have brighter 4.5* μ*m magnitudes. This may suggest that they tend to have smaller mass-to-light ratios, and thus, to be younger than star-forming galaxies fainter at sub-millimeter wavelengths with similar stellar masses. We identify starburst galaxies with high specific star-formation rates among both ALMA-detected and non-detected SMUVS sources. Irrespective of their brightness at sub-millimeter wavelengths, these populations have similar dust reddening values, which may suggest a variety of dust SED shapes among the starburst galaxies at* $z > 2$.

5.1. INTRODUCTION

Star-formation in galaxies is accompanied by dust production, and the ultraviolet (UV) light from young and massive stars in star-formation regions is absorbed by dust and re-emitted as thermal emission at infrared (IR) wavelengths. It is crucial to trace both the dust-obscured and unobscured components of the galaxy spectrum in order to account for the total star-formation activity in galaxies in an unbiased way. The fraction of dust-obscured star-formation in the cosmic star-formation rate density is said to increase with redshifts up to $z \sim 2$ (e.g.,Takeuchi et al. 2005; Burgarella et al. 2013, and Madau & Dickinson 2014 for review). Furthermore, recent sub-millimeter (mm) observations suggest that $\sim$ 40–50% of the total star-forming activity is obscured by dust at higher redshifts, such as $z \sim$ 3–4 (e.g., Bouwens et al. 2016; Zavala et al. 2021) or even out to $z \sim 7$ (Algera et al. 2023).The dust-obscured star-formation is considered to play an important role in galaxy formation and evolution across cosmic time.

Sub-mm bright galaxies (SMGs) were first identified with sub-mm observations with single-dish telescopes, and their observed flux densities at $\sim 850\,\mu$m – 1 mm are typically larger than a few mJy (e.g., Smail et al. 1997; Barger et al. 1998; Hughes et al. 1998). Follow-up observations with high angular resolutions using large radio interferometries, such as the Atacama Large Millimeter/sub-millimeter Array (ALMA), allow us to pin down the positions of SMGs on the sky, and thus, make it easier to find their optical counterparts. With the multi-wavelength photometric information from optical to radio, the physical properties of SMGs are characterized (e.g., Hodge et al. 2013; da Cunha et al. 2015; Michałowski et al. 2017; Miettinen et al. 2017; Dudzevičiūtė et al. 2020). SMGs are said to be typically massive ($\log(\mathrm{M}_* / \mathrm{M}_\odot) > 10$) and have high star formation rates (SFRs) of a few 100–1000 $\mathrm{M}_\odot\,\mathrm{yr}^{-1}$ (see Hodge & da Cunha 2020, for recent review). Furthermore, deep blind surveys (e.g., Dunlop et al. 2017; Aravena et al. 2020; Franco et al. 2020; Yamaguchi et al. 2020) or individual observation programs targeting UV/optical-selected galaxies (e.g., Scoville et al. 2016; Wiklind et al. 2019; Tadaki et al. 2020) with ALMA reveal a population of galaxies with fainter sub-mm fluxes of $\lesssim 1$ mJy. Such relatively sub-mm faint galaxies are also typically massive with $\log(M_* / M_\odot) > 10$ and have SFRs of $\gtrsim 10\,M_\odot \mathrm{yr}^{-1}$.

A systematic comparison between sub-mm detected galaxies and UV/optical-selected galaxies at the same epoch is crucial to understand what galaxy populations are traced by the sub-mm observations and what is the role of such sub-mm detected galaxies on galaxy formation and evolution at high redshifts in a broader context. Deep near-infrared (NIR) and mid-infrared (MIR) photometric data are required to estimate the stellar properties of sub-mm detected galaxies at high redshifts accurately given their strong dust extinction (e.g., Dudzevičiūtė et al. 2020; Franco et al. 2020; Yamaguchi et al. 2020). This makes it possible to compare sub-mm detected galaxies and relatively sub-mm-faint galaxies systematically. The *Spitzer* Matching survey of the UltraVISTA ultra-deep Stripes (SMUVS; P.I. Caputi; Ashby et al. 2018; Ashby et al. 2020) is a *Spitzer* (Werner et al. 2004) Exploration Science Program with the Infrared Array Camera (IRAC; Fazio et al. 2004). SMUVS conducted ultra-deep 3.6μm and 4.5μm imaging observations in part of the COSMOS field (Scoville et al. 2007; COSMOS Project 2020). The survey area is matched with that covered by the UltraVISTA ultra-deep NIR imaging observations (McCracken et al. 2012), as well as the ultra-deep Subaru imaging (Taniguchi et al. 2007). The point-source sensitivity of the

IRAC 3.6 μm and 4.5 μm channels in SMUVS reaches down to 25 mag with 4σ significance (Ashby et al. 2018). The wide-field and deep *Spitzer*/IRAC data by SMUVS enables us to construct a stellar mass-selected galaxy sample at $z > 2$ (Deshmukh et al. 2018), which is expected to be insensitive to the presence of dust obscuration in galaxies. The SMUVS galaxy sample is suitable to systematically investigate the physical properties of dusty and non-dusty galaxies at high redshifts once the observational data at far-IR and/or sub-mm wavelengths is available.

In this study, we combined the SMUVS galaxy catalog with a public sub-mm source catalog constructed with the ALMA archival data in the COSMOS field (A^{3}COSMOS; Liu et al. 2019) to investigate the dust-obscured star-formation activities of galaxies in the SMUVS catalog. At the same time, we also searched for the SMUVS sources located in ALMA maps but have no counterpart in the A^{3}COSMOS catalog. By constructing two samples of galaxies both detected and undetected at sub-mm wavelengths, we aim to conduct a systematic comparison between sub-mm bright and sub-mm faint galaxies at the same epoch.

This paper is organized as follows: in Sect. 5.2, we describe the galaxy catalog obtained by SMUVS briefly and explain the counterpart search for the SMUVS sources at $z > 2$ in a sub-mm source catalog. In Sect. 5.3, we explain our stacking analysis for the ALMA non-detected sources and the SED fitting analysis with the multi-wavelength data from optical to sub-mm. We show our results and discuss the difference between the ALMA-detected and non-detected SMUVS sources at $z > 2$ in Sect. 5.4. In Sect. 5.5, we summarize the main findings of this study. Throughout this paper, we use the cosmological parameters of $H_0 = 70$ km s^{-1} Mpc^{-1}, $\Omega_\mathrm{m} = 0.3$ and $\Omega_\Lambda = 0.7$. We assume a Chabrier (2003) initial mass function (IMF). Magnitudes are given in the AB system (Oke & Gunn 1983).

5.2. ALMA COUNTERPART SEARCH FOR SMUVS GALAXIES

5.2.1. SMUVS GALAXY CATALOG

Source detection and photometry of the SMUVS sources were described in Deshmukh et al. (2018). The source detection in SMUVS was primarily done with UltraVISTA data release 3 (DR3) HK_s stack maps. At the positions of the detected sources in the HK_s images, the photometry on the SMUVS 3.6 and 4.5 μm mosaics was obtained with a PSF-fitting technique using the DAOPHOT package on IRAF. When the photometry was not successfully obtained with this PSF-fitting technique, the fluxes of the IRAC channels are measured with a $2.4''$ diameter circular aperture at the positions of the HK_s stack maps and then converted to the total fluxes by multiplying the aperture fluxes by a factor of 2.13. The sources detected in at least one IRAC channel are referred as the “SMUVS sources” (Deshmukh et al. 2018). There are a total of $\sim 300{,}000$ SMUVS galaxies over 0.66 deg^2.

In this work, we use a newer version of the SMUVS catalog, which includes updated UltraVISTA photometry from DR4. van Mierlo et al. (2022) conducted the Spectral Energy Distribution (SED) fitting for the SMUVS sources with the SED fitting code LEPHARE (Arnouts et al. 1999; Ilbert et al. 2006). They used the following photometric information available in the COSMOS field together with IRAC 3.6 and 4.5μm data from SMUVS: CFHT *u*-band; Subaru *B, V, r,* i_p, z_p, z_{pp}, *IA427, IA464, IA484, IA505, IA527, IA624, IA679, IA709, IA738, IA767, IA827, NB711,* and *NB816*; *HST F814W*; and UltraVISTA *Y, J, H* and K_s. The fluxes of these 26 bands were measured with a 2″ diameter aperture and then converted to the total fluxes by applying point-source aperture corrections in each band (Deshmukh et al. 2018; van Mierlo et al. 2022). Because the source detection and photometry in SMUVS are optimized mainly for galaxies at $z > 2$, we focus on galaxies at $z > 2$. In the following analysis, we use the photometric redshifts, stellar masses and dust reddening values $E(B-V)$ of the best-fit SEDs obtained from LEPHARE.

5.2.2. SUB-MM COUNTERPART SEARCH WITH A^{3}COSMOS CATALOG

We use a public sub-mm source catalog from the A^{3}COSMOS project[1] (Liu et al. 2019) to search for SMUVS sources at $z > 2$ with ALMA counterparts. The A^{3}COSMOS catalog is constructed with the ALMA archival data in the COSMOS field. We used the sub-mm source catalog with the version of 20180801. There are two public catalogs of the continuum sources, namely, the blind source catalog and the prior source catalog. We combined the two source catalogs by matching the coordinates with a 1″ searching radius as done in Liu et al. (2019). Then, we conducted the cross-match with the SMUVS catalog by using the coordinates in the A^{3}COSMOS prior source catalog for the sub-mm sources. In this study, we focused on the sub-mm sources detected at Band 6 (∼1.2 mm) or Band 7 (∼ 870μm). As a result of cross-matching with a matching radius of 1″, we found 157 SMUVS sources at $z > 2$ that have at least one counterpart in the A^{3}COSMOS catalog. The median separation between the coordinates from the SMUVS and A^{3}COSMOS catalog is 0.″17. The separation is smaller than 0.″4 for 90% of the cross-matched sources. We also visually checked whether the dust continuum emission is spatially associated to the stellar continuum emission with the ALMA maps and the K_s-band images from UltraVISTA DR4. We confirmed that the searching radius of 1″ is reasonable for the counterpart search.

In the following, we use the total flux in the A^{3}COSMOS prior source catalog. When the sources were observed with the same band at least twice in different observing programs, we used the information with the closest separation from the SMUVS positions. Among 157 SMUVS sources with A^{3}COSMOS counterpart, 22 sources were detected with both Band 6 and 7. Furthermore, six sources are detected with other bands, such as Band 3, 4 or 8, as well.

5.2.3. SMUVS SOURCES WITHOUT A^{3}COSMOS COUNTERPART

We searched for the SMUVS sources at $z = 2.0$–5.5 that are covered by the ALMA maps in the A^{3}COSMOS catalog but have no counterpart in the A^{3}COSMOS catalog. These SMUVS sources can be regarded as galaxies with fainter sub-mm continuum flux as compared to the sources with A^{3}COSMOS counterparts. The areal coverage of the ALMA maps in A^{3}COSMOS is 79.5 arcmin^2 and 54.7 arcmin^2 for Band 6 and Band 7, respectively (Liu et al. 2019). Because the outer region in an ALMA map has lower sensitivity due to the primary beam attenuation, we consider only the SMUVS sources in the inner regions with the primary beam response of ≥ 0.5. This leads to the exclusion of the sources that are not

---

[1] `https://sites.google.com/view/a3cosmos/home?authuser=0`

detected with dust emission due to shallow sensitivity limits. We also removed the ALMA maps with smaller beam sizes of $b_{\rm maj} \lesssim 0.6''$ in order to ensure that the given upper limits based on the RMS level per beam can be compared with the total sub-mm fluxes of the ALMA-detected sources. When a source was observed multiple times with the same band, we used the map with the smallest RMS level.

We measured the aperture fluxes of the SMUVS sources without a counterpart in the $\rm A^3$COSMOS catalog for a stacking analysis (see Sect. 5.3.1 for more detailed explanation). We used the ALMA maps selected as mentioned above and measured the fluxes at the positions of the SMUVS sources with an $1\rlap{.}''5$ radius aperture. We found that two sources have an aperture flux with $\rm S/N \geq 3$ and that the sub-mm continuum emission is spatially associated to the $K_{\rm s}$-band images, which means that these sources can be regarded as detected at sub-mm wavelengths. One source has a counterpart in the $\rm A^3$COSMOS prior catalog only, and thus, was not identified in our counterpart search described in Sect. 5.2.2, which requires the detection in both the prior and blind source catalog. The other source is not included in both the $\rm A^3$COSMOS prior and blind source catalog probably due to the faintness of the sub-mm flux and/or NIR flux used for the prior fit in Liu et al. (2019). We add the two sources to the sample of the ALMA-detected SMUVS sources and use the aperture fluxes as the total fluxes in the following analysis.

5.2.4. SAMPLE OF SMUVS GALAXIES DETECTED/NON-DETECTED WITH ALMA

We cross-matched the ALMA-detected and non-detected SMUVS sources with spectroscopic redshift catalogs available in the COSMOS field (e.g., Lilly et al. 2007; Comparat et al. 2015; Kriek et al. 2015; Le Fèvre et al. 2015; Hasinger et al. 2018). We found 11 ALMA-detected and 62 non-detected SMUVS sources with spectroscopic redshifts. We then evaluated the photometric redshift accuracy of the two samples with the fraction of outliers, which are defined as $\sigma = |z_{\rm spec} - z_{\rm phot}|/(1+z_{\rm spec}) \geq 0.15$, and the normalized median absolute deviation (MAD), the median of σ multiplied by 1.48 (Laigle et al. 2016). The ALMA-detected SMUVS sources have an outlier fraction of 18% and $\sigma_{\rm MAD} = 0.051$. As for the non-detected SMUVS sources, the outlier fraction is 15% and $\sigma_{\rm MAD} = 0.035$. Both the outlier fraction and $\sigma_{\rm MAD}$ are similar between the ALMA-detected and non-detected SMUVS sources, which means that the accuracy of the photometric redshifts from the SMUVS survey does not strongly depend on the sub-mm brightness.

We also cross-matched our samples with the *Chandra* X-ray point source catalog (Civano et al. 2016). Nine ALMA-detected and 27 non-detected SMUVS sources have X-ray counterpart, and among of them, three and nine sources, respectively, have spectroscopic redshifts too. It turned out that two out of the three ALMA-detected sources with X-ray counterparts and six out of the nine non-detected sources with X-ray counterparts were classified as the photometric redshift outliers. These sources are at $z_{\rm spec} < 2$, and thus, active galactic nuclei (AGN) at lower redshift. This indicates that the SMUVS sources with X-ray counterparts are more likely to be AGN at $z < 2$. Given the possibility that the SED fitting with galaxy templates would not work well for X-ray AGN even for ones with the correct photometric redshifts, we decided to remove all the X-ray sources in the following analysis. We removed the photo-z outliers with no X-ray counterpart as well.

Table 5.1 | The number of the SMUVS sources at $z = 2.0$–5.5 with and without ALMA detection. Among 145 ALMA-detected SMUVS sources, 20 sources are detected with both Band 6 and 7. As for the non-detected SMUVS sources, 87 sources have the flux upper limit in both Band 6 and 7.

ALMA detection	Band 6 (~ 1.2 mm)	Band 7 (~ 870 μm)	Total
Yes	97	68	145
No	1309	637	1859

After removing the photo-z outliers and X-ray-detected sources, the number of the ALMA-detected and non-detected SMUVS sources becomes 150 and 1859, respectively. Moreover, as explained in detail in Sect. 5.3.2, we removed five ALMA-detected SMUVS sources, which are considered to be poorly fitted with MAGPHYS. The number of galaxies in each sample used in the following analysis is summarized in Table 5.1. We assigned 4.2σ upper limits on the sub-mm fluxes of the SMUVS sources without ALMA detection according to the detection limit of 4.2σ for the prior fitting sub-mm source catalog in Liu et al. (2019).

Fig. 5.1 shows the stellar mass of the ALMA-detected and non-detected SMUVS sources at $z = 2.0$–5.5 as a function of redshift. The top and right histogram shows the comparison of the redshift and stellar mass distribution of the two samples, respectively. We note that the stellar masses shown in Fig. 5.1 come from the best-fit SEDs obtained from LEPHARE (van Mierlo et al. 2022). Whereas the ALMA-detected and non-detected SMUVS sources have a similar redshift distribution, the ALMA-detected sources are systematically more massive ($\log(M_*/M_\odot) > 10$) as compared to the non-detected sources. The median stellar mass of the ALMA-detected and non-detected SMUVS sources is $\log(M_*/M_\odot) = 10.51$ and 9.40, respectively. This trend is expected because previous sub-mm observations show that the galaxy selection based on the sub-mm brightness preferentially picks up massive star-forming galaxies (e.g., da Cunha et al. 2015; Dunlop et al. 2017; Yamaguchi et al. 2020; Dudzevičiūtė et al. 2020). In Fig. 5.2, we show the flux (upper limit) at 1.2 mm and 870 μm of the ALMA-detected and non-detected SMUVS sources as a function of stellar mass at $z = 2.0$–3.0 and at $z = 3.0$–5.5, separately. The non-detected SMUVS sources have reasonable upper limits on their continuum fluxes as compared to the dust continuum fluxes of the individually detected sources at a given stellar mass. We note that the ALMA non-detected SMUVS sources include not only sub-mm faint star-forming galaxies but also galaxies with little star-formation because we do not apply any cut on the star-formation activity of galaxies.

5.3. ANALYSIS

5.3.1. STACKING ANALYSIS FOR THE NON-DETECTED SOURCES

We conducted a stacking analysis for the SMUVS sources without an ALMA counterpart to investigate their average sub-mm fluxes. Because the pixel scales and beam sizes vary between ALMA maps from different projects, we decided to follow the stacking method

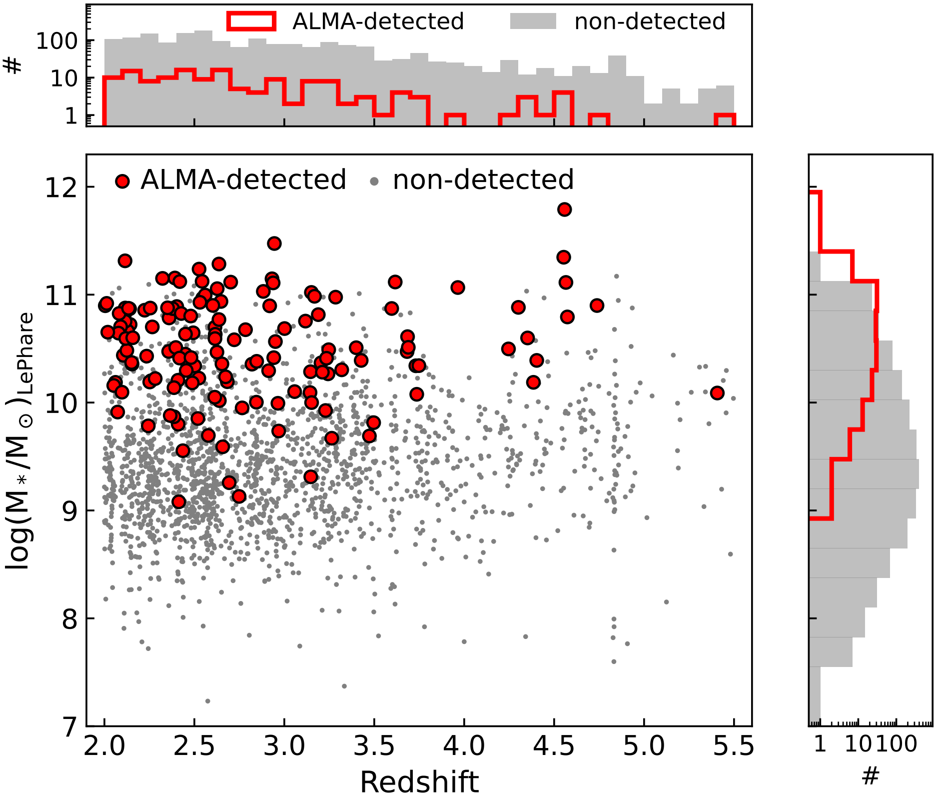

Figure 5.1 | Stellar mass of the ALMA-detected and non-detected SMUVS sources analyzed in this study as a function of redshift. Stellar masses and redshifts of both ALMA-detected and non-detected sources are from the best-fit SEDs obtained from LEPHARE with the 28 band photometry from u-band to 4.5 μm (van Mierlo et al. 2022). ALMA-detected sources are at the high-mass end of the mass distribution of the non-detected SMUVS sources whereas there is no clear difference between the redshift distributions of the two samples.

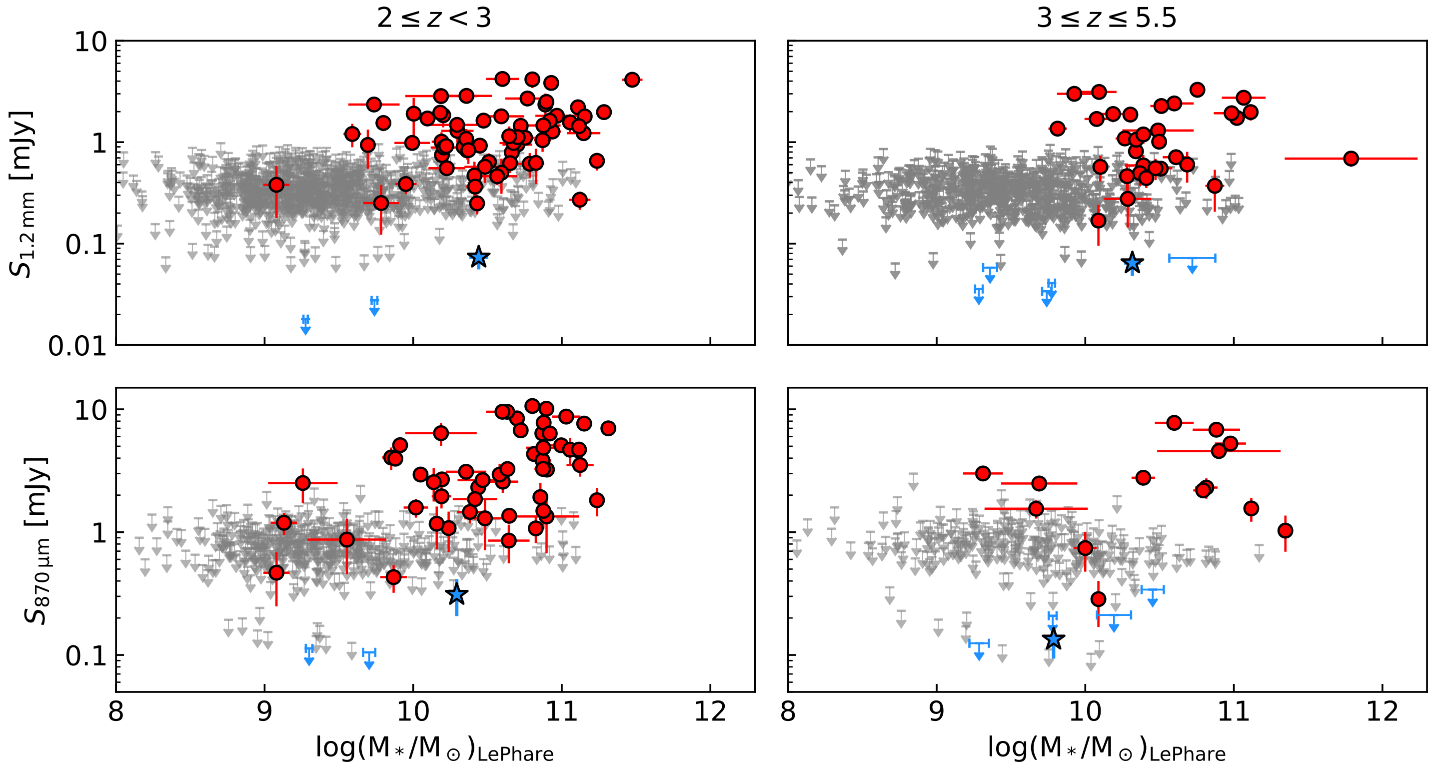

Figure 5.2 | Continuum flux (upper limit) at ~1.2 mm (top) and ~ 870 μm (bottom) as a function of stellar mass of the SMUVS sources in the two redshift bins, namely, $z = 2.0$–3.0 (left) and $z = 3.0$–5.5 (right), analyzed in this study. As for the non-detected SMUVS sources, we show 4.2σ upper limits after correcting for the primary beam attenuation (Liu et al. 2019). The non-detected SMUVS sources have reasonable upper limits on their continuum fluxes as compared to the individually detected SMUVS sources. The results of the stacking analysis for the non-detected sources are also shown with star symbols and arrows (Sect. 5.3.1).

with aperture fluxes applied in Fudamoto et al. (2020), who conducted the stacking analysis with the ALMA maps in the A^{3}COSMOS catalog. As a test, we measured the aperture fluxes of the ALMA-detected SMUVS sources and confirmed that the aperture fluxes show a good agreement with the total fluxes in the A^{3}COSMOS catalog when they are isolated. We conducted this test by changing the aperture radius, namely $r = 1.0$, 1.5, and 2.0$''$. The consistency with the total fluxes in the A^{3}COSMOS catalog does not change depending on the aperture size. Here we use $r = 1.5''$ apertures.

We divided the non-detected SMUVS sources at $z = 2.0$–5.5 with $\log(\mathrm{M}_*/\mathrm{M}_\odot) \geq 9.0$ into 18 subsamples according to their stellar masses, redshifts, and the observed wavelengths (Band 6 or 7) as summarized in Table 5.2. We measured the ALMA aperture fluxes of each non-detected source at the position from the SMUVS catalog. We use the ALMA maps before the primary beam correction released by the A^{3}COSMOS project[2]. The errors on the aperture fluxes are determined from the standard deviation of the aperture fluxes measured at 100 random positions in each ALMA map.

Before stacking, we removed the SMUVS sources that have a close sub-mm bright source which contaminates their aperture fluxes. We also removed passive galaxies, which are considered to be intrinsically faint at sub-mm, in order to increase the signal-to-noise ratio (S/N) of the stacking result. We followed the method applied in Deshmukh et al. (2018) to distinguish passive galaxies from star-forming galaxies. Deshmukh et al. (2018) divided the SMUVS galaxy sample at $z > 2$ into subsamples of passive galaxies, dusty star-forming galaxies, and non-dusty star-forming galaxies based on the rest-frame $u - r$ color and $E(B - V)$. According to their criteria, the non-detected SMUVS sources with $(u - r)_\mathrm{rest} > 1.3$ and $E(B - V) < 0.2$ were classified as passive galaxies and removed from the stacking analysis. The fraction of such sources is 5%.

When we stacked the aperture fluxes for each subsample, the aperture fluxes were weighted according to the RMS values after correcting for the primary beam attenuation at the position of the sources (Fudamoto et al. 2020). Errors on the stacked fluxes were estimated with the jackknife resampling method (e.g., Efron 1982). We generated N samples with the sample size of $N - 1$ from a SMUVS subsample with the size of N. The i-th source was removed from the i-th jackknife sample. Then, we calculated a stacked flux for each jackknife sample in the same manner as done for the SMUVS subsamples. We use the standard deviation of the stacked fluxes of the jackknife samples as an error on the stacked flux of the SMUVS subsample.

Table 5.2 summarizes the results of the stacking analysis. Four out of the 18 subsamples show stacked continuum fluxes with S/N > 3. As expected, subsamples consisting of galaxies with higher stellar masses and at lower redshift tend to have higher S/N. The remaining subsamples show the stacked fluxes with $< 3\sigma$ such that we adopt 3σ flux upper limits for them. The relation between the stacked fluxes and stellar masses of 18 subsamples is shown in Fig. 5.2. The detected subsamples have ~ 1 dex fainter fluxes as compared to the individually detected SMUVS with similar stellar masses. The comparison between the stacked subsamples and individually detected sources would indicate the large scatter of sub-mm continuum fluxes of star-forming galaxies even at the same stellar mass.

---

[2] `https://irsa.ipac.caltech.edu/data/COSMOS/overview.html`

Table 5.2 | Summary of the stacking analysis for the non-detected SMUVS sources at $z = 2.0–5.5$. When S/N< 3, the 3σ upper limits are assigned. The redshifts and stellar masses of the subsamples are estimated by taking a weighted average as done for the aperture fluxes.

Bins		Band-6 (1.2 mm)				Band-7 (870 μm)			
z	$\log(M_*/M_\odot)$	#	Stacked flux [mJy]	z	$\log(M_*/M_\odot)$	#	Stacked flux [mJy]	z	$\log(M_*/M_\odot)$
2.0–3.0	>10.0	83	0.073 ± 0.018	2.49 ± 0.05	10.44 ± 0.06	49	0.31 ± 0.10	2.34 ± 0.06	10.29 ± 0.03
	9.5–10.0	178	< 0.028	2.55 ± 0.04	9.74 ± 0.02	89	< 0.105	2.53 ± 0.06	9.70 ± 0.04
	9.0–9.5	294	< 0.018	2.48 ± 0.03	9.28 ± 0.01	148	< 0.113	2.46 ± 0.04	9.30 ± 0.02
3.0–4.0	>10.0	49	0.064 ± 0.016	3.45 ± 0.09	10.32 ± 0.05	30	< 0.341	3.71 ± 0.06	10.45 ± 0.07
	9.5–10.0	117	< 0.041	3.39 ± 0.05	9.77 ± 0.02	45	< 0.209	3.54 ± 0.07	9.78 ± 0.03
	9.0–9.5	124	< 0.036	3.46 ± 0.06	9.28 ± 0.03	48	< 0.125	3.56 ± 0.09	9.29 ± 0.07
4.0–5.5	>10.0	19	< 0.072	4.88 ± 0.11	10.72 ± 0.15	16	< 0.212	5.31 ± 0.17	10.19 ± 0.11
	9.5–10.0	47	< 0.034	4.57 ± 0.05	9.74 ± 0.03	26	0.134 ± 0.041	4.66 ± 0.25	9.79 ± 0.03
	9.0–9.5	38	< 0.058	4.70 ± 0.14	9.36 ± 0.05	–			

5.3.2. SED FITTING WITH MAGPHYS

We conducted an independent SED fitting of the ALMA-detected SMUVS sources in order to take into account their stellar and dust emission properties simultaneously. We used a SED fitting code MAGPHYS that can fit the SEDs from the optical to radio wavelengths consistently (da Cunha et al. 2008, 2015; Battisti et al. 2020).

MAGPHYS uses the stellar population synthesis models of Bruzual & Charlot (2003) assuming a Chabrier (2003) IMF and uses the two-component dust model of Charlot & Fall (2000) for the dust attenuation. The metallicity range is set to be 0.2–2.0$\times Z_\odot$, and the age range is 0.1–10 Gyr. Star-formation history is parameterized as a continuous delayed exponential function, in which the SFR rises linearly at the earlier epoch and then declines exponentially with the timescale defined by the γ parameter ($\gamma = 0.075$–1.5 Gyr^{-1}). MAGPHYS also includes starbursts of random duration and amplitude to account for the stochastic star-formation. We used the MAGPHYS high-z extension version 2, which includes the 2175Å feature in the dust attenuation curve (Battisti et al. 2020). The high-z extension version 2 uses the intergalactic medium (IGM) absorption in the UV regime from Inoue et al. (2014).

We combined the sub-mm detection(s) from ALMA with the broad-band photometry from the SMUVS catalog (van Mierlo et al. 2022). For bands in the optical to NIR regime, we inspect the S/N in each band, such that if S/N < 3, we instead adopt a 3σ flux upper limit in that band. Redshifts are fixed to photometric redshifts in the SMUVS catalog.

In order to maximize the constraints on the IR SEDs, we added photometric information in the IR regime other than the ALMA data. We used the IR photometric catalog constructed by Jin et al. (2018). This catalog contains multi-wavelength photometry ranging from *Spitzer*/IRAC 3.6 μm to the Karl G. Jansky Very Large Array (JVLA) 1.4 GHz, measured with the "super-deblending" technique developed by Liu et al. (2018). We cross-matched the coordinates of the ALMA-detected SMUVS sources with those of the sources in the super-deblended catalog of Jin et al. (2018) with a searching radius of $1''$. Most of the ALMA-detected SMUVS sources (~ 90%) have a counterpart in the super-deblended catalog. We added the photometric information from *Spitzer*/IRAC 5.8 μm to *Herschel*/SPIRE 500 μm to the photometric catalog of the ALMA-detected SMUVS sources. When S/N < 3, 3σ upper limits were assigned.

In order to evaluate the goodness of the fits obtained with MAGPHYS, we adopt the criterion introduced by Battisti et al. (2019). They classify the sources failed to fit based on their best-fit χ^2 values. They fit a Gaussian distribution to the lower 90 % population of a sample and determine the mean ($\bar{\chi^2}$) and dispersion ($\sigma(\chi^2)$). When $\chi^2 > \bar{\chi^2} + 4\sigma(\chi^2)$, the sources are considered to be poorly fitted. We found that five sources in our sample have a χ^2 value exceeding this criterion. The five sources are removed in the following analysis.

Fig. 5.3 shows the comparison of the stellar masses from LEPHARE and MAGPHYS of the ALMA-detected SMUVS sources at $z = 3.0$–5.5. We find that the stellar masses from MAGPHYS are systematically larger than those from LEPHARE. This effect was also shown in Battisti et al. (2019) (see also Michałowski et al. 2014). The difference between the two stellar mass measurements is ~ 0.25 dex on average.

We also conducted the SED fitting with MAGPHYS for the four stacked subsamples with the detection of $> 3\sigma$ (Sect. 5.3.1). In the following analysis, we use the median IR luminosities obtained with MAGPHYS to investigate the dust-obscured star-formation activities of the ALMA-detected SMUVS sources and the four stacking-detected subsamples. As for the stellar mass, we use the values obtained from LEPHARE for a consistency between the ALMA-detected and non-detected sources.

5.3.3. STAR FORMATION RATES

The absolute UV magnitudes at rest-frame 1450 Å from LEPHARE are available for all the SMUVS sources. We calculated SFRs from the rest-frame UV luminosities ($\mathrm{SFR_{UV}}$) with the following equation from Kennicutt (1998) scaled to a Chabrier (2003) IMF:

$$\mathrm{SFR_{UV}}\,[\mathrm{M_\odot\,yr^{-1}}] = 8.8\times10^{-29}\,L_\nu\,[\mathrm{erg\,s^{-1}\,Hz^{-1}}], \tag{5.1}$$

where L_ν is the luminosity at 1450 Å. As for the non-detected SMUVS sources, we calculated $\mathrm{SFR_{UV}}$ after correcting for the dust extinction using $E(B-V)$ from LEPHARE and the Calzetti et al. (2000) attenuation law. In the following analysis, we used the dust-extinction-corrected $\mathrm{SFR_{UV}}$ as the total SFR for the non-detected SMUVS sources. To estimate errors on $\mathrm{SFR_{UV}}$, we used the uncertainties on the observed fluxes close to 1450 Å in the rest-frame.

In the case of the ALMA-detected sources, we estimated SFRs by combining SFRs from the rest-frame UV luminosities and IR luminosities (e.g., Wuyts et al. 2011; Yamaguchi et al. 2020). IR luminosities are converted to $\mathrm{SFR_{IR}}$ with the Kennicutt (1998) prescription scaled to a Chabrier (2003) IMF and combined with $\mathrm{SFR_{UV}}$ before dust extinction correction as follows:

$$\begin{aligned}\mathrm{SFR_{UV+IR}}\,[\mathrm{M_\odot\,yr^{-1}}] = \quad & \mathrm{SFR_{UV,dust\,uncorr}} \\ & +1.09\times10^{-10}\,L_{\mathrm{IR}}[L_\odot],\end{aligned} \tag{5.2}$$

where L_{IR} is a median IR luminosity obtained from MAGPHYS (Sect. 5.3.2). The errors on $\mathrm{SFR_{IR}}$ are estimated using the 16 and 84 % percentile of the L_{IR} obtained from MAGPHYS.

5.4. RESULTS AND DISCUSSION

5.4.1. NIR/MIR BRIGHTNESS AND COLORS

Fig. 5.4 shows the comparison of observed quantities, namely, K_s-band magnitude, 4.5 μm magnitude, and K_s–[4.5] color, between the ALMA-detected and non-detected SMUVS sources at z = 2.0–5.5. We here gave a weight to each non-detected SMUVS source according to its stellar mass so that the weighted stellar mass distribution of the non-detected sources matches with the stellar mass distribution of the ALMA-detected sources. By using the weighted distribution of the non-detected sources for comparison, we can minimize the effect of the stellar mass dependency of each quantity.

The ALMA-detected and non-detected SMUVS sources at z = 2.0–5.5 have similar K_s-band magnitude distributions. On the other hand, the 4.5 μm magnitude distribution of the ALMA-detected SMUVS sources appears to be shifted toward brighter magnitudes as compared to that of the non-detected sources. When comparing the K_s–[4.5] color

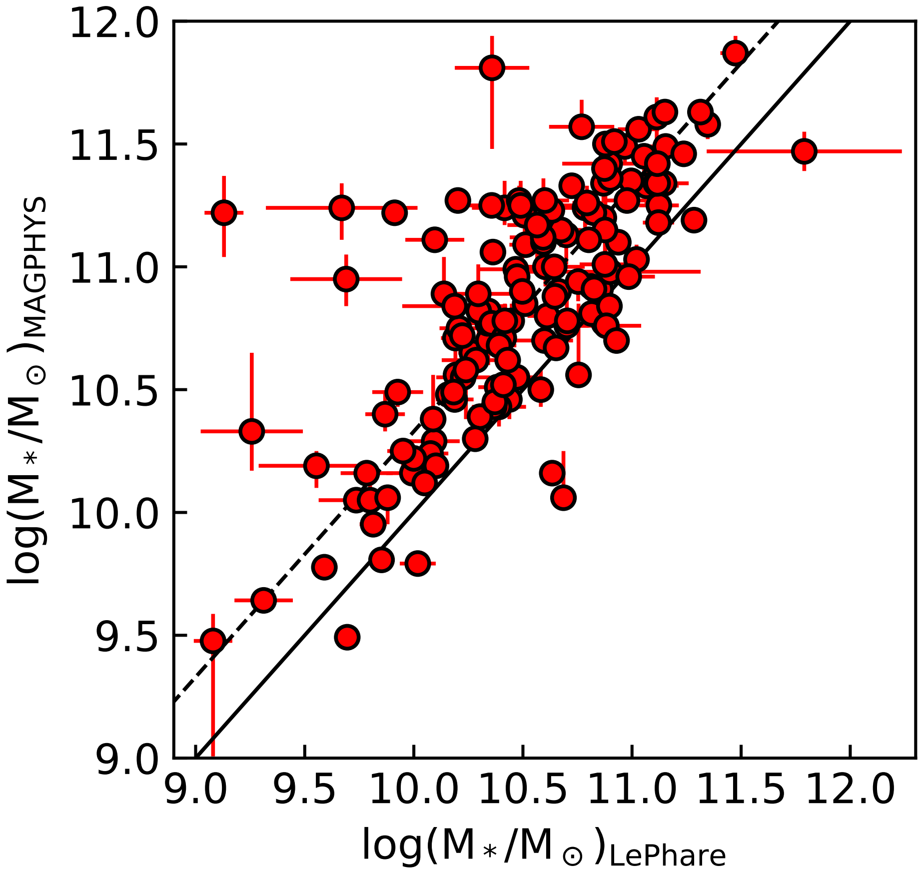

Figure 5.3 | Comparison of the stellar masses obtained from LEPHARE and MAGPHYS for the ALMA-detected SMUVS sources at $z = 2.0$–5.5. The solid line represents to the identity line. The dashed line represents the case when the stellar mass from MAGPHYS is 0.25 dex larger than that from LEPHARE. The stellar masses from MAGPHYS are systematically larger than those from LEPHARE.

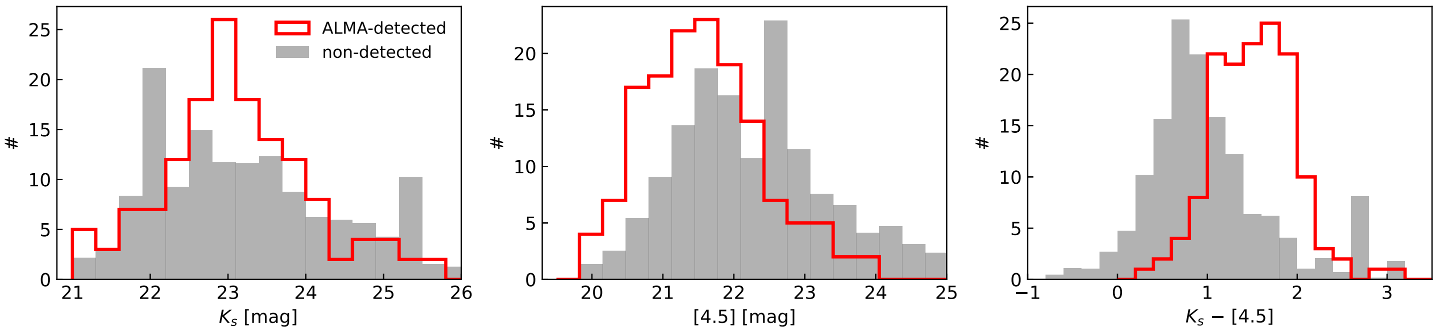

Figure 5.4 | Comparison of $K_{\rm S}$-band magnitude, 4.5 μm magnitude, and $K_{\rm S}$–[4.5] color between the ALMA-detected and non-detected SMUVS sources at $z = 2.0$–5.5. The histograms of the non-detected SMUVS sources are weighted according to the stellar masses so that the stellar mass distribution becomes the same between the ALMA-detected and non-detected sources. The ALMA-detected sources at $z \geq 2$ tend to be brighter at 4.5 μm and have systematically redder $K_{\rm S}$–[4.5] colors than the non-detected sources even when considering the difference of the stellar mass distributions.

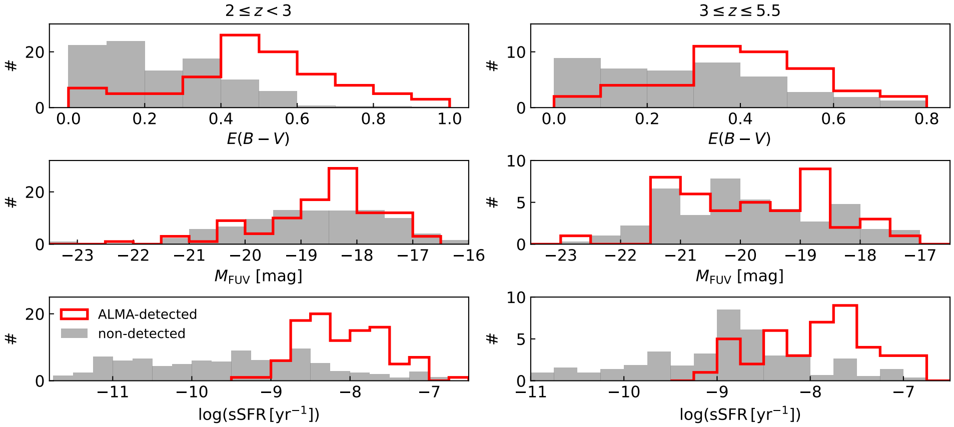

Figure 5.5 | Comparison of the physical quantities between the ALMA-detected and non-detected SMUVS sources at z = 2.0–3.0 (left) and z = 3.0–5.5 (right). Here, the non-detected SMUVS sources are weighted according to their stellar masses as done in Fig. 5.4. The ALMA-detected sources tend to be dustier and more active in star-formation than the non-detected sources.

distribution between the two samples, the ALMA-detected SMUVS sources tend to have redder colors of $K_{\rm S}$–[4.5] $\gtrsim$ 1.

Colors in the NIR and *Spitzer*/IRAC bands are used to select (extremely) dusty galaxies at high redshift (e.g., Wang et al. 2012; Chen et al. 2016; Wang et al. 2016). Wang et al. (2012) selected extremely red objects based on the $K_{\rm S}$–[4.5] colors (KIEROs, $K_{\rm S}$–[4.5]>1.6) and showed that the majority of KIEROs are massive ($\log(M_*/M_\odot)$ = 10–12) star-forming galaxies at z = 2–4. Of the ALMA-detected SMUVS sources, 44% have $K_{\rm S}$–[4.5] > 1.6 and 46% have bluer colors of $K_{\rm S}$–[4.5] = 1.0–1.6. A half of them are not as extremely red as KIEROs. These results suggest that the $K_{\rm S}$–[4.5] color is useful to select galaxies bright at sub-mm wavelengths at $z \geq 2$, and that applying a cut at $K_{\rm S}$–[4.5] ~ 1 would lead to an increase in completeness.

As shown in the next section, we find that the dust reddening values, $E(B-V)$, of the ALMA-detected SMUVS sources are systematically larger than those of the non-detected sources. The observed redder $K_{\rm S}$–[4.5] colors of the ALMA-detected SMUVS sources appear to be consistent with their stronger dust extinction (Wang et al. 2012). On the other hand, the trends of the $K_{\rm S}$-band and 4.5 μm magnitude distributions shown in Fig. 5.4 seem to be difficult to explain only with the different dust extinction strength between the two samples. Brighter 4.5 μm magnitudes of the ALMA-detected SMUVS sources may suggest that galaxies with bright sub-mm emission tend to have smaller mass-to-light ratios at $\lambda_{\rm obs}$ = 4.5 μm, and thus, tend to be younger as compared to those fainter at sub-mm wavelengths with similar stellar masses.

5.4.2. SED PROPERTIES

In Fig. 5.5, we compare $E(B-V)$, the dust *un*corrected absolute UV magnitude ($M_{\rm FUV}$), and specific SFR (= SFR/M$_*$) between the ALMA-detected and non-detected SMUVS sources. Here the histograms for the non-detected sources are weighted according to their stellar masses as done in Sect. 5.4.1. The weights are determined for each redshift bin.

The top two panels in Fig. 5.5 show that the ALMA-detected SMUVS sources tend to have larger dust reddening values than the non-detected sources. Most of the ALMA-detected SMUVS sources have $E(B-V) \geq 0.2$, and extend as far as $E(B-V) = 1.0$. As mentioned in Sect. 5.3.1, Deshmukh et al. (2018) used the rest-frame u–r color and $E(B-V)$ to classify SMUVS sources into three populations, namely, non-dusty star-forming galaxies ($(u-r)_{\rm rest} < 1.3$ and $E(B-V) \leq 0.1$), dusty star-forming galaxies ($E(B-V) \geq 0.2$), and passive galaxies ($(u-r)_{\rm rest} > 1.3$ and $E(B-V) \leq 0.1$). Among the ALMA-detected SMUVS sources, only 4% and 8% are classified as non-dusty star-forming galaxies and passive galaxies, respectively. This means that the classification in Deshmukh et al. (2018) works well for the sub-mm bright sources among the SMUVS sources and that LEPHARE appears to retrieve the dusty SEDs of the sub-mm-detected sources successfully, using only optical to IRAC photometry.

We find no clear difference between the $M_{\rm FUV}$ distributions of the ALMA-detected and non-detected sources. As for the sSFR distributions, sSFRs of the ALMA-detected sources appear to be biased toward higher values with $\log({\rm sSFR}\,[{\rm yr}^{-1}]) \gtrsim -8$. On the other hand, the non-detected sources cover a wide range of sSFR down to $\log({\rm sSFR}\,[{\rm yr}^{-1}]) \sim -11$. The lack of a clear difference between the $M_{\rm FUV}$ distributions may partly reflect the fact that galaxies can be fainter in the rest-frame UV because of either stronger dust extinction or lower star-formation activity.

The ALMA-detected SMUVS sources are systematically dustier and more active in star-formation than the non-detected sources, even after taking into account the difference between the stellar mass distributions. Such active star-formation of the ALMA-detected SMUVS sources would be consistent with their smaller mass-to-light ratios suggested in Sect. 5.4.1.

5.4.3. SMUVS SOURCES ON M_* VERSUS SFR DIAGRAM

Fig. 5.6 shows the M_*–SFR diagram for the ALMA-detected and non-detected SMUVS sources at $z = 2.0$–3.0 and $z = 3.0$–5.5. The non-detected SMUVS sources appear to show a bimodal distribution on this diagram. One sequence corresponds to the main sequence and the other corresponds to the starburst cloud located above the main sequence (e.g., Rodighiero et al. 2011). Such a bimodal distribution of SMUVS sources on the M_*–SFR diagram was reported by Caputi et al. (2017) using Hα excess galaxies at $3.9 \lesssim z \lesssim 4.9$ selected from the SMUVS catalog based on the photometric excess in IRAC 3.6 μm, and later confirmed by Rinaldi et al. (2022) to extend at all redshifts, $z \sim 3.0$–6.5, with an independent analysis. The definition of starburst galaxies is set to be $\log({\rm sSFR}\,[{\rm yr}^{-1}]) \geq -7.6$ in Caputi et al. (2017, 2021).

The ALMA-detected SMUVS sources appear distributed across the two sequences rather than distributed on either the star-forming main sequence or the starburst cloud. They are located at the high-mass end of the distribution of the non-detected SMUVS sources as shown in Fig. 5.3. The fraction of the ALMA-detected sources classified as starburst at $\log(M_*/M_\odot) \geq 9.5$ is 14% at $z = 2.0$–3.0 and 29% at $z = 3.0$–5.5. As for the non-

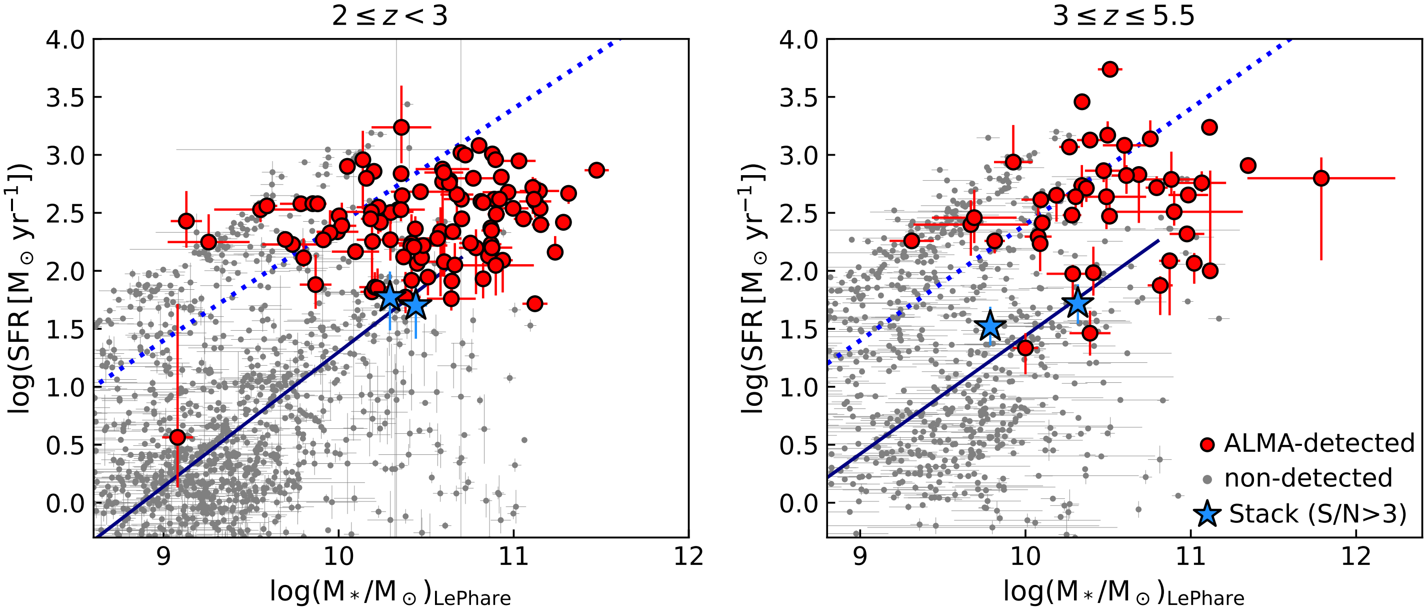

Figure 5.6 | Stellar mass versus SFR diagram of the SMUVS sources at $z = 2.0$–3.0 (left) and $z = 3.0$–5.5 (right). The stacking results with the detection greater than 3σ (Sect. 5.3.1) are also shown. The solid line in each panel represents the star-forming main sequence at $z = 2$–3 (left) and at $z = 3$–4 (right) from Santini et al. (2017). The dotted line shows the lower envelope of starburst galaxies defined by Caputi et al. (2021). The ALMA-detected SMUVS sources are located on and above the star-forming main sequence at the epoch.

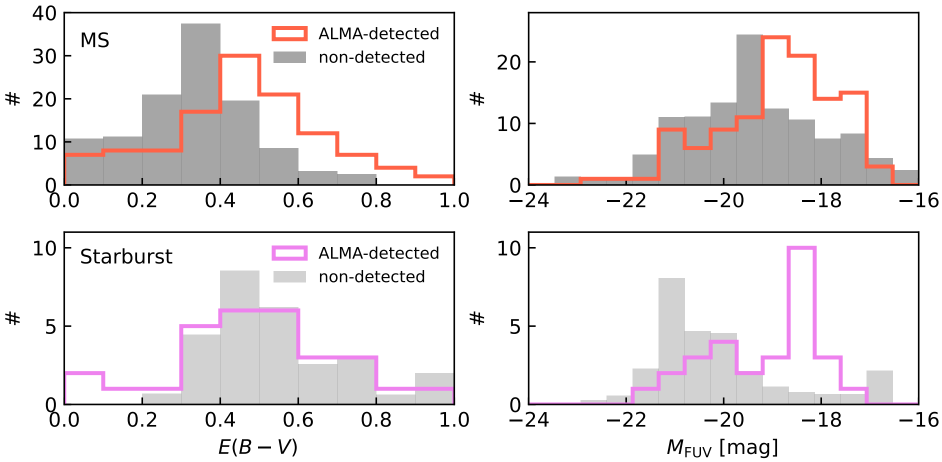

Figure 5.7 | Comparison of $E(B-V)$ (left) and $M_{\rm FUV}$ (right) between the ALMA-detected and non-detected galaxies after dividing the samples into two groups, namely, main sequence galaxies (top) and starburst galaxies (bottom). The non-detected sources are weighted according to their stellar masses. Passive galaxies among the non-detected SMUVS sources are excluded based on the criteria in Deshmukh et al. (2018).

detected SMUVS sources, the starburst fraction at $\log(\mathrm{M}_*/\mathrm{M}_\odot) \geq 9.5$ is 12% at $z = 2.0$–3.0 and 22% at $z = 3.0$–5.5. When we combine the two samples in each redshift bin, the starburst fraction becomes 12% at $z = 2.0$–3.0 and 23% at $z = 3.0$–5.5. The starburst fraction of our sample at $z = 3.0$–5.5 is consistent with the value of 22% obtained for galaxies with $\log(M_*/M_\odot) \geq 9.5$ at $z = 3.0$–5.0 in Rinaldi et al. (2022).

In Fig. 5.6, we also show the stacking results with the detection greater than 3σ (Table 5.2). Given the locus of the stacked subsamples on this diagram, these stacking results seem to reflect the physical properties of typical star-forming galaxies at $z = 2.0$–5.5 at the corresponding stellar mass range.

We calculate the fraction of the dust-obscured star-formation ($f_{\rm obscured} = \mathrm{SFR}_{\rm IR}/\mathrm{SFR}_{\rm UV+IR}$) for these stacked subsamples as well as the individually detected SMUVS sources. Whereas most of the ALMA-detected SMUVS sources have $f_{\rm obscured} \sim 0.99$ irrespective of their stellar masses, the stacked subsamples have $f_{\rm obscured} \sim 0.77$–$0.93$. At a given stellar mass, the non-detected SMUVS sources appear to have a smaller contribution from the dust-obscured star-formation as compared to the individual detected sources on average. A similar trend is reported by Koprowski et al. (2020) using Lyman Break Galaxies at $3 \leq z \leq 5$ with and without ALMA detection.

5.4.4. STARBURST GALAXIES AMONG SMUVS SOURCES

Fig. 5.7 shows the comparison of $E(B-V)$ and $M_{\rm FUV}$ between the ALMA-detected and non-detected SMUVS sources at $z = 2.0$–5.5 after dividing the whole sample into two groups, namely, main sequence galaxies and starburst galaxies (Sect. 5.4.3). Here, we exclude the passive galaxies classified with the Deshmukh et al. (2018) method (Sect. 5.3.1).

As done in Fig. 5.4 and 5.5, the non-detected SMUVS sources are weighted according to their stellar masses. The weights are determined for the main sequence galaxies and starbursts, separately.

As for the main sequence galaxies, the trend seen in the $E(B-V)$ distributions is similar as what we showed for the whole sample in Fig. 5.5. The difference of the M_{FUV} distributions between the ALMA-detected and non-detected main sequence galaxies becomes clearer than the case of the whole sample. The top two panels of Fig. 5.7 indicate that the ALMA-detected main sequence galaxies are fainter in the rest-frame UV due to their stronger dust extinction. They would be more dust-rich than the non-detected main sequence galaxies with similar stellar masses. Different sub-mm brightness between the ALMA-detected and non-detected main sequence galaxies may reflect a variety of dust masses among main sequence galaxies at a given stellar mass.

As for the starbursts, we find that the ALMA-detected and non-detected starbursts have similar $E(B-V)$ distributions. Furthermore, the non-detected starbursts tend to have larger $E(B-V)$ values than the non-detected main sequence galaxies. The large $E(B-V)$ values of the non-detected starbursts seem to contradict the fact that they are faint at sub-mm wavelengths. These results may suggest that such non-detected starbursts have higher dust temperature, which leads to fainter sub-mm fluxes at a given IR luminosity. Indeed, it is suggested that active galaxies above the main sequence tend to have higher dust temperatures (e.g., Elbaz et al. 2011; Magnelli et al. 2014; Schreiber et al. 2018). We may see a variety of dust SED shapes among the starbursts at $z \geq 2$.

5.5. SUMMARY

We investigated the sub-mm properties of galaxies at $z = 2.0$–5.5 selected with the *Spitzer* SMUVS survey in the COSMOS field (Ashby et al. 2018; Deshmukh et al. 2018). We cross-matched the SMUVS catalog with the public sub-mm source catalog constructed with the ALMA archival data (A^{3}COSMOS; Liu et al. 2019). We also searched for SMUVS sources that are covered by the ALMA maps but have no counterpart in the A^{3}COSMOS catalog. We then conducted a stacking analysis for the SMUVS sources without ALMA counterparts to investigate their average sub-mm properties.

The ALMA-detected SMUVS sources are systematically massive with $\log(\mathrm{M}_*/\mathrm{M}_\odot) \geq 10.0$. Furthermore, we find that the ALMA-detected SMUVS sources have systematically redder K_s–[4.5] colors (K_s–[4.5] $\gtrsim 1.0$) than the non-detected sources even when considering the different stellar mass distributions between the two samples. The K_s–[4.5] color together with the stellar mass information would be useful to pick up galaxies with bright sub-mm emission at $z \geq 2$. We also find that the ALMA-detected SMUVS sources tend to have brighter 4.5 μm magnitudes, which may suggest that galaxies with bright sub-mm emission tend to have smaller mass-to-light ratios, and thus, to be younger than those fainter at sub-mm wavelengths with similar stellar masses.

When comparing the SED properties between the ALMA-detected and non-detected SMUVS sources, we find that the ALMA-detected SMUVS sources tend to have larger $E(B-V)$ values and higher sSFRs. SED fitting with LEPHARE on the optical-to-IRAC photometry retrieves the dusty SEDs of the sub-mm-detected sources at $z \geq 2$ successfully. Larger dust reddening values of the ALMA-detected SMUVS sources are consistent with the observed redder K_s–[4.5] colors.

On the M_*–SFR diagram, the SMUVS sources are distributed across two regions, namely the star-forming main sequence and the starburst cloud (Caputi et al. 2017; Rinaldi et al. 2022). Comparing $E(B-V)$ and $M_{\rm FUV}$ between the ALMA-detected and non-detected main sequence galaxies, we find that the ALMA-detected main sequence galaxies have larger $E(B-V)$ values and fainter $M_{\rm FUV}$, which suggests that they are likely more dust-rich than the non-detected main sequence galaxies with similar stellar masses. We find a different trend for the starburst galaxies. The non-detected starbursts have similar $E(B-V)$ values but brighter $M_{\rm FUV}$ as compared to the ALMA-detected starbursts. This may suggest that the non-detected starbursts have higher dust temperatures, and thus, become fainter at sub-mm wavelengths irrespective of their high star-formation activity.

High-resolution imaging observation with the *James Webb Space Telescope (JWST)* will enable us to investigate the rest-frame optical/NIR structures of SMUVS sources at $z > 2$. Investigating their internal structures with multi-band images from *JWST* would lead to further discussion on what causes the difference between the ALMA-detected and non-detected sources or the difference between the main sequence galaxies and starbursts at a given stellar mass. The wide-field observations with NIRCam and MIRI are now being conducted in the COSMOS field (COSMOS-Web; Casey et al. 2023). The NIRCam imaging data in four filters covering 0.54 deg^2 becomes available once the program is completed, and this will be a useful dataset for SMUVS sources.

ACKNOWLEDGEMENTS

We would like to thank the anonymous referee for a careful reading and constructive comments that improved the clarity of this paper. This work was performed with the support of the Canon Foundation in Europe. KC and SvM acknowledge funding from the European Research Council through the award of the Consolidator Grant ID 681627-BUILDUP. Kavli IPMU is supported by the World Premier International Research Center Initiative (WPI), MEXT, Japan.

This paper makes use of the following ALMA data: `ADS/JAO.ALMA#2011.0.00064.S`, `ADS/JAO.ALMA#2011.0.00097.S`, `ADS/JAO.ALMA#2011.0.00539.S`, `ADS/JAO.ALMA#2012.1.00076.S`, `ADS/JAO.ALMA#2012.1.00323.S`, `ADS/JAO.ALMA#2012.1.00523.S`, `ADS/JAO.ALMA#2012.1.00536.S`, `ADS/JAO.ALMA#2012.1.00978.S`, `ADS/JAO.ALMA#2013.1.00034.S`, `ADS/JAO.ALMA#2013.1.00118.S`, `ADS/JAO.ALMA#2013.1.00151.S`, `ADS/JAO.ALMA#2013.1.00208.S`, `ADS/JAO.ALMA#2013.1.00884.S`, `ADS/JAO.ALMA#2013.1.01258.S`, `ADS/JAO.ALMA#2013.1.01292.S`, `ADS/JAO.ALMA#2015.A.00026.S`, `ADS/JAO.ALMA#2015.1.00055.S`, `ADS/JAO.ALMA#2015.1.00137.S`, `ADS/JAO.ALMA#2015.1.00207.S`, `ADS/JAO.ALMA#2015.1.00260.S`, `ADS/JAO.ALMA#2015.1.00379.S`, `ADS/JAO.ALMA#2015.1.00388.S`, `ADS/JAO.ALMA#2015.1.00540.S`, `ADS/JAO.ALMA#2015.1.00568.S`, `ADS/JAO.ALMA#2015.1.00664.S`, `ADS/JAO.ALMA#2015.1.00704.S`, `ADS/JAO.ALMA#2015.1.00928.S`, `ADS/JAO.ALMA#2015.1.01074.S`, `ADS/JAO.ALMA#2015.1.01105.S`, `ADS/JAO.ALMA#2015.1.01111.S`, `ADS/JAO.ALMA#2015.1.01171.S`,

`ADS/JAO.ALMA#2015.1.01212.S`, `ADS/JAO.ALMA#2015.1.01495.S`, `ADS/JAO.ALMA#2016.1.00171.S`, `ADS/JAO.ALMA#2016.1.00279.S`, `ADS/JAO.ALMA#2016.1.00478.S`, `ADS/JAO.ALMA#2016.1.00804.S`, `ADS/JAO.ALMA#2016.1.01040.S`, `ADS/JAO.ALMA#2016.1.01208.S`.

ALMA is a partnership of ESO (representing its member states), NSF (USA) and NINS (Japan), together with NRC (Canada), MOST and ASIAA (Taiwan), and KASI (Republic of Korea), in cooperation with the Republic of Chile. The Joint ALMA Observatory is operated by ESO, AUI/NRAO and NAOJ.

REFERENCES

Algera, H. S. B., Inami, H., Oesch, P. A., et al. 2023, MNRAS, 518, 6142, doi: `10.1093/mnras/stac3195`

Aravena, M., Boogaard, L., Gónzalez-López, J., et al. 2020, ApJ, 901, 79, doi: `10.3847/1538-4357/ab99a2`

Arnouts, S., Cristiani, S., Moscardini, L., et al. 1999, MNRAS, 310, 540, doi: `10.1046/j.1365-8711.1999.02978.x`

Ashby, M. L. N., Caputi, K. I., Cowley, W., et al. 2018, ApJS, 237, 39, doi: `10.3847/1538-4365/aad4fb`

Ashby et al. 2020, Spitzer Matching Survey of the Ultra-VISTA Deep Stripes, IPAC, doi: `10.26131/IRSA401`

Barger, A. J., Cowie, L. L., Sanders, D. B., et al. 1998, Nature, 394, 248, doi: `10.1038/28338`

Battisti, A. J., Cunha, E. d., Shivaei, I., & Calzetti, D. 2020, ApJ, 888, 108, doi: `10.3847/1538-4357/ab5fdd`

Battisti, A. J., da Cunha, E., Grasha, K., et al. 2019, ApJ, 882, 61, doi: `10.3847/1538-4357/ab345d`

Bouwens, R. J., Aravena, M., Decarli, R., et al. 2016, ApJ, 833, 72, doi: `10.3847/1538-4357/833/1/72`

Bruzual, G., & Charlot, S. 2003, MNRAS, 344, 1000, doi: `10.1046/j.1365-8711.2003.06897.x`

Burgarella, D., Buat, V., Gruppioni, C., et al. 2013, A&A, 554, A70, doi: `10.1051/0004-6361/201321651`

Calzetti, D., Armus, L., Bohlin, R. C., et al. 2000, ApJ, 533, 682, doi: `10.1086/308692`

Caputi, K. I., Deshmukh, S., Ashby, M. L. N., et al. 2017, ApJ, 849, 45, doi: `10.3847/1538-4357/aa901e`

Caputi, K. I., Caminha, G. B., Fujimoto, S., et al. 2021, ApJ, 908, 146, doi: `10.3847/1538-4357/abd4d0`

Casey, C. M., Kartaltepe, J. S., Drakos, N. E., et al. 2023, ApJ, 954, 31, doi: `10.3847/1538-4357/acc2bc`

Chabrier, G. 2003, PASP, 115, 763, doi: `10.1086/376392`

Charlot, S., & Fall, S. M. 2000, ApJ, 539, 718, doi: `10.1086/309250`

Chen, C.-C., Smail, I., Ivison, R. J., et al. 2016, ApJ, 820, 82, doi: `10.3847/0004-637X/820/2/82`

Civano, F., Marchesi, S., Comastri, A., et al. 2016, ApJ, 819, 62, doi: `10.3847/0004-637X/819/1/62`

Comparat, J., Richard, J., Kneib, J.-P., et al. 2015, A&A, 575, A40, doi: `10.1051/0004-6361/201424767`

COSMOS Project. 2020, Cosmic Evolution Survey with HST, IPAC, doi: `10.26131/IRSA178`

da Cunha, E., Charlot, S., & Elbaz, D. 2008, MNRAS, 388, 1595, doi: `10.1111/j.1365-2966.2008.13535.x`

da Cunha, E., Walter, F., Smail, I. R., et al. 2015, ApJ, 806, 110, doi: `10.1088/0004-637X/806/1/110`

Deshmukh, S., Caputi, K. I., Ashby, M. L. N., et al. 2018, ApJ, 864, 166, doi: `10.3847/1538-4357/aad9f5`

Dudzevičiūtė, U., Smail, I., Swinbank, A. M., et al. 2020, MNRAS, 494, 3828, doi: `10.1093/mnras/staa769`

Dunlop, J. S., McLure, R. J., Biggs, A. D., et al. 2017, MNRAS, 466, 861, doi: `10.1093/mnras/stw3088`

Efron, B. 1982, The Jackknife, the Bootstrap and Other Resampling Plans (Society for Industrial and Applied Mathematics), doi: `10.1137/1.9781611970319`

Elbaz, D., Dickinson, M., Hwang, H. S., et al. 2011, A&A, 533, A119, doi: `10.1051/0004-6361/201117239`

Fazio, G. G., Hora, J. L., Allen, L. E., et al. 2004, ApJS, 154, 10, doi: `10.1086/422843`

Franco, M., Elbaz, D., Zhou, L., et al. 2020, A&A, 643, A30, doi: `10.1051/0004-6361/202038312`

Fudamoto, Y., Oesch, P. A., Magnelli, B., et al. 2020, MNRAS, 491, 4724, doi: `10.1093/mnras/stz3248`

Hasinger, G., Capak, P., Salvato, M., et al. 2018, ApJ, 858, 77, doi: `10.3847/1538-4357/aabacf`

Hodge, J. A., & da Cunha, E. 2020, Royal Society Open Science, 7, 200556, doi: `10.1098/rsos.200556`

Hodge, J. A., Karim, A., Smail, I., et al. 2013, ApJ, 768, 91, doi: `10.1088/0004-637X/768/1/91`

Hughes, D. H., Serjeant, S., Dunlop, J., et al. 1998, Nature, 394, 241, doi: `10.1038/28328`

Ilbert, O., Arnouts, S., McCracken, H. J., et al. 2006, A&A, 457, 841, doi: `10.1051/0004-6361:20065138`

Inoue, A. K., Shimizu, I., Iwata, I., & Tanaka, M. 2014, MNRAS, 442, 1805, doi: `10.1093/mnras/stu936`

Jin, S., Daddi, E., Liu, D., et al. 2018, ApJ, 864, 56, doi: `10.3847/1538-4357/aad4af`

Kennicutt, R. C. 1998, ApJ, 498, 541, doi: `10.1086/305588`

Koprowski, M. P., Coppin, K. E. K., Geach, J. E., et al. 2020, MNRAS, 492, 4927, doi: `10.1093/mnras/staa160`

Kriek, M., Shapley, A. E., Reddy, N. A., et al. 2015, ApJS, 218, 15, doi: `10.1088/0067-0049/218/2/15`

Laigle, C., McCracken, H. J., Ilbert, O., et al. 2016, ApJS, 224, 24, doi: `10.3847/0067-0049/224/2/24`

Le Fèvre, O., Tasca, L. A. M., Cassata, P., et al. 2015, A&A, 576, A79, doi: `10.1051/0004-6361/201423829`

Lilly, S. J., Le Fèvre, O., Renzini, A., et al. 2007, ApJS, 172, 70, doi: `10.1086/516589`

Liu, D., Daddi, E., Dickinson, M., et al. 2018, ApJ, 853, 172, doi: `10.3847/1538-4357/aaa600`

Liu, D., Lang, P., Magnelli, B., et al. 2019, ApJS, 244, 40, doi: `10.3847/1538-4365/ab42da`

Madau, P., & Dickinson, M. 2014, ARA&A, 52, 415, doi: `10.1146/annurev-astro-081811-125615`

Magnelli, B., Lutz, D., Saintonge, A., et al. 2014, A&A, 561, A86, doi: `10.1051/0004-6361/201322217`

McCracken, H. J., Milvang-Jensen, B., Dunlop, J., et al. 2012, A&A, 544, A156, doi: `10.1051/0004-6361/201219507`

Michałowski, M. J., Hayward, C. C., Dunlop, J. S., et al. 2014, A&A, 571, A75, doi: `10.1051/0004-6361/201424174`

Michałowski, M. J., Dunlop, J. S., Koprowski, M. P., et al. 2017, MNRAS, 469, 492, doi: `10.1093/mnras/stx861`

Miettinen, O., Delvecchio, I., Smolčić, V., et al. 2017, A&A, 606, A17, doi: `10.1051/0004-6361/201730762`

Oke, J. B., & Gunn, J. E. 1983, ApJ, 266, 713, doi: `10.1086/160817`

Rinaldi, P., Caputi, K. I., van Mierlo, S. E., et al. 2022, ApJ, 930, 128, doi: `10.3847/1538-4357/ac5d39`

Rodighiero, G., Daddi, E., Baronchelli, I., et al. 2011, ApJL, 739, L40, doi: `10.1088/2041-8205/739/2/L40`

Santini, P., Fontana, A., Castellano, M., et al. 2017, ApJ, 847, 76, doi: `10.3847/1538-4357/aa8874`

Schreiber, C., Elbaz, D., Pannella, M., et al. 2018, A&A, 609, A30, doi: `10.1051/0004-6361/201731506`

Scoville, N., Aussel, H., Brusa, M., et al. 2007, ApJS, 172, 1, doi: `10.1086/516585`

Scoville, N., Sheth, K., Aussel, H., et al. 2016, ApJ, 820, 83, doi: `10.3847/0004-637X/820/2/83`

Smail, I., Ivison, R. J., & Blain, A. W. 1997, ApJL, 490, L5, doi: `10.1086/311017`

Tadaki, K.-i., Belli, S., Burkert, A., et al. 2020, ApJ, 901, 74, doi: `10.3847/1538-4357/abaf4a`

Takeuchi, T. T., Buat, V., Iglesias-Páramo, J., Boselli, A., & Burgarella, D. 2005, A&A, 432, 423, doi: `10.1051/0004-6361:20042189`

Taniguchi, Y., Scoville, N., Murayama, T., et al. 2007, ApJS, 172, 9, doi: `10.1086/516596`

van Mierlo, S. E., Caputi, K. I., Ashby, M., et al. 2022, A&A, 666, A200, doi: `10.1051/0004-6361/202243950`

Wang, T., Elbaz, D., Schreiber, C., et al. 2016, ApJ, 816, 84, doi: `10.3847/0004-637X/816/2/84`

Wang, W.-H., Barger, A. J., & Cowie, L. L. 2012, ApJ, 744, 155, doi: `10.1088/0004-637X/744/2/155`

Werner, M. W., Roellig, T. L., Low, F. J., et al. 2004, ApJS, 154, 1, doi: `10.1086/422992`

Wiklind, T., Ferguson, H. C., Guo, Y., et al. 2019, ApJ, 878, 83, doi: `10.3847/1538-4357/ab1089`

Wuyts, S., Förster Schreiber, N. M., Lutz, D., et al. 2011, ApJ, 738, 106, doi: `10.1088/0004-637X/738/1/106`

Yamaguchi, Y., Kohno, K., Hatsukade, B., et al. 2020, PASJ, 72, 69, doi: `10.1093/pasj/psaa057`

Zavala, J. A., Casey, C. M., Manning, S. M., et al. 2021, ApJ, 909, 165, doi: `10.3847/1538-4357/abdb27`

6

CONCLUSIONS AND FUTURE PROSPECTS

In this thesis, I have used large near-infrared (NIR) galaxy surveys to embark on multiple lines of research into the nature and evolutionary paths of high-redshift galaxies. The four scientific chapters in this thesis share one overarching theme: all of them are (partially) based on galaxy samples drawn from the *Spitzer* Matching Survey of the UltraVISTA ultra-deep Stripes (PI: K. Caputi, Ashby et al. 2018), a NIR-selected, 28-band photometric galaxy catalog in COSMOS containing over 300 000 galaxies at $z = 0$–9; photometric redshifts and SEDs derived with LEPHARE. This catalog contains photometric filters that provide relatively continuous sampling of the NIR wavelength regime ($\lambda = 1$–$5\ \mu m$), such that it is pre-eminently suitable for measuring stellar masses out to $z \sim 6$ through SED-fitting and simultaneously for high-redshift galaxy detection through the Lyman Break dropout technique. By exploiting this catalog, I investigated a variety of topics relevant to high-redshift galaxy evolution, ranging from preparatory tests for an upcoming space mission to a detailed investigation of the relation between stellar mass and star formation rate (SFR) for galaxies detected at sub-mm wavelengths.

In Chapter 2, we realized that the SMUVS catalog, through its large area size and depth, would make a suitable test ground for high-redshift simulations for the upcoming *Euclid* mission. As part of the pre-launch key projects of the Euclid Consortium, I investigated the recovery and reliability of $z = 6$–8 galaxies expected for the *Euclid* Deep Fields, thereby assessing their value for legacy science. I simulated and subsequently re-fitted combinations of *Euclid* and ancillary optical to NIR photometry from the fiducial best-fit SEDs of $\sim 176\,000$ real galaxies at $z = 1$–8 in the SMUVS catalog (referred to as the UltraVISTA-like bright sample), and $\sim 96\,000$ faint mock galaxies that complement the H-band depth difference between SMUVS and *Euclid*. I found that the recovery of $z > 6$ galaxies with *Euclid* alone will be very effective, with a recovery rate of 91(88)% for the UltraVISTA-like bright and faint mock sample respectively. The expected degree of contamination from fiducial $z = 1$–5.8 galaxies amongst apparent $z > 6$ *Euclid* galaxies will be low for the UltraVISTA-like bright galaxies, at only 18%, and increases for the fainter mock galaxies to

39%. Fortunately, the inclusion of ultra-deep optical data from the Rubin Deep Drilling Fields was found to significantly reduce the degree of contamination, to 4% and 7% for the real and mock samples respectively.

Given the enormous amount of *Euclid* data that will become available in the future, I explored if certain color spaces could be used to pre-select high-redshift galaxies before SED fitting, in an effort to reduce computational expenses. I found that UltraVISTA-like bright $z > 6$ galaxies and contaminants can be successfully separated with an $(I_{\mathrm{E}} - Y_{\mathrm{E}})$ & $(Y_{\mathrm{E}} - J_{\mathrm{E}})$ color cut, although this is impossible for the faint mock sample, as the majority of contaminants have unconstrained $(I_{\mathrm{E}} - Y_{\mathrm{E}})$ colors due to their faintness. Therefore, although we may be able to select a pure sample of bright $z > 6$ galaxies from *Euclid* colors alone, photometric redshifts cannot be circumvented to obtain a complete, statistically representative galaxy sample. Alternatively, I found that a 5σ signal-to-noise cut in any of the *Euclid* NISP bands can considerably reduce contamination of the faint mock $z > 6$ galaxies whilst maintaining completeness.

For the UltraVISTA-like bright sample, I investigated the nature of the $z > 6$ contaminants in more detail, finding that they are mistaken for $z > 6$ galaxies through typical Lyman break and 4000 Å break confusion, through strong dust-reddening, and through ill-defined, flat fiducial SEDs. As expected, I found that ancillary *Spitzer* photometry is essential for recovering stellar masses of $z > 6$ galaxies, as these data constrain the observed SED beyond the 4000 Å break. Lastly, the contaminants could not be effectively separated from true $z > 6$ galaxies based on their *Euclid*-derived physical parameters.

As *Euclid* is expected to detect millions of high-redshift galaxies, all the way out to $z = 10$, its extremely large and uniform observations of our Universe will solve longstanding issues plagued by cosmic variance. For example, no consensus exists on the shape of the bright-end of the galaxy stellar mass function (GSMF) to this day, its uncertainty dominated by cosmic variance and low-number statistics (e.g., Bowler et al. 2015; Bouwens et al. 2015). Down to $z \sim 6$, the combination of deep *Euclid* NIR imaging combined with ancillary *Spitzer* photometry should enable us to accurately measure stellar masses, thereby contributing to a uniform theory on the exact bright-end GSMF shape at this epoch. Beyond $z > 6$, *Euclid*, with its sensitivity and high resolution, will be suitable for galaxy detection, but the lack of mid-infrared (MIR) data supporting the mission means that stellar mass measurements will be inaccessible. For that reason, synergies between the *JWST* and *Euclid* arise for stellar mass studies during the EoR, as *JWST*/MIRI imaging extends to rest-frame 28 μm, enabling us to study the assembly of the very first galaxies.

For Chapter 3, we were inspired by the early *JWST* findings of extremely massive $\log(M_*/M_\odot) \approx 10$-$11$ galaxies at $z > 6$, which let to a sleuth of papers assessing how these galaxies could have possibly built up so much stellar mass under the ΛCDM cosmological framework (Boylan-Kolchin 2022; Haslbauer et al. 2022; Naidu et al. 2022; Lovell et al. 2023; Prada et al. 2023; Steinhardt et al. 2023; Zavala et al. 2023). Right along the arrival of these first *JWST*, we became familiar with the works of Ryan Endsley and co-authors, who studied the interesting AGN-host galaxy candidate COS-87259 at $z \sim 7$ that was also in my own galaxy catalog, albeit it with a significantly lower stellar mass (Endsley et al. 2021, 2022a,b). Therefore, I took this source as a case study to test the dependency of the stellar mass estimates on different SED fitting codes. I ran LEPHARE, PROSPECTOR, and EAZY on optical to NIR photometry, and included MIR to millimeter wavelength data for a fit with

Stardust.

I found that between six set-ups of codes and stellar population models, the stellar masses of COS-87259 span $\log(M_* / M_\odot) = 10.24$–$11.16$, whereas the fits are all of comparable quality. The highest stellar mass estimate is produced by PROSPECTOR with a non-parametric SFH, a set-up that has been frequently used to fit *JWST*-discovered high-redshift galaxies. On the other hand, galaxy templates with strong nebular line and continuum emission yield the lowest stellar mass estimate.

Revisiting the high stellar mass estimate $\log(M_* / M_\odot) = 11.2$ from Endsley et al. (2022b), although I could not replicate this result with any of the code set-ups, I concluded that the high-stellar mass does not violate ΛCDM number density upper limits. Ultimately, a full spectroscopic analysis of the NIR and MIR SED of COS-87259 will provide definite answers on its exact nature, especially to determine how much the AGN is contributing to the observed properties of the host galaxy. Moreover, even *JWST*/NIRCam imaging alone should be very useful for constraining its mass, as Santini et al. (2023) have already demonstrated how NIRCam data reduces the uncertainty on stellar mass measurements of $z > 7$ galaxies by up to a factor 10 compared to the highest quality data that was available pre-*JWST*.

In general, our analysis of COS-87259 showcases the importance of evaluating the properties of candidate EoR galaxies with multiple SED fitting routines, as non-negligible differences introduced between individual codes are ever persistent (e.g., Dahlen et al. 2013; Weaver et al. 2022; Pacifici et al. 2023), and templates suited for $z < 6$ galaxies may not reflect well the newly unveiled physics of the very first galaxies (Steinhardt et al. 2023; Larson et al. 2022).

For Chapter 4, I built upon existing efforts in cosmological fields field to search for extremely red, H- or K_s-band dropout galaxies (e.g., Caputi et al. 2012, 2015; Wang et al. 2019). However, this works stands out as the arrival of deep, highly-resolved *JWST*/NIRCam imaging enabled us for the first time to properly constrain the photometric redshifts and SEDs of this rare galaxy population, as these were only securely detected in *Spitzer*/IRAC imaging up to now.

Using the SMUVS program once again, I identified 26 IRAC-detected galaxies that are completely undetected the latest data release of the UltraVISTA VIRCAM H- and K_s-band imaging. I then followed up on the targets with newly available *JWST*/NIRCam data from the PRIMER program, together with ancillary *HST* optical to NIR imaging. With the improved sensitivity and resolution of these data, I found that half of the IRAC sources are in fact systems of multiple galaxies, and all but four are detected in the short-wavelength *JWST* channels.

From SED fitting, I found that the UltraVISTA dropout galaxies are primarily located at $z > 3$, with typical color excess of $E(B-V) = 0.5 \pm 0.3$ and stellar mass $\log(M_* / M_\odot) = 9.5 \pm 1.0$. Most importantly, 75 % of the sample display a NIRCam-band flux excess that can be interpreted as Hα emission. I derived (Hα + N[II] + S[II]) rest-frame equivalent widths (EW) of ~ 100–2200 Å, and Hα SFRs between ~ 5–$375\ M_\odot \mathrm{yr}^{-1}$. Placing the *JWST*-detected galaxies on the SFR-M_* plane, I found that 35 % are starburst galaxies, 40 % are main-sequence galaxies and the remaining 25 % reside in the star-formation valley. Finally, I identified amongst the 26 dropout candidates one AGN and six sub-millimeter sources, from ancillary X-ray and sub-mm data.

As for future endeavors, the high-redshift Hα emitters are prime candidates for follow-up spectroscopic observations with *JWST*/NIRSpec. Using fixed slit spectroscopy, and in particular the low spectral resolution configuration PRISM/CLEAR which operates at rest-frame $\lambda = 0.6$–$5.3\ \mu$m, the full rest-frame optical spectrum of the galaxies can be measured. Given that the median continuum magnitude in the band that captures the Hα emission line ranges between 26.3 and 24.7 AB magnitude, with less than half an hour observing time for each galaxy, we could obtain continuum SNR measurements of 4.7-7.5σ, assuming an observing mode optimized for faint sources. Such observations would enable a high SNR detection of the Hα line, together with a myriad of other optical emission lines including the unblended O[III]λ4346,λ4959,λ5007, and Hβ lines. The emission line detections could be used to confirm the photometric redshifts of the dropout candidates, as well as provide precise Hα SFRs and gas-phase metallicity and ionization parameter measurements from oxygen line ratios.

Furthermore, in this work, I have restricted the search for H- and K_S-dropout galaxies in UltraVISTA to the PRIMER area, as at the time of writing, this was the only region in COSMOS with substantial *JWST*/NIRCam imaging. However, this means I only utilized 4 % of the full UltraVISTA ultra-deep region (0.7 deg^2). The COSMOS-Web survey (PI: J. Kartaltepe; Casey et al. 2023) will conduct *JWST*/NIRCam imaging over a contiguous 0.54 deg^2 area in COSMOS. Although this program unfortunately does not include NIRCam F356W imaging, upon completion, it will reach 5σ point-source sensitivities of ∼ 27.5–28.2 mag in bands F115W, F150W, F277W, and F444W. In addition, as part of the calibration fields, *Euclid* will conduct deep visible to NIR imaging over the same area, such that the combination of these data should be able to constrain the photometric redshifts of dropout candidates over a large part of the UltraVISTA ultra-deep survey, and potentially discover many more Hα emitters.

In the final Chapter 5, together with my co-author Tomoko Suzuki, we combined the SMUVS catalog with archival sub-mm imaging from the A^{3}COSMOS catalog to investigate the sub-mm properties of galaxies at $z = 2.0$–5.5. By combining the deep optical and NIR photometry from the SMUVS catalog with the ALMA data, we were able to constrain the full optical to IR SED of these galaxies and thereby the full extent of stellar light dust reprocessing. In addition, we compared the sample with SMUVS galaxies that are located in the ALMA maps, but have no detection at sub-mm wavelengths.

We found that the ALMA-detected SMUVS sources are massive with $\log(M_*/M_\odot) \geq 10.0$, and have systematically redder K_S–[4.5] colors than the non-detected SMUVS galaxies, indicating that these two properties may be used to pre-select potential bright sub-mm galaxies at $z \geq 2$. In addition, the mass-matched ALMA-detected galaxies tend to be brighter at 4.5 μm wavelengths, such that galaxies with bright sub-mm emission may have smaller mass-to-light ratios (M/L), and therefore younger ages, than the non-detected galaxies. Between the mass-matched samples, we found large dust extinction values and high specific star formation rates for the ALMA-detected galaxies, such that the dusty SEDs of the sub-mm galaxies are successfully retrieved from optical to NIR data alone.

Subsequently, we re-derived the SED properties of the ALMA-detected SMUVS galaxies with MAGPHYS, thereby including both the SMUVS optical to NIR photometry and FIR/sub-mm data from ALMA and other IR facilities. We also derived the SFRs, using the rest-frame ultraviolet (UV) flux obtained with LEPHARE and the IR luminosity from MAGPHYS. Placing the ALMA-detected and non-detected galaxies on the SFR-M_* plane, we found that both are distributed over the star-forming main sequence and the starburst cloud. Remarkably, the non-detected starbursts have similar similar $E(B-V)$ values than the ALMA-detected starburst, suggesting that the former have higher dust temperatures.

Synergies between *JWST* and ALMA observations are proving to be very useful for high-redshift science. Striking numbers of $z > 12$ Lyman break candidate galaxies are currently being discovered with *JWST*, but some are found to be incredibly dusty star-forming galaxies or AGN host galaxies at $z \lesssim 7$ through ALMA sub-mm detections (Fujimoto et al. 2022; Zavala et al. 2023). Even if no significant ALMA detection is found, its absence and therefrom derived upper limits on sub-mm continuum and line emission can lead to conclusions on the galaxy metallicity or ISM density (Popping 2023; Kaasinen et al. 2023). On the other hand, *JWST* has been able to probe the $< 2\,\mu$m fluxes of ALMA/sub-mm galaxies that were previously undetected in the deepest *HST* imaging, shedding new light on the importance of extremely dust-obscured galaxies at $z > 4$ (McKinney et al. 2023).

Furthermore, ALMA can achieve angular resolution rivaling that of *JWST*/MIRI, enabling for the first time sub-arcsec studies of both the stellar and ionized gas properties of galaxies during the EoR (Álvarez-Márquez et al. 2023; Bakx et al. 2023). Some of the most massive ALMA-detected SMUVS sources in our work would provide excellent targets for spatially-resolved photometric follow-up with *JWST*/NIRCam and MIRI, probing the full IR SED with of galaxies that important constraints on galaxy formation and evolution.

REFERENCES

Álvarez-Márquez, J., Crespo Gómez, A., Colina, L., et al. 2023, A&A, 671, A105, doi: `10.1051/0004-6361/202245400`

Ashby, M. L. N., Caputi, K. I., Cowley, W., et al. 2018, ApJS, 237, 39, doi: `10.3847/1538-4365/aad4fb`

Bakx, T. J. L. C., Zavala, J. A., Mitsuhashi, I., et al. 2023, MNRAS, 519, 5076, doi: `10.1093/mnras/stac3723`

Bouwens, R. J., Illingworth, G. D., Oesch, P. A., et al. 2015, ApJ, 803, 34, doi: `10.1088/0004-637X/803/1/34`

Bowler, R. A. A., Dunlop, J. S., McLure, R. J., et al. 2015, MNRAS, 452, 1817, doi: `10.1093/mnras/stv1403`

Boylan-Kolchin, M. 2022, arXiv e-prints, arXiv:2208.01611. `https://arxiv.org/abs/2208.01611`

Caputi, K. I., Dunlop, J. S., McLure, R. J., et al. 2012, ApJL, 750, L20, doi: `10.1088/2041-8205/750/1/L20`

Caputi, K. I., Ilbert, O., Laigle, C., et al. 2015, ApJ, 810, 73, doi: `10.1088/0004-637X/810/1/73`

Casey, C. M., Kartaltepe, J. S., Drakos, N. E., et al. 2023, ApJ, 954, 31, doi: `10.3847/1538-4357/acc2bc`

Dahlen, T., Mobasher, B., Faber, S. M., et al. 2013, ApJ, 775, 93, doi: `10.1088/0004-637X/775/2/93`

Endsley, R., Stark, D. P., Chevallard, J., & Charlot, S. 2021, MNRAS, 500, 5229, doi: `10.1093/mnras/staa3370`

Endsley, R., Stark, D. P., Fan, X., et al. 2022a, MNRAS, 512, 4248, doi: `10.1093/mnras/stac737`

Endsley, R., Stark, D. P., Lyu, J., et al. 2022b, arXiv e-prints, arXiv:2206.00018. `https://arxiv.org/abs/2206.00018`

Fujimoto, S., Finkelstein, S. L., Burgarella, D., et al. 2022, arXiv e-prints, arXiv:2211.03896, doi: `10.48550/arXiv.2211.03896`

Haslbauer, M., Kroupa, P., Zonoozi, A. H., & Haghi, H. 2022, ApJL, 939, L31, doi: `10.3847/2041-8213/ac9a50`

Kaasinen, M., van Marrewijk, J., Popping, G., et al. 2023, A&A, 671, A29, doi: `10.1051/0004-6361/202245093`

Larson, R. L., Hutchison, T. A., Bagley, M., et al. 2022, arXiv e-prints, arXiv:2211.10035, doi: `10.48550/arXiv.2211.10035`

Lovell, C. C., Harrison, I., Harikane, Y., Tacchella, S., & Wilkins, S. M. 2023, MNRAS, 518, 2511, doi: `10.1093/mnras/stac3224`

McKinney, J., Manning, S. M., Cooper, O. R., et al. 2023, arXiv e-prints, arXiv:2304.07316, doi: `10.48550/arXiv.2304.07316`

Naidu, R. P., Oesch, P. A., Setton, D. J., et al. 2022, arXiv e-prints, arXiv:2208.02794. `https://arxiv.org/abs/2208.02794`

Pacifici, C., Iyer, K. G., Mobasher, B., et al. 2023, ApJ, 944, 141, doi: `10.3847/1538-4357/acacff`

Popping, G. 2023, A&A, 669, L8, doi: `10.1051/0004-6361/202244831`

Prada, F., Behroozi, P., Ishiyama, T., Klypin, A., & Pérez, E. 2023, arXiv e-prints, arXiv:2304.11911, doi: `10.48550/arXiv.2304.11911`

Santini, P., Fontana, A., Castellano, M., et al. 2023, ApJL, 942, L27, doi: `10.3847/2041-8213/ac9586`

Steinhardt, C. L., Kokorev, V., Rusakov, V., Garcia, E., & Sneppen, A. 2023, ApJL, 951, L40, doi: `10.3847/2041-8213/acdef6`

Wang, T., Schreiber, C., Elbaz, D., et al. 2019, Nature, 572, 211, doi: `10.1038/s41586-019-1452-4`

Weaver, J. R., Kauffmann, O. B., Ilbert, O., et al. 2022, ApJS, 258, 11, doi: `10.3847/1538-4365/ac3078`

Zavala, J. A., Buat, V., Casey, C. M., et al. 2023, ApJL, 943, L9, doi: `10.3847/2041-8213/acacfe`

LIST OF PUBLICATIONS

FIRST AUTHOR

1. Euclid Collaboration: **S.E. van Mierlo**, K.I. Caputi et al. (203 additional authors not shown), *Euclid preparation. XXI. Intermediate-redshift contaminants in the search for $z > 6$ galaxies within the Euclid Deep Survey*, Astronomy & Astrophysics, Volume 666, Article Number 200, October 2022, `https://doi.org/10.1051/0004-6361/202243950`.

2. **S.E. van Mierlo**, K.I. Caputi and V. Kokorev, *No Need for Extreme Stellar Masses at $z \sim 7$: A Test-case Study of COS-87259*, The Astrophysical Journal Letters, Volume 945, Issue 2, ID 21, October 2022, `https://doi.org/10.3847/2041-8213/acb773`.

3. **S.E. van Mierlo**, K.I. Caputi, V. Kokorev, and P. Rinalid, *A high incidence of dusty Hα emitters among UltraVISTA dropout galaxies in COSMOS revealed by JWST*, under review at the Astrophysical Journal.

CO-AUTHOR

1. T.L. Suzuki, **S.E. van Mierlo**, K. Caputi, *ALMA sub-/millimeter sources among Spitzer SMUVS galaxies at $z > 2$ in the COSMOS field*, The Astrophysical Journal, Volume 959, Issue 2, ID 82, December 2023, `https://doi.org/10.3847/1538-4357/ad023c`.

2. P. Rinaldi, K.I. Caputi, **S.E. van Mierlo**, M.L.N. Ashby, G.B. Caminha and E. Iani, *The Galaxy Starburst/Main-sequence Bimodality over Five Decades in Stellar Mass at $z \approx 3$–6.5*, The Astrophysical Journal, Volume 930, Issue 2, ID 128, May 2022, `https://doi.org/10.3847/1538-4357/ac5d39`.

3. Euclid Collaboration: E. Merlin, M. Castellano, ... **S.E. van Mierlo**, ... et al. (217 additional authors not shown), *Euclid preparation. XXV. The Euclid Morphology Challenge: Towards model-fitting photometry for billions of galaxies*, Astronomy & Astrophysics, Volume 671, Article Number 101, March 2023, `https://doi.org/10.1051/0004-6361/202245041`.

4. Euclid Collaboration: H. Bretonnière, U. Kuchner, ... **S.E. van Mierlo**, ... et al. (214 additional authors not shown), *Euclid preparation XXVI. The Euclid Morphology Challenge. Towards structural parameters for billions of galaxies*, Astronomy & Astrophysics, Volume 671, Article Number 102, March 2023, `https://doi.org/10.1051/0004-6361/202245042`.

5. Euclid Collaboration: L. Bisigello, C.J. Conselice, ... **S.E. van Mierlo**, ... et al. (195 additional authors not shown), *Euclid preparation: XXIII. Derivation of galaxy physical properties with deep machine learning using mock fluxes and H-band images*, Monthly Notices of the Royal Astronomical Society, Volume 520, Issue 3, Pages 3529–3548, April 2023, `https://doi.org/10.1093/mnras/stac3810`.

6. R. Navarro-Carrera, P. Rinaldi, K.I. Caputi, E. Iani, V. Kokorev, **S.E. van Mierlo**, *Constraints on the Faint End of the Galaxy Stellar Mass Function at $z \sim 4$–8 from Deep JWST Data*, accepted for publication in the Astrophysical Journal.

7. Euclid Collaboration: S. Paltani, J. Coupon, ... **S.E. van Mierlo**, ... et al. (213 additional authors not shown), *Euclid preparation: XXXI. The effect of the variations in photometric passbands on photometric-redshift accuracy*, Astronomy & Astrophysics, Volume 681, Article Number 66, January 2024, `https://doi.org/10.1051/0004-6361/202346993`.

SUMMARY

When you go to a dark, remote place at night and look up, you can see thousands of stars with the naked eye. All these big gas balls are relatively close within our own Milky Way galaxy. With a bit of luck, you might even spot the Andromeda galaxy: our nearest neighbor, which is about 2.5 million light-years away. However, hidden among all those bright points of light in the sky are a staggering number of galaxies that formed billions of years ago and whose light has finally reached us. Unfortunately, our eyes are not sensitive enough to see them, and the Earth's atmosphere blocks much of their light. But with a space telescope, astronomers can study these objects.

By observing these distant galaxies, we are essentially stepping into a time machine. Throughout the cosmic timeline, the Universe has been expanding in an accelerated manner, such that the light from the earliest galaxies has to travel a tremendous distance before reaching us. As the photons travel towards us, their wavelength stretches, shifting the light into the infrared part of the electromagnetic spectrum. By comparing the observed spectra of these galaxies with models, the degree of the so-called redshift z can be determined, which in turn reveals the location of these galaxies in space and time.

The ultimate goal of astronomy is to reconstruct the complete history of our Universe. This is made possible by numerous observations of galaxies at a wide range of redshifts. We know that the earliest galaxies are smaller and younger than the more evolved galaxies we see today. They contain fewer stars but are still actively converting gas into new stars. Deep space observations enable us to reconstruct populations of galaxies up to about one billion years after the Big Bang ($z \approx 6$) Beyond that, it becomes more challenging because there are fewer galaxies (only a few million years have passed, and building a stellar population takes time), and their visibility is greatly inhibited by the presence of large volumes of neutral hydrogen which absorb photons (unlike the mostly ionized Universe we have today, where this does not happen). This period is particularly interesting because the formation of the first galaxies and the accompanying phase transition of the Universe provide valuable insight into the evolution of the Universe.

Many of the new generation space telescopes are designed to observe a wide range of physical processes, including galaxies in the early Universe. Among them is the *Euclid* space telescope, which was launched in July 2023 and will perform deep observations in three extragalactic fields on the sky over the coming years, identifying thousands of galaxies at $z > 6$. On board are several instruments, including cameras sensitive to visible and infrared light, namely the VIS and NISP instruments. In Chapter 2 of this thesis, I examined, prior to the launch, how well *Euclid* would be able to identify $z > 6$ galaxies. To do this, I simulated photometric observations in the four *Euclid* filters, as well as optical/near-infrared filters from ancillary telescopes that will support the *Euclid* mission. The simulations were based on a portion of my catalog of $\sim 300\,000$ galaxies between $z = 0$–9, representative of the physical properties of galaxies over more than 13 billion years of cosmic history. These galaxies were identified with the Spitzer Matching Survey of the UltraVISTA ultra-deep Stripes (SMUVS; PI: K. Caputi; Ashby et al. 2018), after which I derived their redshifts and properties such as stellar mass and age based on photometric observations in 28 filters. This was done by comparing their light to models of stellar populations and selecting the best-fitting model in a process called SED fitting. This catalog, called the SMUVS catalog, forms the basis for each chapter in this thesis to varying degrees.

By applying the SED fitting process to the simulated observations in *Euclid* and other filters for $\sim 176\,000$ galaxies between $z = 1$–8, I examined for true $z > 6$ galaxies how well their *Euclid*-derived redshifts matched. I also investigated the level of "contamination" in my newly obtained, apparent $z > 6$ dataset. Contamination is a known issue in photometric studies of the early Universe, caused by the fact that the optical/near-infrared spectrum of a nearby, old and/or dusty galaxy can easily be confused for a distant galaxy; in these cases, little optical light is emitted compared to infrared light, making the galaxy appear "red". For old galaxies, this is primarily due to a lack of young, bright stars; for dusty galaxies, it is because the light from these young, bright stars is absorbed by cosmic dust and then re-emitted at longer wavelengths. While distant galaxies can also be old and dusty, their red spectrum is primarily explained by another phenomenon. Neutral hydrogen, which exists everywhere in the Universe in between galaxies, absorbs all photons more energetic than UV wavelengths, causing a sharp drop in a galaxy's light spectrum, known as the Lyman break. For distant galaxies, because of the expansion of the Universe, the Lyman break shifts from the UV to the optical regime, resulting in a red spectrum. The optical/near-infrared colors of distant galaxies and old/dusty nearby galaxies are thus very similar and easily confused.

I demonstrated in my research that, if there are only four Euclid observations for a galaxy, the recovery of $z > 6$ galaxies will be very effective, with a recovery rate of $\sim 90\%$. In addition, the contamination of actual $z > 6$ galaxies by interloping, low-redshift galaxies is only 18%. However, this increases to 39% for fainter galaxies with large uncertainties in their photometric observations. Fortunately, by considering more observations for SED fitting, specifically deep optical data from the Rubin telescope, the contamination decreases significantly to a maximum of 7%.

Because *Euclid* will observe millions of galaxies, I looked into effective ways to identify $z > 6$ galaxies without SED fitting, as it is a time-consuming and computationally expensive process. I showed that this is partially possible by imposing restrictions on the *Euclid* colors, where a color represents the difference between two observations at different wavelengths. This technique does not help for the fainter galaxies; for this population, it is more effective to introduce an uncertainty threshold for the observations themselves so that weak measurements with large uncertainties cannot be misinterpreted. Overall, I concluded that SED fitting all potential $z > 6$ galaxies cannot be circumvented.

SED fitting algorithms not only determine the degree of redshift for a galaxy but also important parameters such as the star formation rate and stellar mass. There are dozens of these SED fitting routines, which can produce rather different results for the same object. In Chapter 3, I investigated the level of dispersion for the galaxy COS-87259, for which other researchers had previously determined a redshift of $z = 7$ and a stellar mass of $10^{11.2}\,M_{\odot}$. Most galaxies at that redshift have stellar masses many orders of magnitude smaller, making this a surprising result with significant implications for the formation theories of the Universe. Therefore, I critically examined this galaxy by testing multiple SED fitting routines on an independent photometric dataset that I measured for COS-87259. I found that among six individual routines, the difference in stellar mass can be a full order of magnitude. This is mainly because different routines make different assumptions about the star formation history or the nebular line emission in COS-87259. However, I was unable to reproduce the stellar mass of the other researchers, such that it remains unclear how special COS-87259 in fact is. In the future, this can be clarified with spectroscopic measurements from the James Webb Space Telescope.

And that is not the only thing the James Webb Space Telescope (JWST) will be useful for. This long-awaited infrared telescope, launched in July 2022, has already shaken up the astronomical community in its first year of observations. Unlike previous infrared telescopes, JWST can achieve very deep observations with very high resolution, allowing us to finally reveal the smallest details in the most distant galaxies. In Chapter 4, I used photometric data from JWST to study a set of 26 galaxies. These galaxies were identified based on existing infrared observations but could not be further studied because they appeared absent in observations at shorter near-infrared wavelengths. The lack of data points made it impossible to derive their redshifts and properties until the deep JWST data arrived.

By analyzing the new JWST observations together with existing data from the Hubble Space Telescope using an SED fitting routine, I demonstrated that these 26 galaxies are, in fact, many more: JWST data allows us to distinguish individual galaxies that were blurred together in previous infrared observations with poor resolution. Nearly all of them are located in the first two billion years of the Universe. They are not large in stellar mass, but they contain a lot of cosmic dust. More importantly, I discovered that 75% of these galaxies emit Hα emission. This light comes directly from regions around young stars and is a very suitable indicator of the star formation rate in the galaxies. As a result, I determined that these 26 galaxies, on average, have a high star formation rate, and 35 % are starburst galaxies. This means they are forming an excessive number of stars compared to ordinary galaxies at similar redshifts. All in all, this rare and interesting population has provided us with new insights into the physical conditions of relatively faint galaxies that are often missed in galaxy population studies.

In the final part of this thesis, Chapter 5, we used the SMUVS catalog to study another special population of galaxies. These galaxies are special because they have been observed at very long wavelengths: the sub-/millimeter regime. Light at these wavelengths comes from cosmic dust in a galaxy. This dust consists of small silicate grains that float in the interstellar medium. They absorb the UV light from young stars and re-emit it at sub-/mm wavelengths. This light provides an alternative, indirect method for measuring the star formation rate in a galaxy. We observed the sub-mm light from these galaxies with ALMA, an interferometer consisting of 66 antennas in the Atacama Desert of Chile.

For this research, we focused on galaxies between $z = 2$–5.5. We measured the differences between galaxies that are visible at long wavelengths and those that are not, finding that ALMA-observed galaxies are larger in stellar mass and have redder colors, caused by the abundance of cosmic dust in these galaxies. We measured the star formation rate in both populations using UV and sub-mm light. We found that the ALMA-observed sample consists partially of normal star-forming galaxies and partially of starburst galaxies that a much higher star formation rate. Strangely, we also found galaxies that we classified as starbursts based on their UV light but which were detected in the ALMA observations, even though we would expect them to.

In summary, in this thesis, I used data from various ground- and space-based telescopes to make predictions for the identification of distant galaxies, to determine how dependent stellar mass measurements are on algorithms, to study the properties of a previously unknown population of galaxies, and to investigate how sub-mm galaxies differ from the typical galaxies that we do not see at such long wavelengths. This way, we have yet come one step closer to discovering what is hidden among those bright points of light on the sky.

SAMENVATTING

Als je ‘s nachts naar een donkere, afgelegen plek gaat en omhoogkijkt, zie je met het blote oog wel duizenden sterren. Deze grote gasbollen bevinden zich allemaal vrij nabij in ons eigen melkwegstelsel. Met een beetje geluk kijk je nog wat verder en kun je het Andromedastelsel zien; dit dichtstbijzijnde buurstelsel staat op zo’n 2,5 miljoen lichtjaar van ons af. Maar verstopt tussen al die felle lichtpunten op de hemel bevindt zich een verbluffende hoeveelheid sterrenstelsels die miljarden lichtjaren geleden al gevormd zijn, en wiens licht ons nu eindelijk bereikt heeft. Helaas zijn onze ogen niet gevoelig genoeg om ze te zien en blokkeert de atmosfeer van onze planeet een hoop van hun licht, maar met een ruimtetelescoop lukt het sterrenkundigen toch om deze objecten te bestuderen.

Met het observeren van deze verre stelsels stappen we als het ware in een tijdmachine. Gedurende de gehele kosmische tijdlijn is het heelal steeds sneller, steeds verder uitgedijd, met als gevolg dat het licht van de vroegst gevormde sterrenstelsels een enorme afstand moet afleggen voordat het ons bereikt. Die uitdijing zorgt ervoor dat, terwijl de fotonen naar ons toe reizen, hun golflengte wordt uitgerekt zodat het licht naar het infrarood gedeelte van het elektromagnetisch spectrum verschuift. Door het geobserveerde spectrum van de stelsels met modellen te vergelijken, kan de mate van de zogenaamde roodverschuiving z bepaald worden en daarmee de plaats van deze stelsels in ruimte en tijd.

Het ultieme doel van sterrenkunde is de reconstructie van de complete geschiedenis van ons heelal. Dit wordt mogelijk gemaakt door talloze observaties van sterrenstelsels op een breed scala van roodsverschuivingen. Hierdoor weten we dat de eerste stelsels kleiner en jonger zijn dan de verder geëvolueerde stelsels van nu. Ze bevatten minder sterren, maar zijn tegelijkertijd nog volop bezig met het omzetten van gas in nieuwe sterren. Met diepe ruimte-observaties kunnen we populaties van sterrenstelsels goed reconstrueren tot ongeveer één miljard jaar na de oerknal ($z \approx 6$); daarvoor is het lastiger, omdat er om te beginnen minder sterrenstelsels zijn (er zijn dan immers pas enkele miljoenen jaren verstreken, en het opbouwen van een sterrenpopulatie kost tijd) en hun zichtbaarheid drastisch afneemt door de aanwezigheid van grote volumes neutraal waterstof welke fotonen absorberen (in tegenstelling tot het grotendeels geïoniseerde universum van nu waarin dit niet gebeurd). Juist deze periode is bijzonder interessant, omdat de formering van de eerste sterrenstelsels en de daar bijkomende fasetransitie van het universum ons belangrijke inzichten brengt in de evolutie van het heelal.

Vele van de nieuwe generaties ruimtelescopen zijn zo ontworpen dat ze een grote variëteit aan fysische processen kunnen observeren, waaronder sterrenstelsels in het vroege heelal. Zo ook de *Euclid* ruimtetelescoop, die in juli 2023 werd gelanceerd en de komende jaren diepe observaties in onder andere drie zogenaamde extragalactische velden aan de hemel zal uitvoeren, om zo duizenden $z > 6$ stelsels te identificeren. Aan boord bevinden zich verscheidende instrumenten, waaronder camera’s gevoelig voor zichtbaar en infrarood licht, respectievelijk het VIS- en NISP-instrument. In Hoofdstuk 2 van deze scriptie onderzocht ik, vooraf aan de lancering, hoe goed *Euclid* in staat zal zijn om $z > 6$ sterrenstelsels te identificeren. Hiervoor simuleerde ik fotometrische waarnemingen in de vier *Euclid* filters, en optische/nabij-infrarood filters van andere telescopen die de *Euclid* missie zullen ondersteunen. De simulaties baseerde ik op een deel van mijn catalogus van $\sim 300\,000$ sterrenstelsels tussen $z = 0$–9, representatief voor de fysische eigenschappen van stelsels gedurende ruim 13 miljard jaar van onze kosmische geschiedenis. De stelsels in deze catalogus zijn geïdentificeerd met de *Spitzer* Matching Survey of the UltraVISTA ultra-deep Stripes (SMUVS; PI: K. Caputi; Ashby et al. 2018), waarna ik op basis van fotometrische waarnemingen in 28 filters hun roodverschuiving en eigenschappen als stellaire massa en leeftijd heb afgeleid. Dit deed ik door hun licht vergelijkingen met modellen van sterrenpopulaties, en het best-passende model te kiezen in een proces wat we *SED fitting* noemen. Deze catalogus, genaamd de SMUVS catalogus, vormt in meer of mindere mate de basis voor elk hoofdstuk in deze scriptie.

Door vervolgens het SED-fitting proces toe te passen op de gesimuleerde waarnemingen in de *Euclid* en bijkomstige filters voor onder andere $\sim 176\,000$ sterrenstelsels tussen $z = 1$–8, bekeek ik voor sterrenstelsels waarvan ik wist dat ze $z > 6$ hadden of de *Euclid* data-afgeleide roodverschuiving daarmee overeenkwam. Daarnaast onderzocht ik de mate van “vervuiling” in mijn nieuw-verkregen, ogenschijnlijke $z > 6$ dataset. De vervuiling is een bekend probleem in fotometrische studies van het vroege heelal, en wordt veroorzaakt doordat het optische/nabij-infrarood spectrum van een dichterbij gelegen oud en/of kosmisch stof-behoudend sterrenstelsel makkelijk verward kan worden voor een ver sterrenstelsel; in deze gevallen wordt er weinig optisch licht ten opzichte van infrarood licht uitgestraald, zodat het stelsel er “rood” uitziet. Bij oude stelsels komt dit door een gebrek aan jonge, felle sterren; bij stoffige stelsels juist doordat het licht van jonge, felle sterren geabsorbeerd wordt door kosmisch stof en vervolgens op langere golflengtes weer wordt uitgezonden. Hoewel verre sterrenstelsels ook oud en stoffig kunnen zijn, is hun rode spectrum in de eerste plaats anders te verklaren. Neutraal waterstof, wat zich overal in het heelal tussen sterrenstelsels bevindt, absorbeert alle fotonen energetischer dan UV golflengtes, wat een scherpe daling in het lichtspectrum van een sterrenstelsel veroorzaakt: de zogenaamde Lyman break. Voor verre stelsels verplaatst roodverschuiving de Lyman break van het UV naar het optische regime, resulterend in een rood spectrum. De optische/nabij-infrarode kleuren van verre sterrenstelsels en oude en/of stoffige nabije stelsels zijn dus erg vergelijkbaar, en makkelijk met elkaar te verwarren.

Ik heb in mijn onderzoek aangetoond dat, als er voor een sterrenstelsel enkel vier *Euclid* waarnemingen zijn, deze data in staat is de roodverschuivingen van $\sim 90\%$ van de stelsels correct te achterhalen. Daarnaast is de vervuiling van daadwerkelijke $z > 6$ stelsels door ongewenste, lage-roodverschuiving stelsels slechts 18%. Dit neemt echter toe naar 39% voor minder felle sterrenstelsels die een grote onzekerheid in hun fotometrische waarnemingen hebben. Door meer waarnemingen in acht te nemen voor het SED fitten, specifiek met diepe, optische data van de Rubin telescoop, neemt de vervuiling gelukkig flink af naar maximaal 7%.

Omdat *Euclid* wel miljoenen sterrenstelsels zal waarnemen, heb ik gekeken of er effectieve manieren bestaan om $z > 6$ stelsels te identificeren zonder SED fitting, want dat is een tijdrovend en computer-technisch kostbaar proces. Ik toonde aan dat dit gedeeltelijk mogelijk is door restricties op de *Euclid* kleuren te zetten, waarbij een kleur het verschil tussen twee waarnemingen op verschillende golflengtes is. Deze techniek helpt niet voor de minder felle stelsels; voor deze populatie is het effectiever om een onzekerheidsdrempel voor de waarnemingen zelf te introduceren, zodat zwakke metingen met grote onzekerheden niet verkeerd geïnterpreteerd kunnen worden. Over het algemeen concludeerde ik dat het SED fitten van alle potentiële $z > 6$ niet te ontkomen is.

SED-fitting algoritmes bepalen niet enkel de mate van roodverschuiving voor een stelsel; aan de hand van fotometrische waarnemingen kunnen ook de belangrijke parameters als de mate van stervorming en de stellaire massa bepaald worden. Er bestaan tientallen van deze SED-fitting routines, met als gevolg dat voor hetzelfde object, de resultaten van deze routines nogal kunnen verschillen. In Hoofdstuk 3 heb ik deze mate van dispersie onderzocht voor het sterrenstelsel COS-87259, waarvoor andere onderzoekers eerder een roodverschuiving van $z = 7$ en een stellaire massa van $10^{11.2}\,M_{\odot}$ bepaalden. De meeste sterrenstelsels op die roodverschuiving hebben stellaire massa's vele ordes van grootte kleiner, waardoor dit een nogal verrassend resultaat was, met belangrijke implicaties voor formatie theorieën van het heelal. Daarom heb ik dit stelsel kritisch onderzocht door meerdere SED-fitting routines te testen op een onafhankelijke fotometrische dataset die ik zelf heb gemeten voor COS-87259. Ik vond dat tussen zes individuele routines, het verschil in stellair massa kan wel tienvoudig zijn. Dit komt vooral doordat verschillende routines verschillende aannames over geschiedenis van de sterformatie of de nebulaire emissielijnen in COS-87259 maken. Hoe dan ook, het lukte mij niet om de stellaire massa van de andere onderzoekers te reproduceren, waardoor het nog altijd onduidelijk is hoe speciaal COS-87259 precies is. In de toekomst kan dit opgehelderd worden met spectroscopische metingen met de James Webb Ruimte Telescoop.

Dat is niet het enige waar de James Webb Ruimte Telescoop (JWST) goed voor zal zijn. Deze langverwachte infraroodtelescoop die in juli 2022 werd gelanceerd heeft al in het eerste observatiejaar de sterrenkundige gemeenschap op zijn kop gezet. In tegenstelling tot voorgaande infraroodtelescopen kan de JWST zeer diepe observaties met zeer hoge resolutie maken, waardoor we eindelijk scherp kunnen stellen op de kleinste details in de meest verre sterrenstelsels. In Hoofdstuk 4 gebruikte ik fotometrische data van de JWST om een set van 26 sterrenstelsels te bestuderen. Deze sterrenstelsels heb ik geïdentificeerd met behulp van bestaande infrarood waarnemingen, maar kon ik niet verder bestuderen omdat ze klaarblijkelijk afwezig waren in waarnemingen op lagere golflengtes in het nabij-infrarode regime. Het gebrek aan datapunten maakte het afleiden van hun roodverschuiving en eigenschappen onmogelijk; totdat de diepe JWST data arriveerde.

Door de nieuwe JWST waarnemingen samen met bestaande data van de Hubble Ruimte Telescoop te analyseren met een SED-fitting routine, heb ik aangetoond dat deze 26 sterrenstelsels er in werkelijkheid veel meer zijn: met JWST data kunnen we individuele stelsels onderscheiden die in eerdere infrarood waarnemingen vervaagden door de slechte resolutie. Ze bevinden zich vrijwel allemaal in de eerste twee miljard jaar van het Universum. Ze hebben nog niet zoveel sterren, maar bevatten veel kosmisch stof. Belangrijker, ik ontdekte dat 75% van mijn sterrenstelsels Hα emissie uitzenden. Dit licht is direct afkomstig uit de gebieden rond jonge sterren, en daardoor een zeer geschikte indicator van de mate van stervorming in deze stelsels. Hierdoor bepaalde ik dat deze 26 sterrenstelsels gemiddeld een hoge mate van stervorming hebben, en 35 % van hen starburst stelsels zijn. Dit betekent dat ze bovenmatig veel sterren vormen in verhouding tot gewone stelsels op vergelijkbare roodverschuiving. Al met al heeft deze zeldzame en interessante populatie ons nieuwe inzichten in de fysische omstandigheden van relatief zwakke stelsels die vaak gemist worden in onderzoeken naar sterrenstelselpopulaties gebracht.

In het laatste onderdeel van deze scriptie, Hoofdstuk 5, hebben we de SMUVS catalogus gebruikt om een andere speciale populatie van sterrenstelsels te bestuderen. Deze stelsels zijn special omdat ze ook zijn waargenomen op hele lange golflengtes: het sub-/millimeter regime. Licht van deze golflengtes is afkomstig van kosmisch stof in een sterrenstelsel. Dit stof bestaat uit kleine silicaat granulomen die in het interstellaire medium rondzweven. Ze absorberen het UV licht afkomstig van jonge sterren, en zenden dat vervolgens op sub-/mm golflengtes weer uit. Dit licht biedt daardoor een alternatieve, indirecte methode om de mate van stervorming in een stelsel te meten. We hebben het sub-mm licht van deze sterrenstelsels waargenomen met ALMA: een interferometer bestaande uit 66 antennes in de Atacama woestijn van Chili.

Voor dit onderzoek focusten we ons op sterrenstelsels tussen $z = 2$–5.5. We hebben de verschillen tussen stelsel die wel en niet op langere golflengtes te zien zijn gemeten, en vonden dat ALMA-waargenomen stelsels zwaarder zijn en rodere kleuren hebben, veroorzaakt door de grote hoeveelheden kosmische stof in deze stelsels. We hebben de mate van stervorming gemeten in beide populaties met behulp van het UV en sub-mm licht. We vonden dat de ALMA-waargenomen sterrenstelsels deels normaal stervormende stelsels zijn, en deels starburst stelsels die een veel hogere mate van stervorming hebben. Vreemd genoeg vonden we ook sterrenstelsels die we wel classificeerden als starbursts aan de hand van hun UV licht, maar die we niet terugvonden in de ALMA-observaties, terwijl we dat wel zouden verwachten.

Om het samen te vatten; in deze scriptie heb ik data gebruikt van verscheidende telescopen die zich zowel op aarde als in de ruimte bevinden om voorspellingen te maken voor het identificeren van verre sterrenstelsels, om te bepalen hoe afhankelijk stellaire massa metingen zijn van algoritmes, om de eigenschappen van een voorheen onbekende sterrenstelselpopulatie te bepalen, en om te onderzoeken hoe sub-mm stelsels verschillen van de doorsnee sterrenstelsels die we niet terug zien op zulke lange golflengtes. Op deze manier zijn we weer een stapje dichterbij gekomen in het ontdekken van wat er allemaal tussen die felle lichtpunten op de hemel verstopt zit.

ACKNOWLEDGEMENTS

I would like to thank my cats and bunnies for being my loving companions who provided me with ample cuddles and emotional support whilst writing this thesis. Koda, Mavis, Bella, and Percy, and all the future rescues I hope to provide a safe home for, I dedicate this thesis to you.

Karina, thank you for all the advice you have given me over more than five years of working together. I deeply admire your passion for astronomy and your determination as a scientist. Thank you for being a strong female role model in my life; I have learned a lot about myself under your guidance. You taught me a lot of important science and soft skills over the years and you were always quickly available for helpful comments. I appreciate how you allowed me space and provided me support when I needed it, and really made an effort in supervising me.

Paul, despite that we only communicated in the finalizing months of my PhD, I very much appreciate you for taking on the role as my second promotor and proofreading the full thesis.

Pierluigi, Edoardo, Giulio, Vasily, Rafael, Josie, Guang, Smaran, and Gabriel, you guys are wonderful and helpful people, and I admire all of your hard work. I really appreciate how you all contributed to a safe and friendly atmosphere for our weekly group meetings.

Martine, thank you for all the love and patience you have shown me throughout our many years of friendship: I would not be the same person without you. We started this chapter of our lives in Groningen together, and I am sure there are many mutual chapters to come.

To all my wonderful friends, in no particular order. Jesper, I love how we make a great team for science communication; you are just so much fun. Nick, your thoughtfulness is really inspiring; thank you for the great talks we have had. Danny, I admire your dedication to a seemingly never-ending lists of niche interests; you remind me it is okay to spend time outside of work. Anno, I do not understand how you have the energy to take on all the activities, responsibilities, and hobbies that you do, but I am glad I can be a part of them. Sybrand, Bas, Jermain, Koen, and aforementioned, our D&D sessions have been true highlights over the past few years. Lotte, thank you for being my literal support in LoL, it has been lots of fun. Job and Francis, thank you for the good times in the master room, we really pulled each other through our studies. Jesse, Silke, Hylke, Bas, Tomas, Marenthe, Casper, Thijs, and Mathijn, it would not have been the same without you. To all my friends from outside of Groningen, thank you for letting me vent when I needed it.

To all the teachers at Kapteyn, thank you for providing a nurturing and inspiring environment in which my love for astronomy could flourish. Reynier, your dedication to both scientific and amateur astronomy has been really inspiring. Thank you for taking us to La Palma and for being so approachable and supportive. John, thank you for the time working together on my bachelor thesis and in the program committee, your enthusiasm

for science is infectious. Marlies and Rien, thank you for being such welcoming, hard-working and inspiring people; by your dedicated example, I fell in love with science communication.

To the secretariat and the computer group: the institute would be nothing without you. Thank you for keeping it running. Lucia and Raffaella, you stepped in with great advice and support when I needed it, and I am very thankful that you did.

To my colleagues at the Kapteyn institute, you make our scientific institute special. To my fellow borrel committee members, thank you for pulling through together and organizing an amazing Kastanjefeest. To the members of the Euclid Consortium, thank you for providing a welcoming and supportive environment for young scientists.

I would like to thank my parents, grandparents, and family for believing in me, and indulging my interest for astronomy over the past 15 years. Thank you for attending my ceremonies and public events, and making an effort to understand my work. To my sister Lotte, thank you for all the confidence you have given me with your endless praise; I return that feeling, as I am incredibly proud of you. To my siblings, Mees, Jente, and Brecht, it has been a pleasure watching you grow up, and I can't wait to see what careers you will choose for yourself; I hope you will indulge some well-meant advice from your big sister from time to time.

To my wonderful husband Kwintijn, thank you for all the cups of tea, proofreading of my work, technical support, and most of all, emotional availability. I could not have done this without you.